Lecture Notes in Electrical Engineering 549

Zhongliang Jing *Editor*

Proceedings of International Conference on Aerospace System Science and Engineering 2018

Springer

Lecture Notes in Electrical Engineering

Volume 549

The book series *Lecture Notes in Electrical Engineering* (LNEE) publishes the latest developments in Electrical Engineering - quickly, informally and in high quality. While original research reported in proceedings and monographs has traditionally formed the core of LNEE, we also encourage authors to submit books devoted to supporting student education and professional training in the various fields and applications areas of electrical engineering. The series cover classical and emerging topics concerning:

- Communication Engineering, Information Theory and Networks
- Electronics Engineering and Microelectronics
- Signal, Image and Speech Processing
- Wireless and Mobile Communication
- Circuits and Systems
- Energy Systems, Power Electronics and Electrical Machines
- Electro-optical Engineering
- Instrumentation Engineering
- Avionics Engineering
- Control Systems
- Internet-of-Things and Cybersecurity
- Biomedical Devices, MEMS and NEMS

For general information about this book series, comments or suggestions, please contact leontina.dicecco@springer.com.

To submit a proposal or request further information, please contact the Publishing Editor in your country:

China
Jasmine Dou, Associate Editor (jasmine.dou@springer.com)

India
Swati Meherishi, Executive Editor (swati.meherishi@springer.com)
Aninda Bose, Senior Editor (aninda.bose@springer.com)

Japan
Takeyuki Yonezawa, Editorial Director (takeyuki.yonezawa@springer.com)

South Korea
Smith (Ahram) Chae, Editor (smith.chae@springer.com)

Southeast Asia
Ramesh Nath Premnath, Editor (ramesh.premnath@springer.com)

USA, Canada:
Michael Luby, Senior Editor (michael.luby@springer.com)

All other Countries:
Leontina Di Cecco, Senior Editor (leontina.dicecco@springer.com)
Christoph Baumann, Executive Editor (christoph.baumann@springer.com)

**** Indexing: The books of this series are submitted to ISI Proceedings, EI-Compendex, SCOPUS, MetaPress, Web of Science and Springerlink ****

More information about this series at http://www.springer.com/series/7818

Zhongliang Jing
Editor

Proceedings of International Conference on Aerospace System Science and Engineering 2018

Springer

Editor
Zhongliang Jing
School of Aeronautics and Astronautics
Shanghai Jiao Tong University
Shanghai, China

ISSN 1876-1100 ISSN 1876-1119 (electronic)
Lecture Notes in Electrical Engineering
ISBN 978-981-13-6060-2 ISBN 978-981-13-6061-9 (eBook)
https://doi.org/10.1007/978-981-13-6061-9

Library of Congress Control Number: 2018967748

This Springer imprint is published by the registered company Springer Nature Singapore Pte Ltd.
The registered company address is: 152 Beach Road, #21-01/04 Gateway East, Singapore 189721, Singapore

Contents

Remote Sensing Image Registration Based on the HEIV Model 1
Chen Chen, Yongjun Zhou, Yuanxiang Li, Hongya Tuo and Yu Zhou

Dynamics of Miura Folded Metamaterials 17
Dapeng Zhang and Xiang Zhou

Error in Sound Source Localization of Phased Microphone Array Caused by Installation Position Deviation of Microphone Array 39
Huan Bao, Wei Ma and Mingsui Yang

A Survey on Object Tracking in Aerial Surveillance 53
Junhao Zhao, Gang Xiao, Xingchen Zhang and Durga Prasad Bavirisetti

Application and Improvement of Gas Turbine Blades Film Cooling 69
Koval Svetlana

Damage Tolerance Analysis for Repaired Composite Stringer Panels 93
Lin Ma and Yin Yu

Digital Image Correlation Method Based on SURF in Airship Envelope Measurement 105
Liuyue Zhao, Quanbao Wang, Pingfang Zhou and Dengping Duan

Dynamic Collision Avoidance Strategy for Unmanned Aerial Vehicles Formation Flight 121
Minghua Wang and Shiqiang Hu

Detection of Acoustic Emission Signal Due to Impact Damage of Composite Materials Based EMD 137
Qingwen You, Zhefeng Yu and Jicheng Fang

Mathematical Modeling of Heat Transfer Processes in a Wall with a Regular Pseudo-pore Structure 155
P. Starikov, A. Ionov, S. Seliverstov, I. Borovik and A. Matushkin

Automatic Power Line Detection for Low-Altitude Aircraft Safety Based on Deep Learning 169
Xingchen Zhang, Gang Xiao, Ke Gong, Junhao Zhao and Durga Prasad Bavirisetti

A Method for Enhancing Low-Pressure Ignition of n-Decane Based on Increasing Hydroxyl Free Radicals 185
Yaming Shi, Xiaobin Huang and Hong Liu

A Similarity Comparison Method of Flight Test Points 197
Yibo Liu, Gang Xiao and Yong Chen

Author Index 213

Remote Sensing Image Registration Based on the HEIV Model

Chen Chen, Yongjun Zhou, Yuanxiang Li, Hongya Tuo and Yu Zhou

Abstract In Earth observation missions, a large number of remote sensing images (RSIs) are obtained through satellites and aerial photography. RSIs are often huge and they generally have large edge distortions. Therefore, registration is required when the RSIs are used for mapping and change-detection. Since the RSIs usually have complex variation and the large distortions, the current existing global image registration algorithms cannot achieve high-precision matching of the target area. We propose a method based on the Heteroscedastic error-in-variables (HEIV) model to solve the registration problem of RSIs. Though HEIV model, the registration parameter estimation problem can be expressed as a quasi-linear form of the design matrix, which consists of observation vectors and parameter vectors with heteroscedasticity. Based on the image pre-processing and feature intensity, the HEIV model is utilized to estimate the registration parameters. Experiments are carried by using the RSIs taken with helicopter in comparison with the method based on Harris corner registration and the method based on SIFT registration, respectively. Compared with the Harris, the best group's accuracy is increased by 54.76%. In comparison with the SIFT algorithm, the T-Rank group's increment on RMSE is 1.88%. The results show that our method has more advantages in the parameter estimation of RSI registration and it can be better applied to Earth observation missions.

C. Chen (✉) · Y. Li · H. Tuo
School of Aeronautics and Astronautics, Shanghai Jiao Tong University, Shanghai, China
e-mail: ccceline@sjtu.edu.cn

Y. Li
e-mail: yuanxli@sjtu.edu.cn

H. Tuo
e-mail: hytuo@sjtu.edu.cn

Y. Zhou
School of Naval Architecture, Ocean & Civil Engineering, Shanghai Jiao Tong University, Shanghai, China
e-mail: yjzhou@sjtu.edu.cn

Y. Zhou
Institute of Surveying and Mapping, Information Engineering University, Zhengzhou, China
e-mail: hb48_zy@163.com

Z. Jing (ed.), *Proceedings of International Conference on Aerospace System Science and Engineering 2018*, Lecture Notes in Electrical Engineering 549,
https://doi.org/10.1007/978-981-13-6061-9_1

Keywords HEIV model · Image registration · Structured total least squares · Random sampling consistency

1 Introduction

Image registration is a part of the fundamental problems of remote sensing images processing. It refers to align two or more images of the same target or scene acquired under the same or different time, sensors or views. Image registration is commonly used in the fields of aerospace, geographic information system, image fusion, target recognition, medical image analysis and robot vision. In surveying and remote sensing applications, whether aerial photography or satellite remote sensing, due to the limited area covered by a single image, obtained remote sensing images need to be accurately registered and spliced for subsequent processing.

Remote sensing images have a large amount of information, and the image points of sight have heterogeneous and nonlinear geometric deformation. Traditional affine transformation performs poorly in remote sensing images, and such images may have a large amount of image registration work based on photographic collinear equations, nuclear lines, differential corrections, etc. In addition, when acquiring remote sensing images, the shooting details are often missing, so the traditional photogrammetry processing encounters bottlenecks. This paper proposes to explore the registration of remote sensing images in the field of computer vision.

The registration methods in the field of computer vision are mainly divided into two categories: one is the registration methods based on regional grayscale features and the other is methods based on local features such as image point, line, surface or other features. The regional grayscale feature-based methods mainly focus on gray information of images. Two kinds of algorithms based on image domain or frequency domain are always used throughout this situation. The former mainly includes the cross-correlation method [1], the maximum mutual information method [2] and the maximum likelihood matching method [3]. The latter mainly includes the phase correlation method based on the Fast Fourier Transform [4, 5] or Wavelet transform [6] and so on. The local feature-based methods require a certain number of matching features. Matching point features detection methods include SIFT [7], SURF [8] and Harris [9]. Remote sensing image has a larger coverage area and is strongly affected by photography conditions and terrain conditions, and requires high matching precision, speed and robustness.

Registration is one of the hot issues in the field of remote sensing. In recent years, many new research results have emerged in the fields of registration strategy and registration algorithm. Based on the SURF method, Dong et al. [10] used the Haar wavelet response to establish descriptors and made full use of grayscale information and detail information. Ma et al. [11] adopted greedy method based on the largest group problem to make the control points be evenly distributed and improve the registration accuracy. Cao et al. [12] used the remote sensing image of multispectral information and the land cover patch information for image registration. Han [13]

divided the image into small areas, which were accurately registered separately. Cheng et al. [14] recovered the homography matrix by using the imaging information such as position and pose of sensors and did not have to extract the features to achieve fast image registration. However, due to the position or attitude errors of imaging platform, the registration accuracy is poor.

Commonly registration methods usually extract the features of the whole image and treat the matching points equally to calculate the registration parameters. However, due to the distribution of features, imaging conditions and other factors often have unequal accuracy characteristics. In this paper, the Heteroscedastic errors-in-variables (HEIV) model is introduced [15–17], and a registration method based on HEIV model is proposed. This method sets the corresponding weight according to the extraction accuracy and distribution characteristics of features, thereby improving the registration accuracy. At the same time, the registration accuracy of regions of interest can be enhanced by reasonably setting the weight of matching points in different regions. Experiments demonstrate that the proposed method is better to the traditional global registration method and has strong practicability.

2 The Basic Method of Image Registration

The most typical model of remote sensing image registration is the affine transformation model. Assuming that $U(u, v)$ and $Y(x, y)$ denote the coordinates to be registered and the reference coordinates of a point respectively, a_0, a_1, a_2, b_0, b_1 and b_2 denote six affine transformation parameters, transform model can be expressed as:

$$\begin{cases} x = a_0 u + a_1 v + a_2 \\ y = b_0 u + b_1 v + b_2 \end{cases} \tag{1}$$

Assuming there are n ($n \geq 3$) pairs of matching points, the traditional method of parameter estimation is the least squares solution as follows:

$$\min : \ (\boldsymbol{y} - \boldsymbol{A\theta})^T (\boldsymbol{y} - \boldsymbol{A\theta}) \tag{2}$$

The transformation parameters are

$$\boldsymbol{\theta} = \left(\boldsymbol{A}^T \boldsymbol{A}\right)^{-1} \boldsymbol{A}^T \boldsymbol{y} \tag{3}$$

The above algorithm treats each pair of matching points equally and solves the geometric transformation parameters, while the characteristics of remote sensing images are quite different. Taking high-resolution remote sensing as an example, the features extracted from the building area are quite different from the features extracted from the vegetation area (Fig. 1). Therefore, it is reasonable to give the

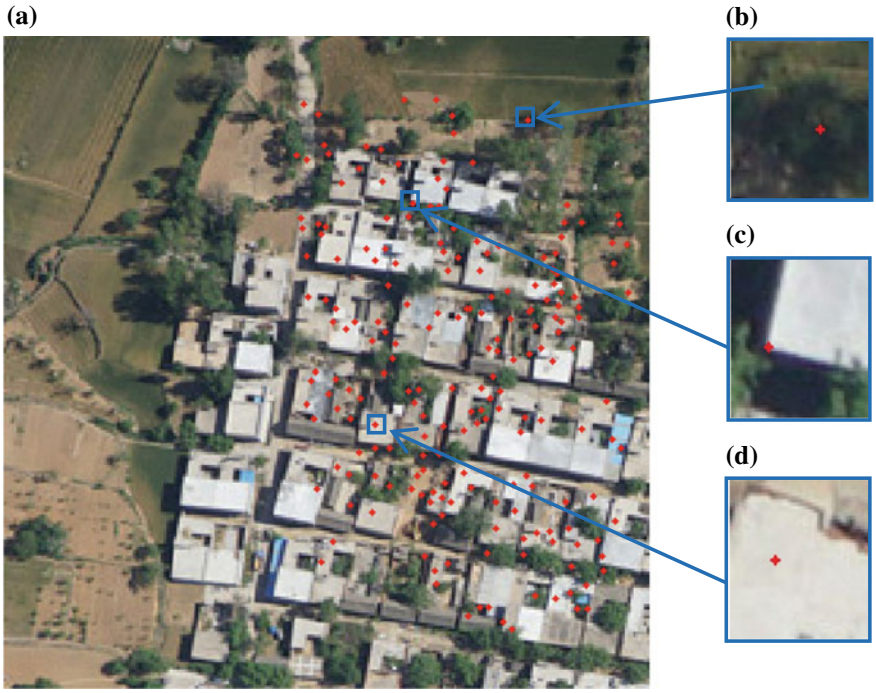

Fig. 1 Feature points extracted from the image. (**a**) is the original image, (**b–d**) is the feature point of different accuracies of the building region and the vegetation region extracted by the SIFT algorithm, respectively

corresponding weight differently according to the accuracy of the features, in this paper, the heteroscedasticity model, which takes into account the unequal precision of feature points, is used for image registration. The extracted feature points which extracted from different regions are shown in Fig. 1.

The figure clearly demonstrates that the points in different regions have different precision. In general cognition, the corner points extracted on a building are more accurate than the points on the vegetation that relies primarily on texture.

For the purpose of mapping, the building part should be registered more accurately than other regions, while the traditional method does not take into account of the accuracy of the various regions on the transformation model. The remote sensing image points of sight have heterogeneous and nonlinear geometric deformation. When these points are used for image registration, they have different effects on the final affine registration parameters.

Therefore, variable heterogeneity noise (HEIV) model is introduced to constrain the point feature points in each region and improve the registration accuracy of the target region.

3 Registration Method Based on the HEIV Model and Parameter Estimation

3.1 Registration Method Based on the HEIV Model

The HEIV model is widely used in the parameter estimation task in computer vision [17]. The problem of vision parameter estimation is expressed as a quasi-linear form consisting of a design matrix consisting of observation vector with heteroscedasticity and parameter vectors:

$$\boldsymbol{\varphi}(\tilde{\boldsymbol{l}}_i)\boldsymbol{\xi} = 0 \tag{4}$$

In Eq. 4, $\boldsymbol{\varphi}(\tilde{\boldsymbol{l}}_i) \in \mathbf{R}^{m\times p}$ is a matrix composed of observation vectors $\tilde{\boldsymbol{l}}_i$, where the superscript "~" indicates the error-free observation and $\boldsymbol{\xi} \in \mathbf{R}^p$ indicates the parameter vector. For the registration problem based on affine transformation, (1) can be expressed as:

$$\begin{aligned}
\boldsymbol{\varphi}(\tilde{\boldsymbol{l}}_i) &= \begin{pmatrix} \tilde{u}_i & \tilde{v}_i & 1 & 0 & 0 & 0 & \tilde{x}_i \\ 0 & 0 & 0 & \tilde{u}_i & \tilde{v}_i & 1 & \tilde{y}_i \end{pmatrix} \\
\boldsymbol{\xi} &= \begin{pmatrix} a_0 & a_1 & a_2 & b_0 & b_1 & b_2 & -1 \end{pmatrix}^{\mathrm{T}} \\
\tilde{\boldsymbol{l}}_i &= \begin{pmatrix} \tilde{u}_i & \tilde{v}_i & \tilde{x}_i & \tilde{y}_i \end{pmatrix}^{\mathrm{T}}
\end{aligned} \tag{5}$$

When the observed value is error free. Equation 4 holds. The observation vector here refers to the coordinate value of the reference points in the reference image and the image to be registered. However, in the registration problem, the observed values often contain errors. Suppose the observational errors follow the normal distribution:

$$\begin{aligned}
\boldsymbol{l}_i &= \tilde{\boldsymbol{l}}_i + \boldsymbol{e}_i \\
\boldsymbol{e}_i &\sim \mathrm{N}(\mathbf{0}, \sigma_0^2 \boldsymbol{Q}_i)
\end{aligned} \tag{6}$$

where $\boldsymbol{l}_i = (\, u_i \;\; v_i \;\; x_i \;\; y_i \,)^{\mathrm{T}}$ indicates the coordinates of the matching points containing the error, σ_0^2 is the unit of error, $\boldsymbol{Q}_i$ represents a cofactor matrix of dimension of 4×4, which can be given according to the matching point extraction accuracy. Considering Eq. 4 is a homogeneous model, it needs extra constraint to get a unique solution. Here, the condition that the L2-norm of the parameter vector is equal to 1 is used as the constraint condition. The numerical algorithm provided next will prove that using the unit vector restriction condition could simplify the calculation. Suppose there are n matching points ($n \geq 3$), then the original registration problem can be expressed as the following optimization problem:

$$\begin{aligned} &\min: \sum_{i=1}^{n} \boldsymbol{e}_i^T \mathbf{W}_i \boldsymbol{e}_i \\ &\text{s.t.: } \boldsymbol{\varphi}(\boldsymbol{l}_i - \boldsymbol{e}_i)\boldsymbol{\xi} = \mathbf{0}; \quad i = 1, \ldots, n \\ &\boldsymbol{\xi}^{\mathrm{T}}\boldsymbol{\xi} = 1 \end{aligned} \tag{7}$$

where $\mathbf{W}_i = \boldsymbol{Q}_i^{-1}$ expresses the weight matrix. The above method takes into account the unequal precision of all observations and is also called the Weighted Total Least Squares (WTLS) or Structured Total Least Squares (STLS) problem. It has been shown that the WTLS method is equivalent to the STLS method if the design matrix is a linear function of the observed values [18]. The registration problem based on the HEIV model is to solve the registration parameters given the two sets of coordinates of the matching point and its prior weight matrix. Then, the geometric transformation and resampling of the image to be registered are carried out. Considering that the existing WTLS method or STLS method solves the problem of more complicated and slow computation, a generalized SVD solution method is adopted here. We define $\boldsymbol{Z}_i$ and $\boldsymbol{E}_{\boldsymbol{Z}_i}$ as:

$$\boldsymbol{Z}_i = \boldsymbol{\varphi}(\boldsymbol{l}_i); \boldsymbol{E}_{\boldsymbol{Z}_i} = \boldsymbol{\varphi}(\boldsymbol{e}_i) \tag{8}$$

Then Eq. 7 is equivalent to:

$$\boldsymbol{Z}_i\boldsymbol{\xi} - \boldsymbol{E}_{\boldsymbol{Z}_i}\boldsymbol{\xi} = \boldsymbol{Z}_i\boldsymbol{\xi} - (\boldsymbol{\xi}^T \otimes \mathbf{I}_2)\mathrm{vec}(\boldsymbol{E}_{\boldsymbol{Z}_i}) = \mathbf{0} \tag{9}$$

where $\mathbf{I}_2$ represents a 2×2-unit matrix, and $\otimes$ represents the Kronecker product of the matrix. The vector $\mathrm{vec}(\boldsymbol{Z}_i)$ is expanded at the observations by only taking the first order Taylor series, which results in:

$$\mathrm{vec}(\boldsymbol{E}_{\boldsymbol{Z}_i}) = \left(\frac{\partial\varphi(\mathrm{vec}(\boldsymbol{Z}_i))}{\partial \boldsymbol{l}_i^{\mathrm{T}}}\right)\boldsymbol{e}_i = \boldsymbol{H}_i\boldsymbol{e}_i \tag{10}$$

where $\boldsymbol{H}_i$ is a 14×4 mapping matrix which is given as

$$\boldsymbol{H}_i^T = \begin{pmatrix} 1&0&0&0&0&0&0&1&0&0&0&0&0&0 \\ 0&0&1&0&0&0&0&0&0&1&0&0&0&0 \\ 0&0&0&0&0&0&0&0&0&0&0&0&1&0 \\ 0&0&0&0&0&0&0&0&0&0&0&0&0&1 \end{pmatrix} \tag{11}$$

After a simple iteration, Eq. 9 can be transformed into:

$$\begin{aligned} &\min: \ f(\boldsymbol{\xi}) = \boldsymbol{\xi}^{\mathrm{T}}\boldsymbol{M}\boldsymbol{\xi} \\ &\text{s.t.: } \boldsymbol{\xi}^{\boldsymbol{T}}\boldsymbol{\xi} = 1 \end{aligned} \tag{12}$$

where $\mathbf{M}$ is a positive definite matrix, its analytical expression is shown as:

$$\boldsymbol{M} = \sum_{i=1}^{n} \boldsymbol{M}_i = \sum_{i=1}^{n} \left\{ \boldsymbol{Z}_i^{\mathrm{T}} \left[\left(\boldsymbol{\xi}^{\mathrm{T}} \otimes \mathbf{I}_2 \right) \boldsymbol{H}_i \boldsymbol{Q}_i \boldsymbol{H}_i^T \left(\boldsymbol{\xi} \otimes \mathbf{I}_2 \right) \right]^{-1} \boldsymbol{Z}_i \right\} \tag{13}$$

The solution to model (13) is a generalized eigenvalue problem. The solution to the parameter corresponds to the eigenvector corresponding to the smallest eigenvalue after M-matrix SVD decomposition. After obtaining the parameters, it is only necessary to divide the last component by one parameter factor to -1 and to obtain six affine transformation parameters. Because the $\mathbf{M}$-matrix contains the parameters, it has to be iteratively calculated. The calculation process is summarized as follows:

(1) Giving the coordinates of the matching point and its co-array by the composition of design matrix:

$$\boldsymbol{Z}_i = \begin{pmatrix} u_i & v_i & 1 & 0 & 0 & 0 & x_i \\ 0 & 0 & 0 & u_i & v_i & 1 & y_i \end{pmatrix};$$
$$(i = 1, \ldots, n);$$

(2) Regardless of the weight of the observed value, calculating the initial value of the parameter $\hat{\boldsymbol{\xi}}_{(0)}$, which is the eigenvector corresponding to the minimum eigenvalue of the matrix $\sum_{i=1}^{n} \boldsymbol{Z}_i^T \boldsymbol{Z}_i$, and sets the number of iterations $k = 0$;

(3) Let $k = k + 1$ for the following iterations:
Calculating the normal Matrix $\mathbf{M}$.

$$\boldsymbol{M}_{(k)} = \sum_{i=1}^{n} \left\{ \boldsymbol{Z}_i^{\mathrm{T}} \left[\left(\hat{\boldsymbol{\xi}}_{(k-1)}^{\mathrm{T}} \otimes \mathbf{I}_2 \right) \boldsymbol{H}_i \boldsymbol{Q}_i \boldsymbol{H}_i^T \left(\hat{\boldsymbol{\xi}}_{(k-1)} \otimes \mathbf{I}_2 \right) \right]^{-1} \boldsymbol{Z} \right\}_i$$

Obtaining the parameter $\hat{\boldsymbol{\xi}}_{(k)}$, which is the eigenvector corresponding to the minimum eigenvalue of the matrix $\boldsymbol{M}_{(k)}$.

(4) If $\left\| \hat{\boldsymbol{\xi}}_{(k)} - \hat{\boldsymbol{\xi}}_{(k-1)} \right\| \leq \varepsilon$ (ε is a given threshold, generally less than 10^{-6}) holds, then the iterations end, else, returning to (3).

(5) Scaling the last component of the parameter to -1 to get the final transform parameter.
The process is represented in the table Algorithm 1 schematically.

Algorithm 1 Calculate transformation parameters based on the HEIV
Input: The coordinates of the matching point $\boldsymbol{Z}$, the weight matrix $\boldsymbol{Q}$
Output: The final transform parameter $\hat{\boldsymbol{\xi}}$

1. $k = 0$

calculate the initial value of the parameter $\hat{\boldsymbol{\xi}}_{(0)}$ by the matrix $\sum_{i=1}^{n} \boldsymbol{Z}_i^T \boldsymbol{Z}_i$

2. $k = k + 1$,
   calculate the Matrix $\mathbf{M}$ to obtain the parameter $\hat{\boldsymbol{\xi}}_{(k)}$
3. If $\left\| \hat{\boldsymbol{\xi}}_{(k)} - \hat{\boldsymbol{\xi}}_{(k-1)} \right\| \leq \varepsilon$
   Output $\hat{\boldsymbol{\xi}}_{(k)}$
   else
   Return **2**.
   end
4. Normalize $\hat{\boldsymbol{\xi}}_{(k)}$ to get the final parameters.

3.2 Method for Calculating Weight of Feature Points in Region of Interest

Compared with the traditional registration method, the fundamental problem of the registration method based on HEIV algorithm is to extract the matched points and give reasonable weight. The proposed method of weight can be given as follows:

(1) While extracting the feature points, the weight corresponding to the feature points is accurately calculated. For example, sing the Harris operator or the Forstner operator. The covariance matrix of the matching points can be precisely achieved.
(2) The empirical weight is given according to the characteristics of feature points, such as the weight in a SIFT-based registration algorithm can be given founded on the similarity of the extracted features. We can also set experience weight according to the feature location, such as the building features are given larger weight and the terrain features are given a smaller weight.
(3) Given the approximate weighting ratio of different types of regions and then using the variance component estimation to accurately determine the ratio, this method requires fewer weight, more matching points, and will increase the computational expenses.

3.3 The Process Flow of Image Registration Based on the HEIV Model

Taking the application of the ground object measurement and the change-detection of the remote sensing images obtained by aerial photography at different times as an example, a uniform geometric transformation of the entire image will result in high

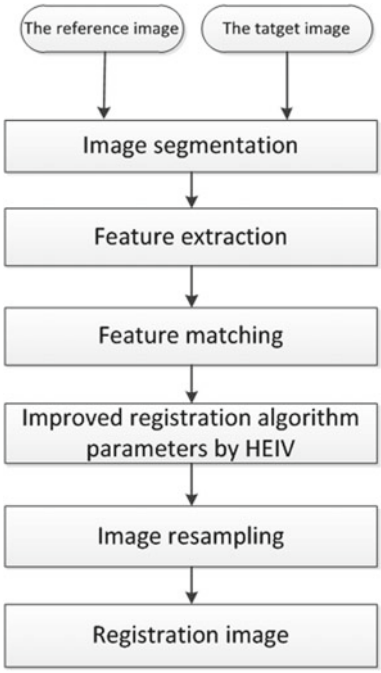

Fig. 2 The image registration based on HEIV algorithm

registration accuracy in the area of feature set and low registration accuracy in other areas. Blocking the entire image will result in noticeable registration errors at the edges of the tiles. In surveying and mapping applications, the registration accuracy of the areas where the objects need to be concentrated should be high as the registration accuracy of the vegetation areas can be appropriately reduced. For arable land survey tasks, high registration accuracy required in arable land area. The HEIV registration method can largely meet the above objectives by reasonably setting the weight of different locations and correcting the distortion of an auxiliary image.

The realization of this method can be divided into the following four steps:

Step 1. Divide the obtained the reference image and the target image into regions of interest and non-regions of interest by watersheds. (This article is divided into building area and vegetation area).
Step 2. According to the segmentation parameters, using SIFT algorithm to extract feature points and use RANSAC method to match, and according to the characteristics of the region and the operator, gave the corresponding weight;
Step 3. Use the HEIV model to improve global affine transformation parameters;
Step 4. The floating image is resampled and interpolated using affine transformation parameters to obtain the registration image.

Algorithm flow chart is as follows (Fig. 2).

4 Experimental Results and Analysis

Aiming at the HEIV-based registration algorithm proposed in this paper, a large number of remote sensing images are used to perform image registration experiments. The proposed method is subjectively and objectively evaluated with SIFT and Harris algorithms. In the subjective aspect according to the picture of the visual effect of as the registration performance evaluation. In the objective aspects, the same name point distance error is regarded as the evaluation index.

Experimental operating environment: CPU for Intel Core i7, 3.20 GHz, 8 GB of memory for the PC, 64 Win7 operating system, and the MATLAB's version is 8.3.0.532 (R2014a).

4.1 Registration Experiment Results

The picture area used in this experiment is the area of Dengfeng City, Henan Province, China. The images used are remote sensing images from helicopter aerial photography and 6 groups are selected for display. Image content for large areas of farmland forest and village construction area, the size of the image interception 360 × 360, resolution of 350 dpi, the pixel resolution of about 1.3 m.

The All-Build group is to give the construction area feature points the maximum weight, ignoring the other area feature points. The T-Fix group is to assign weight to the feature points by region. In this experiment, the weight ratio of buildings and vegetation areas is set to 0.7:0.3. The T-Rank group assigns weight to points according to the intensity of feature points and calculates affine parameters. It first sorts the feature points so that the weight of each point is proportional to the feature intensity.

The experiment compares registration result of the global feature, the All-Build group the T-Rank group and the T-Fix group, which are represented by (f), (g), (h), (i) in Fig. 3, respectively. It is observed that when the All-Build group assigns high weight to the target region according to the prior knowledge of the segmentation, the aliasing effect of the target region can be basically eliminated, the pixel misalignment is reduced, and the visual effect is globally optimal. The T-Fix and T-Rank algorithms are also visually superior to the global registration algorithm, indicating the effectiveness of the proposed algorithm.

As shown in Fig. 4, the following six groups of experiments show that there are differences between the vegetation area and the building area in each group. The size of the construction area increases according to the serial number, and the area of the vegetation area decreases.

Subjective evaluation of the human eye by the above experimental results shows that when the weight of a certain region takes the extreme value, the accuracy of the region is the highest, and the aliasing effect of the target region is basically eliminated to reduce the pixel dislocation.

(a) the reference image

(b) the target image

(c) the reference segment image

(d) the target segment image

(e) All feature points extracted by SIFT algorithm

Fig. 3 Image registration experiment results

(f) Direct registration the registration result

(g) The All-Build group

(h) The T-Rank group

(i) The T-Fix group

Fig. 3 (continued)

4.2 Registration Effect Objectively Evaluation

The root mean square error (RMSE) is used as the measure of the distance between the reference image and the image of the matched points after registration to objectively evaluate the image registration performance.

When the target area is building area, the RMSE is calculated by selecting the correspondence in the building area. According to Table 1, when the weight of the building area is 1 and the weight of the vegetation area is 0 in the All-Build group, the registration error of the building area is the smallest. The registration accuracy of T-Fix group is better than Harris angle algorithm and SIFT global registration method, which proves the effectiveness of the proposed algorithm. Compared with the Harris, the All-Build group's accuracy is increased by 54.76% and the T-Rank group is

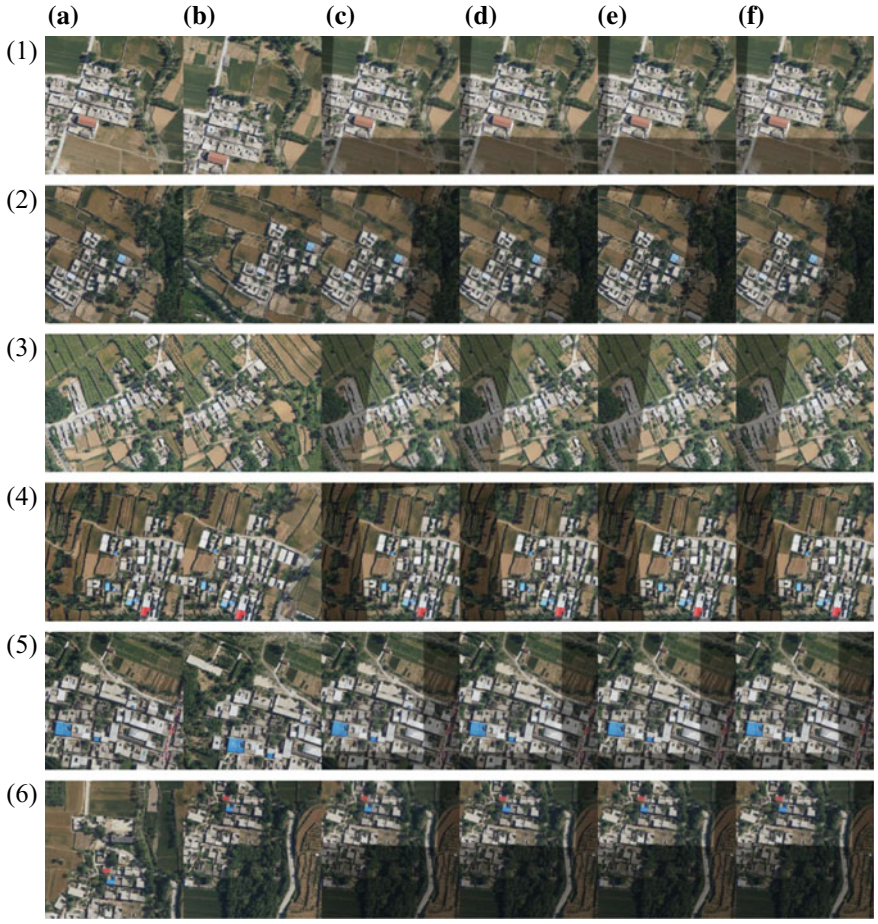

Fig. 4 **a** The reference image, **b** the target image, **c** Harris, **d** SIFT, **e** the all-build group, **f** the T-Fix group

increased by 41.39% In comparison with the SIFT algorithm, the T-Rank group's increment on RMSE is 1.88%, and the best group is All-Build whose increment is 24.26%.

As can be seen in Fig. 5, we can find that when the weight of a certain region takes the extreme value, the registration accuracy of the region increases. On the contrary, the registration accuracy decreases. Each region is weighted by multiple verifications, and the error within a certain range is less than the overall feature points without SIFT. Therefore, choosing the appropriate weight for registration can improve the accuracy of the target region. As can be observed in the above figure, the global optima of sub-regional registration is 0.3, so we give the ratio of the best empirical value of the residual weight of 0.7:0.3.

Table 1 Registration accuracy (unit pixel)

Image groups	Harris	SIFT	All-build	T-Rank	T-Fix
(1)	2.036	0.8727	0.5141	0.5617	0.5108
(2)	0.458	0.5520	0.5282	0.6079	0.5253
(3)	1.483	0.6233	0.3291	0.6101	0.4274
(4)	0.6149	0.6413	0.5164	0.5597	0.5932
(5)	0.8377	0.5152	0.4699	0.6598	0.5168
(6)	0.8508	0.5470	0.4836	0.6819	0.5051
Average value	1.04673	0.62525	0.47355	0.6135	0.5131

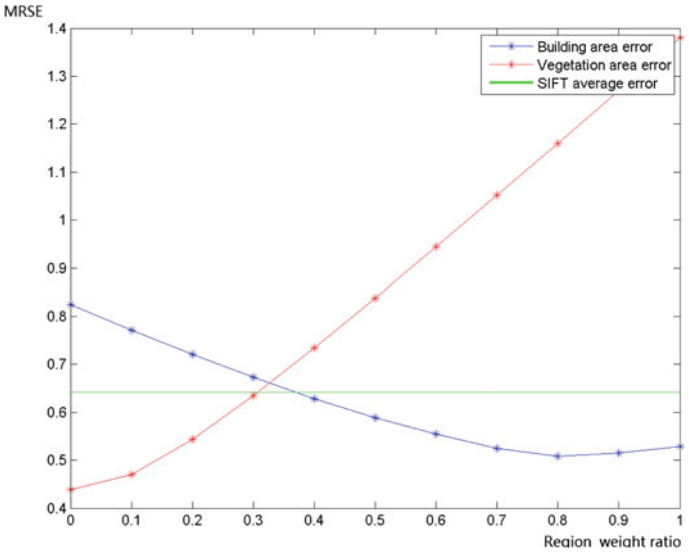

Fig. 5 Impacts of the proportion of vegetation and building areas on the registration accuracy of building areas (The *x*-axis represents the area weight and the *y*-axis represents the registration error. The blue line and the red line represent the error of the building area and the vegetation area respectively. Changes in weight in this area increase and the green line represents the average error in the SIFT algorithm.)

5 Summary

Registration in high-resolution remote sensing images is a fundamental and challenging task. Traditional affine transformation performs poorly in remote sensing images. In this paper, we propose to apply HEIV model to estimate the registration parameter. Under the knowledge of experience, the feature points in each region are given different weight, and refined image registration affine transformation parameters are obtained. The experimental results show that the proposed algorithm has

great advantages in the parameter estimation of the regional remote sensing image registration process and can be applied to the registration of multi-temporal remote sensing images. Moreover, the distribution of the weight of the feature points depends largely on the statistical characteristics of the priori segmentation, the accuracy of the segmentation has an impact on the registration parameters, and the experimental results show that the accuracy of the parameters depends on not only the segmentation of the image, but also on the image distortion. These problems need to be studied in the future.

References

1. Martinez, A., Garcia-Consuegra, J., & Abad, F. (1999). A correlation-symbolic approach to automatic remotely sensed image rectification. In *Geoscience and remote sensing symposium, 1999. IGARSS '99 proceedings. IEEE 1999 international* (Vol. 1, pp. 336–338). IEEE.
2. Colerhodes, A., Zavorin, I., & Moigne, J. L. (2001). Mutual information as a similarity measure for remote sensing image registration. *Proceedings of SPIE—The International Society for Optical Engineering, 4383*(4383), 51–61.
3. Li, W., & Leung, H. (2004). A maximum likelihood approach for image registration using control point and intensity. *IEEE Transactions on Image Processing, 13*(8), 1115–1127.
4. Anuta, P. E. (1970). Spatial registration of multispectral and multitemporal digital imagery using fast fourier transform techniques. *IEEE Transactions on Geoscience Electronics, 8*(4), 353–368.
5. Reddy, B. S., & Chatterji, B. N. (1996). An FFT-based technique for translation, rotation, and scale-invariant image registration. *IEEE Transactions on Image Processing, 5*(8), 1266.
6. Antonini, M., Barlaud, M., Mathieu, P., et al. (1992). Image coding using wavelet transform. *IEEE Transactions on Image Processing*, *1*(2), 205–220. A Publication of the IEEE Signal Processing Society.
7. Lowe, D. G. (2004). Distinctive image features from scale-invariant key-points. *International Journal of Computer Vision, 60*(2), 91–110.
8. Bay, H., Ess, A., Tuytelaars, T., et al. (2008). Speeded-up robust features. *Computer Vision and Image Understanding, 110*(3), 404–417.
9. Harris, C., & Stephens, M. (1988). A combined corner and edge detector. *Alvey Vision Conference, 15,* 50.
10. Dong, Q., Liu, J., & Zhou, Q. (2017). Image registration algorithm based on improved surf and its application to remote sensing image mosaicing. *Journal of Jilin University*, *3*.
11. Xu-Yan, M. A., Yuan, Y., Wang, C.-Y., et al. (2016). Homogenization algorithm for high resolution remote sensing image registration control points. *Remote Sensing Information*, *31*(3), 24–30.
12. Cao, S., Pan, Y.-Z., Zhang, J.-S., et al. (2014). Automatic registration of multi-temporal remote sensing images of land cover patches. *Journal of Surveying & Mapping*, (3), 290–297.
13. Han, Y., Bovolo, F., & Bruzzone, L. (2017). Segmentation-based fine registration of very high resolution multitemporal images. *IEEE Transactions on Geoscience and Remote Sensing, 55*(5), 2884–2897.
14. Zhengang, C., & Zhang, L. (2016). A aerial image stitching method based on UAV pose information. *Journal of Surveying and Mapping*, *45*(6), 698–705.
15. Soderstroma, T., Wang, L. P., Pintelonc, R., & Schoukens, J. (2013). Can errors-in-variables systems be identified from closed-loop experiments? *Automatica*, *49*(2), 681–684.
16. Cerone, V., Piga, D., & Regruto, D. (2012). Setmembership error-in-variables identification through convex relaxation techniques. *IEEE Transactions on Automatic Control, 57*(2), 517–522.

17. Matei, B. C., & Meer, P. (2006). Estimation of nonlinear errors-in-variables models for computer vision application. *IEEE Transactions on Pattern Analysis and Machine Intelligence, 28*(10), 1537–1552.
18. Zhou, Y., Kou, X., Li, J., et al. (2016). Comparison of structured and weighted total least-squares adjustment methods for linearly structured errors-in-variables models. *Journal of Surveying Engineering*, *143*(1), 04016019.

Dynamics of Miura Folded Metamaterials

Dapeng Zhang and Xiang Zhou

Abstract In this paper, we investigated dynamics of Miura-origami structures composed of Miura cells with rigid facets and elastic hinges, under three types of excitation: harmonic force, harmonic displacement and impact. Under the simple harmonic excitations of force and displacement, different crease stiffnesses affected the vibration responses of Miura folded Metamaterials. The results show that the Miura model of the single-degree-of-freedom structure has similar frequency responses under the two kinds of excitation. By changing the crease stiffness, it can change its resonance frequency and achieve a good low-frequency vibration isolation effect. The multi-degree-of-freedom model can reduce the resonance frequency by increasing the number of stacks. Under the impact load, there are two types of mechanical waves: shock wave and vibration wave. Except the first layer, the other Miura units will have the deformation characteristics of stretching before compression. The propagation speed of mechanical waves and ratio of the maximum strain amplitude at different layers can be designed by changing the crease stiffness. Meanwhile, the response of multi-layer stacked Miura folded Metamaterials is very different at steady state. The influence of damping coefficient on vibration wave is more obvious. When the impact load amplitude is changed, the response at steady state is almost constant.

Keywords Miura-origami · Harmonic excitation · Impact · Frequency response

1 Introduction

Most research on folded Metamaterials has been focused on Miura folded Metamaterials and variations derived from them at the present, mainly studying their static and quasi-static mechanical properties (2017). For example, Zhou et al. [1] studied

D. Zhang (✉) · X. Zhou
Department of Aeronautics and Astronautics, Shanghai Jiao Tong University, Shanghai, China
e-mail: Zhang_Dapengsjtu@163.com

X. Zhou
e-mail: xiangzhou@sjtu.edu.cn

Z. Jing (ed.), *Proceedings of International Conference on Aerospace System Science and Engineering 2018*, Lecture Notes in Electrical Engineering 549,
https://doi.org/10.1007/978-981-13-6061-9_2

the quasi-static mechanical properties of Miura and its derived structures, and analyzed their bending and shear properties through finite element modeling. Schenk et al. [2] studied the quasi-static properties of stacked Miura Metamaterials through finite element analysis and discussed its manufacturing process. Liu et al. [3] studied quasi-static deformation characteristics of folded plate made of Elvaloy by experimental analysis and comparing the simulation results. The results show that folding plate made from this material has high reuse rate.

The work on the dynamical analysis of folded Metamaterials was relatively rare. The folded structure was usually simplified to spring-mass equivalent model and multi-link equivalent model to study the dynamic response. Most of the system characteristics were neglected in mentioned. Fang et al. [4] studied the self-stability characteristics of a new Miura folded metamaterial. Experimental analysis showed various dynamic responses under the simple harmonic displacement excitation. With the Fourier transform, the main frequency was studied. It's noted that the folded metamaterial can be designed through adjusting the crease stiffness. Sadeghi et al. [5] designed a kind of quasi zero stiffness characteristics of their folding Metamaterials structure by sealing compressed air in the folding structure. Spring-mass equivalent model was analyzed. Note that the structure could provide effective low-frequency vibration isolation. Yasuda et al. [6, 7] simplified Tachi-Miura polyhedron (TMP) tubular folded metamaterial into the equivalent analysis model of multi-link structure and spring-mass model, and studied the impact response of the metamaterial. The TMP structure is divided into different TMP units by massless partition board, and the propagation characteristics of internal waveform are studied under the effect of instantaneous impact. It reveals that the impact load acting on one end is propagated internally in the form of small-amplitude soliton wave, which shows that the metamaterial has good impact resistance.

2 Origami Modeling and Prototype

Figure 1a shows the prototype consisted of Miura-based cells and separators, which supports the Miura to slide upon. In order to investigate the dynamics without unnecessary complexities, we assume the facets to be rigid, and the creases to be elastic hinges of non-prescribed torsional stiffness. Specifically, we assume that the torsional spring stiffness per unit length for the creases between two facets are the same in a single cell as k_a. Figure 1b shows the second type of Miura configuration with two cells combined. We assign k_a and k_b as the torsional spring stiffness per unit length in two cells, and k_c between them.

Considering that an origin Miura-origami retains a single-degree-of-freedom (DOF) for folding, we use multiple Miura unit cells, and separators (no-mass plates with zero thickness) between them to construct a multi-DOF structure. Figure 2 shows a configuration with multiple DOF composed of 10 stacked Miura cells, separated by no-mass plates, which support the Miura to slide upon. In this paper, we

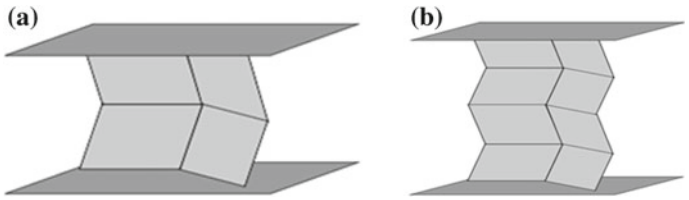

Fig. 1 **a** A configuration with single cell of Miura-ori and two plates supported. **b** A configuration with two cells combined

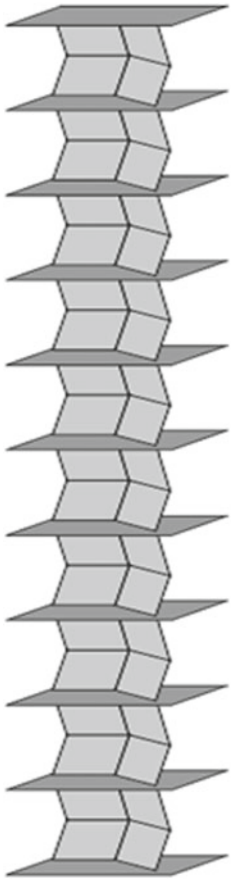

Fig. 2 A configuration with ten stacked Miura-ori with dividing plates

discussed two types of prototypes: all cells with same stiffness and every two units with different stiffness from top to bottom as k_a and k_b.

2.1 Boundary Conditions

Both sides of the Miura cell is able to slide in the surface of the separators, which have only one freedom of vertical direction. We clamped the bottom edge while we discussed the response for harmonic force and impact.

2.2 Excitation

To explore the response of the Miura-based prototype, we applied different kinds of excitation in the vertical direction: harmonic force, harmonic displacement and impact force. We examine in dynamic behavior under various excitation frequencies from 0.01 to 100 Hz, which is divided with logarithmic transformation into 41 sets of data. Each group of data was obtained through a 1000-step virtual experiment and lasted for 20 excitation periods.

The harmonic force is:

$$F = F_0 \times \sin(\text{Time} \times \omega) \tag{1}$$

where F_0 denotes the amplitude of the excitation force, and ω denotes the frequency.

The harmonic displacement:

$$X = X_0 \times \sin(\text{Time} \times \omega) \tag{2}$$

where X_0 is the amplitude of the excitation displacement, and ω is the frequency.

The impact force:

$$\begin{aligned} F = {} & F_0 \times \text{Step}(\text{Time}, 0, 0, 0.1, 1) \\ & + F_0 \times \text{Step}(\text{Time}, 0.1, 0, 0.2, -1) \end{aligned} \tag{3}$$

where F_0 and ω denote the amplitude of the excitation force and the frequency.

3 Results

By applying different kinds of excitation, we examine it dynamic behavior under various frequencies. To derive the frequency response, we define the magnitude of the response force as:

$$F_{\text{mrf}} = (F_{\max} - F_{\min}) \tag{4}$$

where $F_{\max}$ and $F_{\min}$ are the maximum and minimum of the value of the response force.

Considering that the dynamic response of the Miura prototype can be highly nonlinear, we use the root mean square (rms) value of the displacement data to characterize the average vibrational energy. Dividing the rms of the response displacement by the rms of the excitation displacement, we derive the displacement transmissibility of the Miura prototype in terms of the rms value:

$$T_{\text{rms}} = \frac{X_{\text{rms}}}{Y_{\text{rms}}} = \frac{\sqrt{\left(x_1^2 + x_2^2 + \cdots + x_N^2\right)/N}}{\sqrt{\left(y_1^2 + y_2^2 + \cdots + y_N^2\right)/N}} \tag{5}$$

where x_i and y_i $(i = 1, 2, ..., N)$ denote the data points in the displacement time histories, and x_i for the displacement of the top plate, y_i for the excitation.

3.1 Vibration Response of a Single-Degree-of-Freedom Miura Model with Different Crease Stiffness Under Simple Harmonic Force Excitation

The frequency response of the single-layer Miura model with different crease stiffness was analyzed. Model parameters are shown in Table 1. Figure 3 shows that under the harmonic force, the amplitude changes with frequency response force from three stages. The response force amplitude and amplitude of the exciting force are basically identical in the first stage under low-frequency excitation. In the second stage, with no damping in the creases, the amplitude of the response force is much larger than that of the excitation force while resonating. In the third stage, frequency continues to increase and the response force decrease. By changing the stiffness, different resonant frequencies can be obtained. It should be noted that when the crease stiffness is reduced to a certain value, the resonance could cause the whole structure completely folded, for what the crease stiffness should be avoided to set too small.

The two-layer Miura model consists of two Miura units. The frequency response of different stiffness combinations were analyzed with different crease stiffness of the second unit. Figure 4 shows that the frequency response of the two-layer Miura model is similar to the single-layer Miura model in different stages under the simple harmonic force. By changing the crease stiffness of the second Miura unit, different resonant frequencies can be obtained, but the sensitivity is lower.

Table 1 Model parameters of example 1

Model type	$F_0 = 0.01$ N	$X_0 = 0.001$ m
	k/(N m/deg)	k/(N m/deg)
1	$k_a = 0.05 \times 10^{-3}$	$k_a = 0.05 \times 10^{-3}$
1	$k_a = 0.1 \times 10^{-3}$	$k_a = 0.1 \times 10^{-3}$ $k_a = 0.2 \times 10^{-3}$
1	$k_a = 0.2 \times 10^{-3}$	
1	$k_a = 1 \times 10^{-3}$	$k_a = 1 \times 10^{-3}$
1	$k_a = 10 \times 10^{-3}$	$k_a = 10 \times 10^{-3}$
1	$k_a = 100 \times 10^{-3}$	$k_a = 100 \times 10^{-3}$
2	$k_a = k_c = 0.1 \times 10^{-3}$ $k_b = 0.05 \times 10^{-3}$	$k_a = k_c = 0.1 \times 10^{-3}$ $k_b = 0.05 \times 10^{-3}$
2	$k_a = k_c = 0.1 \times 10^{-3}$ $k_b = 0.1 \times 10^{-3}$	$k_a = k_c = 0.1 \times 10^{-3}$ $k_b = 0.1 \times 10^{-3}$
2	$k_a = k_c = 0.1 \times 10^{-3}$ $k_b = 0.2 \times 10^{-3}$	$k_a = k_c = 0.1 \times 10^{-3}$ $k_b = 0.2 \times 10^{-3}$
2	$k_a = k_c = 0.1 \times 10^{-3}$ $k_b = 1 \times 10^{-3}$	$k_a = k_c = 0.1 \times 10^{-3}$ $k_b = 1 \times 10^{-3}$
2	$k_a = k_c = 0.1 \times 10^{-3}$ $k_b = 10 \times 10^{-3}$	$k_a = k_c = 0.1 \times 10^{-3}$ $k_b = 10 \times 10^{-3}$
2	$k_a = k_c = 0.1 \times 10^{-3}$ $k_b = 100 \times 10^{-3}$	$k_a = k_c = 0.1 \times 10^{-3}$ $k_b = 100 \times 10^{-3}$
3	$k_a = 0.1 \times 10^{-3}$ $k_b = 0.1 \times 10^{-3}$	$k_a = 0.1 \times 10^{-3}$ $k_b = 0.1 \times 10^{-3}$

3.2 Vibration Response of Multi-Degree-of-Freedom Miura Model with Different Stacking Numbers Under Simple Harmonic Force Excitation

The multi-layer stacked Miura model is formed by the stack of isolated Miura units with multiple degrees of freedom. The number of stacks was taken as 2, 3 and 4 respectively to analyze the frequency response. Under the excitation, the deformation of Miura units at different layers of the model is not synchronous, both tensile and compression existing in the meantime. Figure 5 shows that as the number of stacks increases, the number of natural frequencies of the model increases, while the maximum response force amplitude decreases correspondingly to the frequency. Beyond the resonant frequency range, the amplitude of excitation response is basically the same.

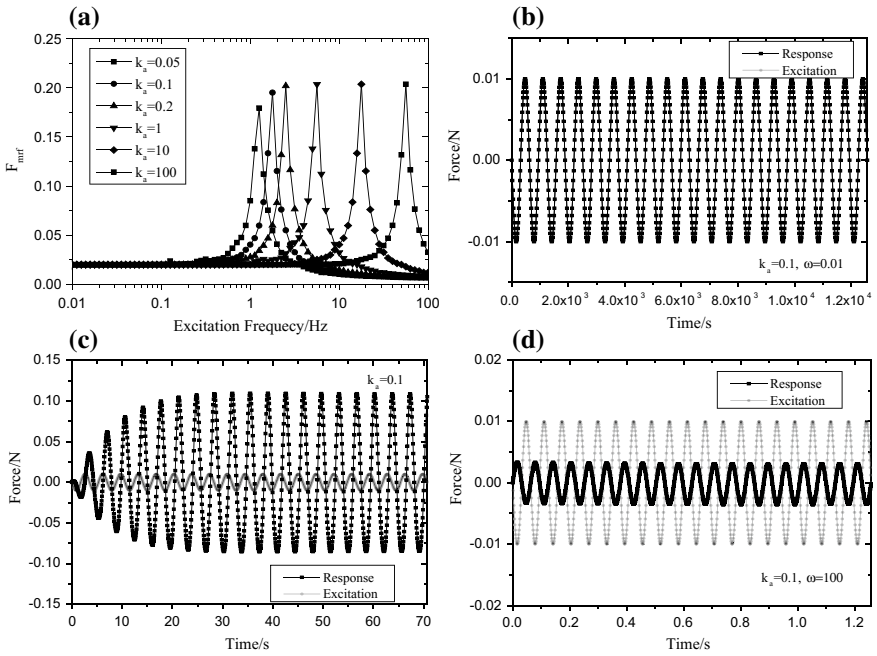

Fig. 3 The response force at the center of the bottom plate, with the torsional spring stiffness per unit length as $k = 0.05, 0.1, 0.2, 1, 10, 100$ N mm/degree, frequency from 0.01 to 100 Hz: **a** the relationship between excitation frequency and maximum amplitude with different spring stiffness; **b** the time-force curve where $k_a = 0.1, \omega = 0.01$ Hz; **c** the time-force curve at the peak where $k_a = 0.1$; **d** the time-force curve where $k_a = 0.1, \omega = 100$ Hz

3.3 Vibration Response of a Single-Degree-of-Freedom Miura Model with Different Crease Stiffness Under Simple Harmonic Displacement Excitation

The frequency response of the single-layer model under the effect of harmonic displacement of motivation (Fig. 6) shows the same change trend with the harmonic force excitation. Displacement transfer values at low frequency is 1. The displacement response of amplitude is far greater than the excitation amplitude at the displacement transfer value corresponding to the maximum frequency when resonating. With further increase of the excitation frequency, displacement transfer value is less than 1. Under two kinds of simple harmonic excitation, the vibration response of the single-degree-of-freedom model is similar. By changing the crease stiffness and the resonance frequency appropriately, a good low-frequency vibration isolation effect can be achieved.

The two-layer model under the harmonic displacement excitation is analyzed with different stiffness combination with the ratio of 0.5, 0.1, 0.2, 0.10, 0.100 and

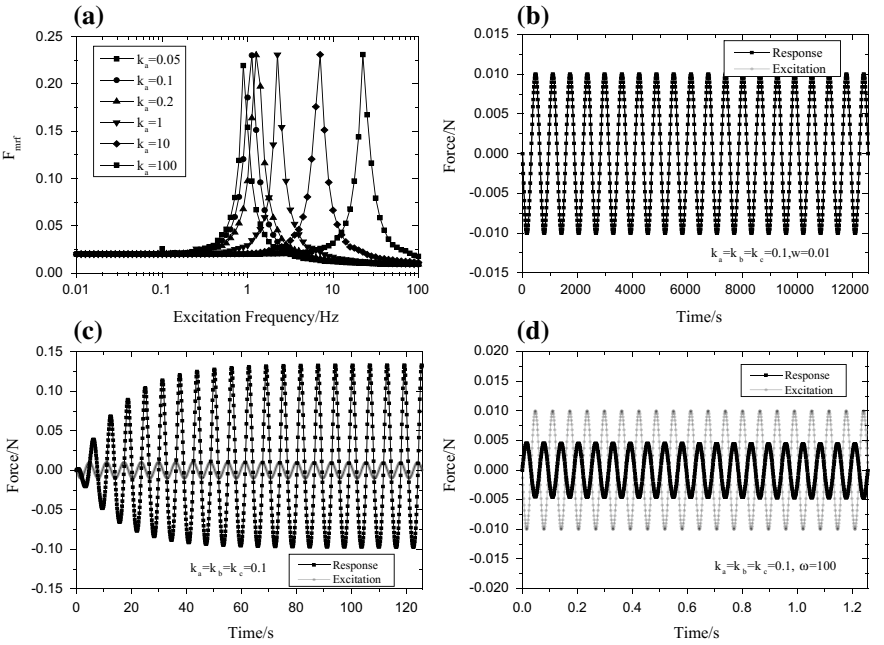

Fig. 4 The response force at the center of the bottom plate, with the torsional spring stiffness per unit length as $k_a = k_c = 0.1$, $k_b = 0.05, 0.1, 0.2, 1, 10, 100$ N mm/degree, frequency from 0.01 to 100 Hz: **a** the relationship between excitation frequency and maximum amplitude with different spring stiffness; **b** the time-force curve where $k_b = 0.1$, $\omega = 0.01$ Hz; **c** the time-force curve at the peak where $k_b = 0.1$; **d** the time-force curve where $k_b = 0.1$, $\omega = 100$ Hz

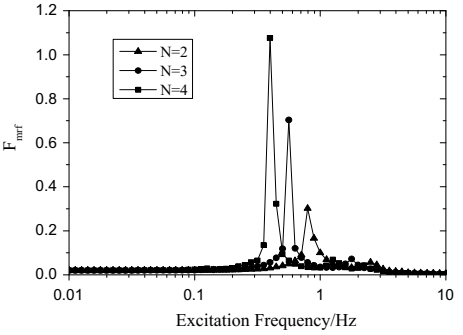

Fig. 5 The response force at the center of the bottom plate, with the torsional spring stiffness per unit length as $k_a = k_b = 0.1$ N mm/degree, frequency from 0.01 to 10 Hz, N = 2, 3, 4

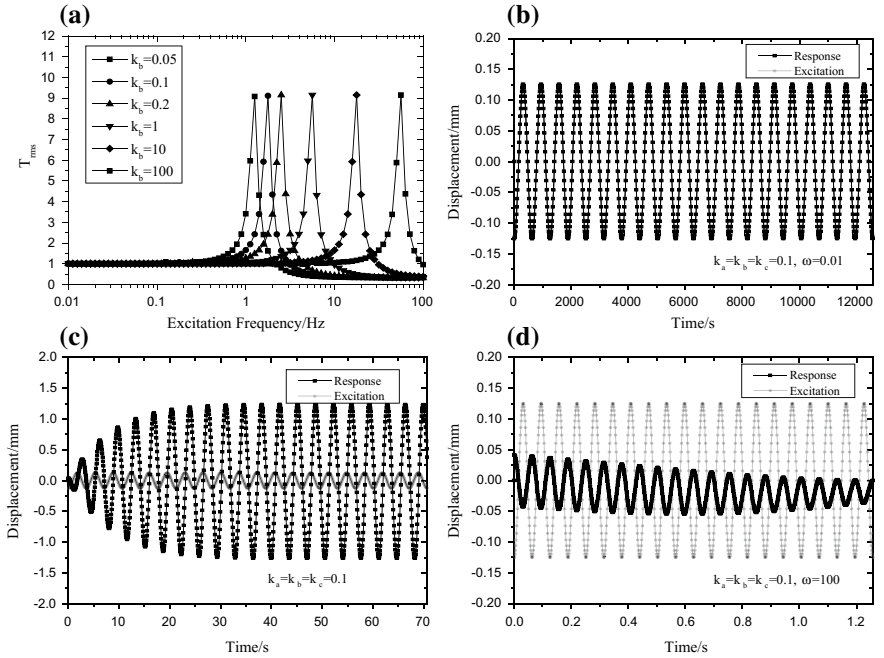

Fig. 6 The response displacement with the torsional spring stiffness per unit length as $k = 0.05, 0.1, 0.2, 1, 10, 100$ N mm/degree, frequency from 0.01 to 100 Hz: **a** the relationship between excitation frequency and T_{rms} with different spring stiffness; **b** the time-force curve where $k_a = 0.1, \omega = 0.01$ Hz; **c** the time-force curve at the peak where $k_a = 0.1$; **d** the time-force curve where $k_a = 0.1, \omega = 10^{1.5}$ Hz

0.1000. The resonance frequency increases with the increase of crease stiffness. The maximum displacement transfer value is not obviously changed. It can be seen that the resonant frequency range is relatively narrow, and the structure's interference resistance to certain external frequency range is increased by adjusting the crease stiffness combination reasonably. With different crease stiffness combination, it can be seen that the overall maximum response displacement transfer value is bigger as shown in Fig. 7.

3.4 Vibration Response of Multi-Degree-of-Freedom Miura Model Under Simple Harmonic Displacement Excitation

In the multi-layer stacked Miura model, 0 10 stacked elements were selected to analyze the displacement—time curve under different response peaks. Under harmonic displacement excitation, with the continuous increase of excitation frequency, time interval between excitation and response increases gradually. When the frequency

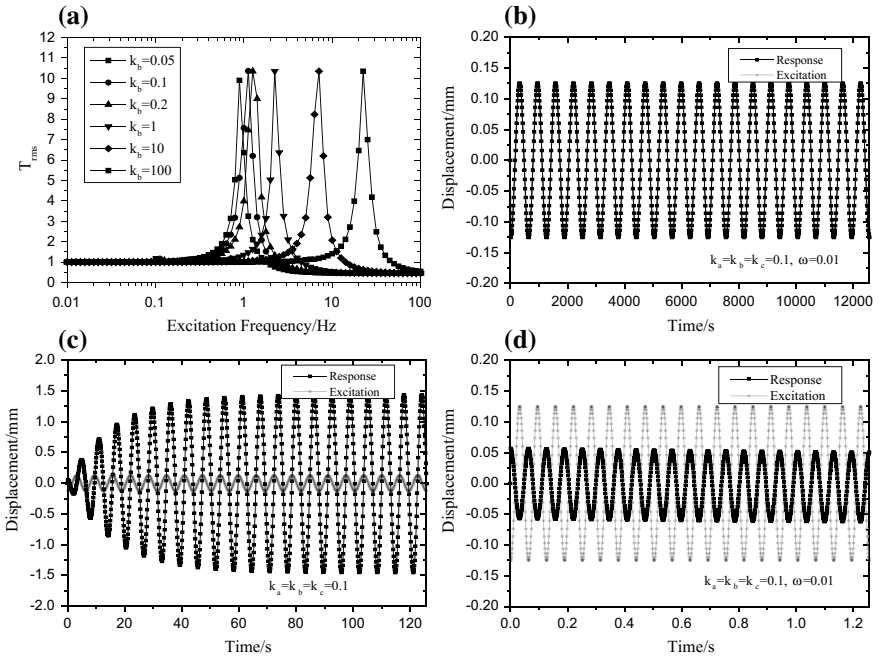

Fig. 7 The response displacement with the torsional spring stiffness per unit length as $k_a = k_c = 0.1, k_b = 0.05, 0.1, 0.2, 1, 10, 100$ N mm/degree, frequency from 0.01 to 100 Hz: **a** the relationship between excitation frequency and T_{rms} with different spring stiffness; **b** the time-displacement curve where $k_b = 0.1, \omega = 0.01$ Hz; **c** the time-displacement curve at the peak where $k_b = 0.1$; **d** the time-displacement curve where $k_b = 0.1, \omega = 10$ Hz

increased to a certain value, the response time of bottom surface element was 20 times of the excitation period. Therefore, the transfer value of displacement is zero. Figure 8 is similar to the previous peak image. The excitation frequency of the multi-layer stacked Miura model reaches the maximum resonance frequency. With further increase of the frequency, the frequency resonance becomes out of sync. Mutual interference occurred in the vibration of different stack units. As a result, the waveform jittered internally. Noted that the response time started to lack behind the excitation and the delay time increases with the increase of the excitation frequency.

3.5 Impact Response of Multi-layer Stacked Miura Folded Metamaterials with Different Crease Stiffness

First of all, after the applied impact, Fig. 9 reveals that the stacked Miura folded metamaterial creates two kinds of mechanical waves: the impact wave with large amplitude and slow propagation speed as shown in Fig. 9 as the notable yellow line

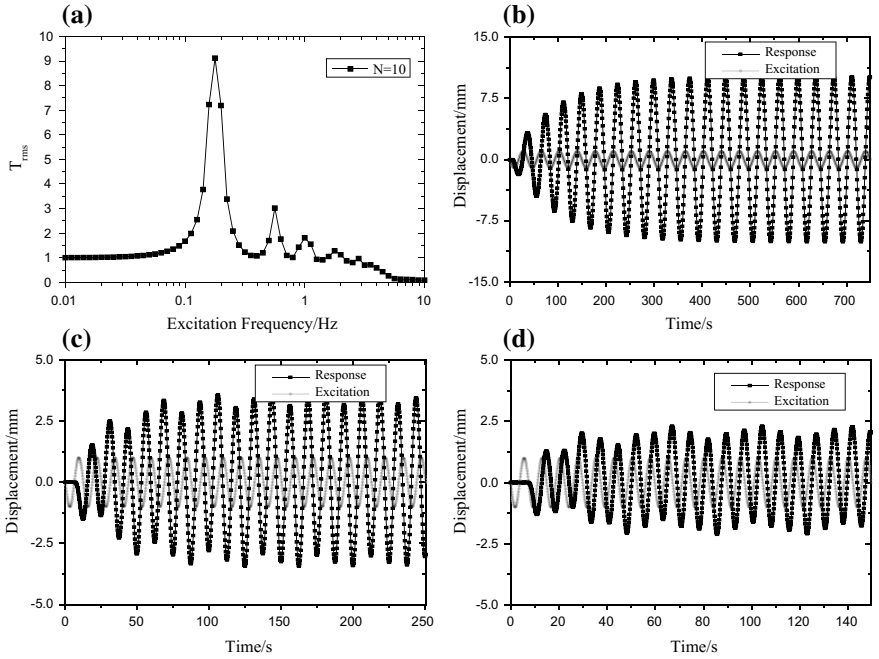

Fig. 8 The response displacement with the torsional spring stiffness per unit length as $k_a = k_b =$ 0.1 N mm/degree, frequency from 0.01 to 10 Hz: **a** the relationship between excitation frequency and T_{rms}; **b** the time-displacement curve at the first peak; **c** the time-displacement curve at the peak at the second peak; **d** the time-displacement curve at the third peak; **e** the time-displacement curve at the fourth peak; **f** the time-displacement curve at the fifth peak

(compression) and the dark blue line (tensile), and the oscillatory wave with small amplitude and fast propagation speed, which is shown in the figure as a light-blue grating with a fast changing frequency between impact waves. When the response reaches a steady state, the amplitude of the overall strain tends to be balanced and much smaller than that of the first time. At the top side of the metamaterial, it's hardly moved, while the fiercest movement at the bottom. Figure 9 shows the largest amplitude of the various layers. It's quite obvious that after the impact, the largest amplitude of the whole structure occurs at the top side. However, it decays rapidly at the second unit because of the folding characteristics of the stacked Miura folded metamaterial, which is noted that this structure has great impact adsorption. Note that in Fig. 12, nearly all the units from different layers start with the deformation of tensile instead of compression at the first time after the impact except the top unit. This is because the Miura folded Metamaterials are single-degree-of-freedom structures. When the compression deformation of the first unit occurs, lower part of the unit starts to move along with the upper part, which denotes that the upper and lower part move toward the middle. The adjacent unit moves with the first unit and starts with tensile.

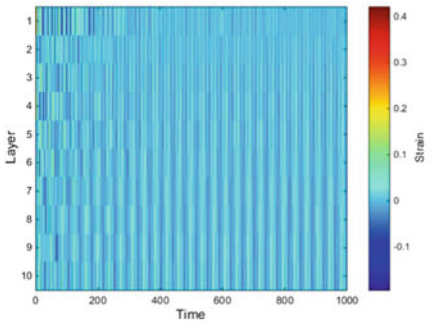

(a) Strain-time grey-scale map

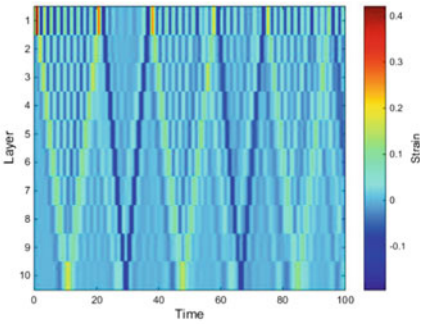

(b) Initial loading strain-time grey-scale map

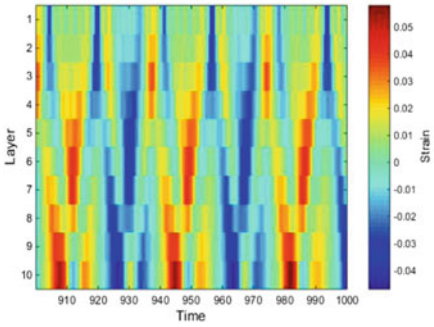

(c) Steady state strain-time grey-scale map

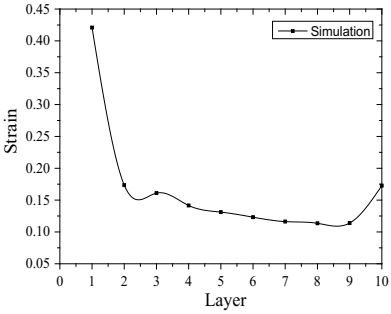

(d) Maximum strain amplitude - layer number curve

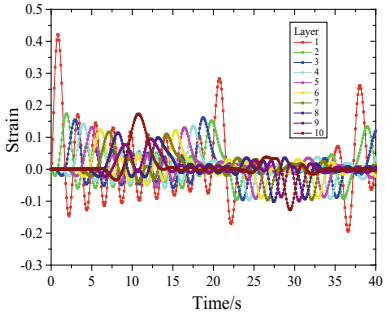

(e) Strain - time curve of each layer in a short time

Fig. 9 The system parameters are ka = 0.1, and $c = 0$. The impact response of multi-layer stacked Miura folded metamaterials within 1000 s

To explore the influence of the crease stiffness of stacked Miura folded metamaterial after impact, we increase the crease stiffness k. The results is shown in Fig. 10. Can be seen from the figure, after the crease stiffness increase, the propagation speed of the mechanical waves is accelerated, as shown as the fast color-changing. Under the impact, the strain of the maximum amplitude would decrease along with the augment of crease stiffness significantly, with the shallower gray-scale color. The ratio of the maximum amplitude of the top to the bottom decreases while the stiffness increasing.

In ADAMS, the impact response of multi-layer stacked Miura model with damping of 0 and crease stiffness of $k = 10$ is simulated, and the results are shown in Fig. 11. It can be seen from Fig. 11 that the propagation speed of two kinds of mechanical waves inside the multi-layer stacked Miura folded metamaterial is faster, and the gray-scale map shows that the color change frequency is accelerated. As the crease stiffness continues to increase, the movement of the steady-state part model is unified, and the maximum strain amplitude appears at the bottom of the model. Increasing the crease stiffness, the strain of the maximum amplitude would decrease significantly to 0.02, so as the ratio of the maximum amplitude of the top to the bottom. However, the change of crease stiffness does not affect the phenomenon that the maximum strain of multi-layer stacked Miura folded Metamaterials starts at the second layer and rapidly decays under the impact load.

3.6 Impact Response of Multi-layer Stacked Miura Folded Metamaterials with Different Damping Coefficients

Further research about the influence of the damping to the response of the impact has been conduct. In ADAMS, the impact response of multi-layer stacked Miura model with damping of 0.001 and crease stiffness of 0.1 is simulated, and the results are shown in Fig. 12. Figure 12 reveals that the stacked Miura folded metamaterial creates two kinds of mechanical waves: the impact wave with large amplitude and slow propagation speed and the oscillatory wave with small amplitude and fast propagation speed as shown in Fig. 12 without much difference compared with no-damping model. The amplitude of the strain decays rapidly because of the existence of the damping. The boundaries also gradually blurred, and it's almost invisible of the yellow line and blue line on behalf of the impact waves. The ratio of the maximum amplitude of the top to the bottom doesn't change a lot. Note that in Fig. 12, nearly all the units from different layers start with the deformation of tensile instead of compression at the first time after the impact except the top unit, which is quite the same as no damping model.

In ADAMS, the impact response of multi-layer stacked Miura model with damping of 0.01 and crease stiffness of 0.1 is simulated, and the results are shown in Fig. 13. Figure 13 reveals that with larger damping coefficient, the gray-scale map faded more quickly. The ratio of the maximum amplitude of the top to the bottom

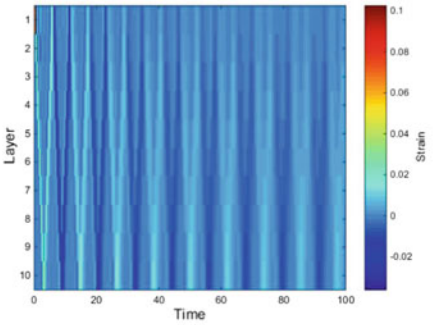

(a) Strain-time grey-scale map

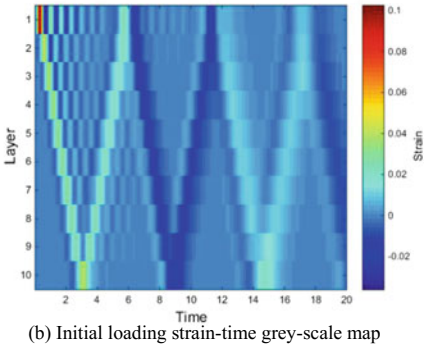

(b) Initial loading strain-time grey-scale map

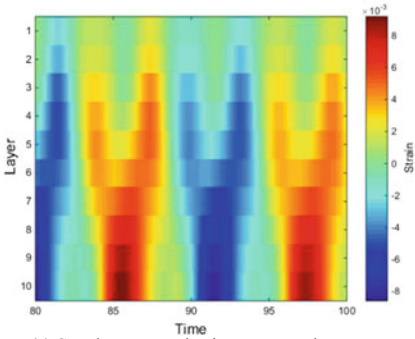

(c) Steady state strain-time grey-scale map

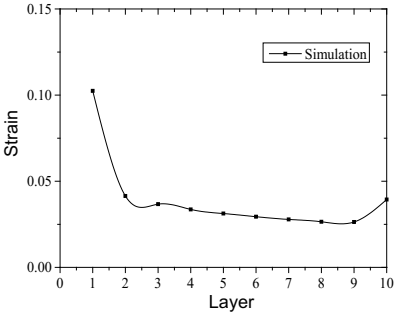

(d) Maximum strain amplitude - layer number curve

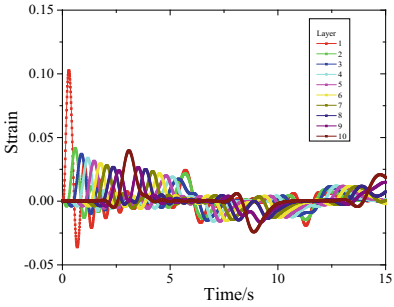

(e) Strain - time curve of each layer in a short time

Fig. 10 The system parameters are ka = 1, and $c = 0$. The impact response of multi-layer stacked Miura folded Metamaterials within 100 s

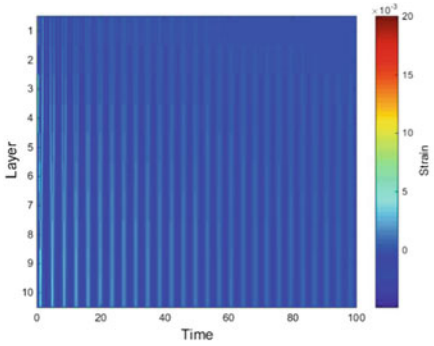

(a) Strain-time grey-scale map

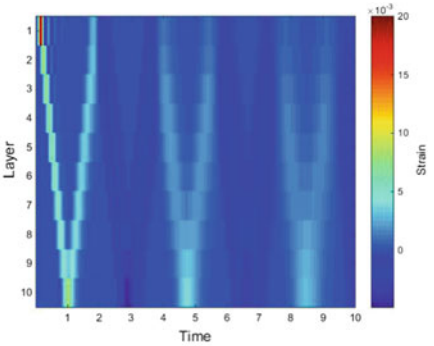

(b) Initial loading strain-time grey-scale map

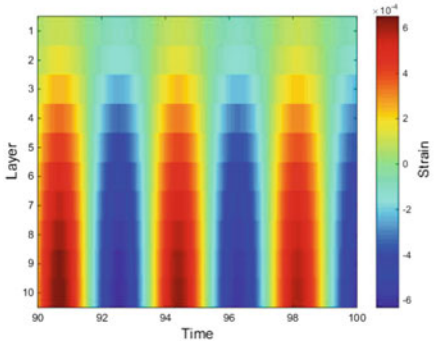

(c) Steady state strain-time grey-scale map

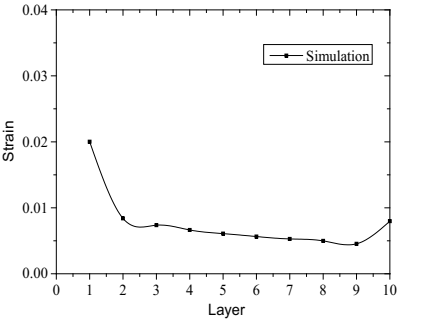

(d) Maximum strain amplitude - layer number curve

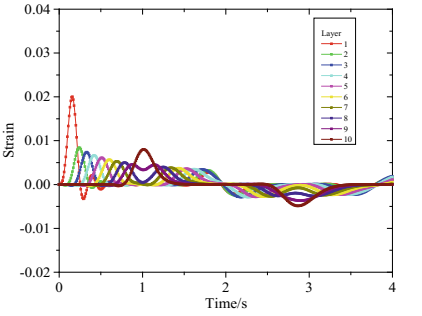

(e) Strain - time curve of each layer in a short time

Fig. 11 The system parameters are ka = 10, and $c = 0$. The impact response of multi-layer stacked Miura folded Metamaterials within 100 s

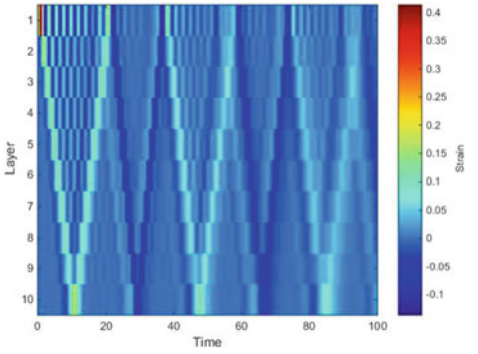

(a) Strain-time grey-scale map

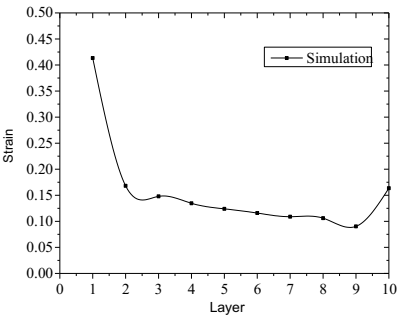

(b) Maximum strain amplitude - layer number curve

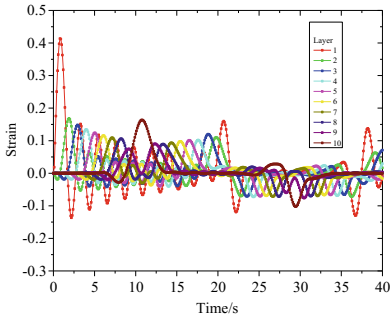

(c) Strain - time curve of each layer in a short time

Fig. 12 The system parameters are ka $= 0.1$, and $c = 0.001$. The impact response of multi-layer stacked Miura folded Metamaterials within 100 s

doesn't change either. Note that in Fig. 13, increasing the damping coefficient, the tensile strain disappears at the first time.

In ADAMS, the impact response of multi-layer stacked Miura model with damping of 0.01 and crease stiffness of 0.1 is simulated, and the results are shown in Fig. 14. Figure 14 reveals that with larger damping coefficient, the gray-scale map faded more quickly. The ratio of the maximum amplitude of the top to the bottom doesn't change either. Note that in Fig. 14, increasing the damping coefficient, the tensile strain disappears completely.

It can be concluded that the damping coefficient increases, the velocity of mechanical waves remains constant, and the attenuation range of strain increases significantly. The strain at each layer of the multi-layer stacked Miura folded Metamaterials disappears rapidly with time. Furthermore, the damping in the model structure has a more obvious impact on the vibration wave of the impact response. When the damping coefficient increases to a certain value, the internal vibration wave and the phenomenon of first stretching and then compression gradually disappeared.

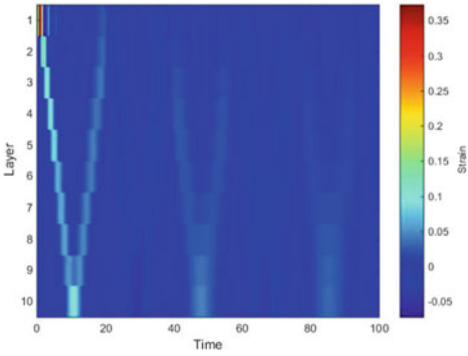

(a) Strain-time grey-scale map

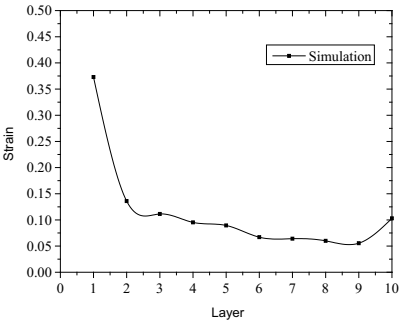

(b) Maximum strain amplitude - layer number curve

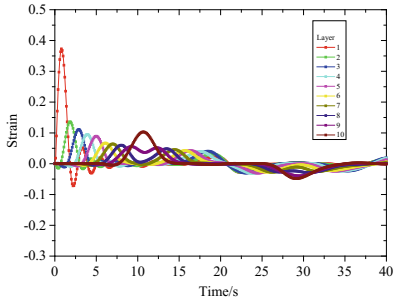

(c) Strain - time curve of each layer in a short time

Fig. 13 The system parameters are ka $= 0.1$, and $c = 0.01$. The impact response of multi-layer stacked Miura folded Metamaterials within 100 s

3.7 Impact Response of Multi-layer Stacked Miura Folded Metamaterials with Different Load Amplitudes

We now further investigate the influence of the amplitude of the impact force. In ADAMS, the impact response of multi-layer stacked Miura model with damping of 0, crease stiffness of 0.1 and $F_0 = 0.05$ is simulated, and the results are shown in Fig. 15. Can be seen from the figure, First of all, under the impact load, the response of the multi-layer stacked Miura folded Metamaterials is still the superposition of two mechanical waves. As the amplitude of impact load decreases, the amplitude of the overall strain decreases significantly, and the color of gray image becomes lighter. When various waveforms interfered with each other to reach steady state, the amplitude of strain was different, but the gray scale was almost the same.

In ADAMS, the impact response of multi-layer stacked Miura model with damping of 0, crease stiffness of 0.1 and $F_0 = 0.15$ is simulated, and the results are shown in Fig. 16. As the amplitude of impact load increases, the amplitude of the overall strain increases significantly, and the color of gray image becomes darker. When

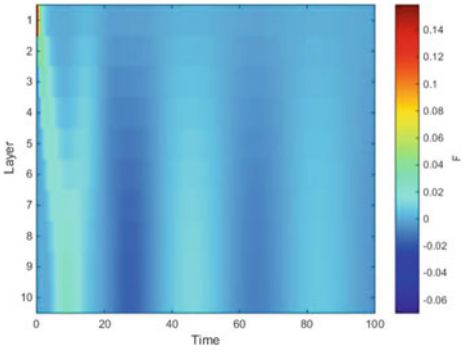

(a) Strain-time grey-scale map

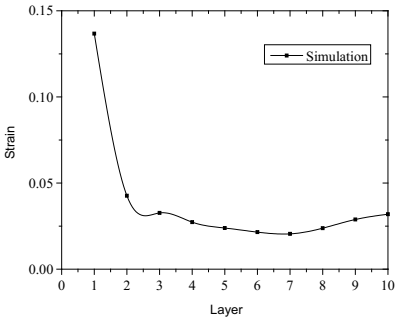

(b) Maximum strain amplitude - layer number curve

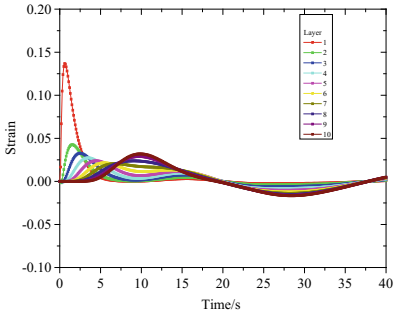

(c) Strain - time curve of each layer in a short time

Fig. 14 The system parameters are ka $= 0.1$, and $c = 0.1$. The impact response of multi-layer stacked Miura folded Metamaterials within 100 s

various waveforms interfered with each other to reach steady state, the gray scale hardly defers. The amplitude of the impact makes a difference of the strain but not of the motion at steady stage.

3.8 Impact Response of Multi-layer Stacked Miura Folded Metamaterial Under Pulse Loading

At the same time, the impulse impact load with a time interval of 10 s is analyzed. In ADAMS, the impact response of the multi-layer stacked Miura model with damping 0 and crease stiffness $k = 0.1$ was simulated. The impulse impact load was set to 10 s each time, as shown in Fig. 17. First of all, two kinds of waveforms, impact wave and oscillatory wave can be seen from the figure. During the 0–20 s period, just after the impact wave reaches the bottom, the second impact load begins to operate, which are independent of each other. In 20–40 s period, after the first impact

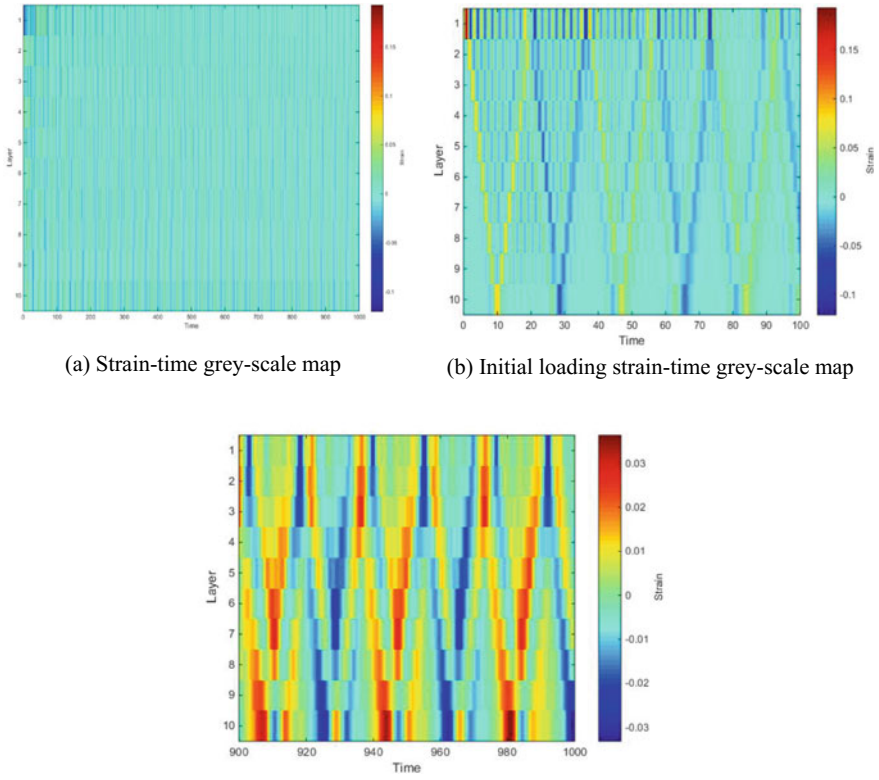

(a) Strain-time grey-scale map

(b) Initial loading strain-time grey-scale map

(c) Steady state strain-time grey-scale map

Fig. 15 The system parameters are ka $= 0.1$, and $c = 0$, $F_0 = 0.05$. The impact response of multi-layer stacked Miura folded Metamaterials within 100 s

wave back to the top, in the form of tensile strain continues to pass down, while the third impact load to start, have taken place in both the mutual interference and offset, in this time period, impact waveform is almost invisible. In later period, due to the time of pulse load the movement is not synchronized, and makes the whole deformation happened interference or overlay, make the follow-up waveform is relatively complex, strengthen and weakness of two kinds of changes, at the same time, vibration wave amplitude increases with impact wave in the strong interference.

4 Conclusion

In this paper, we investigate dynamics in Miura-origami structure composed of Miura cells with rigid facets and elastic hinges, under three types of excitation: harmonic force, harmonic displacement and impact. ADAMS was used to analyze three typical

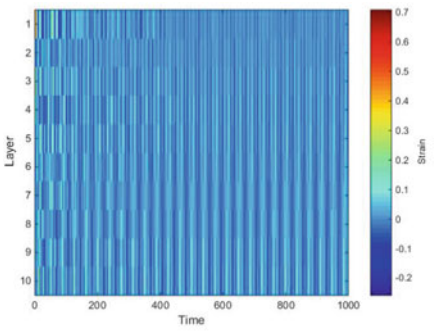

(a) Strain-time grey-scale map

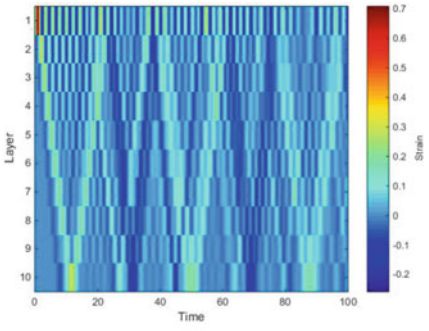

(b) Initial loading strain-time grey-scale map

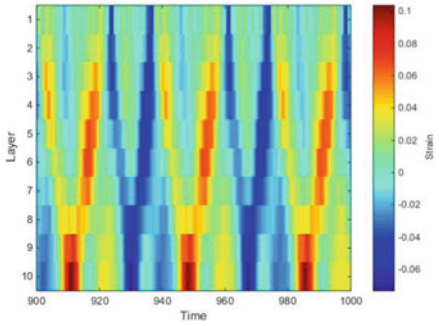

(c) Steady state strain-time grey-scale map

Fig. 16 The system parameters are ka $= 0.1$, and $c = 0$, $F_0 = 0.15$. The impact response of multi-layer stacked Miura folded Metamaterials within 100 s

Fig. 17 The system parameters are ka $= 0.1$, and $c = 0$. The impulse impact response of multi-layer stacked Miura folded Metamaterials within 100 s

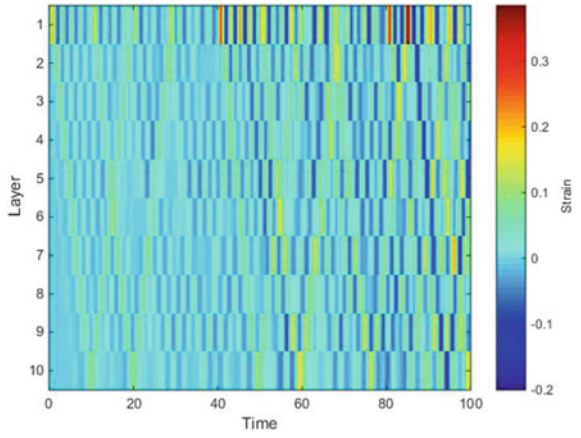

structural models. Under the simple harmonic excitation of force and displacement, different crease stiffness affected the vibration response of Miura folded Metamaterials. The results show that the Miura model of the single-degree-of-freedom structure has similar frequency response under the two kinds of excitation. By changing the crease stiffness, it can change its resonance frequency and achieve a good low-frequency vibration isolation effect. The multi-degree-of-freedom model can reduce the resonance frequency by increasing the number of stacks. It provides some theoretical references for vibration isolation design of Miura folding structure. ADAMS was used to study the impact response of different crease stiffness and damping. The results show that, under the impact load, there are two types of mechanical waves: shock wave and vibration wave. Except the first layer, the other Miura units will have the deformation characteristics of stretching before compression. The propagation speed of mechanical waves and ratio of the maximum strain amplitude at different layers can be designed by changing the crease stiffness. Meanwhile, the response of multi-layer stacked Miura folded Metamaterials is very different at steady state. The influence of damping coefficient on vibration wave is more obvious. When the impact load amplitude is changed, the response at steady state is almost constant.

References

1. Zhou, X., Wang, H., & You, Z. (2014). Mechanical properties of miura-based folded cores under quasi-static loads. *Thin-Walled Structures, 82,* 296–310.
2. Schenk, M., Guest, S. D., & Mcshane, G. J. (2014). Novel stacked folded cores for blast-resistant sandwich beams. *International Journal of Solids and Structures, 51*(25–26), 4196–4214.
3. Liu, S., Lu, G., Chen, Y., & Leong, Y. W. (2015). Deformation of the miura-ori patterned sheet. *International Journal of Mechanical Sciences, 99,* 130–142.
4. Fang, H., Li, S., Ji, H., & Wang, K. W. (2017). Dynamics of a bistable miura-origami structure. *Physical. Review E*, *95*(5–1), 052211.
5. Sadeghi, S., & Li, S. (2017). Harnessing the quasi-zero stiffness from fluidic origami for low frequency vibration isolation. In *ASME 2017 Conference on Smart Materials, Adaptive Structures and Intelligent Systems* (pp. V002T03A008).
6. Yasuda, H., Lee, M., & Yang, J. (2016). Tunable wave dynamics in origami-based mechanical metamaterials. In *ASME 2016 International Design Engineering Technical Conferences and Computers and Information in Engineering Conference* (pp. V05BT07A012).
7. Yasuda, H., Chong, C., Charalampidis, E. G., Kevrekidis, P. G., & Yang, J. (2015). Formation of rarefaction waves in origami-based metamaterials. *Biomedical Image Understanding, Methods and Applications*. Wiley.

Error in Sound Source Localization of Phased Microphone Array Caused by Installation Position Deviation of Microphone Array

Huan Bao, Wei Ma and Mingsui Yang

Abstract Microphone array measurement technology has a wide range of applications in noise location due to its good performance for far-field measurement. In practical applications of microphone arrays, there are inevitably various installation deviations, and these deviations affect the final measurement accuracy. At present, only a preliminary study has been conducted on the installation deviation of microphones in the engineering and academia, and there is still a lack of detailed and comprehensive analysis of installation errors. In this paper, the measurement error caused by the array installation position often encountered in the microphone array source positioning is studied. The study shows that the positioning error varies approximately linearly with the mounting declination and vertical offset installation deviation. The small axial offset installation deviations will not have a significant effect on positioning results; In general, the influence of installation deviation on the sound source intensity is more complicated, and compared to the stationary sound source, the array installation deviation has greater influence on the rotating sound source. This study can provide guidance for controlling the measurement error in the practical application of the microphone array, thereby improving the measurement accuracy of the microphone array.

Keywords Microphone array · Sound source localization · Measurement error · Stationary sound source · Rota-ting sound source

H. Bao
School of Mechanical Engineering Shanghai, Jiao Tong University, Shanghai 200240, China

W. Ma (✉)
School of Aeronautics and Astronautics, Shanghai Jiao Tong University, Shanghai 200240, China
e-mail: mawei@sjtu.edu.cn

M. Yang
AECC Shenyang Engine Research Institute, Shenyang 110015, China

Z. Jing (ed.), *Proceedings of International Conference on Aerospace System Science and Engineering 2018*, Lecture Notes in Electrical Engineering 549,
https://doi.org/10.1007/978-981-13-6061-9_3

1 Introduction

With the development of society, more and more attention has been paid to the harm of noise to physical health, and the comfort of the environment has become more and more important. Accordingly, noise localization becomes more and more important for noise reduction. Microphone array measurement technology is a far-field acoustic experiment test technology. An array with multiple microphones which can record sound pressure signal in the far field during the experiment, then Intensity distribution of the sound source of the scanning grid line or surface can be obtained through algorithms. The main advantage of the microphone array measurement technology lies in that it is located far away from the strong mutual interference region and can avoid intrusion and interference in the flow field, Expanding the size can improve spatial resolution, increasing the number of microphones can easily promote the dynamic range [1].

Measurement accuracy and speed have always been two important indicators of noise location, and ensuring measurement accuracy is also a prerequisite for accelerating the calculation speed. In order to improve the measurement accuracy, a lot of research has been done in the academic circles. Most of the researches are based on the optimization of the microphone array algorithm. The conventional delay-and-sum beamforming algorithm can easily distinguish incoherent stationary noise sources with good robustness [2]. However, it has low spatial resolution with poor measurement accuracy at low frequencies. Later, Dougherty et al. improved it and proposed functional beamforming which greatly improves the spatial resolution and dynamic range [3].

In the measurement of rotational noise sources, Sijtsma, P and Oerlemans, S proposed the rotating beamforming method by using the motion compensation method in the time domain to overcome the Doppler effect during the source rotating [4]. But such high-frequency sampling and linear interpolation methods to solve the motion compensation will inevitably cause a certain measurement error. Therefore, Pannert, W and Maier, C proposed a kind of modal decomposition method directly transformed the beamforming to the frequency domain to overcome the trouble of linear interpolation in time domain [5]; In order to further improve the accuracy of beamforming results, Brooks and Humphreys applied the mathematical Gauss-Seidel iteration to the deconvolution algorithm and proposed the DAMAS algorithm to further process the beamforming results in the three-dimensional sound sources positioning and coherent sound sources separation [6–8]. Dougherty and Stoker used the CLEAN algorithm in astronomy for the first time to suppress the generation of sidelobe signals in microphone array data processing [9]; Later Sijtsma extended the CLEAN to CLEAN-SC to improve coherent noise source measurements [10]. Studies have shown that DAMAS has certain advantages in low frequencies measurement accuracy and anti-array coordinate deviations, but it is somewhat inferior to CLEAN-SC in coherent noise sources measurement and computational efficiency [11, 12]. In order to further improve the DAMAS computational efficiency to highlight advantages at low frequency, Wei Ma and Xun Liu also proposed three kinds

of compression computational grid technologies that greatly reduce the DAMAS computation time and achieve significant results in various beamforming algorithms [13–15].

In practice, the measurement accuracy is often determined not only by the algorithm, but also by various installation deviations and these installation deviations will significantly affect the final measurement accuracy. For example, Tóth, B et al. studied the non-uniform distribution of annular arrays to improve the measurement accuracy of rotational noise and found that the deviations of the angular spacing between adjacent microphones can cause a decrease in the sound source intensity [16]. However, currently the engineering and academia have only carried out preliminary research on the installation deviation of the microphone position, and there is still lack of detailed and comprehensive analysis of the installation deviation. Therefore, this paper will study the measurement error caused by the array installation deviation often encountered in microphone arrays measurements. The research method uses numerical simulation, mainly to avoid the influence of installation and measurement errors in the experiment. This paper focuses on three types of installation deviations: tilt angle deviation, vertical offset deviation, and axial offset deviation. The types of sound sources include static sound sources and rotational sound sources. The measurement error is calculated by beamforming algorithm. Then giving position error trend curve and intensity trend curve under different installation deviations to explore the internal rule. In order to make the results more objective, we further expand the results, adding different rotation radius of the sound source and different grid resolutions for comparison to reach a comprehensive conclusion.

2 Installation Deviation Type and Error Analysis Method

2.1 Installation Deviation Type

Firstly, assume that when measured, the center normal of the array plane coincides with the center normal of the scan plane (this kind of installation is easier to implement in experiments), but it is difficult to achieve an unbiased agreement in actual measurements. There exists many kinds of deviations in the installation of the array, but basic deviation types only have three: (a) the slope of the array installation causes angular deviation $\Delta\theta$; (b)The center normal of the array plane does not coincide with that of the scan plane. the vertical displacement of the array plane causes vertical offset deviation $\Delta x/y$; (c) The microphone array approaching or deviating the scan plane causes axial offset Δz, As shown in Fig. 1. Other installation deviations are combinations of these three basic installation deviations.

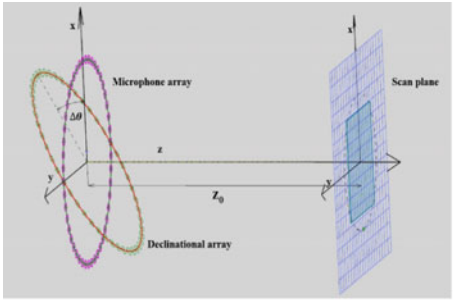

(a) Declination

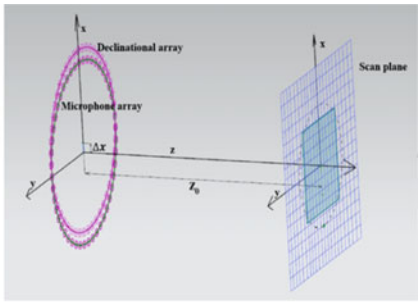

(b) Vertical offset

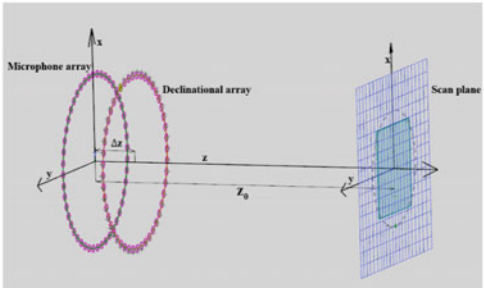

(c) Axial offset

Fig. 1 Schematic diagram of array installation deviation **a** Declination **b** Vertical offset **c** Axial offset

2.2 Methods of Error Analysis

The simulation uses conventional beamforming and rotating beamforming based on modal decomposition [5] for stationary sound sources and rotating sound sources respectively and processes the beamforming results by DAMAS deconvolution. The specific steps are divided into the following 4 steps:

Step1:

Calculate the Propagation Vector Matrix $\mathbf{G}'$ Using Microphone array with deviation. Then simulate the sound pressure $\left[P'\right]$ (Contains installation deviation information) measured in the actual measurement according to $\mathbf{G}'$ and the given sound source distribution $\mathbf{X}$.

$$\left[b' = S * CSM * S^{\mathrm{H}}\right]$$

Step2:

According to P' in the first step, calculate the cross-spectrum matrix $\mathbf{CSM} = P' * (P')^{\mathrm{H}}$ (Superscript H indicates conjugate transpose), Then calculate the steering

Table 1 Simulation information

Type	Stationary sound source	Rotating sound source
Sound speed c_0(m/s) Sound source frequency f(KHz)	343 3	343 3
Sound source intensity(pa)	1	1
Sound source radius(m)	–	0.1
Sound source speed(rpm) Rotating direction	– –	2000 Anti-clock
Number of grids	2601	4900
Grid size(m)	0.01	0.01
Number of DAMAS iterations	2000	2000
Array shape Number of microphones Array diameter D(m) Deflection range $\Delta\theta(^\circ)$ Vertical offset range Δx(m) Axial offset range Δz(m) Positioning distance range z_0 (m)	Ring circle 64 1 $-10 \sim 10$ $-0.1 \sim 0.1$ $-0.1 \sim 0.1$ $0.5 \sim 1$	Ring circle 64 1 $-10 \sim 10$ $-0.1 \sim 0.1$ $-0.1 \sim 0.1$ $0.5 \sim 1$

vector **S** by using the ideal microphone coordinate position with no deviation and bring it into beamforming algorithm to get the dirty map.

Step3:

Then use the b' obtained in the previous step to perform DAMAS deconvolution algorithm [6]: $Ax' = \mathbf{b}'$ to get the clean map: x' (Note that A must be a point spread function (PSF) matrix calculated using the correct microphone array position with no deviation).

Step4:

Finally, use the correct sound source distribution x in step 1 and the error sound source distribution x' in step 3 to calculate the positioning error $\left[\Delta = \left\|x - x'\right\|_2\right]$ and make dimensionless positioning error curve. The change information of intensity of the sound source is selected from clearest point in the clean map (Table 1).

Installation deviation definition: The upper half of the scanning plane is used as a reference. The positive installation declination angle indicates forward inclination, and the negative installation declination angle indicates backward inclination. The positive vertical offset indicates displacement of x/y positive axle, and the negative vertical offset indicates displacement of the x/y negative axis. A positive axial offset indicates that the array is mounted close to the scan plane, and a negative axial offset indicates that the array mounted far from the scan plane. All sound source position and intensity information obtained from clearest point in DAMAS iteration results. Since the positioning error will vary with the size of the installation deviation and the positioning distance, in order to find out the general variation rule, the final position

error Δ is dimensionlessly divided by the width of the lobe: $B = 1.22z_0c_0/Df$; the dimensionless position error: $\Delta\delta = \Delta/B$

3 Error Analysis Results

3.1 Stationary Sound Source

Figure 2 shows the variation curve of the dimensionless positioning error of the three kinds installation deviations. From Fig. 2a, it can be seen that the position error caused by the positive and negative installation deflection is approximately linearly symmetrical. The comparison of the positional errors under the three positioning distances is given in the figure. It can clearly be seen that the error curves under different positioning distances are approximately coincident. This means that the dimensionless position error is basically independent of the positioning distance z_0. when $z_0 = 0.5$, the absolute error of the installation deflection at 3° and 4° is equal. Actually, it does not mean that the position error between 3° and 4° increases by 0. because the sound source is positioned between two adjacent grid points when installation deflection is increased from 3° to 4°, that is, if the position of the two positioning site is closest to the same grid point, then sound source will be displayed on the same grid successively. As shown in Fig. 3. In other words, if the resolution of the grid is a bit higher, they can be distinguished, this will be explored in detail later.

From Fig. 2b, it can be found that the dimensionless position error behaves as a linear symmetric distribution with the vertical deviation of the array, and decreases with the increase of the positioning distance. It is emphasized that the error here is not absolute error. In fact, the absolute error is approximately equal in the three kinds positioning distance, in order to compare them conveniently we treat them non-dimensionally. From Fig. 2c, the axial installation deviation does not have a significant effect on the positioning. The position error is zero for all three simulation conditions. The dimensionless positioning error caused by the above three installation deviations can be seen that the impact of the deflection deviation is the most significant, the vertical offset effect is followed, and the axial offset effect is the smallest.

Figure 4 shows that stationary sound source intensity varies with installation deviation under three kinds positioning distance. The sound source intensity curves caused by deflection show an approximately symmetrical distribution, with fluctuations at about 92.5 dB. The small positioning distance will enlarge intensity error range but reduce intensity error caused by Vertical offset. The intensity error caused by vertical offset is relatively gradual compared with deflection. The intensity due to positive and negative axial offsets changes linearly; It can be found that when the array is installed close to the sound source, the sound source will be strengthened, when away from the sound source, the sound source will be weakened. This kind of

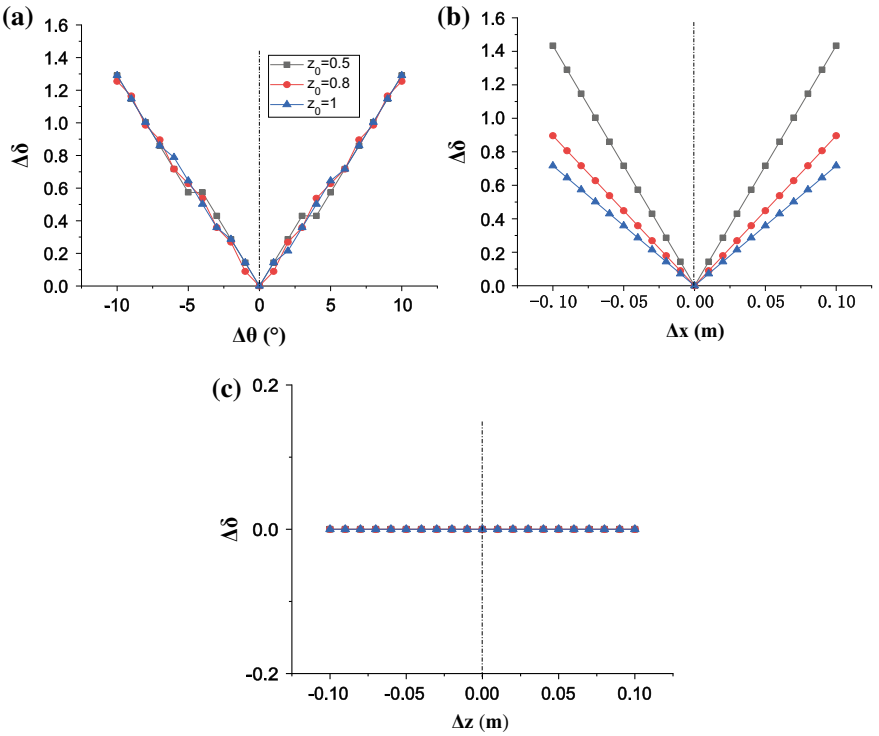

Fig. 2 **a** Position error curve varies with the installation deflection **b** The position error curve varies with the vertical offset **c** Position error curve varies with the axial offset

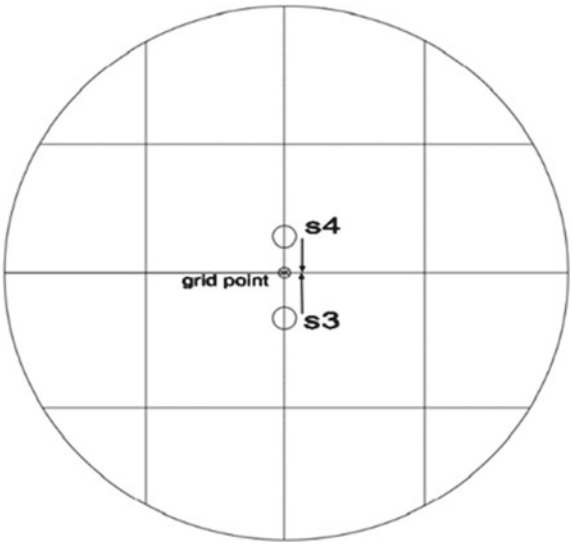

Fig. 3 The 3° deflection source S3 and the 4° deflection source S4 are both located on the same grid

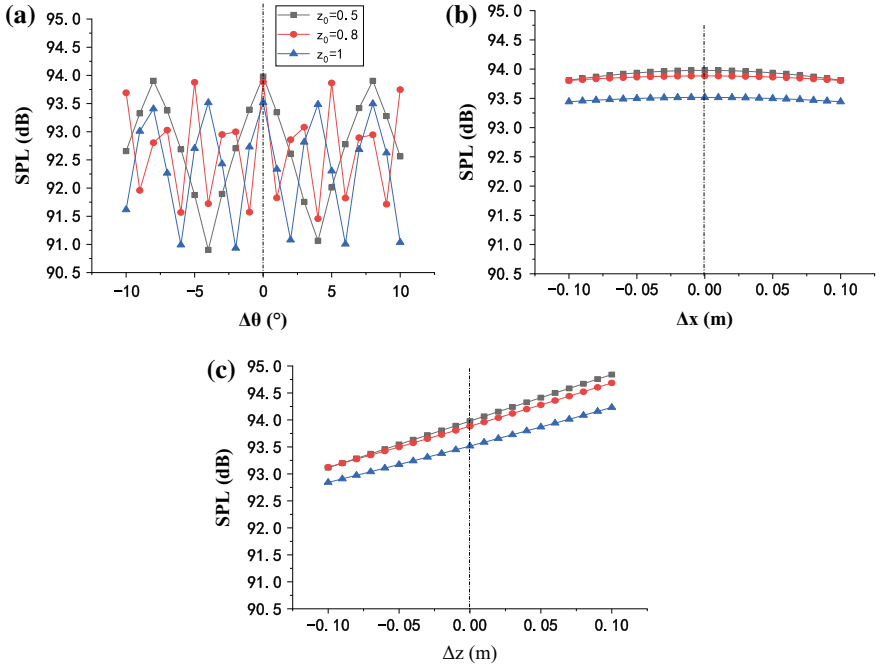

Fig. 4 Stationary sound source intensity **a** Installation deflection **b** Vertical offset **c** Axial offset

reinforcement may even exceed the maximum intensity (1 pa) that the sound source should have, which is obviously different from other installation deviations. Observing carefully, we can see that the slope of the three lines decreases slightly as the positioning distance increases. In other words, the closer the positioning distance is, the larger the range of the intensity error is. The difference between maximum and minimum is about 0.3 dB.

From the above analysis, the installation deflection has the greatest influence on the sound source intensity. The small positioning distance easily amplify the intensity error caused by the deflection. But the too large positioning distance will make measured sound source intensity level drop. Therefore, choosing an appropriate positioning distance in the experiment is very important for suppressing the intensity error and improving the sound source measurement accuracy.

3.2 Rotating Sound Source

Figure 5 shows the non-dimensional position error curve of the rotating sound source with three kinds of array installation deviation. From Fig. 5a, the symmetrical position error curves increase linearly with the installation deflection; The small positioning

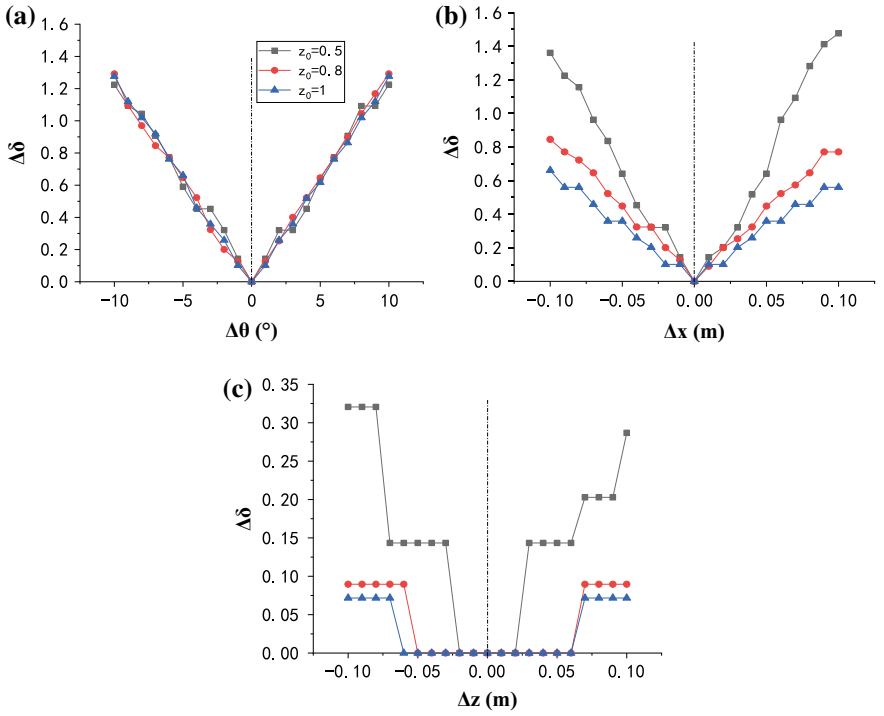

Fig. 5 **a** Position error curve varies with the installation deflection; **b** The position error curve varies with the vertical offset; **c** The position error curve varies with axial offset

distance will occur "step-type growth" as in Fig. 1, and the dimensionless position errors generated at different positioning distances are approximately the same. In Fig. 5b, when the positioning distance increases, the dimensionless position error caused by the vertical offset will gradually decrease, and the phenomenon of "step-type growth" will become more obvious. This also indicates that the rotating sound source has a certain anti-jamming ability compared with the stationary sound source under the long positioning distance, that means the position error will increase slowly with the same vertical installation deflection. In Fig. 5c, the rotation beamforming algorithm is sensitive to the axial installation offset, but the no error of the position can still be achieved within a small deviation range and anti-jamming ability increases with the increase of the positioning distance. However, when the positioning distance is small, the rate and magnitude of error growth will increase fast.

In Fig. 6, the intensity curve of the rotating sound source varies with three kinds of installation deviations. In general, the sound source intensity variation curve is more complex than the stationary one, and more often it shows irregular fluctuations. The fluctuation of the sound source intensity will increase in small positioning distance. In addition, from the comparison of the above three figures, the maximum variation range of sound source intensity caused by the vertical offset installation deviation

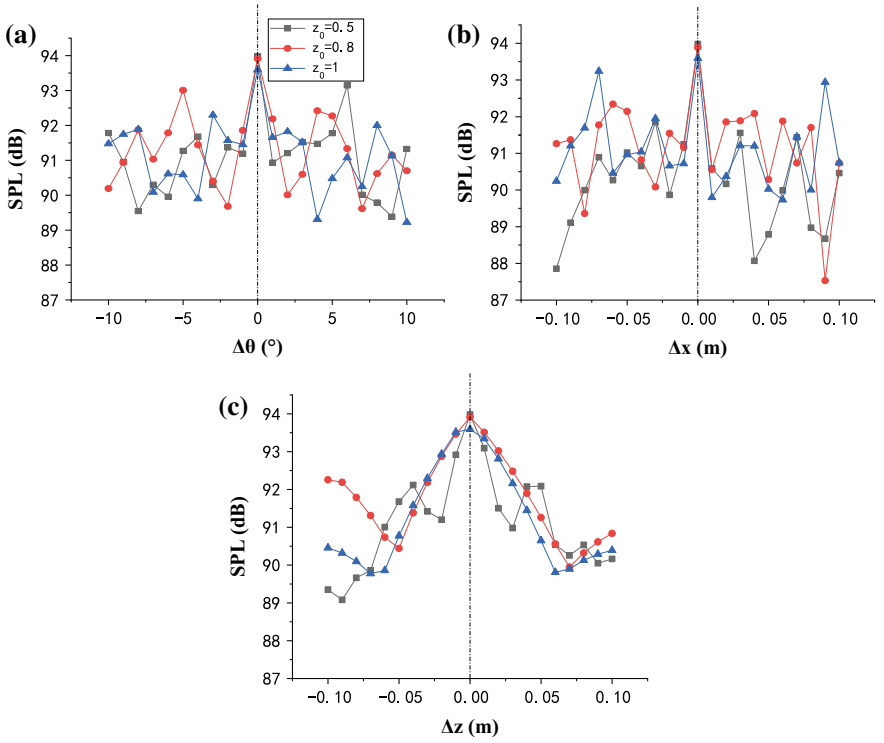

Fig. 6 Rotating sound source intensity **a** Installation deflection **b** Vertical offset **c** Axial offset

is about 6.12 dB, and the minimum variation range of the sound source intensity caused by installation deflection is about 4.43 dB. Compared with stationary sound source, the intensity of the rotating sound source is more sensitive to changes in the installation deviation, which indicates that the position of the microphone in the measurement of the rotating sound source is more stringent.

From the above analysis, the position error caused by the installation deflection is more prominent than the other two installation deviations. In practice, rotating sound source have many different radius, so think about whether this variation trend will change with the radius of the source.

In order to facilitate the verification, we modify original simulation conditions setting positioning distance to 3 m; The measurement open angle is 60°; The total number of grid points is 2500 (the grid size is approximately 0.07 m). Other conditions remain unchanged. In this way, a relatively large measurement area can be obtained. Set three groups of different rotating sound source radii respectively r = 0.35 m; r = 0.7 m; r = 1 m. The final simulation results are shown in Fig. 7. The dimensionless error trend and range are basically consistent with Fig. 5a, and the difference in position error obtained by simulation under different rotation radius conditions is small. Therefore, it is concluded that the position error caused by the

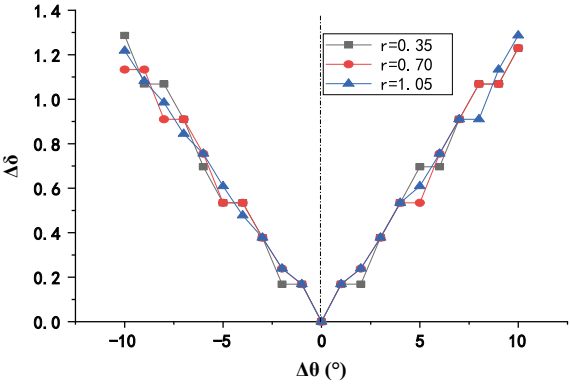

Fig. 7 Comparison of position error caused by deflection under different rotation radius

installation deflection has no relation with the rotation radius. That is to say, the estimation of the position error caused by the installation deflection is suitable for rotating sources with different radii.

3.3 Effect of Grid Resolution on Positioning Error

To verify the phenomenon in Figs. 3 and 8 shows the comparison of positional errors at the three grid resolutions. The grid size changes by keeping the scan plane size constant and reducing the number of grids. The grid size of 0.01 m represents the one used as before. In this simulation, the positioning distance $z_0 = 0.8$ m is selected. From the above four figures, the grid resolution does not affect the trend of positioning error obviously. Even if the resolution of the grid is large, it will not deviate too much from the trend of the mainstream, but it will show "step-type" growth frequently, and the difference between two types of sound sources is quite small. It may temporarily appear that there is no error increase under some adjacent installation deviation, but when the deviation continues to increase, the positioning error will increase sharply with a larger step. The grid resolution has a greater influence on the position error caused by the vertical offset of the array compared with deflection. Therefore, the following conclusion can be drawn: If the grid resolution is sufficient to distinguish the location of the sound source, an appropriate increase in the grid size will play a role in suppressing the position error caused by installation deviation.

4 Conclusion

This paper specifically explores the sound source position error and intensity error caused by array installation errors. The research shows that the array installation

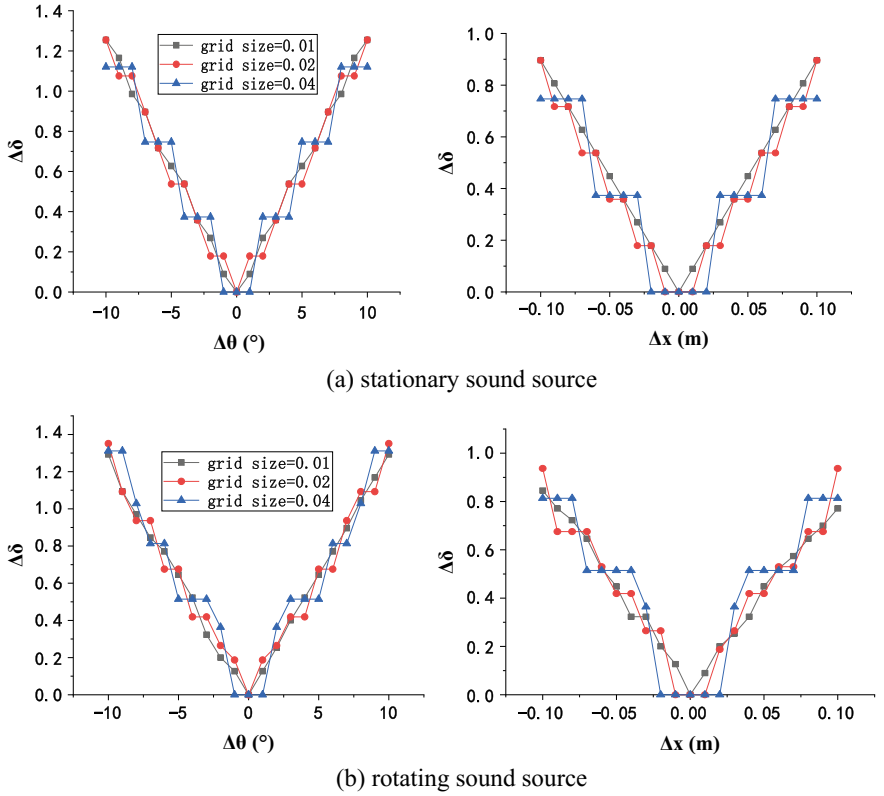

Fig. 8 Effect of grid resolution on sound source positioning error **a** Stataionary sound source **b** Rotating sound source

deviation will significantly affect the beamforming result, especially for installation deflection. Regardless of the stationary or rotating sound source, the position error caused by the deflection and vertical offset is linearly distributed. In addition, the variation of the rotating sound source intensity caused by the installation deviation shows irregular random fluctuations, and its fluctuation range is also significantly higher than that of the stationary sound source. From the result of expansion, there is no obvious relationship between the position error of the rotating sound source and the source radius. Under the premise of maintaining the proper resolution, properly increasing the grid size will help to suppress positioning errors caused by array misalignment. Finally, for the exploration of the array installation deviation, this article has only done a small part of the work. In the future, we can further explore the influence of the sound source frequency, signal-to-noise ratio, and array shape on the positioning error caused by the array installation deviation, so as to optimize the strong anti-installation-deviation experimental scheme.

References

1. Michel, U. (2006). History of acoustic beamforming. In: *Proceedings of the 1st Berlin Beamforming Conference*, pp. 1–17.
2. Dougherty, R. P. (2002). *Beamforming in acoustic testing[M]*. Aeroacoustic Measurements: Springer.
3. Dougherty, R. (2014). Functional beamforming for aero-acoustic source distributions. In *Proceedings of the AIAA/CEAS Aerostatics Conference* 3066.
4. Sijtsma, P., et al. (2001). Location of rotating sources by phased array measurements. *In Proceedings of the 7th AIAA/CEAS Aeroacoustics Conference and Exhibit.*
5. Pannert, W., & Maier, C. (2014). Rotating beamforming motion-compensation in the frequency domain and application of high-resolution beamforming algorithms. *Journal of Sound and Vibration, 333*(7), 1899–1912.
6. Brooks, T. F., Humphreys, W. M. A. (2004). Deconvolution approach for the mapping of acoustic sources (DAMAS) determined from phased microphone arrays. In: *Proceedings of the AIAA/CEAS Aerocoustics Conference*, 2004–2954, *294*, 856–879.
7. Brooks, T. F., Humphreys, W. M. (2005). Three-dimensional application of DAMAS methodology for aeroacoustic noise source definition. In: *Proceedings of the AIAA/CEAS Aerocoustics Conference,* 2005–2960.
8. Brooks, T. F., Humphreys, W. M. (2006). Extension of DAMAS phased array processing for spatial coherence determination (DAMAS-C). In: *Proceedings of the AIAA/CEAS Aerocoustics Conference*, 2006–2654.
9. Dougherty, R. P., Stoker, R. W. (1998). Sidelobe supperss-ion for phased array aeroacoustic measureements. In: *Proceedings of the 4th AIAA/CEAS Aeroacoustics Conference.*
10. Sijtsma, P. (2007). CLEAN based on spatial source coherence. *International Journal of Aeroacoustics, 6,* 357–374.
11. Herold, G., et al. A comparison of microphone array methods for the characterization of rotating sound sources. BeBeC-2018-D22.
12. Sarradj, E., et al. Array methods: Which one is the best. BeBeC-2018-S01.
13. Ma, W., & Liu, X. (2017). DAMAS with compression computational grid for acoustic source mapping. *Journal of Sound and Vibration,410*, 473–484.
14. Ma, W., & Liu, X. (2017). Improving the efficiency of DAMAS for sound source localization via wavelet compression computational grid. *Journal of Sound and Vibration, 395,* 341–353.
15. Ma, W., & Liu, X. (2018). Compression computational grid based on functional beamforming for acoustic source localization. *Applied Acoustics-134*(1), 75–87, London.
16. Tóth, B., et al. Rotating beamforming with uneven microphone placements. BeBeC-2018-D23.

A Survey on Object Tracking in Aerial Surveillance

Junhao Zhao, Gang Xiao, Xingchen Zhang and Durga Prasad Bavirisetti

Abstract Nowadays the Unmanned Aerial Vehicle (UAV) has been widely used due to its low-cost and unique flexibility. Specifically, the high-altitude operational capability makes it the ideal tool in military and civilian surveillance system, in which object tracking based on computer vision is the core ingredient. In this paper, we presented a survey on object tracking methods in aerial surveillance. After briefly reviewing the development history and current research institutions, we summarized frequently used sensors in aerial platform. Then we focused on UAV-based tracking methods by providing detailed descriptions of its common framework (ego motion compensation, object detection, object tracking) and representative tracking algorithms. Through discussing the requirement of a good tracking system and deficiency of current technologies, future directions for aerial surveillance were proposed.

Keywords Object tracking · UAV · Aerial surveillance · Computer vision

1 Introduction

Nowadays, UAV is widely used and continually expanding its market because of its low-cost, unique flexibility and high-altitude operational capability. Compared to human, UAV can carry out tasks including but not limited to disaster search [1], power lines detection [2], traffic monitoring [3] etc. safely, easily and efficiently. According to Carroll and Rathbone [4], the estimated budget for traffic data collection is about

J. Zhao · G. Xiao (✉) · X. Zhang · D. P. Bavirisetti
School of Aeronautics and Astronautics, Shanghai Jiao Tong University, Shanghai, China
e-mail: xiaogang@sjtu.edu.cn

J. Zhao
e-mail: jhzhao_16@sjtu.edu.cn

X. Zhang
e-mail: xingchen@sjtu.edu.cn

D. P. Bavirisetti
e-mail: bdps1989@sjtu.edu.cn

Z. Jing (ed.), *Proceedings of International Conference on Aerospace System Science and Engineering 2018*, Lecture Notes in Electrical Engineering 549,
https://doi.org/10.1007/978-981-13-6061-9_4

Fig. 1 Aerial surveillance over a highway

$5 million per in an average metropolitan area, while using UAV, we can reduce the total cost by 20% and half of collecting procedures. Therefore, UAV is called the best tool for performing 3D (the Dull, the Dirty and the Dangerous) tasks [5].

Object tracking is one of the hot topics in the field of computer vision, which uses a bounding box locks onto the region of interest (ROI) such as person and vehicle. Give the initial location of the target, then computer can find its location in the next sequences. This technology is one of the important applications used in UAV for ground strike, criminal vehicle etc. as well as plays an important role in other process such as estimating velocity and position of an object [6], UAV landing [7], search and rescue [1]. Particularly, in aerial surveillance, through object tracking technologies, traffic flow over a highway during a period can be estimated and a proactive approach can be adopted for an effective traffic management by identifying and evaluating potential problems before they occur [4], as shown in Fig. 1.

In general, tracking accuracy reflects the tracking performance. Various factors affect this performance such as illumination change, abrupt motion, scale variation and full or partial occlusion [8]. Although the tracking algorithm is more and more robust and efficient, no one can handle all scenarios [8]. In addition, different from static camera, aerial object tracking is also influenced by low-sampling rate, resolution and unstable camera platform, which caused by running vehicle and wind that lead to tracking drifts. When the altitude of the flight is great, the objects on the ground looks so small that it is hard to detect them. Hence, realizing a robust and stable tracking algorithm or system is still an issue to be addressed immediately.

The rest of the paper is organized as follows: Sect. 2 introduces the history and current research institutions of UAV vision, while Sect. 3 summarizes the sensors used in aerial platform. Section 4 mainly discusses the tracking framework and algorithm, collected common datasets and evaluation metrics. Future directions are given in Sect. 5. Finally, Sect. 6 concludes this paper.

2 The Development of UAV Vision

2.1 History of UAV Vision

The first aerial video was captured by Nadal, a famous French photographer in December, 1858 [9]. He used an old-fashioned wet plate camera on the hot air balloon. Then, in World War II, the main belligerent countries used aerial camera to carry out reconnaissance, but this way could not meet the needs of real-time. Then, people concentrated on inventing airborne optoelectronic platform. The famous tactical UAV—"Scout", Israel created, was able to send video, which was obtained through the visible light sensors in the optoelectronic platform, back to display. During the Lebanese war in 1982, Israel became the first country to use the real-time image transferring technology in aerial platform [10]. Since the 1990s, UAVs were used almost exclusively in military applications and they also have been finding commonplace usage in civilian applications. For instance, New Mexico State University used UAV to observe whether fishermen were fishing in legal areas [11].

2.2 Current Research Institution

Medioni from Institute for Robotics and Intelligent Systems, University of Southern California and his research group devote themselves to aerial vision research [12]. They are developing the system of wide area aerial surveillance and aim to build an efficient, scalable framework to provide activity inference from airborne imagery [13]. This system includes image mosaicking, video stabilization, object detection and tracking, and activity inference from wide area aerial videos [14–16].

The Air lab of Carnegie Mellon University develops and tests perception and planning algorithms for UAVs [17]. Their research fields include indoor scene understanding, indoor flight in degraded visual environments, micro air vehicle scouts for intelligent semantic mapping etc.

UAV Vision is a company that design and manufacture high performance, lightweight, gyro-stabilized camera payloads for ISR applications [18]. Their sensors can be installed in different aircraft such as fixed wing UAV, multi rotor UAV or rotary wing UAV and carry out various tasks like disaster management, search and rescue. Particularly, when using their CM202U, user can track a moving vehicle from a long distance [19], as shown in Fig. 2.

DJI is a famous company about UAV in China which manufactures and designs UAV, cameras, flight control systems etc. [20]. In civil domain, their products are globally used for music, television and film industries. According to the statistics, DJI is the world's leader in the civilian drone and aerial imaging technology industry, accounting for 85% of the global consumer drone market [21].

In addition, some associated conferences and journals are also offer platforms to UAV researchers and fans. For instance, automated vehicles symposium [22], Inter-

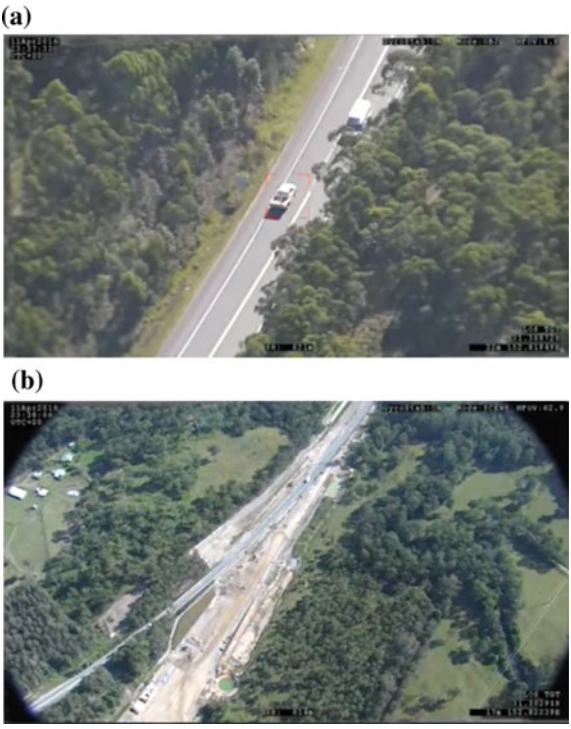

Fig. 2 Tracking a moving vehicle for law enforcement applications

national Conference on Unmanned Aircraft Systems [23] and International Journal of Intelligent Unmanned Systems.

3 Sensors Used in Aerial Platform

Without the airborne optoelectronic platform, the UAV vision cannot be developed. Therefore, the advancement of optoelectronic platform will benefit this technology. This section introduces some common sensors used in aerial platform. Each sensor has its own imaging mechanism and characteristic, which are described in Table 1.

4 Aerial Platform Based Object Tracking

In this section, we first review the object tracking algorithms, which are used in the UAV, followed by common datasets and evaluation metrics.

Table 1 Common sensors and main features

Type of sensor	Main feature
Visible light sensor	Image has high contrast; rich information of color, appearance, shape, geometry and texture; high temporal and spatial resolution
Infrared sensor	It can work day and night; the detection range is from a few thousand meters to more than ten thousand meters; it can be divided into near infrared, mid infrared and long infrared bands
Synthetic aperture radar	It works all day. It has penetrating ability with high resolution
Laser imaging radar	It includes three functions of ranging, velocity measurement and imaging; it has high anti-interference ability, resolution and accuracy
Low light level sensor	Used for night detection, ranging from 800 to 1000 m
Multi-spectral or hyper-spectral sensor	Multiple spectral segments can be used to measure targets precisely at the same time. Its usages are topographic mapping, monitoring and analysis

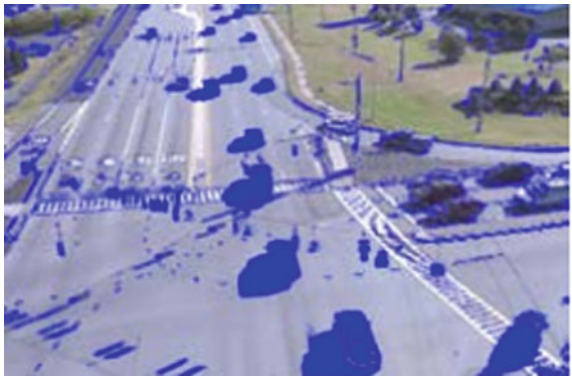

Fig. 3 False alarms due to moving camera [24]

4.1 Common Framework

Object tracking in aerial surveillance is to estimate the states of the target on the ground through detection algorithm or selecting ROI manually to give the initialized state of it. As shown in Fig. 3, the aerial platform based object tracking consists three main steps. They are (1) Ego Motion Compensation; (2) Object Detection and (3) Object Tracking. Behavior analysis for decision making is the output.

Ego Motion Compensation. Ego Motion Compensation is for the image stabilization because of the moving camera by registering video frames onto a reference plane. It is the basic step, otherwise we will get false alarms in the next step for pixel intensity of the background changing, as shown in Fig. 3.

The compensation algorithm can be divided into gray-level [25] based, feature [26] based and transform domain [27] based. In aerial surveillance, feature based methods are often used. Through extracting feature information such as corners, points, lines and edges etc. of two images to carry out the match between them and establish affine model to finish the registration.

Object Detection. The means of detection are various. If we focus on a suspicious object, we can select ROI manually. When the UAV flies high to monitor the traffic condition, there are many vehicles on the ground and detection algorithm is needed, in which false alarms may occur. Usually, optical flow [28], frame differencing [29] and background subtraction [30] are common methods for detection.

Optical flow is defined as the apparent motion of the brightness patterns or the feature points in the image, which can be calculated from the movement of pixels with the same brightness value between two consecutive images [31]. Frame differencing uses the difference of two adjacent frames to detect moving objects. The concept of background subtraction is using the gray difference between the current image and background image to detect object. In addition, parallax, similar appearance, objects merge or split, occlusion etc. will affect detection accuracy [32].

Object Tracking. Object tracking method can be divided as generation methods [33] and discriminant methods [34]. The former methods means in the current frame modeling the object area and in the next frame to find the most similar area as the predicted location. The latter methods means in the current frame extract the features of object and background as positive and negative samples respectively to train classifier. In the next frame, use the classifier to distinguish foreground and use the result to update the classifier. Now, discriminant method is popular because it is more robust.

There are three main modules in object tracking [8]. First, target representation scheme: define an object as anything that is of interest for further analysis [35]. Second, search mechanism: estimate the state of the target objects. Third, model update: update the target representation or model to account for appearance variations.

In aerial surveillance tracking, data associative trackers which belongs to generation methods are often used. It takes input as a number of data points of the form (X, t) where X is a position (usually in 2- or 3-space), and t is the timestamp associated with that position [36]. The tracker then assigns an identifier to each data point indicating its track ID of each object.

Behavior Analysis. Behavior analysis includes the recognition of event, group activity, human roles, and traffic accident prediction etc. It is the output of aerial surveillance tracking for administrators to make decisions. Probabilistic network method is widely used because of its robustness to small changes of motion sequences in time and space scales.

Its function is to define each static posture of a movement as a state or a set of states. Through network to connect these states and using probability to describe the switching between state and state. Hidden Markov Models [37] and Dynamic Bayesian Networks [38] are the representations.

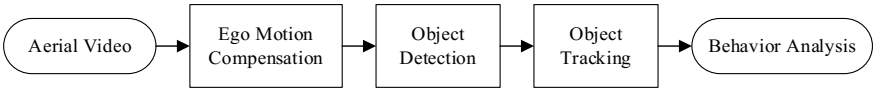

Fig. 4 Common framework of aerial platform based object tracking

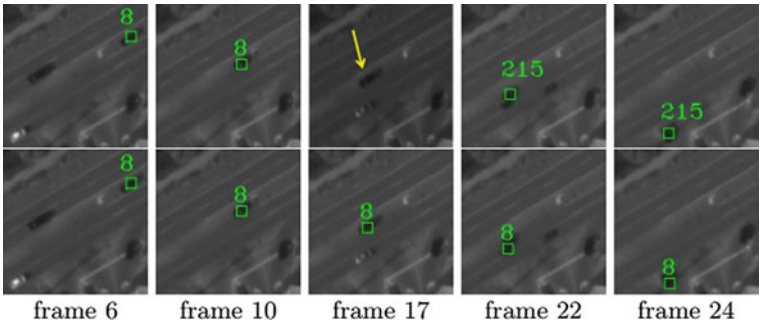

Fig. 5 Results of DBT only (first row) and DBT & LCT (second row)

4.2 Object Tracking Algorithms

In [39], Medioni et al. presented a methodology, in 1997, to perform the analysis of a video stream took from an UAV whose goal was to provide an alert mechanism to a human operator. It was the beginning of their video surveillance and monitoring (VSAM) project. The main procedure follows Fig. 4. In [32, 40], they also followed this and plotted the object trajectory showed in the mosaic image to help to infer their behavior. Nevertheless, these methods cannot deal with the effect of parallax which will lead to false alarm of detection.

Recently, in 2017, they used detection-based tracker (DBT) and local context tracker (LCT) simultaneously to track the vehicles on the ground [41]. Because the object in the airborne images is small, gray and the displacement of a moving target is large, rely merely on DBT is unreliable. By introducing LCT, which explores spatial relations for a target to avoid unreasonable model deformation in the next frame, to relax the dependency on frame differencing motion detection and appearance information. Here, DBT explicitly handles merged detections in detection association. The results showed that this method has a high detection rate, except for its high computation time and inability to long-term occlusion (Fig. 5).

Ali et al. proposed COCOA system for tracking in aerial imagery [42]. The whole framework likes [32, 40]. The system works well but the scenario is simple and no vehicles merging occurs. In [43], they used motion and appearance context for tracking and re-acquiring. It is the first time to use context knowledge in aerial imagery processing. Briefly, the appearance context is used to discriminate whether the objects are occluded or not and similar motion context of the unoccluded objects is used to predict the location of occluded ones as shown in Fig. 6. Obviously, it

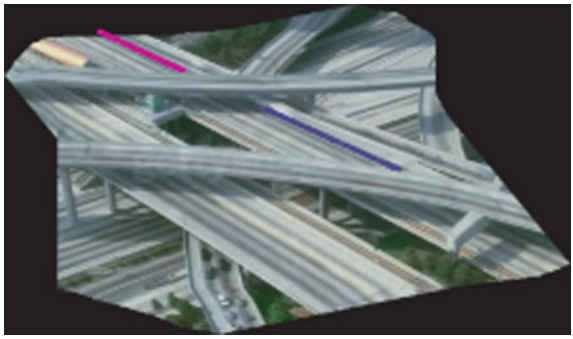

Fig. 6 Using motion context to handle occlusion

can handle occlusion while it needs reference knowledge and does not take slow or stopped vehicles into account.

Perera et al. proposed a tracking method under the conditions of long occlusion and split-merge simultaneously [44]. The object detection is performed by background modeling which flags a pixel whether it belongs to foreground or background. A simple nearest-neighbor data association tracker is used, in which Kalman filter updates the position and velocity of objects. Long occlusion is solved by tracklets linking according one-to-one correspondence. In terms of merges and splits, suppose two objects A and B merge for a while, so that

$$\begin{aligned} A &= \{T_{a,1}, \ldots, T_{a,m}, T_{c,1}, \ldots, T_{c,o}, T_{d,1}, \ldots, T_{d,p}\} \\ B &= \{T_{b,1}, \ldots, T_{b,n}, T_{c,1}, \ldots, T_{c,o}, T_{e,1}, \ldots, T_{e,q}\} \end{aligned} \tag{1}$$

where T_c represents the merging period, the rest are splitting one. Using the pairwise assumption:

$$\begin{aligned} P(A, B) = {} & P(\{T_{a,1}, \ldots, T_{a,m}\}) \times P(\{T_{b,1}, \ldots, T_{b,m}\}) \\ & \times P_m(\{T_{a,m}, T_{b,n} \rightarrow T_{c,1}\}) \times P(\{T_{c,1}, \ldots, T_{c,o}\}) \\ & \times P_s(\{T_{c,o} \rightarrow T_{d,1}, T_{e,1}\}) \times P(\{T_{d,1}, \ldots, T_{d,p}\}) \\ & \times P(\{T_{e,1}, \ldots, T_{e,q}\}) \end{aligned} \tag{2}$$

with P_m and P_c denote the probability of a merge and split, respectively. The results showed that tracker will not be confused after two vehicles merging and continue tracking on the same vehicle when they split, as shown in Fig. 7. However, this method needs 30 frames to initialize the background model and does not take slow or stopped vehicles into account.

Xiao et al. proposed a joint probabilistic relation graph approach to detect and track vehicles [45], in which background subtraction is used because it can make up the drawback of three-frame subtraction that it is hard to detect slow or stopped vehicles. Vehicle behavior model is exploited to estimate potential travel direction and speed for each individual vehicle. In line with expectations, more stopped and

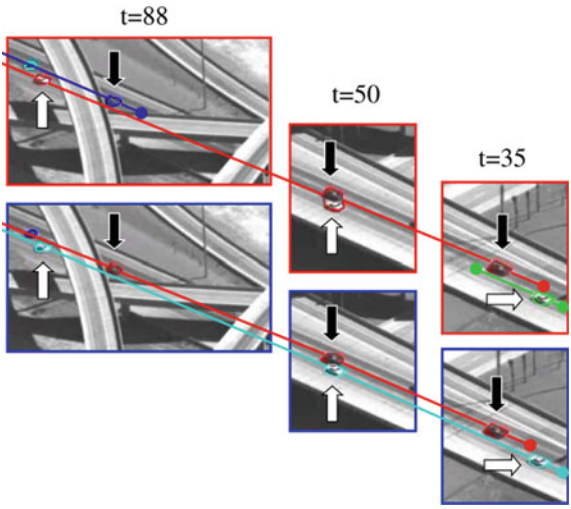

Fig. 7 The images (red border) confused while the images (blue border) show linking after merge processing

slow vehicles are detected, while due to the overlap when two vehicles merge, the detection accuracy will be affected. In the results, track identifications were missed that all detected vehicles were marked as the same color.

Keck et al. realized the real-time tracking of low-resolution vehicles for aerial surveillance [36]. The airborne images are characterized that they have 100 megapixels, which will increase the burden of computation. To solve this problem, they divided the large images into tiles and set TileProcessors to process tiles in parallel. FAST-9 algorithm (feature based), three-frame difference and Kalman filter are used to perform registration, detection and tracking respectively. Through quantitative results, the detection and tracking accuracy are high. Because of parallelism, the efficiency of computation can meet the need of real-time. However, occlusion, merge and split, same appearance of objects will affect these accuracy.

Some state-of-the-art methods are summarized in Table 2.

4.3 Common Datasets

Some common datasets of airborne imagery that can be used for object tracking are collected and listed below:

VIVID datasets [48]. This datasets is created for tracking ground vehicles from airborne sensor platforms. Its functions includes ground-truthed data set, some baseline tracking algorithm and a mechanism for compare yours results with ground-truth.

UAV123 dataset [49]. All videos in this dataset are captured from low-altitude UAVs. It contains a total of 123 video sequences and more than 110 K frames.

Table 2 Object tracker in aerial surveillance, their components and performance

References	Registration	Detection	Tracking	Slow or stopped	Occlusion	Merge and split	Track identifications	Computational efficiency
[46]	Feature points	Motion pattern	Motion pattern	✗	✓	✗	✓	N/A
[14]	Gray-level	Background subtraction	Motion pattern	✗	✗	✗	✓	High
[41]	✗	Optical flow	Local context	✓	✗	✓	✓	High
[43]	✗	Manually	Motion context and appearance context	✗	✓	✗	✓	N/A
[47]	✗	✗	Meanshift	✗	✗	✗	✗	N/A
[44]	KLT features	Background model	Nearst-neighbor data association	✗	✓	✓	✓	Low
[45]	Geography features	Three-frame subtraction & background subtraction	Graph match & vehicle behavior model	✓	✗	✗	✗	High
[36]	Feature points	Three-frame difference	Kalman filter	✗	✗	✗	✓	High
[13]	Feature points	Background model	Graph-based model	✗	✓	✗	✗	N/A

CLIF 2006 dataset [50]. This datasets is established by Air Force Research Labs of America. It is used for the research of aerial surveillance. Its features are high altitude, large field of view and small objects.

SEAGULL dataset [51]. A multi-camera multi-spectrum (visible, infrared, near infrared and hyper-spectral) image sequences dataset for research on sea monitoring and surveillance. The image sequences are recorded from a fixed wing UAV flying above the Atlantic Ocean.

In addition, Image Sequence Server dataset [52], WPAFB 2009 dataset [53], UCF Aerial Action Data Set [54] and UCLA Aerial Event Dataset [55] are also common aerial image datasets.

4.4 Evaluation Metrics

When tracking algorithm is performed, the results should be evaluated both qualitatively and quantitatively to illustrate whether the algorithm is robust or not.

Qualitative evaluation. Generally, we use a bounding box or more to contain the object(s) in pixels we want to track. Then, evaluation is carried out by our eyes.

If the tracking algorithm is robust and accurate, the bounding box will lock on the appearance of the object as much as possible, whenever occurs illumination change, occlusion, abrupt motion etc. Otherwise, when it drifts, it is weak and inaccurate.

Quantitative evaluation. Only qualitative evaluation is not persuasive. Quantitative evaluation always couples with qualitative one.

In [8], author introduces four metrics for evaluation of single object. They are Center Location Error (CLE), Distance Precision (DP), Overlap Precision (OP) and Frames Per Second (FPS).

CLE refers to the Euclidean distance between the estimated location and ground-truth location of the object. The smaller the value is, the better the performance is.

$$\mathrm{CLE} = \sqrt{(x - x_0)^2 + (y - y_0)^2} \tag{3}$$

DP refers to the percentage of the frames whose CLE is smaller than a threshold among the whole sequences. The higher the value is, the better the performance is.

$$\mathrm{DP} = \frac{N_{\mathrm{CLE} \le \mathrm{th}}}{N} \times 100\% \tag{4}$$

OP refers to the percentage of the frames in which the overlap rate between bounding box and area of ground-truth is higher than a threshold. The higher the value is, the better the performance is.

$$\mathrm{OP} = \frac{N_{\phi \ge \mathrm{th}}}{N} \times 100\%, \phi = \frac{A_{\mathrm{output}} \cap A_{\mathrm{ground\ truth}}}{A_{\mathrm{output}} \cup A_{\mathrm{ground\ truth}}} \tag{5}$$

FPS refers to the how many frames the algorithm can process in one second. The higher the value is, the better the performance is:

$$\mathrm{FPS} = N/t \tag{6}$$

5 Future Directions

Although those state-of-the-art methods have lower false alarms and higher tracking accuracy, some issues are still "bottlenecks" that constrain the further development of UAV-based tracking.

(1) **Appearance change**

When object moving, the pose and shape may change. Additionally, illumination variation will also affect tracker.

(2) **Occlusion**

Because object lost in view during occlusion, trackers may not resume tracking when occlusion ends.

(3) **Complex background**

Due to the high-altitude angle of surveillance, objects may drown in background that brings difficulty to detection.

(4) **Merge and split**

When objects merge, some trackers consider them as one object that lose identities even switch track ID.

(5) **Computation efficiency**

With the improvement of sensors, the rising of megapixels and more objects being tracked, the amount of calculation will be greater. The requirements of efficient algorithm and high performance hardware facilities need to be meet.

In the future, some improvements and innovations maybe realized:

(1) **Rarely use traditional generation methods**

Detection-based tracking method will be the mainstream for aerial surveillance, in which background information, local models and dynamic model are critical components [8]. Fully using background information can separate object and background well. Local model can fight against appearance change. Dynamic model is used for prediction that search region can be minimized.

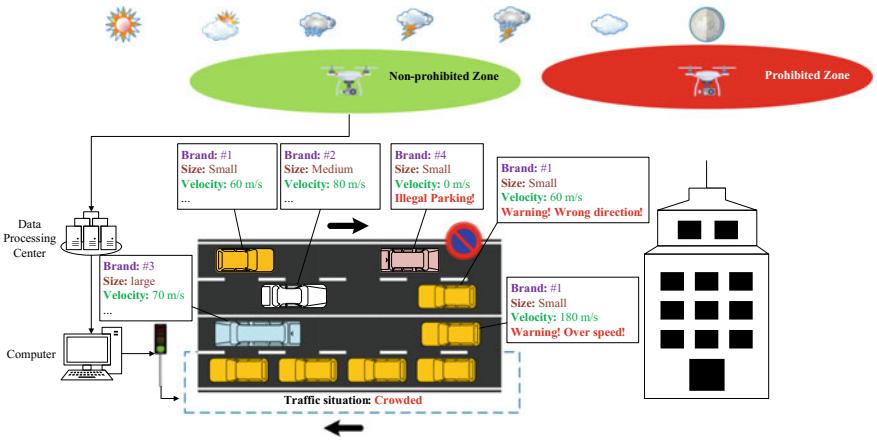

Fig. 8 The UAV-based traffic surveillance system in the future

(2) **Surveillance with AI technology**

Now the Artificial Intelligence (AI) has been widely and deeply studied. The technologies of machine learning (ML) and deep learning (DL) have shown their great power in the field of computer vision, automation and even Go [56]. Through the feature extraction and training of massive data, computers can even compete with humans and they can do some work instead of us. As shown in Fig. 8, if supported by the department of transportation and automobile manufacturer, we can train models by the data (prior knowledge) they offered and use detection and tracking algorithm to realize UAV traffic monitoring. After UAV taking and transferring videos to the data processing center (DPC), the brand, size, velocity etc. can be recognized online. At the same time, situation estimation and congestion judgment will be performed by object tracking. These information will be all received by the operators who are in front of computer. Then they can make decision that whether send out a warning signal or give priority of driving.

(3) **No ego motion compensation**

Advanced technology of UAV stabilization such as flight control and wind estimation may decrease the needs of ego motion compensation that this step can be optional.

(4) **Lower computation burden**

Advanced hardware, processor and efficient algorithms in aerial platform can relax the computation burden that the situation of scene and the processed data can be reflected to the observers in real-time.

(5) **Persistent working ability**

UAVs should meet the needs of working all-time and all-weather if they are used in engineering. Working merely in good weather is far from enough. The technology of waterproof and battery etc. should be progressed as soon as possible.

(6) **More open airspace**

The limited flying space will make the UAV useless. In the future, more airspace will be available for operators. While UAVs are flying, operators should also obey the flight rules in the non-prohibited zone and keep in mind that prohibited zone is inviolable at all times.

6 Conclusion

This paper presents a survey of object tracking in aerial surveillance. First, the development history and current research institutions are reviewed. Then, frequently used sensors are summarized which are followed by the detailed descriptions of the common frame work and representative tracking algorithms of aerial surveillance. Some suggestions and future directions are proposed for the deficiency of the current technologies in which we conclude that by combining advanced algorithm with AI technology, the UAV can play a greater role in the field of aerial surveillance.

Acknowledgements This paper is sponsored by National Program on Key Basic Research Project (2014CB744903), National Natural Science Foundation of China (61673270), Shanghai Pujiang Program (16PJD028), Shanghai Industrial Strengthening Project (GYQJ-2017-5-08), Shanghai Science and Technology Committee Research Project (17DZ1204304) and Shanghai Engineering Research Center of Civil Aircraft Flight Testing.

References

1. Chikwanha, A., Motepe, S., & Stopforth, R. (2012, November). Survey and requirements for search and rescue ground and air vehicles for mining applications. In *Proceeding of the 19th Conference on Mechatronics and Machine Vision in Practice* (pp. 105–109).
2. Bian, J., Hui, X., Yu, Y., Zhao, X., & Tan, M. (2017, December). A robust vanishing point detection method for UAV autonomous power line inspection. In *Proceeding of the Conference on Robotics and Biomimetics on IEEE* (pp. 646–651).
3. Ke, R., Li, Z., Tang, J., Pan, Z., & Wang, Y. (2018). Real-time traffic flow parameter estimation from UAV video based on ensemble classifier and optical flow. In *IEEE Transaction on Intelligent Transportation Systems*.
4. Carroll, E. A., & Rathbone, D. B. (2002, January). Using an unmanned airborne data acquisition system (ADAS) for traffic surveillance, monitoring and management. In *Proceedings of the Conference on ASME 2002 International Mechanical Engineering Congress and Exposition* (pp. 145–157).
5. Clapper, J. R., Young, J. J., Cartwright, J. E., & Grimes, J. G. (2009). Office of the secretary of defense unmanned systems roadmap (2009–2034). *United States Department of Defense, Tech. Rep*.
6. Mercado, D., Colunga, G. R. F., Castillo, P., Escareño, J. A., & Lozano, R. (2013, May). Gps/ins/optic flow data fusion for position and velocity estimation. In *Proceeding of the Conference of Unmanned Aircraft Systems on IEEE* (pp. 486–491).

7. Yang, S., Scherer, S. A., Schauwecker, K., & Zell, A. (2013, May). Onboard monocular vision for landing of an MAV on a landing site specified by a single reference image. In *Proceeding of the Conference on Unmanned Aircraft Systems on IEEE* (pp. 318–325).
8. Wu, Y., Lim, J., & Yang, M. H. (2013). Online object tracking: A benchmark. In *Proceeding of the Conference on CVPR* (pp. 2411–2418).
9. Taylor, J. W. R., & Munson, K. (1977). Jane's pocket book of remotely piloted vehicles: Robot aircraft today. *Collier Books*.
10. Huang, M., Zhang, B., & Ding, Y. L. (2018). Development of airborne photoelectric platform at abroad. *Aeronautical Manufacturing Technology, 9,* 70–71.
11. http://www.borderlandnews.com/stories/borderland/20040319–95173.shtml.
12. http://iris.usc.edu/people/medioni/current_research.html.
13. Reilly, V., Idrees, H., & Shah, M. (2010, September). Detection and tracking of large number of targets in wide area surveillance. In *Proceeding of the Conference on ECCV* (pp. 186–199).
14. Prokaj, J., Zhao, X., & Medioni, G. (2012, June). Tracking many vehicles in wide area aerial surveillance. In *Proceeding of the Conference on CVPR Workshops* (pp. 37–43).
15. Prokaj, J., & Medioni, G. (2011, June). Using 3d scene structure to improve tracking. In *Proceeding of the Conference on CVPR* (pp. 1337–1344).
16. Prokaj, J., Duchaineau, M., & Medioni, G. (2011, June). Inferring tracklets for multi-object tracking. In *Proceeding of the Conference on Computer Vision and Pattern Recognition Workshops* (pp. 37–44).
17. http://theairlab.org/.
18. https://uavvision.com/about/.
19. https://www.youtube.com/watch?v=pgYDoU8BiiE.
20. https://www.dji.com/cn.
21. http://thedronegirl.com/2017/02/26/dji-yuneec-autel-mota/.
22. http://www.automatedvehiclessymposium.org/avs2018/proceedings.
23. http://www.uasconferences.com/.
24. Yuan, C., Medioni, G., Kang, J., & Coehn, I. (2011, December). Detection and tracking of moving objects from a moving platform in presence of strong parallax. *U.S. Patent 8,073,196*.
25. Barnea, D. I., & Silverman, H. F. (1972). A class of algorithms for fast digital image registration. *IEEE Transaction on Computers, 100*(2), 179–186.
26. Lowe, D. G. (2004). Distinctive image features from scale-invariant keypoints. *International Journal of Computer Vision, 60*(2), 91–110.
27. Fan, X., Rhody, H., & Saber, E. (2005, December). Automatic registration of multisensor airborne imagery. In *Proceedings of the 34th Conference on Applied Imagery and Pattern Recognition Workshop* (p. 6).
28. Bouchahma, M., Barhoumi, W., Yan, W., & Al Wardi, H. (2017, October). Optical-flow-based approach for the detection of shoreline changes using remote sensing data. In *Proceeding of the 14th Conference on Computer Systems and Applications* (pp. 184–189).
29. Srivastav, N., Agrwal, S. L., Gupta, S. K., Srivastava, S. R., Chacko, B., & Sharma, H. (2017, January). Hybrid object detection using improved three frame differencing and background subtraction. In *Proceedings of the 7th Conference on Cloud Computing, Data Science and Engineering-Confluence* (pp. 613–617).
30. Ahmed, A. H., Kpalma, K., & Guedi, A. O. (2017, December). Human detection using HOG-SVM, mixture of Gaussian and background contours subtraction. In *Proceedings of 13th the Conference on Signal-Image Technology and Internet-Based Systems* (pp. 334–338).
31. Chao, H., Gu, Y., & Napolitano, M. (2013, May). A survey of optical flow techniques for uav navigation applications. In *Proceeding of the Conference on Unmanned Aircraft Systems* (pp. 710–716).
32. Cohen, I., & Medioni, G. (1998, November). Detecting and tracking moving objects in video from an airborne observer. In *Proceeding of the Conference on IEEE Image Understanding Workshop* (Vol. 1, pp. 217–222).
33. Cheng, Y. (1995). Mean shift, mode seeking and clustering. *IEEE Transaction on Pattern Analysis and Machine Intelligence*, *17*(8), 790–799.

34. Kalal, Z., Matas, J., & Mikolajczyk, K. (2010, June). PN learning: Bootstrapping binary classifiers by structural constraints. In *Proceeding of the Conference on CVPR* (pp. 49–56).
35. Yilmaz, A., Javed, O., & Shah, M. (2006). Object tracking: A survey. *ACM Computing Surveys (CSUR), 38*(4), 13.
36. Keck, M., Galup, L., Stauffer, C. (2013, January). Real-time tracking of low-resolution vehicles for wide-area persistent surveillance. In *Proceeding of the Conference on Applications of Computer Vision* (pp. 441–448).
37. Gong, S., & Xiang, T. (2003, October). Recognition of group activities using dynamic probabilistic networks. In *Proceeding of the Conference on Computer Vision* (pp. 742–749).
38. Pavlovic, V., Frey, B. J., & Huang, T. S. (1999). Time-series classification using mixed-state dynamic Bayesian networks. In *Proceeding of the Conference on CVPR* (Vol. 2, pp. 609–615).
39. Medioni, G., & Nevatia, R. (1997). Surveillance and monitoring using video images from a UAV. In *Proceeding of the Conference on IUW*.
40. Cohen, I., & Medioni, G. (1998). Detection and tracking of objects in airborne video imagery. In *Proceeding of the Conference on CVPR Workshop on Interpretation of Visual Motion*.
41. Chen, B. J., & Medioni, G. (2017, March). Exploring local context for multi-target tracking in wide area aerial surveillance. In *Proceeding of the Conference on Applications of Computer Vision* (pp. 787–796).
42. Ali, S., & Shah, M. (2006, May). COCOA: Tracking in aerial imagery. In *Airborne Intelligence, Surveillance, Reconnaissance (ISR) Systems and Applications III* (Vol. 6209, p. 62090D).
43. Ali, S., Reilly, V., & Shah. (2007, June). Motion and appearance contexts for tracking and re-acquiring targets in aerial videos. In *Proceeding of the Conference on CVPR* (pp. 1–6).
44. Perera, A. A., Srinivas, C., Hoogs, A., Brooksby, G., & Hu, W. (2006, June). Multi-object tracking through simultaneous long occlusions and split-merge conditions. In *Proceeding of the Conference on CVPR* (Vol. 1, pp. 666–673).
45. Xiao, J., Cheng, H., Sawhney, H., & Han, F. (2010). Vehicle detection and tracking in wide field-of-view aerial video. In *Proceeding of the Conference on CVPR* (pp. 679–684).
46. Yu, Q., & Medioni, G. (2009, June). Motion pattern interpretation and detection for tracking moving vehicles in airborne video. In *Proceeding of the Conference on CVPR* (pp. 2671–2678).
47. Fang, P., Lu, J., Tian, Y., & Miao, Z. (2011). An improved object tracking method in UAV videos. *Procedia Engineering, 15,* 634–638.
48. Collins, R., Zhou, X., & Teh, S. K. (2005). An open source tracking testbed and evaluation web site. *IEEE International Workshop on Performance Evaluation of Tracking and Surveillance, 2,* 35.
49. Mueller, M., Smith, N., & Ghanem, B. (2016, October). A benchmark and simulator for uav tracking. In *Proceeding of the Conference on ECCV* (pp. 445–461).
50. https://www.sdms.afrl.af.mil.
51. Jha, M. N., Levy, J., & Gao, Y. (2008). Advances in remote sensing for oil spill disaster management: state-of-the-art sensors technology for oil spill surveillance. *Sensors, 8*(1), 236–255.
52. http://i21www.ira.uka.de/image_sequences/.
53. https://www.sdms.afrl.af.mil/index.php?collection=clif2006.
54. http://crcv.ucf.edu/data/UCF_Aerial_Action.php.
55. Shu, T., Xie, D., Rothrock, B., Todorovic, S., & Chun Zhu, S. (2015). Joint inference of groups, events and human roles in aerial videos. In *Proceedings of the Conference on CVPR* (pp. 4576–4584).
56. Wang, F. Y., Zhang, J. J., Zheng, X., Wang, X., Yuan, Y., Dai, X., … Yang, L. (2016). Where does AlphaGo go: From church-turing thesis to AlphaGo thesis and beyond. *IEEE/CAA Journal of Automatica Sinica*, *3*(2), 113–120.

Application and Improvement of Gas Turbine Blades Film Cooling

Koval Svetlana

Abstract A higher thermal efficiency and a larger power generation of aircraft turbine engine have long been pursued by researchers. To achieve this target, the turbine inlet temperature must be raised. Gas turbines are operated at around 1800 °C now and definitely will be higher than 2000 °C someday. This temperature induces excessive thermal stresses on the turbine blade, thus the possibility of thermal failure is enhanced. The blade leading edge is the area with the highest thermal load in a gas turbine, and the film cooling is the most effective method to protect the blade from ablating. The flow structure complexity of coolant ejected from the film holes is determined by the blowing ratio, distribution of the film holes, direction of the film holes and the pressure gradient in the main stream direction. This paper analyzed the use of film cooling in gas turbine blades, as well as analyzed ways of raising its effectiveness.

Keywords Blade profile · Heat transfer · Film cooling · Cooling effectiveness

1 Introduction

Gas turbine engines (GTE) are widely applied in aviation, energy, ship propulsion, to drive compressors gas transportation systems, as well as in the technological cycles of some chemical productions. The basic requirements for all GTE, regardless of their destination, are a high efficiency, operational reliability and long service life. The main method of increasing the efficiency of the GTE was, and still increase the gas temperature before the turbine, which in modern gas-turbine engine reaches 1500–1600 °C, which significantly exceeds the permissible temperature level in modern high-temperature alloys used for the manufacture of nozzle and working blades. In this regard, to ensure that they use high efficiency air cooling systems.

K. Svetlana (✉)
Shanghai Jiao Tong University, Shanghai, China
e-mail: koval-svetlana@ro.ru

Z. Jing (ed.), *Proceedings of International Conference on Aerospace System Science and Engineering 2018*, Lecture Notes in Electrical Engineering 549,
https://doi.org/10.1007/978-981-13-6061-9_5

The most thermally loaded element profile of the turbine blade is a portion of the input edge that caused, on the one hand, the high intensity heat from the gas in the vicinity of the point of braking the flow and on the other a smaller heat exchange surface area on the cooler side.

The use of film cooling for this region especially important. Flow structure at blowing cooler on the front edge is substantially different from the structure that is formed around the flat surface, which is caused by the presence of a hard braking of the flow and significant gradients of velocity and static pressure.

Unfortunately, in the open literature are not enough works devoted to the preferred location of the rows of film cooling holes on the front edge, the use of surface recesses and efficiency of film cooling on curved surfaces from cross sections of the injection. Thus, the issues of further improvement of film cooling systems, input edges of blades of gas turbines, study of flow structure and obtaining generalizing dependency is a relevant research direction of great importance for gas turbine construction and other high-temperature energy systems.

2 Research Status and Challenges

This section provides an overview of the cooling systems of modern gas-turbine engine blades. The analysis of use of film cooling in gas turbine blades, as well as analyzed ways of increase its effectiveness. Considered the features of the application of film cooling on the inlet edge of the blades of GTE.

2.1 Trend of the Gas Temperature Before the Turbine and Development of Cooling Systems for Blades

Raising the gas temperature at the turbine inlet is one of the main ways to increase efficiency, specific power, and improved weight and size parameters of gas turbine engines for any purpose. Despite the use of new heat-resistant materials [1–6], the introduction of technology of single crystal casting and casting with directional solidification, and the application of protective coatings, the achievement of such high-temperature gas (up to 1600 °C) became possible mainly due to improvement of cooling system of blades. In Fig. 1 [7] shows that the rate of growth of the gas temperature surrounding the rotor blade of the first stage significantly exceeds the growth rate of allowable temperature for the material used for the blades.

In the vast majority of modern gas-turbine engine for cooling of nozzle and rotor blades is applied open air cooling system. This system is relatively simple in construction and reliable in operation, it is essentially the only practically used for cooling gas turbine blades. In Fig. 2 shows the blades cooled with different schemes of the flow of the cooler.

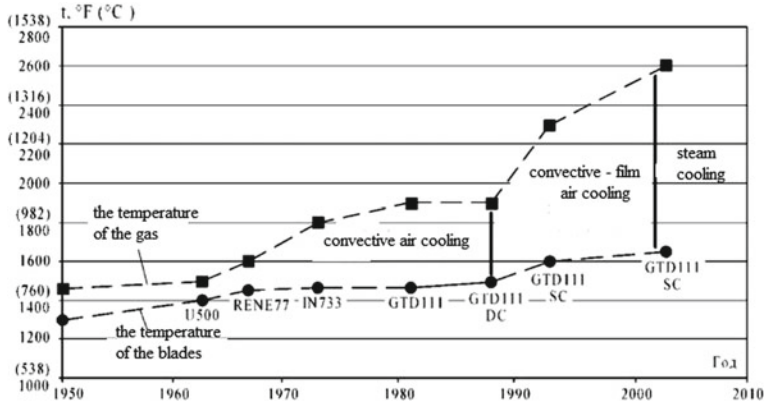

Fig. 1 The increase in the gas temperature before the turbine and the allowable temperature of the rotor blade

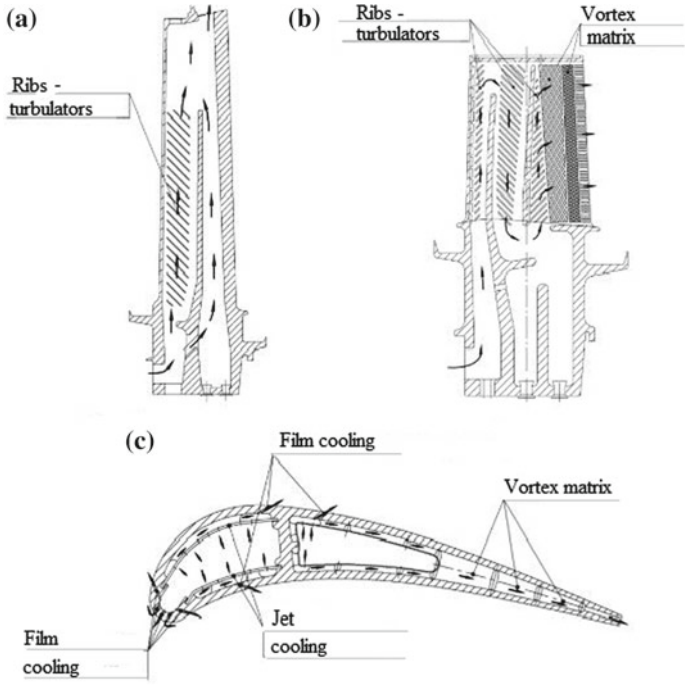

Fig. 2 The schema of vanes with different schemes of flow of the cooling air: **a** longitudinal (radial), **b** radial-transverse (combined), **c** transverse

2.2 Perspective of the Cooling System

Considering the cooling blades of modern gas-turbine engine, there are still some common design solutions, thereby guaranteeing that the temperature of the blades at the reached temperatures of the gas before the turbine. In Fig. 3 shows the structure [8] of the nozzle vanes of the first stage, common to most engines. The internal cavity consists of three separate cavities, each with a perforated baffle. Convective cooling of a greater part of the profile of the blade is provided by jet air cooling of the internal surfaces of the walls through the holes in the baffles. In the region of the inlet edge of the plot jet cooling is absent because of the high backpressure from the gas. For blade cooling in the area of the trailing edge (narrow profile) used the columns-turbulence. Virtually the entire blade profile convection cooling combined with a strong film cooling.

An overview of the structures of the cooled rotor blades of modern gas-turbine engine has shown that, regardless of the power, the vast majority of them have a loop diagram of the flow of the refrigerant in the channels, usually in combination with film cooling.

From the performed analysis, it follows that to achieve the necessary depth of cooling in the convection schemes are used, additional turbulence of the flow (columns–tabulators) and jet cooling.

Intensification of heat transfer in this case is achieved through constant destruction of the boundary layer when flow separation and additional turbulence in the flow at the heat exchange surface due to the creation of vortex structures.

Also, is developing new schemes, e.g. cyclone cooling, is investigated in [9, 10], the basic principle of which is tangential supply of cooling air to the channel through discrete holes or slots. At the same time, despite the development of convective schemes:

- Application of film cooling is the only component in the cooling systems of the blades of the first turbine stages and used as a cooling profile of the scapula (input edge, a back, a trough), and for cooling the end surfaces;

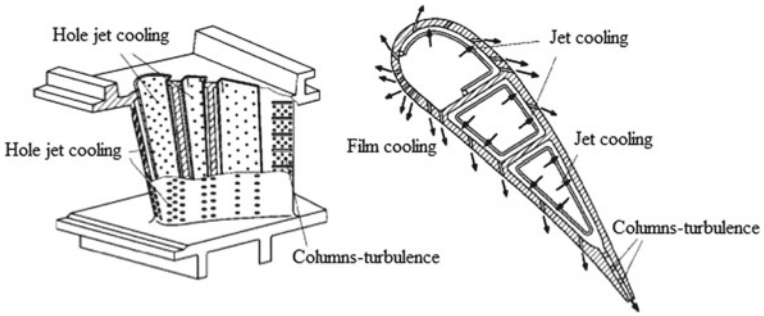

Fig. 3 A typical cooling system of the nozzle blades

- Film cooling combined with most methods of convective cooling;
- The development of the film cooling determines the growth efficiency of the cooling system of the blade on the whole.

So, it is film cooling selected for further study.

2.3 Application of Film Cooling

2.3.1 The Mechanism of Film Cooling

Film cooling is a cooling surface of the blades with a protective layer of cooling air (Fig. 4) increasing the thermal resistance between gas and wall of blades, and thereby reduces the heat flux into the blade. The decrease in heat flow avoids the arising convective cooling, growth of the temperature gradient in the wall of the scapula, leading to increased thermal stresses. Mixing the blown air with the main flow causes uneven temperature protective layer in the longitudinal direction, which leads to the necessity of using several points of issue cooler on the surface in the course of the main flow (gas flow).

In Fig. 5 [11] presented a design scheme for film cooling, where,

1. is the elementary area (with surface contacts only the cooling air);
2. transitional area (mixing of air with the cooling air);
3. main flow (fast attenuation of the effectiveness of film cooling).

Film cooling is characterized by the adiabatic effectiveness of film cooling, which is determined by the formula:

$$\eta = \frac{T_\Gamma - T_{\text{CT}}}{T_\Gamma - T_{\text{B}}}, \tag{1}$$

where,

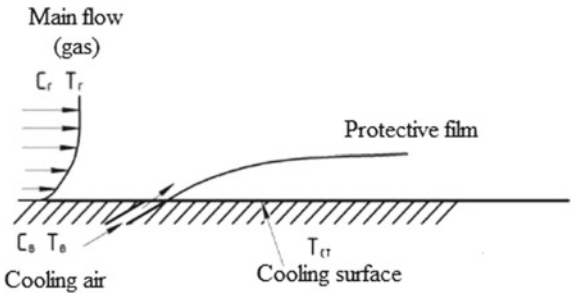

Fig. 4 Principal diagram of film cooling

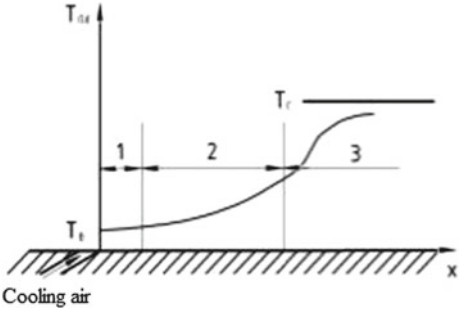

Fig. 5 A design scheme for film cooling

T_Γ total temperature of the main flow (gas) given the coefficient of restitution;
T_{CT} adiabatic wall temperature (the protected surface);
T_B full-blown temperature (cooling) air.

One of the main parameters influencing the characteristics of the film cooling is the injection parameter, defined as the ratio of speeds of the cooling and main flows:

$$m = \frac{\rho_B U_B}{\rho_\Gamma U_\Gamma}, \tag{2}$$

where,

ρ_B, ρ_Γ density, respectively, air and gas;
U_B, U_Γ speed, respectively, air and gas.

2.3.2 Film Cooling Cooled Blades

In relation to the cooling systems of the blades, in film cooling, cooling air is supplied to the surface of the blade through a series of discretely located holes, causing the magnitude of the effectiveness of film cooling is substantially not uniform in the longitudinal and in the transverse direction. In this regard, the effectiveness of film cooling is defined locally for each point of the wall, and is used for analysis averaged in the transverse direction values.

The effectiveness of film cooling depends on many factors, geometric and gas-dynamic character, which can be systematized in the form presented in Table 1.

A large number of published studies [12–17] is devoted to experimental study of film cooling effectiveness on the basis of which the obtained generalized dependences for calculation of efficiency of film cooling, as well as developed techniques that take into account the influence of various factors such as turbulence, acceleration of the external flow, the swirling flow and the curvature of the surface.

The results of numerous studies, e.g. [18–20] show that the actually achieved effectiveness of film cooling of the blades when using cylindrical holes is low.

Table 1 Factors that affect the effectiveness of film cooling

The parameters of the main and cooling streams	The geometric parameters and configuration of the holes
The ratio of speeds of the cooling and main flows (m)	The shape of the holes
The momentum flux ratio of the cooling and main flows	The angle of the axis of the hole to the wall (α)
The turbulence of the main flow (Tu)	The angle of inclination to the bore axis to the direction of the main flow (β)
The ratio of the densities of the cooling and main flows	The distance between the holes, relative distance between the holes (p/d)
The Mach number of the main flow	The relative length of the hole (l/d)
The unsteadiness of the main flow	The distance between rows of holes and the number of rows
The convergent/diffusivity channel	The curvature of the surface
Rotation of the scapula	Surface roughness

Even [20] in the immediate area of blowing cooler difficult to ensure the effectiveness of film cooling to one row of discrete holes at the level of $\eta \approx 0.3$, and at a distance of 20 diameters of the holes ($x/d = 20$), its value generally does not exceed 0.15. Improving the efficiency of film cooling by increasing the number of rows of perforation leads to an increase in cooling air flow and reduce efficiency as turbine and engine as a whole. A number of studies it was found that the reason for the low efficiency of film cooling, largely due to the interaction of the jets of the cooler with the main stream, which has a complex character and is accompanied by a strong vortex formation.

In [21] proposed the following classification of the main vortex structures caused by the release of cooler in film cooling of a flat surface:

- Kidney shaped vortex—a vortex, consisting of two vortices of opposite rotation in the core of the jet;
- Horseshoe vortex—the vortex caused by the sudden deceleration of the boundary layer before the leading edge of the jet;
- Half wake vortex pair in the low pressure zone behind the jet;
- Half wall vortex pair, caused by kidney vortex;
- Lip vortex, caused by the interaction of main flow with the front edge of the jet cooler.

The presence of all these vortices is confirmed by experiments on visualization of flow. It was found that the greatest influence on the effectiveness of film cooling render the formation of "kidney" of the vortex in the jet (Fig. 6), the intensity of which increases sharply with the increase of the injection parameter m. This is due to the presence of a "suction" of gas from the main flow to a protected surface directly under stream cooler.

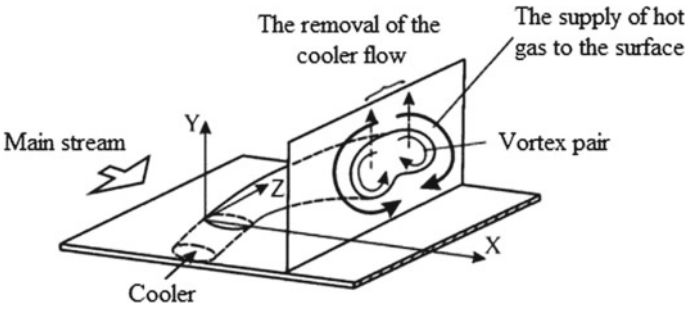

Fig. 6 Schematic diagram of the formation of «kidney» vortex

Therefore, to prevent the formation of kidney vortex and the elimination of separation of streams currently sent a large number of studies that have the following directions:

- The use of surface grooves, including grooves, located on the cooled surface at the exit of the hole;
- Application of fan holes extending to the exit of the protected surface.

The following are the features of these methods that improve the efficiency of film cooling.

2.3.3 Methods of Increasing the Effectiveness of Film Cooling Fan Hole Film Cooling

As an example, Fig. 7 shows the geometry of the fan holes, is investigated in [22, 23], and Fig. 8—some results of experiments to determine the effectiveness of film cooling.

As can be seen from Fig. 8, with the increase of the injection parameter increases the efficiency of film cooling, and, in contrast to the cylindrical holes, even when $m = 2$ in the zone of injection, the film cooling efficiency is not reduced. In [24] reviewed the use of rolling holes more complex configurations, shown in Fig. 9.

As a result of researches it was established that in the range of $0.5 \leq m \leq 2.5$ values of film cooling effectiveness in the case of fan-shaped holes is much higher than when using cylindrical holes (Fig. 10). The highest values of the efficiency of film cooling was achieved in the variant *a*, which, unlike other variants, the effectiveness of film cooling continues to increase, even at values of $m > 2.0$.

The conducted studies [25–27] show an increase in the efficiency of film cooling application fan holes is cylindrical while maintaining the consumption of the cooler. It is also very important that some studies have recorded a decrease in the efficiency of film cooling in the area of injection, even when $m > 2$. The disadvantage of such systems, film cooling is necessary to note that the technology of their production is much harder and more expensive than cylindrical.

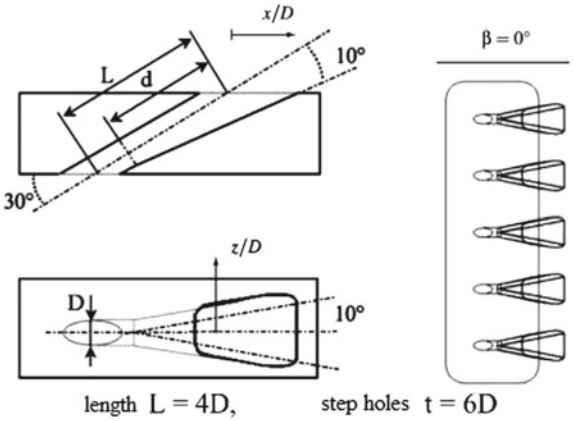

Fig. 7 An example of the geometry of the fan holes

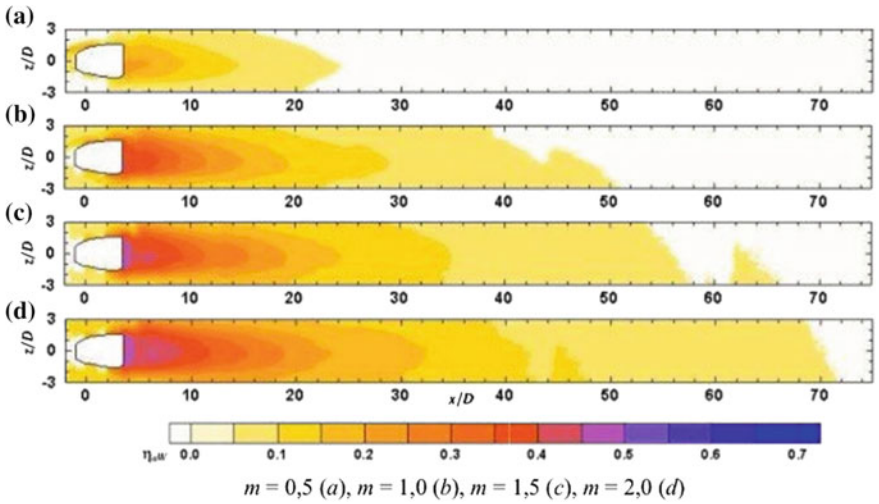

Fig. 8 The effectiveness of film cooling using a fan hole film cooling at different injection settings

However, there is evidence that in the latest developments of cooled blades of high-temperature GTE overseas fan holes are used as the relevant parts of the blades and end surfaces.

The use of fan holes currently is widely used in practice. As an example, in Fig. 11 presented of nozzle blade of the first stage of GTD large production capacity General Electric Frame 9E.

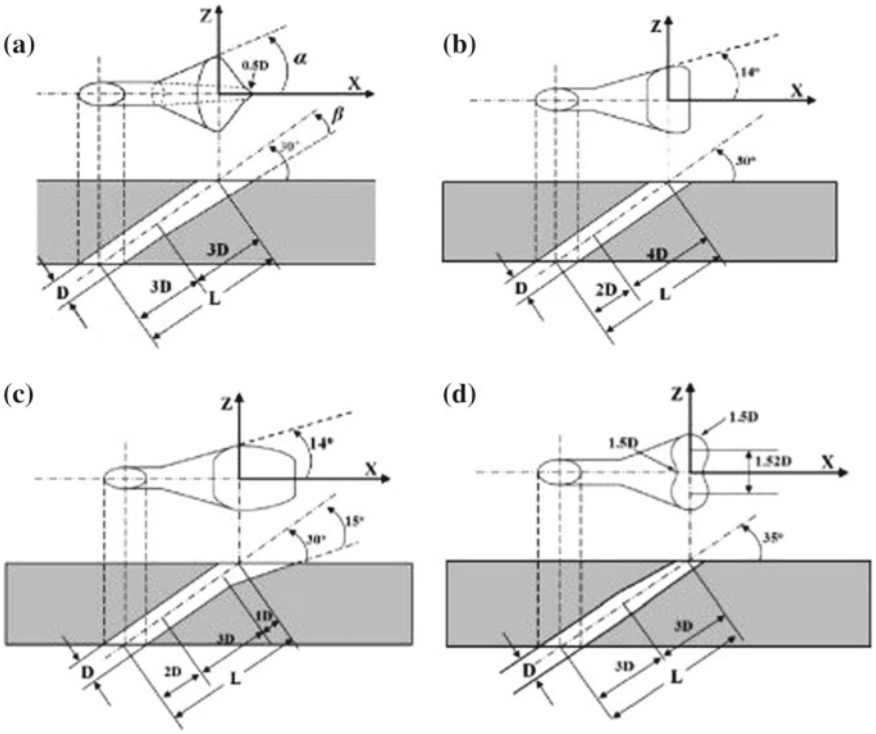

Fig. 9 Configuration for the fan holes studied in [24]

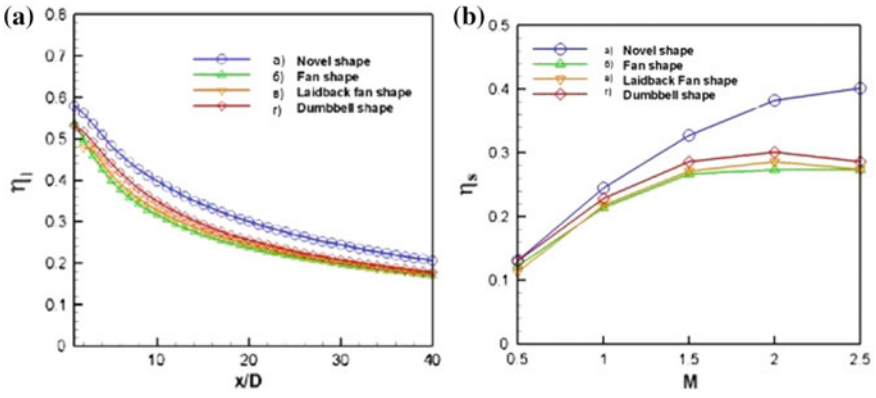

Fig. 10 The distribution of film cooling effectiveness for different configurations of radial holes studied in [24]

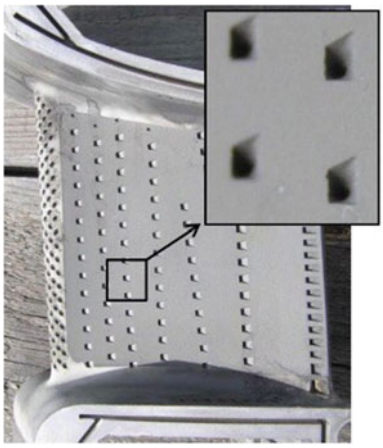

Fig. 11 The use of fan holes on the nozzle blade of the first stage of the GTD Frame 9E

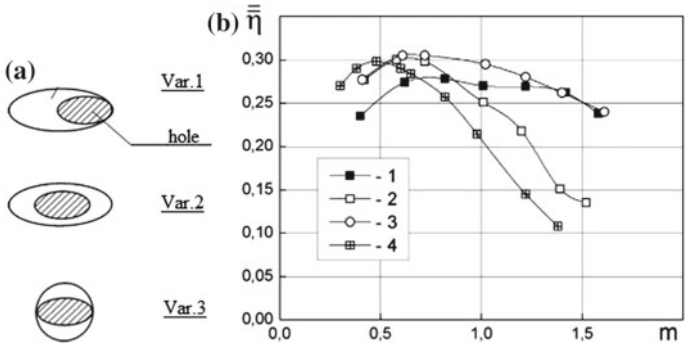

Fig. 12 The options of the recesses (**a**) and the dependence of the average surface ($0 < x/d < 22$) the effectiveness of film cooling from of the injection parameter (**b**) 1–3—holes in options 1–3, 4—basic configuration

Surface grooves on the exit of the holes

In [28] in comparison with the baseline configuration (a number of cylindrical holes without grooves), considers the deepening of elliptic and circular shape (Fig. 12a) on the surface of the blade model from the vacuum (on the back).

Partial results of these studies are shown in Fig. 12b. As can be seen from the figure, the use of grooves at the exit of the holes allows you to raise the level of efficiency almost 2 times. The best performance indicators are obtained for cavities of circular shape (var. 3).

In [29] presents the results of experimental studies of the effectiveness of film cooling by two rows of holes located in hemispherical cavities as shown in Fig. 13. It is obtained that the cooling efficiency for the system of holes in hemispherical depressions substantially (large the parameters of injection at the initial part up to

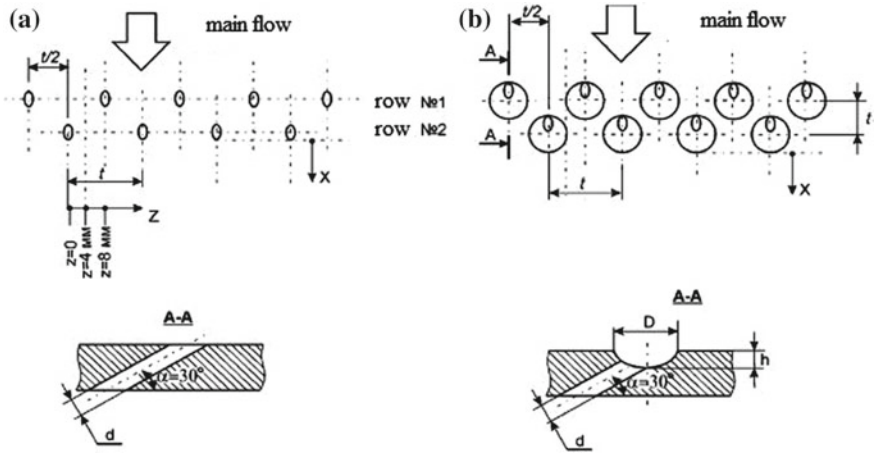

Fig. 13 Diagram of a film cooling system double row of cylindrical holes (**a**) and openings in the hemispherical recesses (**b**)

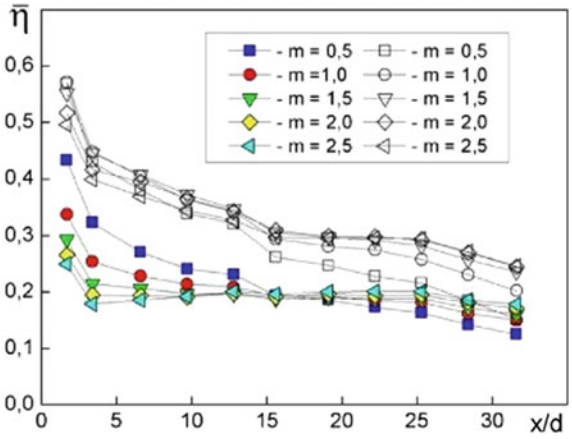

Fig. 14 Comparison of cooling efficiency in the case of use of holes in the hemispherical recesses (filled symbols—a system of holes; empty—the system of the holes in the holes)

2 times) higher than the efficiency for the system of inclined holes without grooves (Fig. 14).

In [30] it is shown that at certain Reynolds numbers in the hemispherical recesses occurs unsteady pulsating vortex is oscillating in the angular and the longitudinal direction (Fig. 15). Vortex periodically discharged into the main stream, creating for deepening a wide trail that is the basis of the oscillating film cooling. However, the oscillating vortex in the recesses stable only at low Reynolds numbers.

In more detail, this configuration of the system of holes in hemispherical cavities was studied in [31, 32]. The studies showed that the flow of the cooler through holes

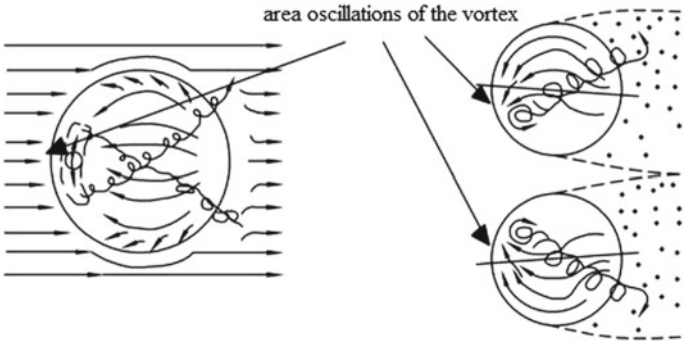

Fig. 15 The oscillation of the vortex in a hemispherical recess

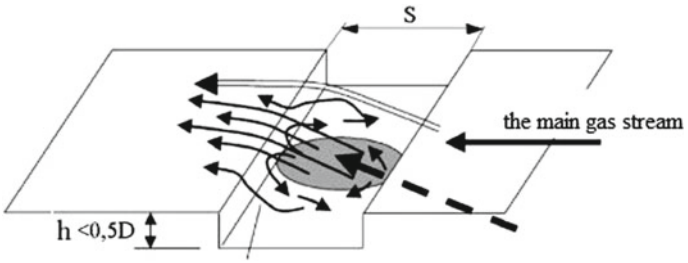

Fig. 16 The scheme of interaction of flow in the trech

in the hemispherical recesses allows to increase the cooling efficiency up to 120%, and to obtain a more uniform film of cooler in comparison with the conventional system. The main reason for the increase of efficiency is a significant reduction in isolation of the chiller from the cooling surface and decreases the intensity of the "kidney" of the vortex in the zone of the blowing of the cooling air.

Another trend in the application of surface recesses is release of air from the cylindrical holes into the grooves of the shallow depth of the trench, perpendicular to the direction of the main flow. In [33] the mechanism of increase of efficiency of film cooling application of transverse grooves is shown. As can be seen from Fig. 16, the presence of the groove prevents the direct penetration of the jet of the refrigerant in the main flow and interaction with him.

In [34], it is shown that the presence of the trench leads to more uniform spreading of the cooling flow along the cooling surface. In [35] investigated the trenches with different relative depth h/d. Studies have shown that the highest results of the efficiency of film cooling gives a trench with low values of $h/d = 0.43$, and exceeds the efficiency of cylindrical holes in 1.5–1.7 times [36]. The disadvantage of such systems as applied to turbine blades is the reduction of strength due to local thinning of the wall of the scapula and the emergence of stress concentrators.

2.3.4 Features Film Cooling of the Inlet Edge

The most thermally loaded element profile of the blade is an input edge. Ensuring sufficient depth cooling input edges is a very complex task, due to, on the one hand, the high intensity heat from the gas in the vicinity of the zone of inhibition of the flow and on the other a smaller heat exchange surface area from the cooling air.

Flow structure in film cooling of the leading edge is much more complicated than in the case of the plane wall, due to the presence of a hard braking of the flow, which leads to the appearance of gradients of velocity and pressure in this area. The release of the cooling air on the surface of the leading edge film cooling provides not only the input edge, but also a significant part of the profile of the blade. In this regard, the issue of improving the efficiency of film cooling of the inlet edge requires separate consideration.

In the work [37] was considered the flow structure of the jet cooler blowing on the front edge. It was determined that the course is complicated by the different directions of the speed of the jet and the speed of the basic flow, the spatial spread of the jet cooler and a high pressure gradient in the direction of the main flow.

Blowing cooler on the front edge of the kidney vortex (two counter-rotating vortex) has the greatest impact on the effectiveness of film cooling. Vortex is formed from the main part of the jet cooler. A characteristic feature of this vortex is its high intensity. On removal from the place of blowing its structure is similar to the structure of the vortex on a flat wall. Vortex "draws" the hot gas in the stream of the cooler, pushing the cold core of the jet cooler from the wall, reducing thus the efficiency of film cooling.

Analysis of constructions of real blades, have shown a variety of options for layouts of the holes on the front edge. The most common are three piece systems with radial or parallel radar cylindrical holes, staggered as in [38–40]. In [41] investigated the variants with the deflection angles of the lateral holes 15° and 50° from the center line. In [42], the deviation angles were 15° and 44°. At the same time, most of the work is devoted to investigation of efficiency only on the site in the immediate vicinity of the holes ($x/d < 10$), which does not allow to determine the effectiveness of film cooling for the rest of the profile.

In addition, the literature contains no practical guidance on the application of the studied configurations.

In [43, 44] performed an experimental and numerical study of the effectiveness of film cooling and the influence of blown air on the intensity of heat transfer. Partial results of this work are presented in Fig. 17.

Received that, despite the staggered arrangement of holes, the jet of air, produced by two rows of holes practically coincide in the transverse direction, resulting in significant unevenness in the effectiveness of film cooling. Increase the intensity of heat transfer for hole while up to 60–70%.

In the experiments on the model of the inlet edge of the blade with three rows of holes were studied in the holes with the angle of the fan extension portion in the lateral direction of 5° to the side, in the longitudinal—0°. Axis all holes were targeted at an angle of 30° in the direction of height of the blade. The ratio of the

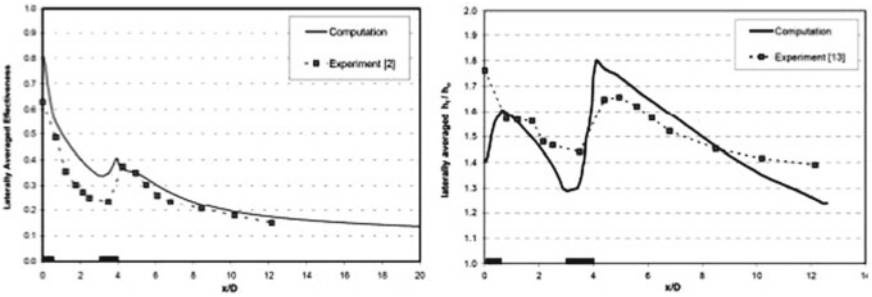

Fig. 17 The results of studies of the effectiveness of film cooling and heat transfer intensity at $m = 2$ [43, 44]

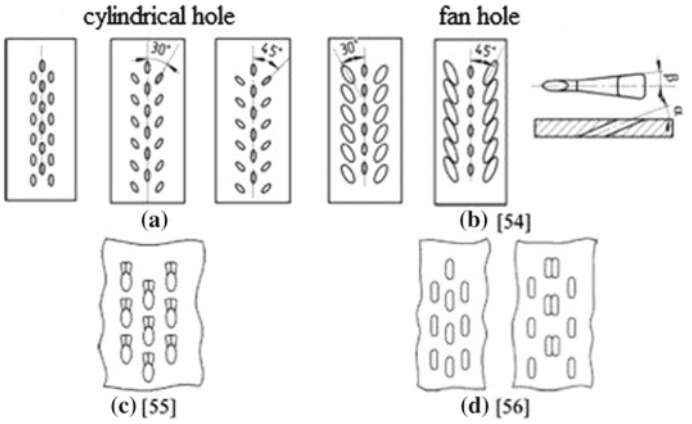

Fig. 18 The configuration of the holes film cooling

diameters of the holes to the diameter of the inlet edge—0.067. Hole the middle number for all cases is cylindrical, the axis of the fan-shaped holes were investigated in the frontal plane were deployed at 30° and 45° from the vertical axis of the blade, the pitch of the holes in the height direction $t/d = 4$. In all experiments, the degree of turbulence of the main flow (Tu) was 9%. These and most other studies carried out for the plane wall with a rounded edge in the area of the incident flow, so do not allow to consider the influence of some factors characteristic for the gas flow in the interscapular channel grating profiles. In [45–47] examined different configurations of the location of the holes film cooling on the front edge and the use of fan-shaped holes, as shown in Fig. 18.

From the results of the experiments (Fig. 19) it was found that the highest values of film cooling effectiveness achieved with the fan holes deployed at an angle of 45° from the vertical axis of the blade.

So, in the section of injection for a number of radial holes, with $m = 1.5$ is reached, the values $\eta \approx 0.57$, while in the same rotation angles of the embodiment

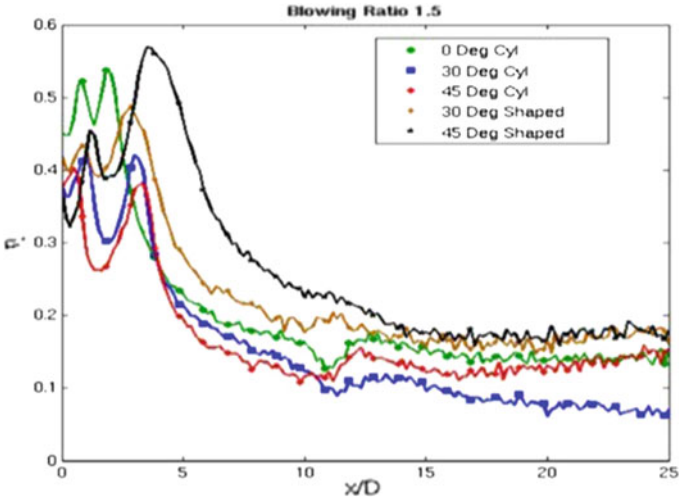

Fig. 19 The results of studies of the effectiveness of film cooling [45]

with cylindrical holes—$\eta \approx 0.38$ in. In the cross section $x/d = 20$ in the version with radial holes is obtained $\eta \approx 0.18$, with a cylindrical hole $\eta \approx 0.07$.

Increasing the efficiency of film cooling application fan holes on the front edge is also obtained in [48], which were numerically and experimentally investigated a flat wall with a cylindrical input edge with four rows of inclined holes.

In [49] for film cooling of the inlet edge made a study of the influence of rotation on the distribution of the efficiency of film cooling on the profile of the blade. The results of the work noted that the rotation speed is a very important factor influencing the distribution of film cooling effectiveness. The increase in speed led to a decrease in the average effectiveness of film cooling. Of great importance in terms of the playing rotation the angle of attack, this changes (Fig. 20).

It is found that when the rotational speed of 2400 rpm at zero angle of attack the air is equally coming all the way back and the trough. When the rotor speed is increased to 3000 rpm it has a negative angle of attack, the air better down to the trough, which led to a decrease in the efficiency of film cooling of the back. When speed reduction is observed the opposite effect. The influence of the injection parameter at different frequencies of rotation was also different.

Most represented in the literature of studies conducted on the portion of the input edges followed by a flat section. This configuration provides close to the real blade pressure distribution and air velocity near the leading edge. However, on a straight stretch during the relaxation of longitudinal stream gradients of velocity and pressure are not available, which does not match the case of the use of film cooling on the turbine blade. In this regard, there is a need to conduct research on curved (convex and concave) surfaces with the actual geometry of the inter-blade channel, which

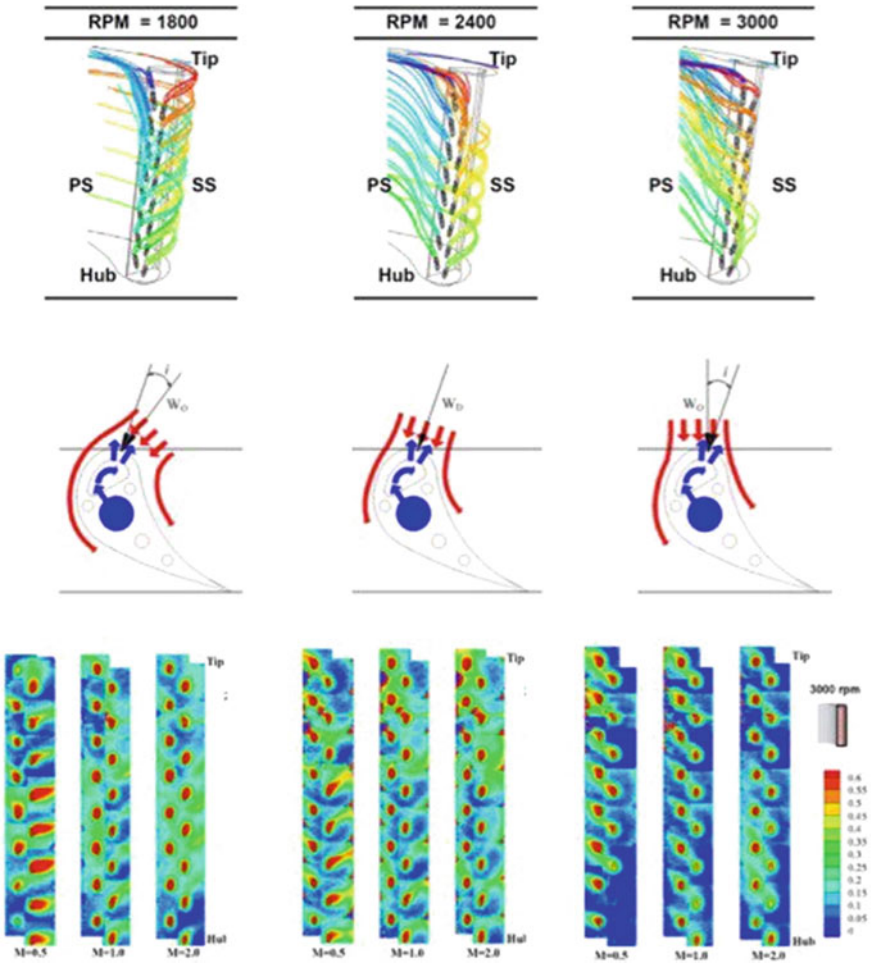

Fig. 20 The results of the study of the influence of rotation on the effectiveness of film cooling

will enable to determine the influence of gradients of velocity and pressure on the efficiency of film cooling.

The results of experiments [50] showed that due to the presence of a longitudinal pressure gradient at a constant pressure cooling injection parameter between the backrest and the trough is changed. Its least value is observed at the trough, and the highest on the back. At low settings, the injection of film cooling is only on the convex surface. With the increase of the injection parameter, the cooling flow gets on the concave surface, but the uneven distribution of the chiller is maintained.

In [51] investigated the influence of degree of curvature on film cooling effectiveness in the range of the injection parameter from 0.3 to 2.7. The resulting efficiency of film cooling on a convex surface, at low settings, the injection is higher than for

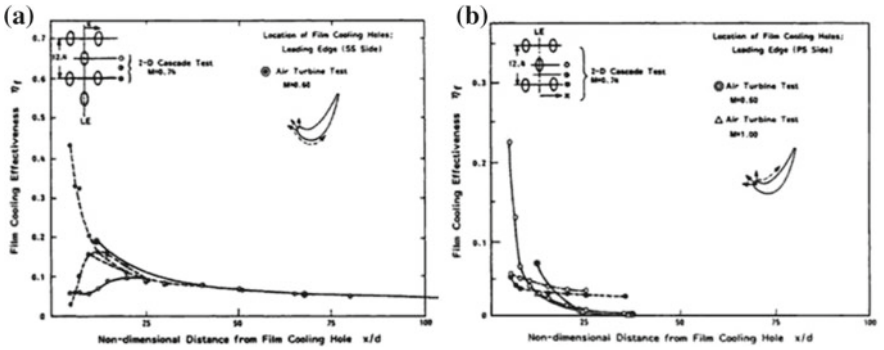

Fig. 21 Distribution of the effectiveness of film cooling in areas of the backrest (**a**) and trough (**b**)

flat and concave. For high injection parameters, the reverse was true: on the convex and flat surfaces the increase of the injection parameter to a certain value improves the efficiency of the film of the veil.

A number of other studies [52–54] also showed a significant effect of surface curvature on the effectiveness of film cooling.

Figure 21 presents the results of a study of the effectiveness of film cooling in areas of the back and trough, presented in [55].

Film cooling of the inlet edge implemented three rows of holes inclined at an angle of 45° to the direction of the main flow. Obtained that even at a slight distance from the input edge values of the efficiency of film cooling on the back and the trough are different. Thus, if the phase backs, even at $x/d > 50$ the magnitude of the effectiveness of film cooling is maintained at the level of 0.06–0.09, for nothing is at $x/d > 10$, its value is greater than 0.05.

Based on the review done on the present research it can be noted that, despite the large number of works devoted to film cooling, the question of film cooling input edges, which is the most thermally loaded element profile has not been studied. The main disadvantages that are made in this area of research are the following:

- Most of the works devoted to the study of film cooling effectiveness only on the site in the immediate vicinity of the holes ($x/d < 10$), which does not allow to determine the effectiveness of film cooling for the rest of the profile;
- The works are not given recommendations for the application configuration and the location of the holes film cooling on the front edge;
- Existing methods of increasing the efficiency of film cooling was tested, mainly for application on flat walls and their effectiveness on the portion of the input edges is studied insufficiently;
- The flow parameters in the performed studies often do not correspond to the actual operating conditions of gas turbine blades.

2.4 Purpose and Objectives of the Study

The above review has shown the relevance and great practical importance of further study of the film cooling of the inlet edges of gas turbine blades. Taking into account the fact that previously found the optimal values of the geometric parameters of the film cooling holes, which in turn are imposed technological constraints, further research can be carried out at constant geometric parameters of the holes at the inlet edge at the same parameters of the main flow. The main directions of this study are: the study of different configurations of the location of the holes on the inlet edge, the use of fan holes of film cooling and recesses at the outlet of the holes for film cooling of the inlet edge, as well as determining the effect of the curvature of the wall corresponding to the actual profile of the blade and the inter-blade channel.

On the basis of this, the aim of the work is to improve the film cooling systems of the inlet edges of gas turbine blades when the cooler is fed through a three-row system of radial and parallel cylindrical holes, fan holes, holes in hemispherical depressions and trenches, to determine the physical structure of the flow and dependencies characterizing the efficiency of film cooling.

Taking into account the need to study a large number of geometric configurations of holes, determine the local values of the cooling efficiency to perform this study the method of mathematical modeling—a numerical method of research based on the use of computational fluid dynamics. When choosing this research method, the following was taken into account:

- The numerical method for studying hydrodynamics and heat transfer is currently the most promising [56]. Its advantages include the absence of the need to simplify the geometry and the specified physical conditions, the possibility of a detailed analysis of the results of the study, low cost of material and time costs with the possibility of studying a large number of options considered;
- Analyzing the methodology of modern research, it can be seen that almost all the experimental work of the previous five years, for example [57], accompanied by CFD-computational Fluid Dynamic (CFD—Computational Fluid Dynamic), which after verification with experimental data allow to obtain an additional amount of research results. According to the use of CFD calculations of blade cooling system elements is now a prerequisite for ensuring the accuracy and reliability of determining the temperature state at the design stage of the turbine engine.

To achieve this goal, the following research tasks were set and solved:

- For the model of the inlet edge of a real blade with profiled (curved) surfaces behind it, determine the influence of factors taking place in the real inter-blade channel on the distribution of the film cooling efficiency when blowing the cooler at the inlet edge through a system of radial cylindrical holes.

To obtain general conclusions on the effectiveness of the studied film cooling systems, the simulation is performed for four values of the blowing parameter $m =$ 0.5; 1.0; 1.5, and 2.0, which are in the range important for practical application.

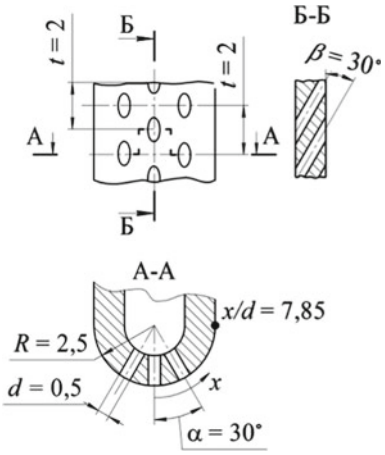

Fig. 22 The configuration of the holes

Geometric dimensions (Fig. 22) and the main gas-dynamic parameters for the study should be typical for the working blade of the high-pressure turbine GTE of average power (25–35 MW). The diameter of the holes $d = 0.5$ mm, the relative pitch of the holes in the transverse direction $t/d = 4$; the angle of inclination of the holes to the cooling surface $\alpha = 30°$; the ratio of the diameter of the holes to the diameter of the inlet edge $d/2R = 0.1$.

3 Conclusion

1. So far, the film cooling is indispensable to the nozzle and rotor blade of the first stage of high-pressure turbine although the convective cooling technology has made great progress.
2. Aimed to improve the efficiency of film cooling efficiency compared to the cylindrical holes, a series of film cooling configuration has been developed based on the flat surface. Few of the configurations can be readily available to the turbine blade.
3. Based on the review done on the present research it can be noted that the leading edge is the most easily ablated region, and the use of different methods to improve the efficiency of film cooling is considered very limited. Most research work is focused on the influence of film cooling holes shape on the cooling performance, and less consideration was given to the influence of the main stream flow characteristics in cascade. Thus, despite large number of works has been devoted to film cooling, the film cooling boundary conditions has not been studied thoroughly. The model of study is inconsistent with the actual situation. It is mainly caused by the following two reasons. Fist, most research scope ($x/d < 10$) cannot cover

engine working conditions. Second, the recommendations for film cooling effectiveness improvement are performed only for flat plate. To improve the research validity, the factors mentioned above should be paying more attention.

References

1. Ольховский, Г. Г. (2004). Газовые турбины для энергетики. Теплоэнергетика. 1, 33–43.
2. Ольховский, Г. Г. (2004). Энергетические ГТУ за рубежом. Теплоэнергетика.
3. Takeishi, K., Mori, H., Tsukagoshi, K., & Takahama, M. (1996). Development and shop test of a new 25–35 MW class gas turbine MF-221. In *ASME Paper No. 96-GT-425*, p. 8.
4. Ковецкий, В. М., & Ковецкая, Ю. Ю. (2008). Газотурбинные двигатели в энергетике: достижения, особенности, возможности. Проблемы общей энергетики. Т. 17, 24–30.
5. Халатов, А. А., Романов, В. В., Дашевский, Ю. Я., & Письменный, Д. Н. (2010). Тенденции развития систем охлаждения лопаток высокотемпературных энергетических ГТД. Часть 1. Современное состояние. Промышленная теплотехника. Т. 32, No. 1, 53–61.
6. Халатов, А. А., Романов, В. В., Борисов, И. И., Дашевский, Ю. Я., & Северин, С. Д. (2010). Теплообмен и гидродинамика в полях центробежных массовых сил. К.: Изд. Ин-та технической теплофизики НАН Украины. Т. 9: Тепломассообмен и гидродинамика при циклонном охлаждении лопаток газовых турбин, 317 с. ISBN: 978- 966-02-5694-1.
7. Boyce, M. (2002). *Gas turbine engineering handbook* (p. 815). Houston: Gulf Publishing. ISBN: 0-88415-732-6.
8. Aoki, S., Tsukuda, Y., Akita, E., Tomat, R., & Schips, C. (1994). Development of the next generation 1500 °C class advanced gas turbine for 50 Hz utilities. In *ASME Paper No. 96-GT-314*, p. 8.
9. укин, В. К., & Халатов, А. А. (1982). Теплообмен, массообмен и гидродинамика закрученных потоков в осесимметричных каналах. М.: Машиностроение, с. 200.
10. Халатов, А. А., Авраменко, А. А., & Шевчук, И. В. (2000). Теплообмен и гидродинамика в полях центробежных массовых сил в 9 т. К.: Изд. Ин-та технической теплофизики НАН Украины, Т. 3: Закрученные потоки. 474 с.
11. Локай, В.И., Бодунов, М. Н., уйков, В. В., & укин, А. В. (1985). Теплопередача в охлаждаемых деталях газотурбинных двигателей летательных аппаратов. М.: Машиностроение, 216 с.
12. Goldstein, R. J., Eckert, E. R. G., & Burggraf, F. (1974). Effects of hole geometry and density on threedimensional film cooling. *International Journal of Heat and Mass Transfer, 17*(5), 595–607.
13. Bogard, D. (2006). Airfoil film cooling. In *The gas turbine handbook* (pp. 309–321), Sect. 4.2.2.1. London, NY: National Energy Technology Laboratory.
14. Репухов, В. М. (1980). Теория тепловой защиты стенки вдувом газа [Текст] Киев: Наукова Думка, 296 с.
15. Кутателадзе, С. С., & Леонтьев А. И. (1972). Тепломассобмен и трение в турбулентном пограничном слое [Текст]. М.:Энергия. 132, 344 с.
16. Халатов, А. А., Авраменко, А. А., & Шевчук, И. В. (1992). Теплообмен и гидродинамика около криволинейных поверхностей [Текст]. Киев: Наукова Думка, 138 с.
17. Волчков, Э. П. (1983). Пристенные газовые завесы [Текст]/ Э.П. Волчков. – Новосибирск: Издательство « Наука » Сибирское отделение, 240с.

18. Baldauf, S., & Scheurlen, M. (2002). Correlation of film cooling effectiveness from thermographic measurements at engine like conditions. In *ASME Paper No. GT2002-30180*, p. 14.
19. Швец, И. Т., Дыбан, Е. П., Репухов, В. М., Богачук-Козачук, К. А., & Попович, Е. Г. (1972). Эффективность тепловой защиты адиабатной стенки за участком перфорации [Текст]. В кн.: Тепло- и массоперенос. Т. 1. – Минск, 1972, С. 79–82.
20. Lutum, E. Influence of the hole length-to diameter ratio on film cooling with cylindrical holes. In *ASME Paper 98-GT-10*.
21. Sgarzi, O. Analysis of vortices in three-dimensional jets introduced in a cross-flow boundary-layer. In *ASME Paper 97-GT-517*.
22. Brauckmann, D., & Wolfersdorf, J. (2005). Application of steady and transient IR-thermography measurements to film cooling experiments for a row of shaped holes. In *ASME Paper GT2005-68035*, p. 11.
23. Brauckmann, D., & Wolfersdorf, J. (2005). Influence of compound angle on adiabatic film cooling effectiveness and heat transfer coefficient for a row of shaped film cooling holes. In *ASME Paper GT2005-68036*, p. 9.
24. Lee, K., Kim, S., & Kim, K. (2012). Numerical analysis of film-cooling performance and optimization for a novel shaped film-cooling hole. In *ASME Paper No. GT2012-68529*, p. 11.
25. Saumweber, C., Schulz, A., & Wittig, S. (2003). Free-stream turbulence effects on film cooling with shaped holes. *Journal of Turbomachinery, 125*(1), 65–73.
26. Lee, K., & Kim, K. Y. (2010). Shape optimisation of laidbak fan-shaped film-cooling hole to enhance cooling performance. In *ASME Turbo 133 Expo–2010*, GT2010-22398, p. 12.
27. Dittmar, J., Schulz, A., & Wittig, S. (2003). Assessment of various film cooling configurations including shaped and compound angle based on large scale experiments. *Journal of Turbomachinery, 125*(1), 57–64.
28. Dorrington, J., Bogard, D., & Bunker, R. (2007). Film effectiveness performance for coolant holes embedded in various shallow trench and crater depressions. In *ASME Paper GT2007-27992*, p. 10.
29. Халатов, А. А., Борисов, И. И., Коваленко А. С., Дашевский, Ю. Я., Северин, С. Д., Шевцов, С. В., & Безлюдна, М. В. (2012). Пленочное охлаждение плоской поверхности двухрядной системой отверстий в сферических углублениях. Современные технологии в газотурбрстроении. 5 с.
30. Халатов, А. А., Борисов, И. И., & Шевцов С. В. (2005). Теплообмен и гидродинамика в полях центробежных массовых сил: Т. 5. Тепломассообмен и теплогидравлическая эффективность 134 вихревых и закрученных потоков. К.: Ин-т техн. теплофизики НАН Украины, 500 с.
31. Халатов, А. А., Борисов, И. И., Коваленко, А. С., Дашевский, Ю. Я., & Шевцов, С. В. (2012). Эффективность пленочного охлаждения плоской поверхности системой наклонных отверстий, расположенных в сферических углублениях [Текст]. Промышленная теплотехника. Т. 34, No. 3, С. 5–12.
32. Безлюдная, М. В. (2015). Эффективность пленочного охлаждения при подаче охладителя в двухрядную систему поверхностных углублений полусферической формы [Текст]: дисс. канд. техн. наук: 05.14.06: защищена 30.06.15/ Безлюдная Мария Владимировна; науч. рук. А.А. Халатов; ИТТФ НАНУ. Киев, 2015. 140 с.
33. Bunker, R. S. (2002). Film cooling effectiveness due to discrete holes within a transverse surface slot. In *ASME Paper GT2002-30178*.
34. Wang, T., Chintalapati, S., Bunker, R. S., & Lee, C. P. (2000). Jet mixing in a slot. *Experimental Thermal and Fluid Science, 22,* 1–17.
35. Bunker, S. R. (2002). Film cooling effectiveness due to discrete holes within a transverse surface slot. In *Proceedings of ASME Turbo Expo–2002*, p. 10 (1 CD-ROM, Title from the screen).
36. Пахомов, М. А., Терехов, В. И., Халатов, А. А., & Борисов, И. И. (2015). Тепловая эффективность пристенной газовой завесы при ее вдуве через круглые отверстия в траншее// Теплофизика и аэромеханика. Том 22, No 3. с. 343–352.

37. Chernobrovkin, A., & Lakshminarayana, B. (1998). Numerical simulation and aerothermal physics of leading edge film cooling. In *ASME 135 Paper No. 98-GT-504*, p. 11 [CD].
38. Li, S., Yang, S., & Han, J. (2013). Effect of coolant density on leading edge showerhead film cooling using PSP measurement technique. In *ASME Paper No. GT2013-94189*, p. 11 [CD].
39. York, W., & Leylek, J. (2002). Leading-edge film-cooling physics: Part I—Adiabatic effectiveness, In *ASME Paper No. GT2002-30166*, p. 10 [CD].
40. Liu, C., Zhu, H., & Zhang, Z. (2012). Experimental investigation on the leading edge film cooling of cylindrical and laid-back holes with different hole pitches. In *ASME Paper No. GT2012-68027*, p. 12 [CD].
41. Sakai, E., Takahashi, T., Funazaki, K., Salleh, H., & Watanabe, K. (2009). Numerical study on flat plate and leading edge film cooling. In *ASME Paper No. GT2009-59517*, p. 13 [CD].
42. Мик, В. Дж., & Мейл, Р. Е. (1989). Завесное охлаждение и теплообмен на лобовой части затупленного тела (включая участок расположения отверстий вдува) [Текст]. Современное машиностроение, серия А. No. 1. С. 71–80.
43. York, W. D., & Leylek, J. H. (2002). Leading-edge film-cooling physics: Part 1—Adiabatic effectiveness. In *ASME Paper GT-2002-30166*, p. 10.
44. York, W. D., & Leylek, J. H. (2002). Leading-edge film-cooling physics: Part 2—Heat transfer coefficient. In *ASME Paper GT-2002-30167*, p. 10.
45. Lu, Y., Allison, D., & Ekkadl, S. V. Influence of hole angle on leading edge showerhead film cooling. In *ASME Paper GT2006-90370*, p. 8.
46. United States Patent US08087893. *Turbine Blade with showerhead film cooling holes*. George Liang; Florida Turbine Technologies, Inc., Jupiter.
47. United States Patent US 8317473B1. *Turbine blade with leading edge cooling*. George Liang; Florida Turbine Technologies, Inc., Jupiter, date of Patent: January 3, 2012.
48. Funazaki, K., Kawabata, H., & Takahashi, D. (2012). Experimental and numerical studies on leading edge film 136 cooling performance: Effects of hole exit shape and freestream turbulence. In *ASME Paper GT2012-68217*, p 11.
49. Yang, H., Chen, H. C., Han, J. C., & Moon, H. K. (2005). Numerical prediction of film cooling and heat transfer on the leading edge of a rotating blade with two rows holes in a turbine stage at design and off design conditions. In *ASME Paper GT-2005-68335*, p. 10.
50. Халатов, А. А., & Коваленко, А. С. (2006). Теплообмен и гидродинамика в полях центробежных сил: Т. 5. Теплообмен и гидродинамика ускоренного потока в плоских криволинейных каналах. К.: Наукова думка, 224 с.
51. Шварц, С., Голдстейн, Р., & Эккерт, Е. (1991). Влияние кривизны на характеристики завесного охлаждения. Современное машиностроение. Сер. А No. 10. С. 116–123.
52. Локай, В. И., укин, А. В., & Хайрутдинов, Р. М. (1978). Экспериментальное исследование пленочного охлаждения криволинейных поверхностей [Текст]. Изв. вузов. сер. Авиационная техника. No. 3. С. 150–153.
53. Репухов, В. М., & Богачук-Козачук, К. А. (1975). Влияние закрутки основного потока на эффективность пленочного охлаждения при осесимметричном обтекании цилиндра [Текст]. В кн.: Теплофизика и теплотехника. Вып. 29. – Киев С. 43–46.
54. Мэйл, Р. Э., Коппер, Ф. К., & Блэр и др, М. Ф. (1977). Влияние кривизны линий тока на завесное охлаждение [Текст]. Энергетические машины и установки. Т. 99, No. 1. С. 87–93.
55. Takeishi, K., Aoki, S., Sato, T., & Tsukagoshi, K. (1992). Film cooling on a gas turbine rotor blade. *ASME Journal of Turbomachinery, 114,* 828–834.
56. Андерсон, Д., Таннехилл, Д., & Плетчер, Р. (1990). Вычислительная гидромеханика и теплообмен: в 2 т.; [пер. с англ.]. М.: Мир. Т. 1. 384 с. 136.
57. Li, X., Ren, J., & Jiang, H. (2014). Film cooling modeling of turbine blades using algebraic Anisotropic turbulence models. In *ASME Paper GT2014-25191*, p. 12.

Damage Tolerance Analysis for Repaired Composite Stringer Panels

Lin Ma and Yin Yu

Abstract In this paper, the damage tolerance of repaired composite panels with an M style stringer was analysed through a finite element model. Firstly, an interface unit is introduced to make connection relationship between the panel and stringer. The strength and damage tolerance are analysed by using nonlinear finite element method (FEM). Then the panel laminates with internal presupposition damage are analysed. The damage tolerance is determined under four-point bending load by simulation. Then the failure laminated panel was repaired by patching method. Finally, the structure strength and damage tolerance of the repaired panel with stringer was analysed. The research results can provide some theoretical support for the repair of aircraft composite materials in the future.

Keywords Aircraft composites · Damage tolerance · Repair

1 Introduction

With the increasing proportion of composite materials in aircraft structure design, the analysis on damage tolerance of aircraft composite structures has attracted more and more attention from scholars at home and abroad. Recently, Carbon fibre-reinforced laminated composite structure has an extensive utilization in aerospace due to its relative higher specific strength, higher specific stiffness and excellent designability. As a typical aircraft structure, the laminated composite panel with M style stringer has lower interlaminar strength and poor impact toughness, which is totally different with the isotropic materials. Moreover, during its manufacturing and service life, the laminated composite panels are liable to have damage such as interface debonding,

L. Ma · Y. Yu (✉)
School of Aeronautics & Astronautics, Shanghai Jiao Tong University, Shanghai, China
e-mail: yuyin@sjtu.edu.cn

L. Ma
e-mail: linm0109@sjtu.edu.cn

Z. Jing (ed.), *Proceedings of International Conference on Aerospace System Science and Engineering 2018*, Lecture Notes in Electrical Engineering 549,
https://doi.org/10.1007/978-981-13-6061-9_6

interlayer delamination etc. The consideration of initial damage in the form of cracks or equivalent damage is absolutely necessary to ensure structural safety [1].

Researches have shown that the panels with stiffener are liable to have debonding damage between panel and stringer when exposed to flexure loads, which is mainly caused by the out-plane bending load that transferred from panels under bending loads [2]. The residual strength of the stiffened composite laminated panels will have a catastrophic decrease once the debonding damage occurred during its service life. Consequently, the debonding damage should be taken into serious consideration for the designers when conduct strength analysis on the composite laminated panels with stringers. Recently, the debonding damage theoretical analysis of the stiffened panels almost mainly based on the numerical simulation (ABAQUS CAE) [2–7]. Meanwhile, both the domestic and foreign researchers mainly have the following three analysis methods for debonding and delamination of the stiffened panels: virtual crack closure technique (VCCT), energy method and interface element method. In addition, the interface element method which is based on the cohesive zone theory [8], is a relative comprehensive methodology that combines the strength criterion and fracture mechanics and could conduct a more accurate simulation on the initiation and revolution of the cracks occurred in the interface, which is a more reasonable simulation to actual debonding and delamination situation.

Aircraft structures require regular inspections to ensure its safety, efficiency and integrity [9]. Obviously, if the damage is not really extensive, partial structural repair could be the feasible solution comparing with replacing the entire component which is not cost-effective in many cases [10, 11]. While what should be taken into serious consideration is that structural bonding repairs, especially with primary structures, pose several scientific challenges with the current existing repair technologies [10].

In this paper, a finite element model for the laminated composite panel with a M-stringer under four-point bending load was established based on the element software—ABAQUS. An interface element was introduced to simulate the joint face between the stringer and the skin. The failure criterion of the bond interface and the composite laminate are Quads [12] failure criterion and Hashin [13] failure criterion, respectively. The nonlinear finite element analysis method was introduced. The influence of the debonding area and its location on the strength of the composite stringer panel was analysed. Finally, the composite stringer panel with debonding was repaired with a sticking patch, the strength of the composite panel after repair was studied, and the influence of the repair parameters such as thickness of the patch and length of the overlap joint were also analysed.

2 Damage Model

The damage in composite laminated panels with stringer is relatively complicated comparing to traditional metal structure due to the different layup angles, various layers and anisotropic mechanical properties. The damage models in composite laminated structure include debonding, delamination, fibre brittle and matrix crack. In

this paper, the failure initiation of the composite laminate and debonding between skin panel and stringer with a pre-existed damage was analysed by using the finite element method.

2.1 Interface Damage Model

The mechanical behaviour of the adhesive interface between stringer and skin panel was simulated by the Cohesive model existing in the ABAQUS.

Cohesive element can be treated as two surfaces consisting of 2-dimension elements that are separated by a unit thickness. The two surfaces are connected with the adjacent layers by solid elements. The constitutive equation of the cohesive element was adopted the typical cohesive bi-linearity constitutive model, as shown in Fig. 1, which could have a good convergence and decrease the calculation cost.

This bi-linearity constitutive model is based on the assumption that the materials properties are all linear softening. And one of the prominent characters for the softening model is that the cohesive zone can still carry loads when the damage has already initiated for a while. Figure 1 shows the typical relation for the traction, t, to the relative displacement, δ, on the interface. When $\left[\delta < \delta^0\right]$, there is no damage in the material; when $\delta = \delta^0$, the damage in the cohesive interface began to propagate, the traction, t, reaches its critical value, t^{c}, at the same time; when the relative separation displacement reaches the maximum value, δ^{m}, damage propagate through all the material; when $\delta > \delta^{\mathrm{m}}$, the material will lose its loading-carry ability, which means that the interface has been destroyed completely.

As for the cohesive model, its damage process has two stages: damage initiation and damage evolution [12]. Damage initiation refers to the beginning of degradation of the response of a material point. The damage begins when the stresses and/or strains satisfy certain damage initiation criteria, and there are four typical damage initiation criteria in ABAQUS, maximum nominal stress criterion, maximum nominal strain criterion, quadratic nominal stress criterion and quadratic nominal strain criterion. In

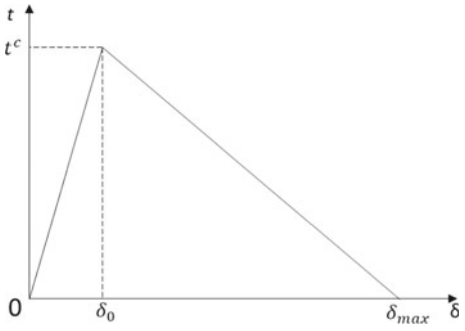

Fig. 1 Typical cohesive bi-linearity constitutive model

this paper, the quadratic nominal stress criterion was selected to predict the damage initiation under mixed-mode loading:

$$\left[\left\{\frac{\langle t_{\mathrm{n}}\rangle}{t_{\mathrm{n}}^{0}}\right\}^{2}+\left\{\frac{t_{\mathrm{s}}}{t_{\mathrm{s}}^{0}}\right\}^{2}+\left\{\frac{t_{\mathrm{t}}}{t_{\mathrm{t}}^{0}}\right\}^{2}=1\right]$$

where t_{n}^{0}, t_{s}^{0} and t_{t}^{0} are the peak values of the nominal stress when the deformation is either purely normal to the interface or purely in the first or the second shear direction, respectively. With the initial constitutive thickness is 1, the nominal strain components are equal to the respective components of the relative displacement—δ_{n}, δ_{s}, and—δ_{t} between the top and bottom of the cohesive layer. And the symbol $\langle\ \rangle$ is Macaulay bracket operator, which means,

$$\langle t_{\mathrm{n}}\rangle=\begin{cases} t_{\mathrm{n}},\ t_{\mathrm{n}}>0 \\ 0,\ t_{\mathrm{n}}\leqslant 0 \end{cases}$$

Then comes to the damage evolution, the damage evolution law can be specified based on effective displacement and energy. For the effective displacement method, there are linear damage evolution, Exponential damage evolution and Tabular damage evolution. While for the energy method, the fracture energy should be specified as a material property, and the damaged response in ABAQUS can be linear or exponential. The widely used evolution laws based on energy include power law form and Benzeggagh-Kenane (BK) form [14, 15]. In this paper, the BK form was selected to define the damage evolution of the cohesive interface:

$$G^{\mathrm{C}}=G_{\mathrm{n}}^{\mathrm{C}}+\left(G_{s}^{\mathrm{C}}-G_{\mathrm{n}}^{\mathrm{C}}\right)\left\{\frac{G_{\mathrm{S}}}{G_{\mathrm{T}}}\right\}^{\eta}$$

$$G_{\mathrm{S}}=G_{\mathrm{s}}+G_{\mathrm{t}}$$

$$G_{\mathrm{T}}=G_{\mathrm{S}}+G_{\mathrm{n}}$$

where G^{C} refers to the mixed-mode fracture energy; η is a parameter that is related with material; $G_{\mathrm{n}}^{\mathrm{C}}$, $G_{\mathrm{s}}^{\mathrm{C}}$ and $G_{\mathrm{t}}^{\mathrm{C}}$ refer to the critical fracture energies required to cause failure in the normal, the first and the second directions, respectively. In addition, the values of the critical energies can be obtained from the corresponding areas of the triangle consisting of the curve and the x-axis in the typical cohesive bi-linearity constitutive model. The cohesive interface material properties are specified according to Ref. [3] and [16] as listed in Table 1.

Table 1 Cohesive material properties

K_{n}	K_{s}	K_{t}	t_{n}^{0}	t_{s}^{0}	t_{t}^{0}	$G_{\mathrm{n}}^{\mathrm{C}}$	$G_{\mathrm{s}}^{\mathrm{C}}$	$G_{\mathrm{t}}^{\mathrm{C}}$
968,750	358,824	358,824	15.5	24.4	24.4	0.019	0.214	0.214

2.2 Composite Laminate Damage Model

The fibre-reinforced composite materials are elastic-brittle materials with anisotropic behaviour, which means the undamaged response of the material is linearly elastic. The damage modes in fibre-reinforced composite laminate materials include fibre tension/compression, matrix tension/compression and delamination. The most widely used failure criterion for fibre-reinforced composites is the Hashin damage initiation criterion [11, 14, 15, 17, 18], which can be described as:

Fibre tensile damage value ($\hat{\sigma}_{11} \geq 0$):

$$F_{\mathrm{f}}^{\mathrm{t}} = \left(\frac{\hat{\sigma}_{11}}{X^{\mathrm{T}}}\right)^2 + \alpha\left(\frac{\hat{\tau}_{12}}{S^{\mathrm{L}}}\right)^2$$

Fibre compression damage value ($\hat{\sigma}_{11} < 0$):

$$F_{\mathrm{f}}^{\mathrm{c}} = \left(\frac{\hat{\sigma}_{11}}{X^{\mathrm{C}}}\right)^2$$

Matrix tension damage value ($\hat{\sigma}_{22} \geq 0$):

$$F_{\mathrm{m}}^{\mathrm{t}} = \left(\frac{\hat{\sigma}_{11}}{Y^{\mathrm{T}}}\right)^2 + \alpha\left(\frac{\hat{\tau}_{12}}{S^{\mathrm{L}}}\right)^2$$

Matrix compression damage value $\left[(\hat{\sigma}_{22} < 0)\right]$:

$$F_{\mathrm{m}}^{\mathrm{c}} = \left(\frac{\hat{\sigma}_{22}}{2S^{\mathrm{T}}}\right)^2 + \left[\left(\frac{Y^{\mathrm{C}}}{2S^{\mathrm{T}}}\right)^2 - 1\right]\frac{\hat{\sigma}_{22}}{Y^{\mathrm{C}}} + \left(\frac{\hat{\tau}_{12}}{S^{\mathrm{L}}}\right)^2$$

where

X^{T} longitudinal compressive strength;
X^{C} transverse tensile strength;
Y^{T} transverse tensile strength;
Y^{C} transverse compressive strength;
S^{L} longitudinal shear strength;
S^{T} transverse shear strength;
α a coefficient that determines the contribution of the shear stress to the fibre tensile initiation criterion.

When the damage value above is larger than 1.0, then the damage will begin at the corresponding layer and direction. If there is a damage evolution model corresponding to the damage initiation model, the maximum value of this variable does not exceed 1.0. However, if there is no damage evolution model after the damage initiation, this variable will have values higher than 1.0, which indicates by how much the criterion has been exceeded.

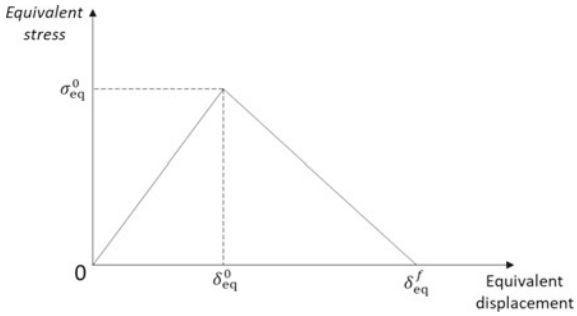

Fig. 2 Bilinear damage evolution model for composites

Table 2 Material properties of the lamina

Material	Modulus/MPa	Strength/MPa	Fracture toughness/(N/mm)
Lamina	$E_1 = 158{,}000$ $E_2 = 9650$ $G_{12} = G_{13} = 4600$ $G_{23} = 3683$ $v_{12} = 0.31$	$X^{\mathrm{T}} = 2000$ $X^{\mathrm{C}} = 1000$ $Y^{\mathrm{T}} = 80$ $Y^{\mathrm{C}} = 200$ $S^{\mathrm{L}} = 85$ $S^{\mathrm{T}} = 35$ $\alpha = 0$	$G_{1\mathrm{C}}^{\mathrm{T}} = 90$ $G_{1\mathrm{C}}^{\mathrm{T}} = 80$ $G_{2\mathrm{C}}^{\mathrm{T}} = 0.22$ $G_{2\mathrm{C}}^{\mathrm{C}} = 1.0$

Note The specific values of the strengths ang fracture toughness are all based on the Ref. [16], which means that they are not the exact experimental results for the sake of time. While the final results are reasonable and can be used to explain the approximate tendency

After the beginning of damage, the evolution rule of damage variable is usually controlled by fracture energy release rate [19, 20]. In this paper, the energy damage evolution was defined according to Refs. [19, 21–23]. And the softening stress-strain response method is linear (Fig. 2), which is the default method in ABAQUS. The material properties for the composite lamina used in the skin panel with a M-stringer are listed in Table 2.

3 Skin-Stringer Analytical Model

3.1 Geometry Dimension

The geometric dimension and the loading type of the skin-stringer model is shown in Fig. 3, the dimension of the skin panel is 320 mm × 190 mm × 6.358 mm, layup: [45/−45/0/45/−45/90/0/45/90/−45/45/0/−45/45/90/−45/0]s. As for the stringer, layup: [45/0/0/−45/0/0/90]s. The skin-stringer will be under four-point bending load, as shown in Fig. 3a. And the double patched repair structure without damage in the

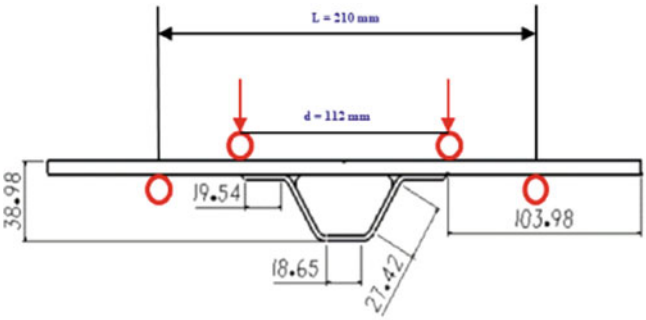

(a) loading mode

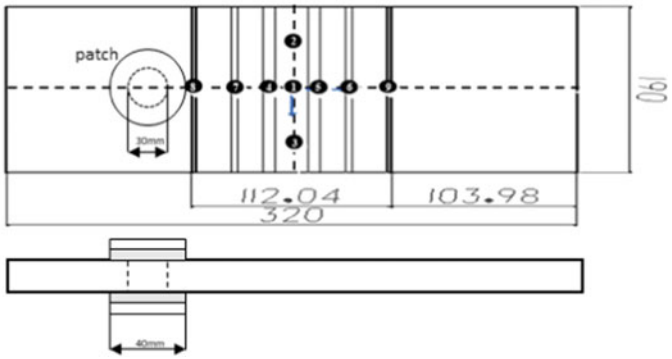

(b) schematic diagram of gluing and repairing laminated plates

Fig. 3 Geometry dimension of the stringer panel

patch is shown in Fig. 3b. The boundary conditions are: loading edges have degree of freedom (DOF) along the loading direction, and the supporting edges have all the DOFs except the loading direction.

3.2 Finite Element Model

The finite element model was established in ABAQUS, as shown in Fig. 4, there is a cohesive element between the skin panel and stringer, and the patch and skin near the damage area. The damage was introduced in the M-stringer which is shown in detail in Fig. 4. The composite laminate element is a 4-node doubly curved thin or thick shell, reduced integration, hourglass control, finite membrane strains, S4R. While the interface element is COH3D8, an 8-node three-dimensional cohesive element. The ultimate load is calculated and shown in Table 3 and Fig. 7.

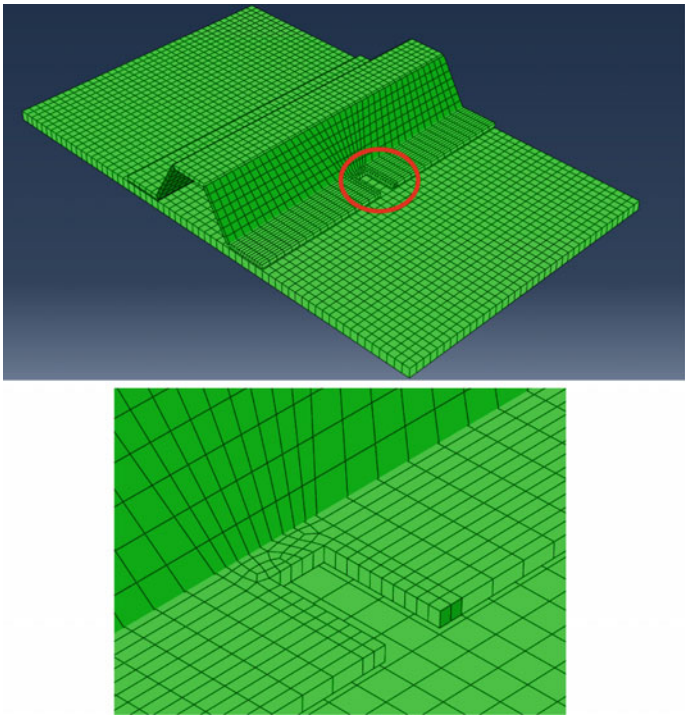

Fig. 4 Finite element model for the M-stringer skin with a damage and no-patch in the stringer

Table 3 Ultimate loads of the different finite element mode

Mode	Ultimate load/kN
No-damage	52.2
No-patch	41.8
Patch	49.6
Patch-debond	44.7

Then the damage in the stringer was repaired by using a single patch method, the lap length between the patch and damage is half of the damage width, as shown in Fig. 5. The composite layup angles and layers of the patch is the same with the stringer. And the patch was related to the stringer by an 8-node three-dimensional cohesive element. The ultimate load under four-point bending load was recorded.

In order to character the damage tolerance in the patch, a debond in the interelement between patch and stringer was introduced, as shown in Fig. 6. Then the ultimate load under four-point bending load was also recorded of the patched structure with a debond.

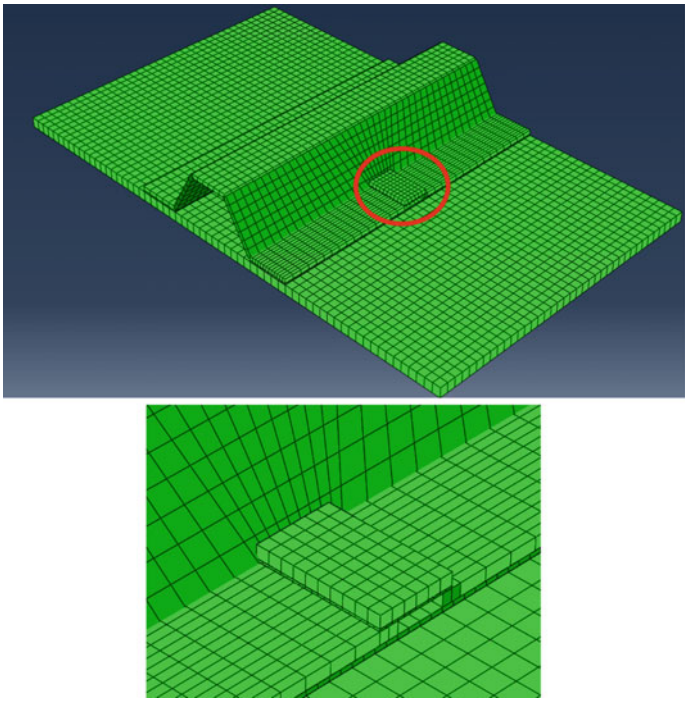

Fig. 5 Finite element model for the M-stringer skin with a damage and patch in the stringer

4 Conclusion

The ultimate loads of double patched repair skin panels with a M-stringer under four-point bending load were investigated theoretically using finite element model. The final results of the structure with different size of damage in the repair area were analysed, as shown in Fig. 7, the ultimate load with a patch without damage in the patch will recover to the 95% of strength that with no damage, and the damage in the patch will reduce the ultimate load to 44.7 kN. The results show that the damage in the patch after repair has significant effect on the whole structure, so the damage tolerance after repair should be taken into serious consideration, and the relationship between damage size and ultimate load should be with further research.

From a long-term perspective, the damage tolerance of repaired stringer skin panel can be affected by extensive factors such as the repair method: digging or patching; the patch lap length; the geometry dimension of the initial damage in the laminate; the defects in the patch et al. The damage tolerance for the repaired composite structure should be with extensive researches both in mechanism and the mechanical properties.

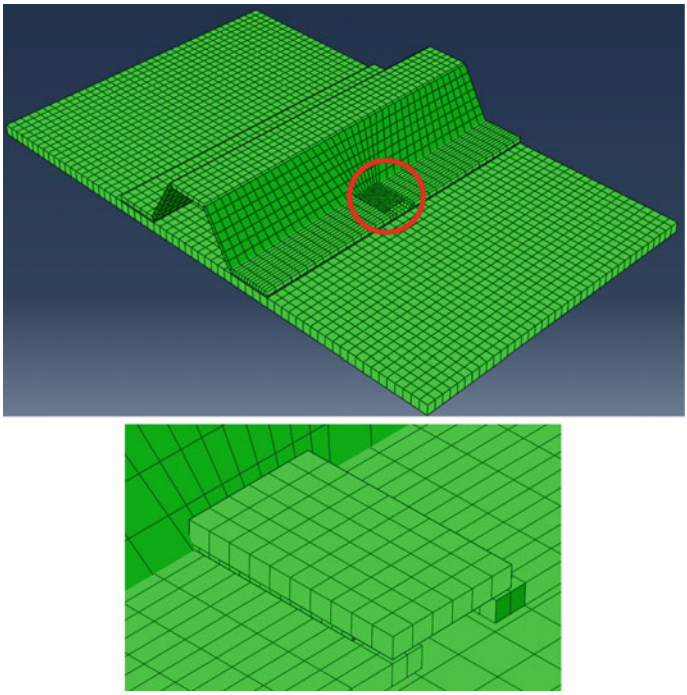

Fig. 6 Finite element model for the M-stringer skin with a damage and patch with debond in the stringer

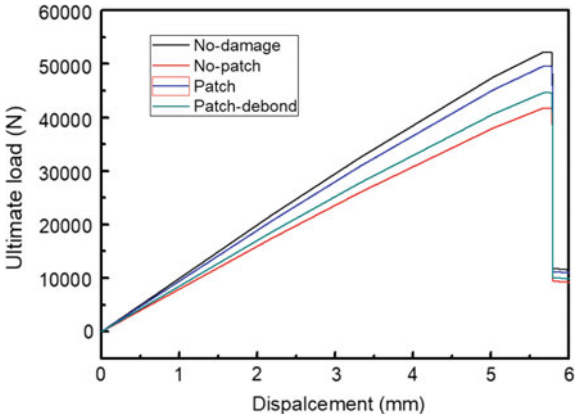

Fig. 7 The ultimate load with displacement curves for the no-damage, no-patch, patch and patch-debond mode of the M-stringer skin panels

References

1. Miedlar, P. C., Berens, A. P., Gunderson, A., & Gallagher, J. P. (2002). *USAF damage tolerant design handbook: Guidelines for the analysis and design of damage tolerant aircraft structures*.
2. Bertolini, J., Castanie, B., Barrau, J. J., et al. (2008). An experimental and numerical study on omega stringer debonding. *Composite Structure, 86*(1), 233–242.
3. Davilla, C., & Camanho, P. (2008). Analysis of the effects of residual strains and defects on skin/stiffener debonding using decohesion elements. In *AIAA*.
4. Krueger, R., Cvitkovich, M. K., O'Brien, T. K., et al. (2000). Testing and analysis of composite skin/stringer debonding under multi-axial loading. *Journal of Composite Materials, 34*(15), 1263–1300.
5. Kusugal, S., Kadadevarmath, R. S., & Mallapur, D. G. (2017). Stress and damage tolerance analysis of stiffened panel with passenger door cutout in airframe structure using FEA. *Materials Today: Proceedings, 4*(10), 10696–10703.
6. Camanho, P. P., & Dávila, C. G. (2002). *Mixed-mode decohesion finite elements for the simulation of delamination in composite materials*.
7. Reinoso, J., Blázquez, A., Távara, L., et al. (2016). Damage tolerance of composite runout panels under tensile loading. *Composites Part B Engineering, 96,* 79–93.
8. Dugdale, D. S. (1960). Yielding of steel sheets containing slits. *Journal of the Mechanics and Physics of Solids, 8*(2), 100–104.
9. Bazargan, M. (2010). *Airline operation and scheduling*. Farnham: Ashgate Publishing Limited.
10. Katnam, K. B., Silva, L. F. M. D., & Young, T. M. (2013). Bonded repair of composite aircraft structures: A review of scientific challenges and opportunities. *Progress in Aerospace Sciences, 61,* 26–42.
11. Armstrong, K. B., & Barrett, R. T. (2005). Care and repair of advanced composites. *Society of Automotive Engineers*.
12. Hibbit, D., Karlsson, B., & Sorenson, P. (2010) *ABAQUS analysis user's manual*.
13. Hashin, Z. (1981). Fatigue failure criteria for unidirectional fiber composites. *Journal of Applied Mechanics, 47*(2), 329–334.
14. Benzeggagh, M. L., & Kenane, M. (1996). Measurement of mixed-mode delamination fracture toughness of unidirectional glass/epoxy composites with mixed-mode bending apparatus. *Composites Science and Technology, 56,* 439–449.
15. Hashin, Z., & Rotem, A. (1973). A fatigue criterion for fiber-reinforced materials. *Journal of Composite Materials, 7,* 448–464.
16. Wu, Z., & Chen, J. (2017). Research on low speed impact of composite laminated structures based on Hashin criterion. *Journal of shenyang university of aeronautics and astronautics, 34*(5):12–20 (in Chinese). 吴振, 陈健. 基于Hashin准则的复合材料层合结构低速冲击研究[J]. 沈阳航空航天大学学报, 2017, 34(5)12–20.
17. Barbero, E. J. (2013). *Finite element analysis of composite materials using Abaqus*™. Boca Raton: CRC press (学习教材).
18. Matzenmiller, A., Lubliner, J., & Taylor, R. L. (1995). A constitutive model for anisotropic damage in fiber-composites. *Mechanics of Materials, 20,* 125–152.
19. Sun, J., Zhang, X., & Gong, Z., et al. (2013). Failure mechanism analysis of cap type steel bar debonding of composite materials. *Journal of Aeronautics, 34*(7), 1616–1626 (in Chinese). 孙晶晶, 张晓晶, 宫占峰,等. 复合材料帽型筋条脱粘的失效机理分析[J]. 航空学报, 2013, 34(7)1616-1626.
20. Maimí, P., Camanho, P. P., Mayugo, J. A., et al. (2007). A continuum damage model for composite laminates: Part II – Computational implementation and validation. *Mechanics of Materials, 39*(10), 909–919.
21. Caminero, M. A., Rodríguez, G. P., & Muñoz, V. (2016). Effect of stacking sequence on Charpy impact and flexural damage behavior of composite laminates. *Composite Structures, 136,* 345–357.

22. Vicente, J. L. M., Moreno, M. C. S., Torija, M. A. C., et al. *Multiaxial behavior of notched composite structures manufactured by different procedures*.
23. Lapczyk, I., & Hurtado, J. A. (2007). Progressive damage modeling in fiber-reinforced materials. *Composites: Part A, 38*(11), 2333–2341.

Digital Image Correlation Method Based on SURF in Airship Envelope Measurement

Liuyue Zhao, Quanbao Wang, Pingfang Zhou and Dengping Duan

Abstract Digital image correlation (DIC) based on computer vision is introduced to the measurement of airship envelope because the material has the characteristics of small modulus and large strain range which bring some difficulties to the traditional contact methods. This paper presents a proposed DIC initial value estimation algorithm by introducing SURF (Speeded Up Robust Feature) method to improve the correlation and system automation, which makes the instability and the initial value sensitivity problems of further optimization algorithm solved. Firstly, SURF is used to detect the feature points in the images. Then, the SURF feature points are associated with sub-regions by selecting *N* feature points, which means that per sub-region is represented by few feature points. Finally, the selected points in the images before and after the deformation are accurately matched so that displacement and strain initial values are obtained for Newton-Raphson (N-R) method. The algorithm is verified by simulated speckle experiment and airship envelope tensile experiment and is compared with the traditional initial value estimation method. The results show that the proposed algorithm can provide more stable and accurate initial value estimation which not only reduces operational complexity but also speeds up the matching process.

Keywords Initial value estimation · Digital image correlation · Feature points · Airship envelope stretch · Matching algorithm

L. Zhao (✉) · Q. Wang · P. Zhou · D. Duan
Institute of Aeronautics and Astronautics, Shanghai Jiaotong University, Shanghai, China
e-mail: moon16@sjtu.edu.cn

Q. Wang
e-mail: quanbaowang@sjtu.edu.cn

P. Zhou
e-mail: zhoupf@sjtu.edu.cn

D. Duan
e-mail: ddp@sjtu.edu.cn

Z. Jing (ed.), *Proceedings of International Conference on Aerospace System Science and Engineering 2018*, Lecture Notes in Electrical Engineering 549,
https://doi.org/10.1007/978-981-13-6061-9_7

1 Introduction

The mechanical property measurement of airship envelope materials is of great significance for airship evaluation and design. Since the most airship envelopes are made of a kind of laminated composite material, which has the characteristics of small modulus and large strain range resulting in the measurement difficulty of contact methods, digital image correlation (DIC) [1–4] based on computer vision is widely used, which has a large strain range and does not affect the performance of the envelope material. DIC uses image processing technology to measure the strain of a material structure according to texture or artificial speckle on the object surface. By calculating the correction degree to match the corresponding points of the speckle image before and after the strain, the displacement information and strain information are determined, where the pixel coordinates of the extreme point in the correlation function is corresponding with the pixel of matching points. The high accuracy, wide measurement range, simple equipment and low environment make DIC widely used in engineering practice [5, 6].

The DIC system stores the images in the form of a matrix. $f(x, y)$ and $g(x', y')$ represent respectively the image before and after deformation. A sub-region centered (x_0, y_0) is selected from the reference image and then the most relevant sub-region in the deformed image is found by a certain correlation search method. Thereby, the displacement and strain of the measuring point are measured. The process of DIC is shown in Fig. 1.

DIC method divides the search process into two parts: integer pixel initial value estimation and sub-pixel displacement search. The search speed lies in the initial value of the deformed parameter. After attaining the initial value, Newton-Raphson

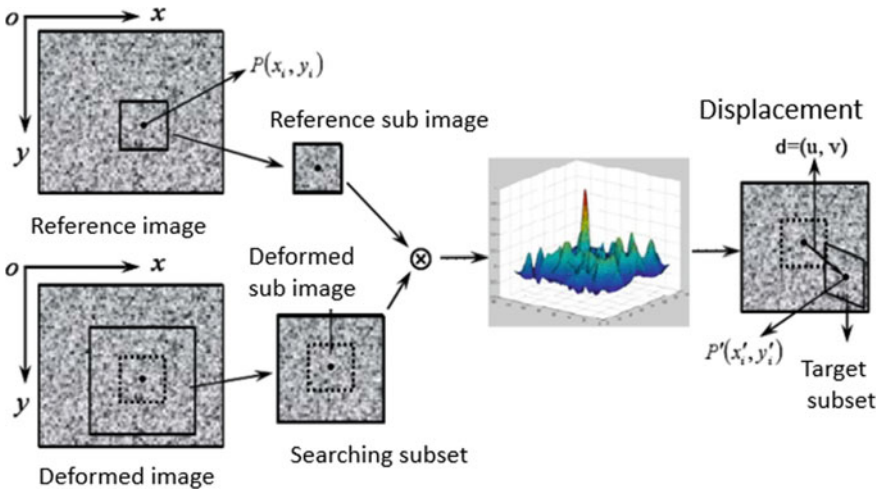

Fig. 1 The process of digital image correlation

Method is the most widely used to match sub-pixel, which is proved that N-R method can converge effectively only in 7 pixels [4]. The common initial value estimation methods are as follows: Coarse–fine search method [7] searches the whole field pixels for initial values. The method has a large amount of calculation. For the envelope deformation, the regression correlation effect is obvious and the estimation precision is reduced. Adjacent domain search method [8] searches for the first point in full field and the other points are searched only in the limited neighborhood around it. It can be integrated into other initial value estimation methods to improve the computing speed. As the same, it can't be applied directly in airship envelope measurement. Human–computer interaction method [9] refers to the process of manually picking 1 or more matching points. Then the neighborhood search method is used to search the neighboring points in a small range. The advantage of this method is that the arbitrary deformation can be allowed and the calculation amount can be simplified. However, taking the point artificially is not conducive to the automatic system. In addition, global optimization methods are researched, such as genetic algorithm [10] and differential evolution method [11], which don't need initial value estimation. However, due to huge computational cost, they are rarely used in engineering practice. In 2013, Huajun [12] and others presented the combination of SURF and DIC, but the method can't locate the center point of matched deformed images, which is the premise of calculating the displacement of per sub-region and mean strain of the whole image.

Therefore, there are two major DIC initial value estimation methods: coarse–fine method and human–computer interaction method. The former can't avoid the decorrelation effect caused by large deformation of airship envelope and the human–computer interaction method is inaccurate, difficult for system automation. A new method of initial value estimation based on SURF feature point matching is presented, which can be used to get better estimated values and overcome the shortcomings of major traditional methods in engineer practice. By detecting and matching the SURF feature points of the speckle image to match the sub-region associated with the feature points near the center point, the displacement parameters as a reliable initial value, are obtained by solving correlation function. The better estimation of initial value can reduce the sub-pixel iteration process and make N-R method converge quickly.

2 Initial Value Estimation Method Based on SURF

2.1 The Principle of DIC

In order to describe the relationship between the corresponding point coordinates of the image before and after and the deformation, the first-order displacement shape function [8] are selected, which can handle the rigid and the affine transformation, and the form is as follows:

$$\begin{cases} x_0' = x_0 + u + u_x \times \Delta x + u_y \times \Delta y \\ y_0' = y_0 + u + v_x \times \Delta x + v_y \times \Delta y \end{cases} \tag{1}$$

In the formula, (x_0, y_0) is the center point of the sub-region in the reference image. (x_0', y_0') is the pixel coordinate of the matching point correspondingly. $\overrightarrow{P} = (u, v, u_x, u_y, v_x, v_y)$ is the displacement pending parameter. u represents the displacement of the sub-region in x direction and v represents the displacement in y direction. u_x, u_y, v_x, v_y is the displacement gradient of the sub-region in the direction x and y. $\Delta x, \Delta y$ is the distance from the center point of sub-region. The first-order shape function can describe the deformation of the sub-region under the general stress state more accurately.

In order to evaluate the similarity of image sub-areas, select the normalized covariance cross-correlation function [8] which has the strong anti-interference ability, as the following:

$$C\left(\overrightarrow{P}\right) = \frac{\sum_{x=-m}^{m}\sum_{y=-m}^{m}[f(x,y) - f_m] \times \left[g(x',y') - g_m\right]}{\sqrt{\sum_{x=-m}^{m}\sum_{y=-m}^{m}[f(x,y) - f]^2}\sqrt{\sum_{x=-m}^{m}\sum_{y=-m}^{m}[g(x',y') - g_m]^2}} \tag{2}$$

The sub-region size is $(2m + 1) * (2m + 1)$. f_m, g_m is the average gray value of the reference and the deformed image sub-region respectively.

The key of the algorithm is the correlation search. When the correlation coefficient C takes the extreme value, which means $\Delta C = 0$, the image sub-regions before and after the deformation are most similar. This is a nonlinear equation about $\overrightarrow{P}$, which can be iteratively solved by Newton-Raphson (N-R) method [3]. The expression is as follows.

$$\overrightarrow{P} = \overrightarrow{P_0} - \frac{\Delta C\left(\overrightarrow{P_0}\right)}{\Delta\Delta C\left(\overrightarrow{P_0}\right)} \tag{3}$$

$\overrightarrow{P_0}$ is the initial estimation value of the deformation parameters. The iteration can converge to a reliable solution only if the initial value is close to the real solution. If the initial value is reasonable, the deformation value may be obtained by performing several correlation calculations. Otherwise, it will take a lot of time or attain a wrong solution.

2.2 The Principle of SURF

In 2006, Bay [13] presented SURF (speeded up robust features) method which has applied widely. The SURF algorithm is a fast and accurate feature point detection algorithm. The feature points are certain invariant points in the image which are invariant to illumination intensity, rotation, scaling, and even affine transformation.

Scale space theory is the basic theory of feature point detection. The principle is based on searching for effective extreme points in the multi-scale space of digital images which has certain invariability when the image scale changes.

In 1984, Koenderink [13] proved that a Gaussian convolutional kernel is the only linear kernel that implements the scale transformation. Therefore, the image processed by Gaussian filter is insensitive to the scale transformation. The relationship between digital image $I(x, y)$ and scale space function $L(x, y, \sigma)$ are as follows:

$$\begin{aligned} L(x, y, \sigma) &= G(x, y, \sigma) * I(x, y) \\ G(x, y, \sigma) &= \frac{1}{2\pi\sigma^2} e^{-\frac{x^2+y^2}{2\sigma^2}} \end{aligned} \tag{4}$$

* represents the convolution in the x and y directions. σ is a scale factor and $G(x, y, \sigma)$ is a two-dimensional Gaussian function. In this way, the points with invariant features can be detected. Stratified sampling generates a multi-scale image, then build differential pyramid, find extreme points and filter low-contrast extreme points.

In the SURF algorithm, Harr wavelet features in the neighborhood are calculated to determine the main direction of the feature points and generate the feature point descriptors. All feature points can be matched according to the Euclidean distances of their feature vectors. In this paper, Nearest Neighbor (NN) is used for matching calculation.

2.3 The Implementation of DIC Based on SURF

In SURF, some feature points are on behalf of the whole image. In DIC, the image sub-region gray matrix represents the sub-region, and the image correlation method is based on the uniqueness of the feature points to perform search matching, so they are ideologically common. However, feature point matching is more focused on the detection of invariant feature points and it is impossible to detect and match any point in the image, which causes that this method can't be used directly for measurement. The accuracy of the point matching algorithm is low, and it is not suitable for direct measurement.

Therefore, this paper proposes an initial value estimation method based on SURF feature point detection. This method uses the SURF algorithm to detect and match feature points in the deformation region, and then associates the detected SURF

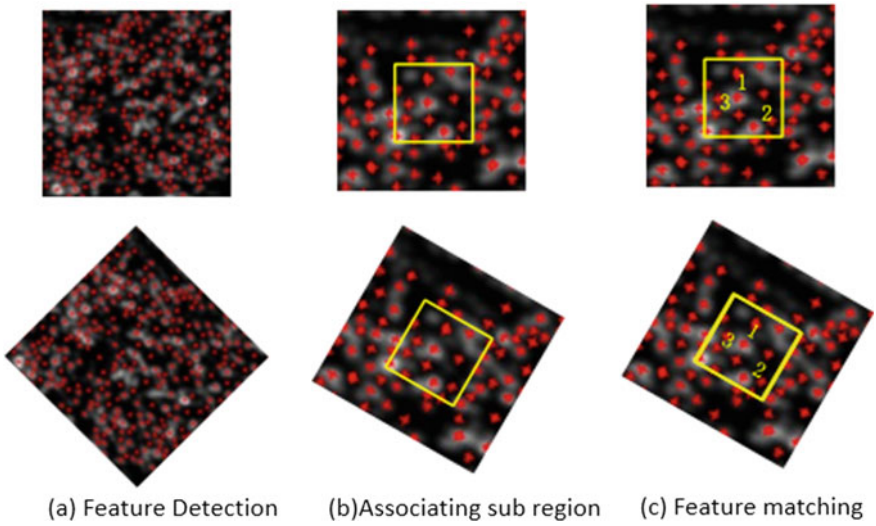

Fig. 2 Relationship between feature points sub-region

feature points with the reference sub-region. The N feature points closest to the center of the reference sub-area are calculated. In this way, the pixel coordinates of the target sub-region containing the SURF matching feature points can be obtained easily.

After the SURF algorithm is used to detect and match the feature points in the deformation region, the SURF feature points are associated with the image sub-regions. There are enough SURF feature points near the sub-region of the speckle image. Thus, the N feature points nearest to the center of the image sub-region can be selected. Associated with sub-regions, obtain the sub-region displacement by the coordinates of feature points equations.

The principle of the image sub-region matching method based on feature point detection is shown in Fig. 2. The feature point is regarded as the invariant points inside the sub-region. The feature point moves with the deformation of the sub-region. That is, the feature point contains the displacement information of sub-region.

According to the above matching feature point pairs, we can bring matching point coordinates into solving the pending displacement parameters $(u, v, u_x, u_y, v_x, v_y)$, which needs 6 effective equations to solve. We need to take at least three valid matching points. After selecting the three matching points, they are organized into a matrix:

$$\begin{pmatrix} x_1' \\ x_2' \\ x_3' \end{pmatrix} = \begin{pmatrix} x_1 \\ x_2 \\ x_3 \end{pmatrix} + \begin{bmatrix} 1 & \Delta x_1 & \Delta y_1 \\ 1 & \Delta x_2 & \Delta y_2 \\ 1 & \Delta x_3 & \Delta y_3 \end{bmatrix} \begin{pmatrix} u \\ u_x \\ u_y \end{pmatrix}$$

$$\begin{pmatrix} y_1' \\ y_2' \\ y_3' \end{pmatrix} = \begin{pmatrix} y_1 \\ y_2 \\ y_3 \end{pmatrix} + \begin{bmatrix} 1 & \Delta x_1 & \Delta y_1 \\ 1 & \Delta x_2 & \Delta y_2 \\ 1 & \Delta x_3 & \Delta y_3 \end{bmatrix} \begin{pmatrix} v \\ v_x \\ v_y \end{pmatrix} \tag{5}$$

By solving the above linear equations, the initial displacement parameters $(u, v, u_x, u_y, v_x, v_y)$ can be obtained. Subsequent neighboring points are also processed using the neighborhood search method until the initial value estimation process is completed. When the number of effective equations is larger than that of variables, it is an over-determined equation group. This paper uses the least square method to optimize it.

3 Experimental Verification and Analysis

3.1 The Experiment of Simulate Speckle Image

(1) *Translation experiment*

In order to avoid the systematic errors in the actual measurement process, simulated speckle matching experiments are performed to verify the effectiveness of the initial value estimation of DIC based on SURF algorithm.

First, the random speckle is simulated according to the method of the article as in [14]. The algorithm uses the following function to generate the simulated speckle before and after the deformation:

$$I_1(r) = \sum_{k=1}^{s} I_0 \exp\left(-\frac{|r - r_k|}{a^2}\right) \tag{6}$$

$$I_2(r) = \sum_{k=1}^{s} I_0 \exp\left(-\frac{|r - U(r) - r_k|}{a^2}\right) \tag{7}$$

In the formula, s is the total number of speckle particles and a is the size of speckle particles. I_0 is the peak value of speckle particles. r_k is the position of each speckle particle distributed randomly. $U(r)$ is the preset displacement which is calculated by the following formula.

$$\begin{cases} x' = x + u + u_x \times \Delta x + u_y \times \Delta y \\ y' = y + u + v_x \times \Delta x + v_y \times \Delta y \end{cases} \tag{8}$$

According to this method, the relevant parameters of the simulated speckle are set: the number of speckles s is 2000. The speckle size a is 4 pixels. The image resolution is 512 × 512 pixels, and the preset displacement of the deformed speckle pattern is

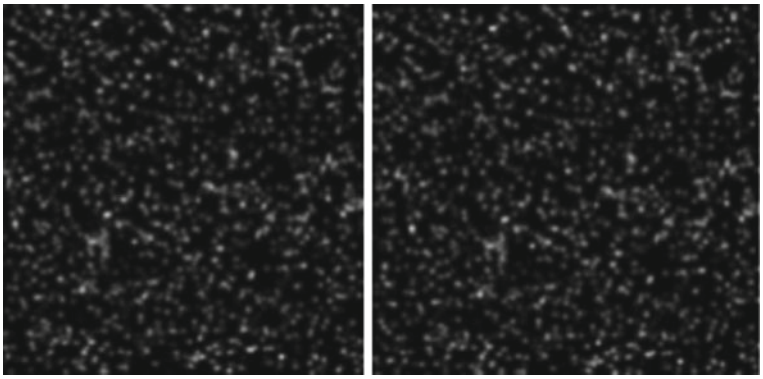

(a) Reference image (b) Translated image

Fig. 3 Simulated speckle pattern

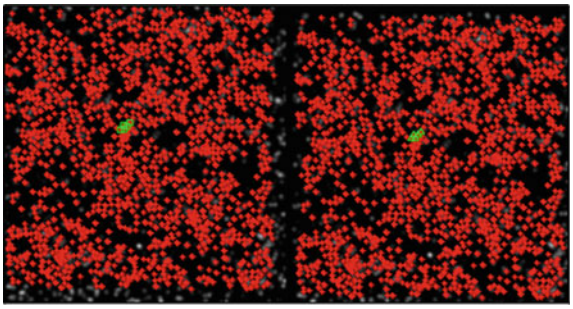

Fig. 4 Feature points

(5.2, 5.2) pixel. The simulated speckle pattern before and after the deformation is shown Fig. 3.

Take the center sub-region of the reference image, whose center point is P(256, 256), and estimate the initial value of the displacement. First, the SURF algorithm is used to detect the feature points in the reference and deformed images and then match them. Then, take the effective feature point near the center point P and filter out the four nearest feature points from P, as shown in Fig. 4. Substituting the coordinates of effective feature points into the equations and listing the equations, the least-squares method is used to solve the over-determined linear equations. The red dot is the feature point and the green dot represents the effective feature point in Fig. 4.

Change the preset displacement of the deformed picture and repeat the experiment. Start from the displacement of 5.2 pixel, increasing 5 pixel sequentially for the 5 times to 25.2 pixel, in which the relative data are calculated. The results are shown in Table 1. It can be observed that the estimation method based on feature point matching has high accuracy. In the 5 groups of experiments, the absolute error of the estimation and real value is within 1 pixels and the relative error is less than 4%.

Table 1 Matching results of feature matching method (u direction)

Test	Preset displacement (u_0)	Estimation value (u)	Absolute error ($\|u - u_0\|$)	Relative error ($\|u - u_0\| / u_0$)
1	5.2	5.186823	0.01317	0.002534038
2	10.2	10.26231	0.06231	0.006108824
3	15.2	15.10985	0.09015	0.005930921
4	20.2	20.85569	0.65569	0.032459901
5	25.2	26.64008	0.74008	0.029368254

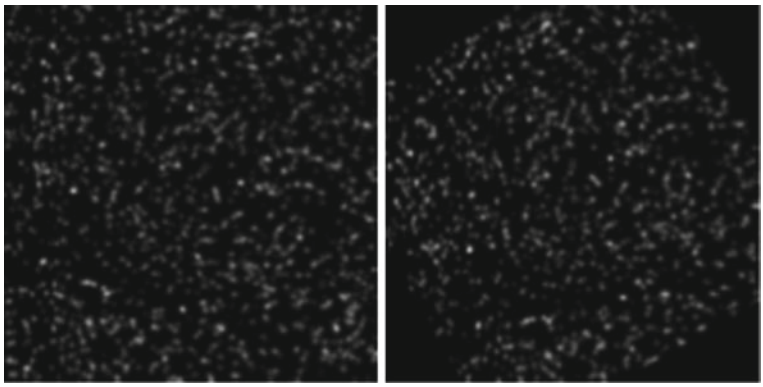

(a) Reference image (b) Rotated image

Fig. 5 Simulated speckle pattern

The calculation results are very stable and can provide a good initial value for the subsequent sub-pixel matching process.

The initial values of other sub-regions can be estimated by the same method. The above initial value estimation process is performed on the 60–450 pixel deformed region with a preset displacement of 5.2 and the search interval is 10 pixels. Therefore, by combining the above single point matching experiments with the whole field matching experiment results, it can be concluded that the feature matching method is stable and accurate for translation transformation. The displacement vector field is corresponding with our preset displacement.

(2) *Rotation experiment*

In order to verify that DIC based on SURF is insensitive to affine transformation, the experiment of the rotation deformation is carried on. Figure 5a is a reference image, and Fig. 5b is a deformed image rotated around the center point P. Set the size of the sub-area to be 21 × 21 pixel and the feature point to be 4 to estimate the initial value of the deformed area. The experiment results are shown in Figs. 6 and 7. From the experimental results, we can find that the initial value of the estimated trend is in line with our preset deformation law.

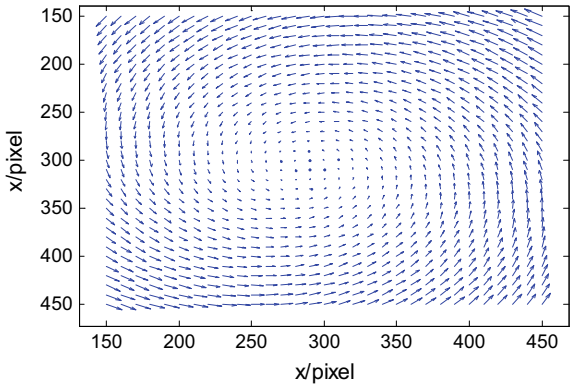

Fig. 6 Deformation displacement vector field

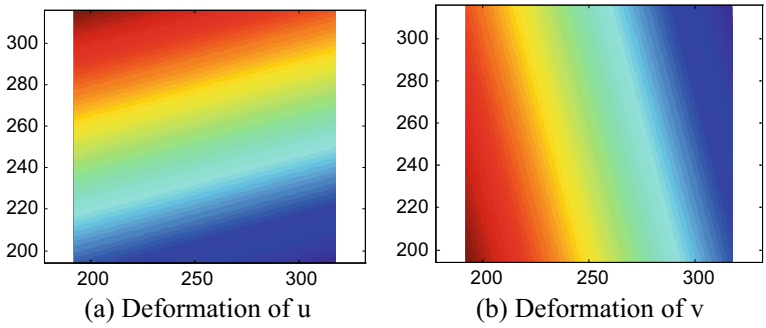

Fig. 7 Deformation of different directions

In order to further verify the calculation results, we randomly select a sub-region center for sub-pixel optimization, comparing the results before and after optimization and analyzing the accuracy of its estimation.

3.2 The Experimental Process on Airship Envelope Specimens

The airship envelope material used in the experiment is a new type of bidirectional fiber-reinforced multi-layer composite material developed by 46 institute, which has greater strength and better flexibility. According to [3], the average strain is greater than 3% belonging to large strain measurement. The basic material parameters provided by the manufacturer are: thickness $t = 0.247$ mm, surface density $= 86$ g/m^2. According to the National Experiment Standard for fiber weaving materials, the

Fig. 8 Experiment specimen

materials are made into strips with a length of 370 mm and a width of 50 mm and the measurement area is 70 mm in the middle.

(1) *Sample preparation*

Samples were prepared according to Fig. 8, and speckles were randomly drawn in the experiment area using different color markers. In order to ensure the effectiveness of the experiment, three specimens numbered 1, 2, and 3 were produced.

(2) *Experiment system*

Connect and test the camera, computer and other hardware. After confirming that the system works, adjust the tripod to ensure the camera is level. The experiment system is shown in Fig. 9.

(3) *Specimen stretching and picture storage*

After the camera was calibrated, the computer controls the stretching machine to start the stretching of the specimen at a speed of 2 mm/min. At the same time, the camera started to take deformation pictures at a rate of 1 frame per second After the stretching process is completed, the deformation pictures corresponding to 100, 300, 500, 700, 900, 1100, and 1300 N are extracted as valid data for calculation.

(4) *Experiment results*

(1) *Estimated value contrasted with traditional method*

At present, the major methods of the initial value mentioned in documents are rough-precise method and human–computer interaction method. The former method is rarely used now, so this paper compares the proposed feature matching method with human–computer interaction method.

For the No. 1 specimen, the initial value estimation is obtained using human–computer interaction method and feature matching method respectively, comparing their

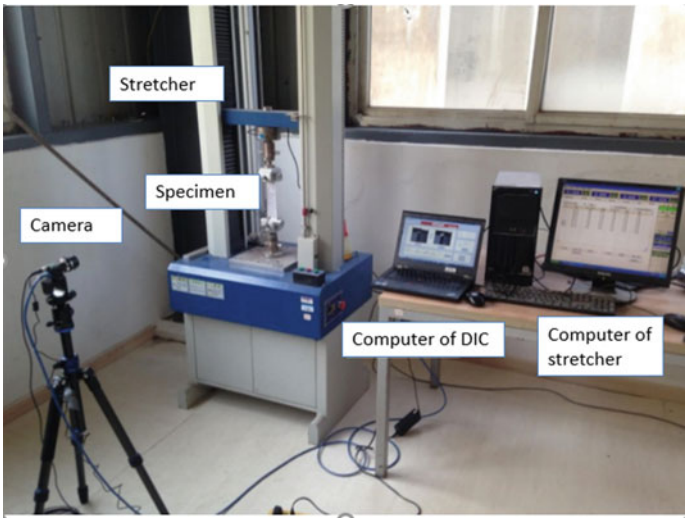

Fig. 9 Experiment system

Table 2 Initial value in u direction

Experiment conditions		Exact value	Human–machine interaction		Feature matching method	
Pull/F	Stress/Mpa	u_0	u_1	$\lvert u_1 - u_0 \rvert$	u_2	$\lvert u_2 - u_0 \rvert$
100	8.09717	−0.519	0	0.519	−0.8807	0.3617
300	24.2915	−0.3123	2	2.3123	0.0945	0.4068
500	40.4858	−0.2157	5	5.2157	−0.1716	0.0441
700	56.6802	−0.3108	2	2.3108	−0.2766	0.0342
900	72.8745	−0.3847	4	4.3847	−0.1207	0.264
1100	89.0688	−0.4594	0	0.4594	−0.5348	0.0754
1300	105.263	−0.224	5	5.224	−0.2227	0.0013

sub-pixel search optimization result based on the estimated values. The estimated results of the u direction are shown in Table 2. In the u direction, the average error of human–machine interaction is 2.918 pixel and its standard deviation is 2.055. The average error of the feature matching method is 0.169 pixel, which is 17 times smaller than the human–computer interaction method and the standard deviation is 0.170, indicating that the method is more stable.

It can be further calculated from Table 3 that the average error of human–machine interaction in v direction is 1.653 pixels, and the standard deviation is 0.639. The average error of the feature matching method is 0.265 pixel, which is 6 times smaller than the human–computer interaction method. The standard deviation is 0.202 and

Table 3 Initial value in v direction

Experiment conditions		Exact value	Human–machine interaction		Feature matching method	
Pull/F	Stress/Mpa	v_0	v_1	$\lvert v_1 - v_0\rvert$	v_2	$\lvert v_2 - v_0\rvert$
100	8.09717	−8.6737	−7	1.6737	−8.7972	0.1235
300	24.2915	−14.5368	−13	1.5368	−14.8825	0.3457
500	40.4858	−18.5999	−17	1.5999	−18.3266	0.2733
700	56.6802	−21.8417	−21	0.8417	−22.0032	0.1615
900	72.8745	−24.946	−22	2.946	−25.1029	0.1569
1100	89.0688	−28.335	−27	1.335	−28.4461	0.1111
1300	105.263	−33.637	−32	1.637	−32.9554	0.6816

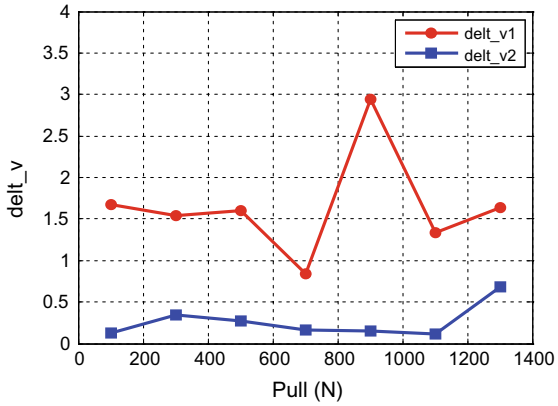

Fig. 10 Initial value estimation error distribution in v direction

its fluctuations are also small. Initial value estimation error distribution in v direction is shown in Fig. 10.

From the above experimental results, it can be concluded that the average error and standard deviation of the initial value estimation of the feature matching method are far less than the human–computer interaction method, and its accuracy is obviously improved. The displacement in v direction is far more than that in u direction, which is corresponding with our pull direction. The SURF feature matching method also avoids the manual point-input process of the human–computer interaction method during the experiment process.

(2) *Calculation of Young's modulus*

As shown in Fig. 11, in order to solve the tensile Young's modulus of the material, two points are taken at the border of the measurement area of the specimen (the red rectangle represents the selected point), and the average strain in the deformation zone is obtained through the distance based on the two points. The stress–strain

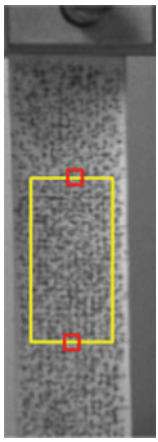

Fig. 11 Modulus measurement

Table 4 Average strain of three specimens at different loads

	F/N	Strain/Mpa	delt_v_1	delt_v_2	delt_v_3
1	100	8.097166	0.004908	0.004385	0.004542
2	300	24.2915	0.013115	0.011765	0.011932
3	500	40.48583	0.017874	0.017213	0.017225
4	700	56.68016	0.021697	0.020834	0.021248
5	900	72.87449	0.024787	0.02418	0.024302
6	1100	89.06883	0.028546	0.027491	0.027693
7	1300	105.2632	0.033236	0.031014	0.031334

curve is then plotted for each load. The slope of the curve is the tensile modulus of the material.

The average strain of the three test specimens is shown in Table 4. The relationship between stress and strain is plotted and its slope is calculated by a linear fitting function.

The stress–strain relationship of the three specimens is shown in Fig. 12. Fit the three lines and record the slope. The lastic modulus of the three specimens is $E_1 = 3.6064$ GPa, $E_2 = 3.696$ GPa, $E_3 = 3.7122$ GPa and the average value is $E_m = 3.6715$ GPa. The measured modulus is nearly the same as the standard model 3.6 GPa given by the manufacturer. Therefore, it can be considered that the tensile modulus of the envelope based on the DIC proposed in this paper is feasible and reliable.

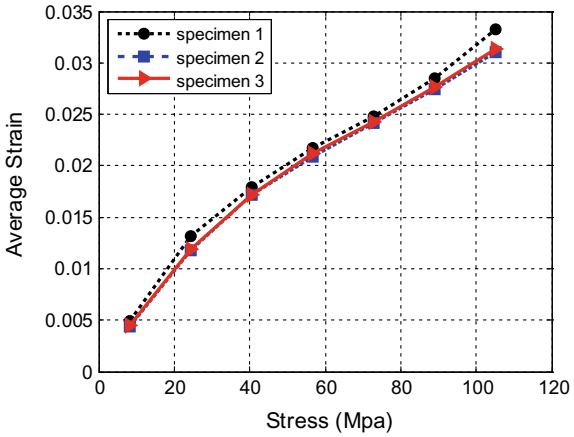

Fig. 12 Stress–strain relationship

4 Conclusions

Due to the sensitivity for initial values of N-R method and the disadvantages of traditional estimated methods, a DIC method based on SURF is proposed. By detecting and matching the feature points of the image to match the sub-region before and after the deformation, the equation of matching points are obtained through taking the matching point coordinates into shape function. Then the least-squares method is used to get the displacement parameters as a reliable initial value. The estimated value is further calculated as an iterative initial value for the N-R method, and more accurate sub-pixel displacement and strain information are obtained.

In the translation and rotation experiment of the simulated speckle, the absolute error of the estimated and real value is within 1 pixels, which can effectively ensure the convergence and speed up the calculation in the further optimization method. Meanwhile, using N-R method to optimize the initial value, DIC method based on SURF is verified in the tensile test of airship envelope. The Young's modulus of the envelope material is calculated based on the average strain, which is very close to the standard modulus given by the manufacturer. And the average error between the estimation and the exact solution is smaller than the traditional method. In short, the DIC method proposed in this paper can effectively measure the deformation and strain information of the airship envelope. Compared with the most frequently used traditional human–computer interaction method and global search method, this method is more accurate and avoids the manual operation process and instability caused by human factors.

References

1. Sutton, M. A., McNeill, S. R., Helm, J. D., et al. (2000). Advances in two-dimensional and three-dimensional computer vision. *Topics in Applied Physics, 77*(1), 323–372.
2. Bing, P., Xie, H., Xu, B., et al. (2005). Development of sub-pixel displacements registration algorithm in digital image correlation. *Advances in Mechanics, 35*(3), 345–352.
3. Bing, P., Hui-Min, X., Bo-Qin, X., et al. (2006). Performance of sub-pixel registration algorithms in digital image correlation. *Measurement Science & Technology, 17*(6), 1615.
4. Vendroux, G., & Knauss, W. G. (1998). Submicron deformation field measurements: Part 2. Improved digital image correlation. *Experimental Mechanics, 38*(2), 86–92.
5. Peters, W. H., & Ranson, W. F. (1982). Digital imaging techniques in experimental stress analysis. *Optical Engineering, 21*(3), 427–431.
6. Yan, H., & Wang, M. (2008). Orientation of mouse using digital speckle correlation method. *Acta Optica Sinica, 28*(3), 467–471.
7. Zhang, Z. F., Kang, Y. L., Wang, H. W., et al. (2006). A novel coarse-fine search scheme for digital image correlation method. *Measurement, 39*(8), 710–718.
8. Liu, J. Y., & Iskander, M. (2004). Adaptive cross correlation for imaging displacements in soils. *Journal of Computing in Civil Engineering, 18*(1), 46–57.
9. Pan, B. (2009). Large-deformation measurement based on reliable initial guess in digital image correlation method. *Acta Optica Sinica, 29*(2), 400–406.
10. Shaopeng, M., Guanchang, J., Tsinghua University, et al. (2003). Digital speckle correlation method improved by genetic algorithm. *Acta Mechanica Solida Sinica, 16*(4), 366–373.
11. Bing, P., & Xie, H. M. (2007). Digital image correlation method with differential evolution. *Journal of Optoelectronics Laser, 18*(1), 100–103.
12. Huajun, Z., Guihua, L., Cheng, L., et al. (2013). Reliable initial guess based on SURF feature matching in digital image correlation. *Acta Optica Sinica, 33*(11), 1112005.
13. Bay. H., Tuytelaars, T., & Gool, L. V. (2006). SURF: Speeded up robust features. In *European Conference on Computer Vision* (pp. 404–417). Springer.
14. Yamaguchi, I. (1981). Speckle displacement and decorrelation in the diffraction and image fields for small object deformation. *Optica Acta, 28*(10), 1359–1376.

Dynamic Collision Avoidance Strategy for Unmanned Aerial Vehicles Formation Flight

Minghua Wang and Shiqiang Hu

Abstract Unmanned aerial vehicles (UAV) have been widely used in many fields. UAV formation flight can complete more assignments than single UAV. Collision avoidance is an important part of UAV formation flight. In this paper, we put forward a three-dimensional method of dynamic collision avoidance for UAV formation flight based on the theory of velocity obstacle. The collection of all possible accelerations of the UAV can be obtained by the input of UAV. Considering that the relative velocity between the UAV and obstacle must be out of the collision cone, we can obtain the collection of feasible accelerations next moment. Then we choose the acceleration which is able to let the UAV closest to the target next moment in the collection as the real acceleration. The maximum and minimum velocity should also be set up. Each UAV can determine the best acceleration next time for itself. In addition to formation keeping, this paper also presents how to split the formation on the basis of the direction of each UAV. Numerical simulation is used to test the performance of this method at the end of this paper.

Keywords Unmanned aerial vehicle (UAV) · Collision avoidance · Velocity obstacle · Formation flight

1 Introduction

The technology of single unmanned aerial vehicle (UAV) has become relatively mature after decades of development. It plays an important role in military and civilian affairs, such as fire monitoring, search and rescue and reconnaissance. The formation flight can accomplish more tasks than single UAV. Cooperative operation of multi-UAVs can not only carry equipment separately to complete the transportation

M. Wang (✉) · S. Hu
School of Aeronautics and Astronautics, Shanghai Jiao Tong University, Shanghai, China
e-mail: wangminghua@sjtu.edu.cn

S. Hu
e-mail: sqhu@sjtu.edu.cn

Z. Jing (ed.), *Proceedings of International Conference on Aerospace System Science and Engineering 2018*, Lecture Notes in Electrical Engineering 549,
https://doi.org/10.1007/978-981-13-6061-9_8

of larger equipment, but also fulfil the missions such as high-precision positioning, 3D modelling and multiangular imaging. Formation flight can expand the scope of reconnaissance, monitoring and search in the case of aerial photography and aerial monitoring. In addition, the formation design can make the impact of wreck of single UAV reduce to the bottom, which greatly improves the reliability.

UAVs must have the ability to avoid obstacles for almost any tasks. Static obstacles include trees, buildings and so on. Dynamic obstacles include birds, other airplanes, kites and so on. At low altitude, humans and animals may become obstacles. In order to complete missions successfully, UAVs should be able to discover obstacles and then avoid collision. Especially in civilian affairs, safety is the first.

Nowadays, there are already many researches on collision avoidance for single UAV and collision avoidance for UAV formation flight in static environment. For single UAV, conventional proportional navigation guidance method [1], reference point guidance [2], velocity obstacle [3] and some other methods [4, 5] are used for collision avoidance. For UAV formation flight, most collision avoidance strategy are for static obstacles. A* algorithm and model predictive control are widely used in this situation [6, 7].

However, there are not yet enough methods of collision avoidance for UAV formation flight in dynamic environment. Recently, Seo et al. put forward a strategy of collision avoidance for UAVs formation flight based on geometry [8]. This strategy only changes the velocity direction of UAV and doesn't change the magnitude of velocity, which obviously cannot achieve optimal results. In addition, while avoiding the obstacle, UAVs doesn't consider the target. It is necessary to judge whether to complete obstacle avoidance all the time.

Velocity obstacle was put forward early [9]. It is a very useful method and has been used widely in collision avoidance of robots. After decades of development, there are some variants, such as selective velocity obstacle (SVO) [10], reciprocal velocity obstacle [11] and probabilistic velocity obstacle (PVO) [12].

In this paper, we put forward a three-dimensional method of dynamic collision avoidance for UAV formation flight based on the theory of velocity obstacle and collision cone. In addition to formation keeping, this paper also presents how to split the formation on the basis of each UAV. Collision avoidance among UAVs in the same formation is also considered. Numerical simulation is used to test the performance of this method at the end of this paper.

2 Collision Avoidance Strategy

2.1 Velocity Obstacle

Velocity obstacle is generally two-dimensional in the past.

We can first consider a UAV and an obstacle in a 2-D plane. This method assumes that the UAV is a point and the obstacle is a sphere. In Fig. 1a, the position of UAV u

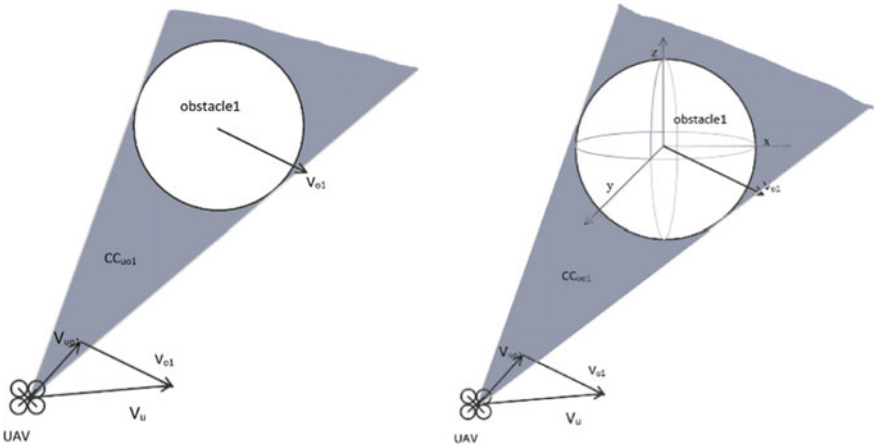

(a) Two-dimensional (b) Three-dimensional

Fig. 1 Collision cone between UAV and obstacle

is $[x_u, y_u]$ and the position of obstacle o1 is $[x_{o1}, y_{o1}]$. v_{o1} is the velocity of obstacle and v_u is the velocity of UAV. The relative velocity is $v_{ou1}(v_{ou1} = v_u - v_{o1})$. CC_{uo1} is the collision cone between UAV and obstacle, namely the shadow in Fig. 1a. We can define it mathematically:

$$CC_{ou1} = \left\{ v_{ou1} | \exists t > 0, \left(x_u + v_{ou1}\vec{i} \times t, y_u + v_{ou1}\vec{j} \times t \right) \in o \right\} \tag{2.1}$$

where o is the obstacle, $\vec{i}$ and $\vec{j}$ are the unity vectors of x and y directions.

The Velocity Obstacle VO is defined as:

$$VO = CC_{ou1} \oplus v_{o1} \tag{2.2}$$

where $\oplus$ is the Minkowski vector sum operator.

If there are more than one obstacle, VO can be defined as:

$$VO = \bigcup_{i=1}^{n} VO_i \tag{2.3}$$

where n is the number of obstacles.

When it comes to three-dimensional, the definition is similar. As shown in Fig. 1b, the collision cone turns into three-dimensional and can be defined as:

$$CC_{ou1} = \left\{ v_{ou1} | \exists t > 0, \left(x_u + v_{ou1}\vec{i} \times t, y_u + v_{ou1}\vec{j} \times t, z_u + v_{ou1}\vec{k} \times t \right) \in o \right\} \tag{2.4}$$

where o is the obstacle, $\vec{i}$, $\vec{j}$ and $\vec{k}$ are the unity vectors of x, y and z directions.

The Velocity Obstacle (VO) is defined in the same way:

$$\mathrm{VO}_i = \mathrm{CC}_{\mathrm{ou}i} \oplus v_{\mathrm{o}i}, \quad \mathrm{VO} = \bigcup_{i=1}^{n} \mathrm{VO}_i \tag{2.5}$$

where $v_{\mathrm{o}i}$ is the velocity of the i-th obstacle and n is the number of obstacles.

When the velocity of UAV v_{u} belongs to VO, it must satisfy the following formula:

$$\vec{v}_{\mathrm{ou}} \bullet \vec{l}_{\mathrm{ou}} > 0 \,\text{and}\, \mathrm{d}(\vec{v}_{\mathrm{ou}}, \mathrm{o}) < r_{\mathrm{o}} \tag{2.6}$$

where $\vec{v}_{\mathrm{ou}} = \vec{v}_{\mathrm{u}} - \vec{v}_{\mathrm{o}}$, $\vec{l}_{\mathrm{ou}} = \mathrm{pos}_{\mathrm{o}} - \mathrm{pos}_{\mathrm{u}}$ ($\mathrm{pos}_{\mathrm{o}}$, $\mathrm{pos}_{\mathrm{u}}$ are the position of obstacle and UAV). $\bullet$ represents dot product between vectors. $\mathrm{d}(\vec{v}_{\mathrm{ou}}, \mathrm{o})$ is the distance between the line of $\vec{v}_{\mathrm{ou}}$ and the centre of obstacle. r_{o} is the ratio of obstacle.

2.2 Acceleration Selection for Single UAV

Considering the input of the UAV, we can get the collection of all of the feasible acceleration which is recorded as A_{u}. For example, the input of quadrotor is the rotate speed of the four rotors and then the acceleration can be acquired through the dynamic model. The collection of velocity of UAV at $t + \Delta t$ can be acquired.

$$V_{t+\Delta t} = v_{\mathrm{u}t} \oplus (A_{\mathrm{u}} \times \Delta t) \tag{2.7}$$

where $v_{\mathrm{u}t}$ is the velocity of UAV at time t and Δt represents a very short period of time.

In consideration of Velocity Obstacle and the limit of velocity, the feasible velocity collection at $t + \Delta t$ is $V_{\mathrm{u},t+\Delta t}$:

$$V_{\mathrm{u},t+\Delta t} = \left\{ v_{\mathrm{u},t+\Delta t} | v_{\mathrm{u},t+\Delta t} \in V_{t+\Delta t}, v_{\mathrm{u},t+\Delta t} \notin \mathrm{VO}, v_{\min} \le v_{\mathrm{u},t+\Delta t} \le v_{\max} \right\} \tag{2.8}$$

where $v_{\min}$ and $v_{\max}$ are the minimum and maximum value of velocity.

For each $v_{\mathrm{u},t+\Delta t} \in V_{\mathrm{u},t+\Delta t}$, we can get the correspondent position ($p_{\mathrm{u},t+\Delta t}$) of UAV at time $t + \Delta t$.

$$p_{\mathrm{u},t+\Delta t} = \left[x_{\mathrm{u},t+\Delta t}, y_{\mathrm{u},t+\Delta t}, z_{\mathrm{u},t+\Delta t} \right] = p_{\mathrm{u}t} + \frac{\left(v_{\mathrm{u},t+\Delta t} + v_{\mathrm{u}t} \right)}{2} \times \Delta t \tag{2.9}$$

where $p_{\mathrm{u}t}$ is the position of UAV at time t: $p_{\mathrm{u}t} = [x_{\mathrm{u}t}, y_{\mathrm{u}t}, z_{\mathrm{u}t}]$.

The position of target is given at first. Then we can acquire the distance at time $t + \Delta t$ between UAV and the target for each $v_{\mathrm{u},t+\Delta t} \in V_{\mathrm{u},t+\Delta t}$. Finally, we will choose

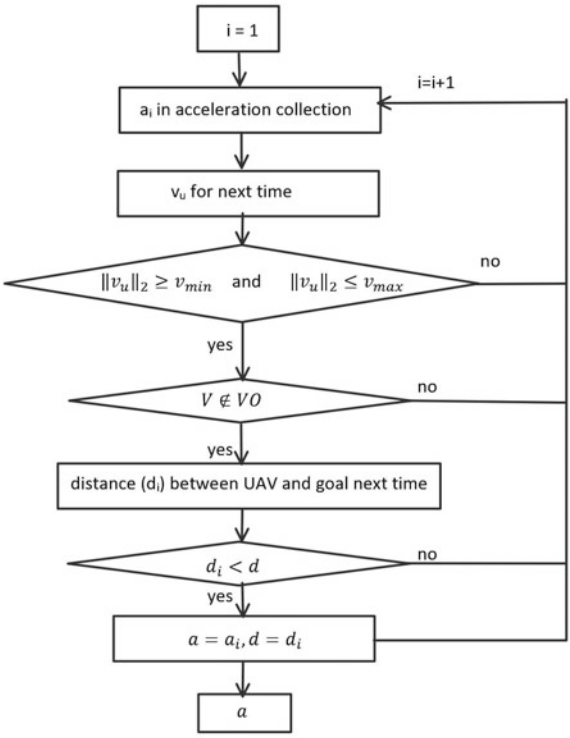

Fig. 2 Flow chart of acceleration selection

the velocity corresponding to the shortest distance. Then we will get the selected acceleration in the end. Figure 2 shows the flow chart of the process of selection.

2.3 Formation Keeping and Splitting

For formation flight of UAVs, we must consider formation splitting and configuration while avoiding collision. While considering formation splitting, we should first divide the obstacle into four parts based on the *xy* and *yz* plane fixed on the obstacle as shown in Fig. 3. The four parts can be marked as I,II,III and IV.

Figure 4 shows the formation keeping and splitting strategy. The formation consists of five UAVs. UAV1 is in the middle of the formation and others are around it. Each UAV can acquire its best acceleration next time according to the method in Sects. 2.1 and 2.2. If the formation must be unchanged, all the UAVs should choose the same acceleration that allows the velocity of each UAV outside collision cone among the five best accelerations. The condition of formation keeping is shown in Fig. 4a. While considering formation splitting, the UAVs should be divided into

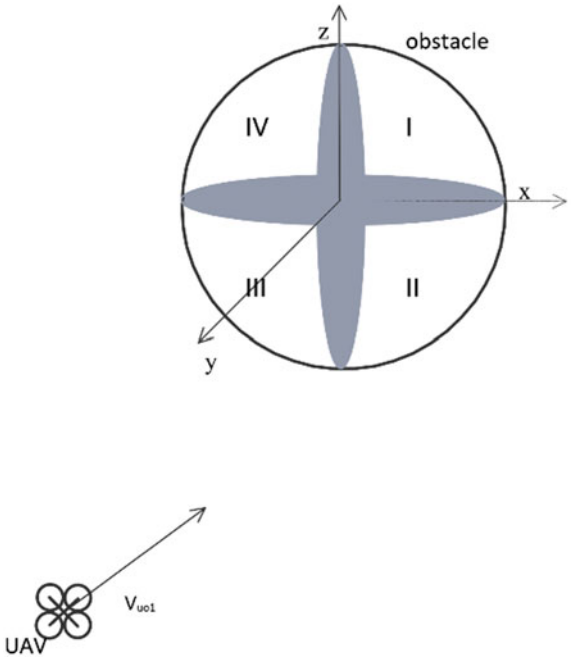

Fig. 3 Four parts divided based on the obstacle

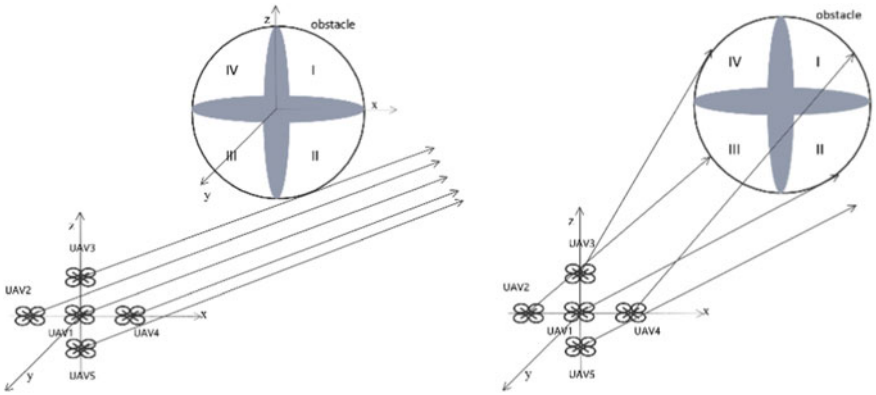

Fig. 4 Formation keeping and splitting strategy **a** Formation keeping **b** Formation splitting

groups according to the direction of velocity next time and the four parts of the obstacle as shown in Fig. 4b.

While formation keeping, the final acceleration of the whole formation is selected from the selected acceleration of the UAVs. The selection rule is that the final accel-

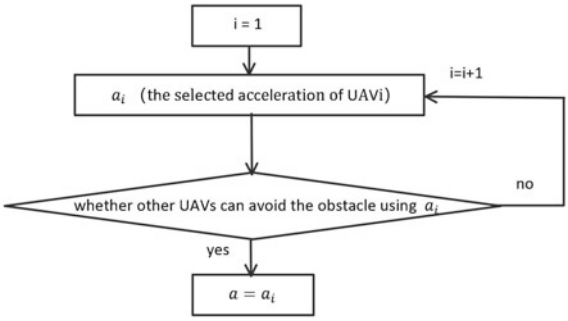

Fig. 5 Flow chart of acceleration selection for formation keeping

eration can let each UAV in the formation complete collision avoidance. Figure 5 shows the flowchart of selection.

While formation splitting, UAVs in the formation can be divided into four parts at most. In the same part, UAVs must keep in a new formation, the acceleration selection is the same as formation keeping. In fact, after formation splitting we can set different targets to complete formation reconfiguration based on the mission.

Then we should judge which part the UAV belongs to. Firstly we should define some angles. As shown in Fig. 6, V_{uo1} is the relative velocity next moment on the basis of the selected acceleration. β is the angle between the tangent line and the connected line of the center of UAV and obstacle. β is always defined as nonnegative. θ is the angle between the horizontal axis and the connected line. θ_v is the angle between the horizontal axis and the line of v_{ou}. θ and θ_v both belong to the scope $[-\pi, \pi]$. They are positive while above the horizontal axis and negative while under the horizontal axis. $\Delta\theta$ is defined as:

$$\Delta\theta = \theta_{\text{v}} - \theta \tag{2.10}$$

While in three-dimensional space, we consider xy and yz plane. The horizontal axis is the x axis in xy plane and y axis in yz plane. Then we can get $\Delta\theta_{xy}$, $\Delta\theta_{yz}$, β_{xy}, β_{yz}. The division is shown in Table 1.

Table 1 Parts division while formation splitting

	$\Delta\theta_{yz} \geq \beta_{yz}$	$\Delta\theta_{yz} \leq -\beta_{yz}$
$\Delta\theta_{xy} \geq \beta_{xy}$	I	II
$\Delta\theta_{xy} \leq -\beta_{xy}$	IV	III

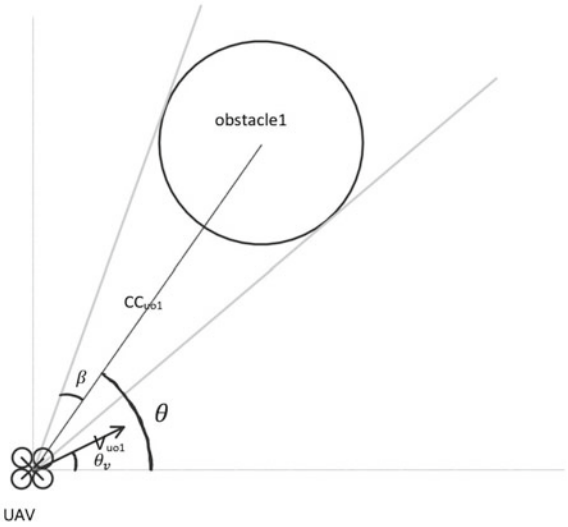

Fig. 6 Definition of angles

2.4 Collision Avoidance Within the Formation

When the formation is split, we must consider the case that UAVs in the formation may collide among themselves. Thus, we must add collision avoidance strategy among UAVs.

In this paper, we also use the method in Sects. 2.1 and 2.2 to avoid collision among UAVs in formation.

First, we should set up a minimum safe distance d_{safe}. When $d < d_{\text{safe}}$ (where d is the distance between two UAVs), the collision between UAVs occurs. The minimum safe distance is dependent on the size of UAV and some other factors. Then we need to set up a threshold of distance d_{th}. When $d < d_{\text{th}}$, the UAVs treat each other as obstacle. The selection of the threshold is important. The threshold must meet the requirement: $d_{\text{th}} > d_{\text{safe}}$. In addition, it cannot be too large considering the formation keeping.

3 Numerical Simulation

In order to verify the effectiveness of the algorithm, we use Matlab & Simulink to simulate.

Table 2 The starting point and target of the UAVs

	Starting point (m)	Target (m)
UAV1	(0, 0, 0)	(250, 250, 250)
UAV2	(−5, 0, 0)	(245, 250, 250)
UAV3	(0, −5, 0)	(250, 245, 250)
UAV4	(0, 0, −5)	(250, 250, 245)
UAV5	(−5, −5, −5)	(245, 245, 245)

3.1 Simulation Conditions

The obstacle detection distance of UAV is set as 500 m. Since rotor drone can hover, the minimum velocity of UAV is set as zero. The maximum velocity is set as 20 m/s. The starting point and target of the five UAVs are shown in Table 2.

3.2 Formation Keeping with Two Obstacles

In this condition, the formation is kept while avoiding obstacle. The radio of obstacle1 is 10 metres and the radio of obstacle2 is 12 metres. The acceleration range of the UAV is: $-3 \leq a_x \leq 3$, $-3 \leq a_y \leq 3$, $-3 \leq a_z \leq 3$. The entire simulation lasts 50 s. Communication delay is 0.1 s.

Figure 7 shows the distance between UAVs and the centre of obstacle1 and Fig. 8 show the distance between UAVs and the centre of obstacle2. Figure 9 shows trajectories of UAVs in the case of formation keeping with two obstacles. We can see from Figs. 7and 8 that the minimum distance between UAVs and the centre of obstacle is bigger than the ratio of obstacle. Therefore, the collision avoidance is successful.

3.3 Formation Splitting

In this condition, the formation can be split while avoiding collision. The radio of obstacle is 10 metres. The acceleration range of the UAV is: $-10 \leq a_x \leq 10$, $-10 \leq a_y \leq 10$, $-10 \leq a_z \leq 10$. The entire simulation lasts 50 s.

The minimum safe distance $d_{\text{safe}} = 1\text{m}$ and the threshold $d_{\text{th}} = 4\text{m}$

We can see from Fig. 10 that the minimum distance between UAVs and the centre of obstacle is bigger than the ratio of obstacle. Figure 11 shows the trajectories of UAVs in the case of formation splitting. In Fig. 12, the distance between UAVs in the formation is greater than 2 m, which is obviously bigger than the safe distance.

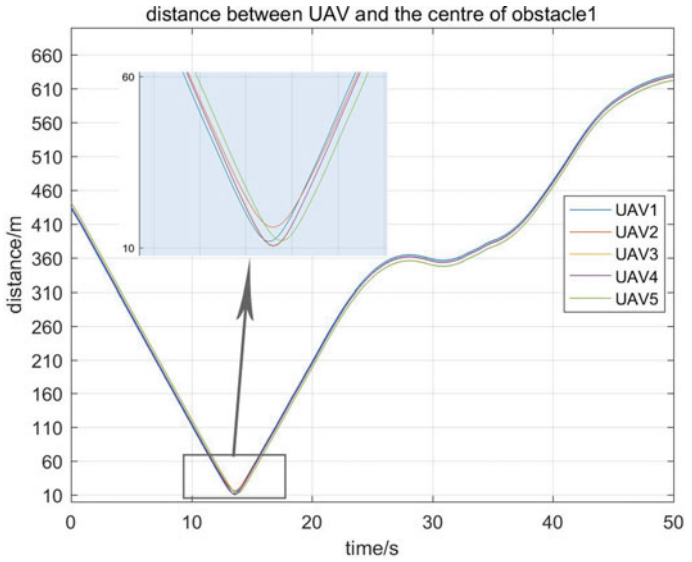

Fig. 7 Distance between UAVs and the centre of obstacle1

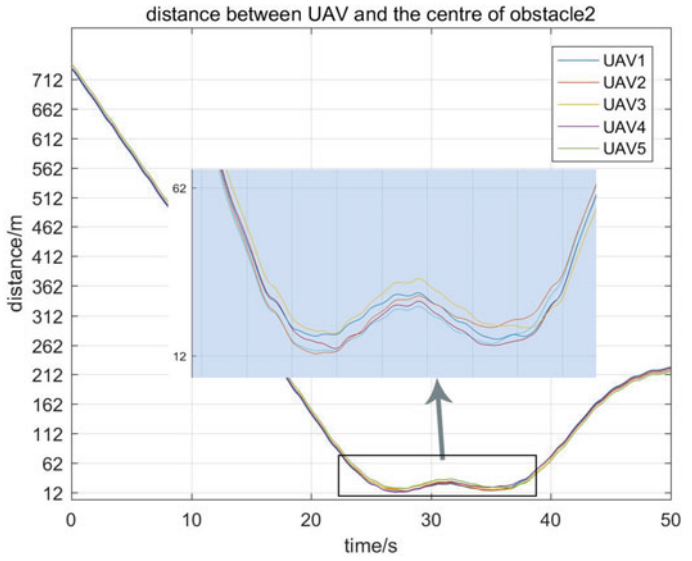

Fig. 8 Distance between UAVs and the centre of obstacle2

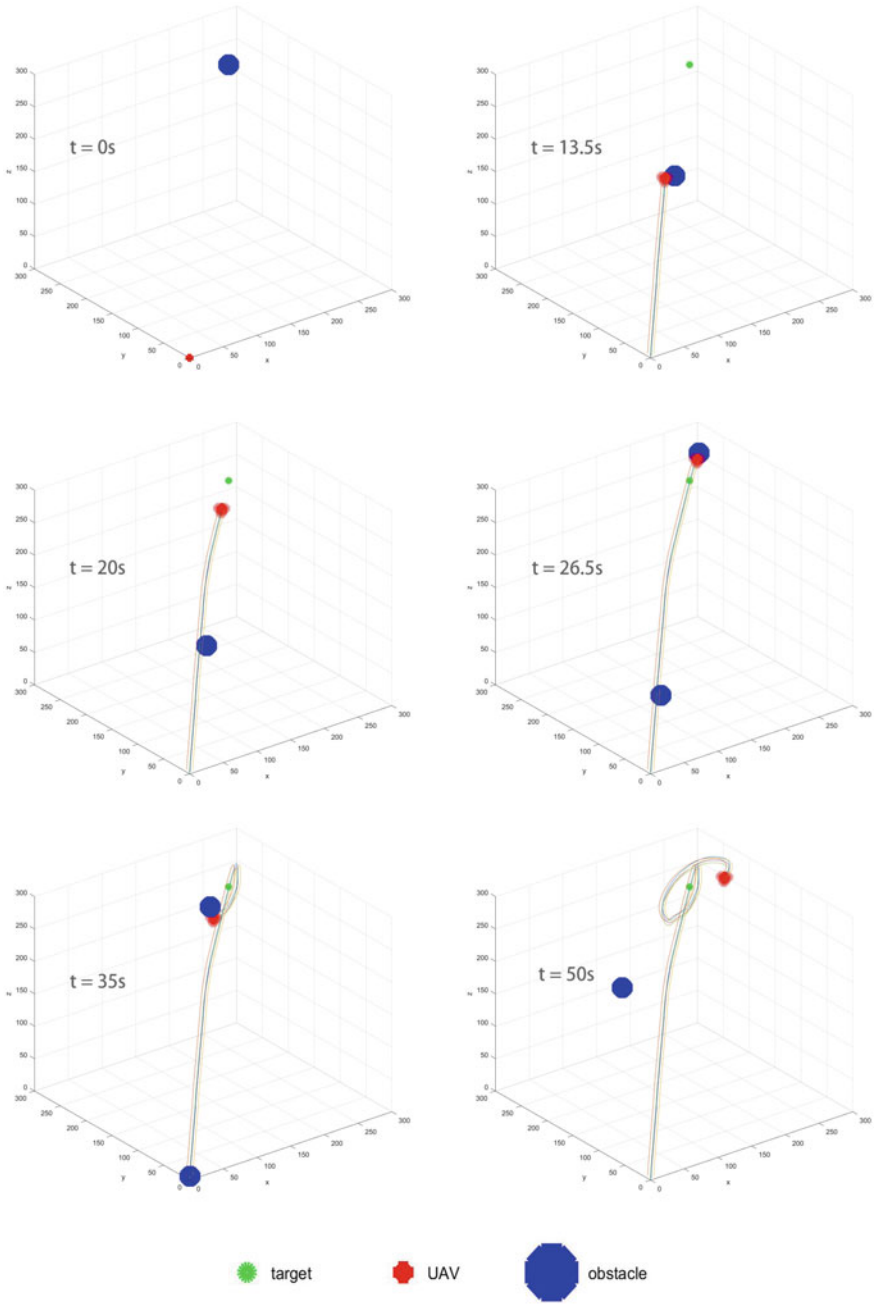

Fig. 9 Trajectories of UAVs in the case of formation keeping with two obstacles

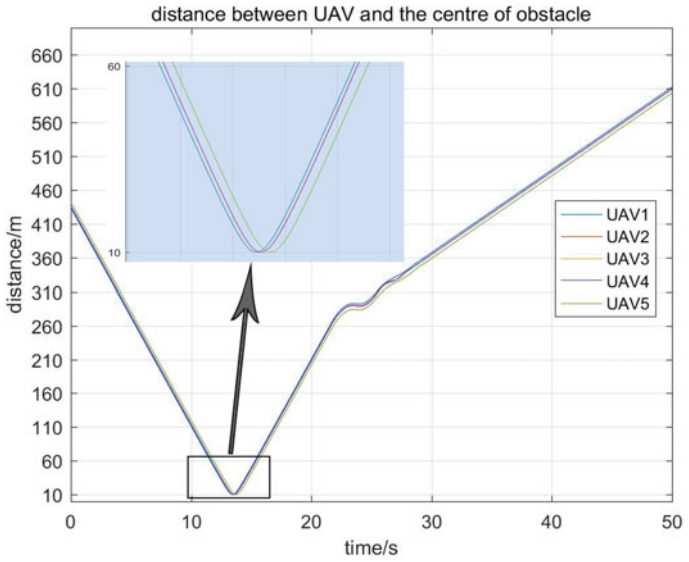

Fig. 10 Distance between UAVs and the centre of obstacle

3.4 Analysis of the Simulation

As shown in Figs. 7, 8 and 10, we can see that this method has a good performance on collision avoidance with external obstacles and can tolerate little communication delay.

While applied in collision avoidance among UAVs in the formation, the distance is much more shorter. This means UAVs need higher acceleration to get good performance. This method is good at obstacles which can be discovered far away from UAVs. When the obstacle is close, the relative size of acceleration and the communication delay has bigger influence on final performance.

4 Conclusion

This paper presents a strategy of collision avoidance between UAV formation and moving obstacles based on the theory of velocity obstacle. The maximum and minimum velocity and acceleration collection can be set up according to the dynamic model and inputs of UAVs. The condition of formation keeping and splitting are both considered. At last, the result of numerical simulation is presented to prove the performance of this method.

Currently, we just give the collection acceleration directly and don't involve a specific model. In addition, we just choose the best acceleration by a simple regulation.

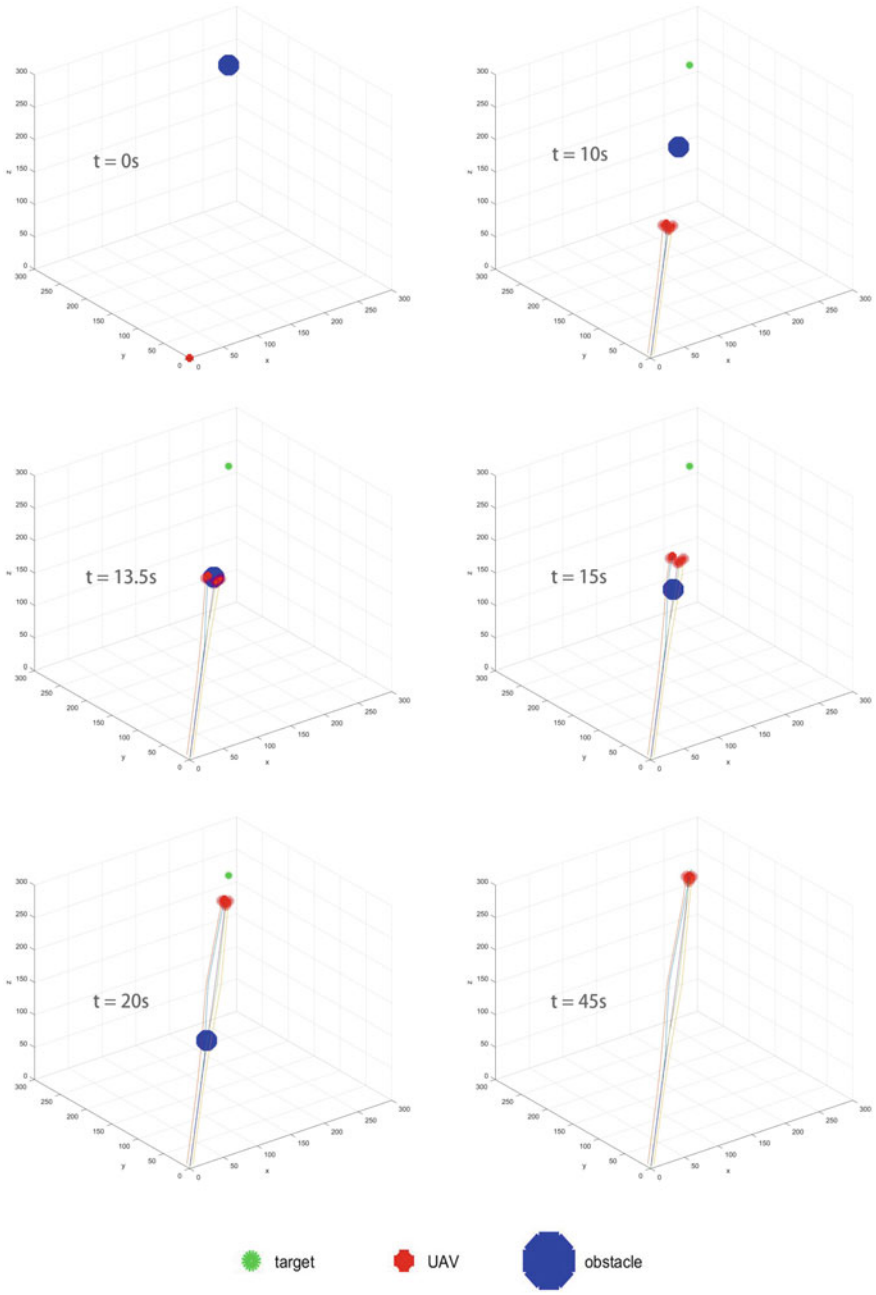

Fig. 11 Trajectories of UAVs in the case of formation splitting

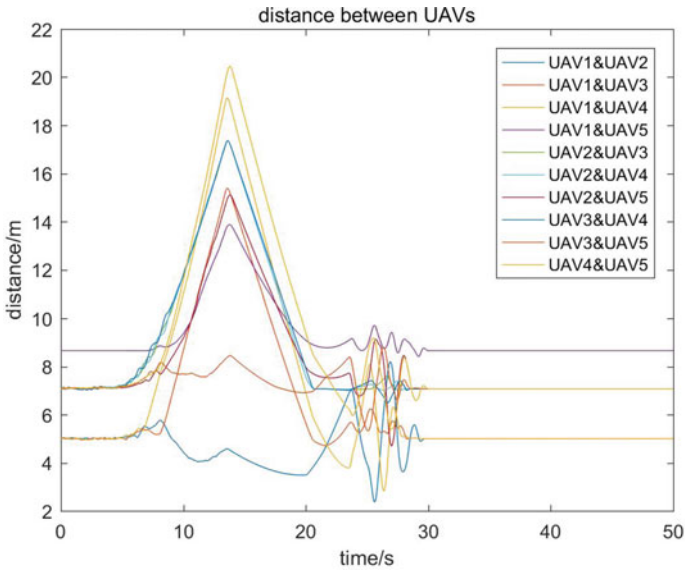

Fig. 12 Distance between UAVs in the formation

In the future, we will combine it with a type of rotor UAV and try to optimise the method of selection based on some other theories to reduce the amount of calculation.

References

1. Han, S. C., Bang, H., & Yoo, C. S. (2009). Proportional navigation-based collision avoidance for uavs. *International Journal of Control, Automation and Systems, 7*(4), 553–565.
2. Wei, R. X., Zhou, K., Wang, S. L., Xiao-Ming, Q. I., & Luo, P. (2015). Uav guidance law for obstacle avoidance in unknown environment. *Systems Engineering & Electronics, 37*(9), 2096–2101.
3. Yang, X. X., Zhang, Y., & Zhou K. K. (2017). Autonomous obstacle avoidance algorithm for UAV in dynamic uncertain environment. *Systems Engineering and Electronics, 39*(11), 2546–2552.
4. Schmitt, L., & Fichter, W. (2014). Collision-avoidance framework for small fixed-wing unmanned aerial vehicles. *Journal of Guidance Control Dynamics, 37*(4), 1323–1329.
5. Cetin, O., & Yilmaz, G. (2016). Real-time autonomous uav formation flight with collision and obstacle avoidance in unknown environment. *Journal of Intelligent and Robotic Systems, 84*(1–4), 1–19.
6. Hafez, A., & Givigi, S. (2016). Formation reconfiguration of cooperative UAVs via learning based model predictive control in an obstacle-loaded environment. In: *IEEE Systems Conference* (pp. 1–8).
7. Ma, X., Jiao, Z., Wang, Z., & Panagou, D. (2016). Decentralized prioritized motion planning for multiple autonomous UAVs in 3D polygonal obstacle environments. In: *Proceedings of the International Conference on Unmanned Aircraft Systems* (pp. 292–300). IEEE.

8. Seo, J., Kim, Y., Kim, S., & Tsourdos, A. (2017). Collision avoidance strategies for unmanned aerial vehicles in formation flight. *IEEE Transactions on Aerospace & Electronic Systems* pp(99), 1–1.
9. Fiorini, P., & Shiller, Z. (1996, April). Time optimal trajectory planning in dynamic environments. In *Proceedings of the 1996 IEEE International Conference on Robotics and Automation* (Vol. 2, pp. 1553–1558). IEEE.
10. Jenie, Y. I., Kampen, E. J. V., Visser, C. C. D., Ellerbroek, J., & Hoekstra, J. M. (2015). Selective velocity obstacle method for deconflicting maneuvers applied to unmanned aerial vehicles. *Journal of Guidance, Control and Dynamics, 38*(6), 1–6.
11. Van, d. B. J., Lin, M., & Manocha, D. (2008). Reciprocal velocity obstacles for real-time multi-agent navigation, 1928–1935.
12. Fulgenzi, C., Spalanzani, A., & Laugier, C. (2007). Dynamic obstacle avoidance in uncertain environment combining PVOs and occupancy grid. In *Proceedings of the IEEE International Conference on Robotics and Automation* (pp. 1610–1616). IEEE.

Detection of Acoustic Emission Signal Due to Impact Damage of Composite Materials Based EMD

Qingwen You, Zhefeng Yu and Jicheng Fang

Abstract Drop-weight impact test and small-mass impact test were carried out on composite laminates. The contact force and AE signal were measured during the tests, and the correspondence between AE signals and damage were analyzed respectively. For the drop-weight impact test, the contact force dropped and the frequency of the AE signal increased suddenly when the delamination appeared. Then the AE signal was decomposed using empirical mode decomposition (EMD). The amplitude anomaly were found in the first several intrinsic mode functions (IMFs), which could be used as a signal to characterize damage.; In the small-mass impact test, the contact force and AE signal were investigated in the same way. Additionally, Fourier transform (FFT) was used to find whether there is delamination. Results reveal that when laminates suffers the drop-weight impact, AE signals, combined with EMD, can be used for real-time health monitoring, For the plates impacted by small-mass objects, AE signal, EMD and Fourier transform can be used to determine whether there is delamination in the laminate.

Keywords Acoustic emission · Composite laminates · Drop-weight test · Small-mass impact test · Health monitor

1 Introduction

1.1 Background

Due to high strength ratio and high stiffness ratio, composite materials are widely used in many fields such as aircraft and ships. On the other hand, composite materials, such

Q. You (✉) · Z. Yu · J. Fang
School of Aeronautics and Astronautics, Shanghai Jiao Tong University, Shanghai, China
e-mail: youqingwen1@163.com

Z. Yu
e-mail: yuzf@sjtu.edu.cn

Z. Jing (ed.), *Proceedings of International Conference on Aerospace System Science and Engineering 2018*, Lecture Notes in Electrical Engineering 549,
https://doi.org/10.1007/978-981-13-6061-9_9

as Carbon Fiber Reinforced Plastic (CFRP), are prone to delaminate after impact, and the compressive strength can be significantly reduced. And the delamination is hardly observed by naked eyes. Therefore, it is important to find a method which can detect the signal of damage. Acoustic emission (AE) is a technique for detecting and analyzing damage by detecting AE signals. Since the composite material generates elastic waves when damage appears, the abnormal signal can be detected non-destructively. Then we can find whether there is delamination or not.

When the composite material is impacted by foreign objects, the response mode of the plate is divided into two types: large mass impact and small-mass impact according to the mass ratio of the foreign object and the composite material. When the mass ratio is greater than 2, the plate is dominated by a quasi-static response. In this case, the impact history is long and the propagation of the bending wave is affected by the boundary. The contact force and displacement change synchronously [1, 2]. While if the mass ratio is less than 0.23, a small-mass impact yields. In this situation, the plate has a wave control response, and the bending wave propagation is not affected by the boundary. The contact force and the displacement of the plate are not synchronized. When the airplane takes off and lands, the skin of its structure is extremely vulnerable to impact by stones, other debris and so on. These are small-mass impact problem. Therefore, it is of great practical significance to study the small-mass impact of composite laminates. Ye Wenxun [3] measured the contact force of small-mass impact by a "mouse-trap" hammer machine. It was also found that when the force gradually rises to a certain value, the laminate would delaminate and then the delamination expands rapidly. The force at this time is called the delamination threshold load (DTL). Therefore, the sudden drop of contact force can be a characteristic of the delamination.

When the laminate is impacted by a foreign object, it may undergo various damages such as matrix cracking, delamination, fiber breakage, etc. And the AE signals corresponding to these failure modes have different frequencies [4]. The methods used for detecting these damage include C-scan, X-ray, acoustic-ultrasonic detection, and AE detection. AE detection is an effective dynamic health monitoring technology. Analysis of AE signals can be used to distinguish matrix cracking, delamination, and fiber breakage. The whole process of the damage evolution can be characterized through the parameters of the AE signal. Chen Hao [5] studied AE signal due to an impact on resin-based laminates with a low speed, and summarized the parameters of different damage models by studying the distribution rules of high-energy damage points. Ajit Mal [6] studied the influence of the position of the AE sensor when composite materials is impacted with a low speed. Mikael Johnson [7] compared the experimental results and numerical simulation results of the matrix damage evolution of composite materials, and found that the simulation results are quite different due to the complex damage. Tao Fu [8] and José Martínez-Jequier [9] conducted a three-point bending experiment on the composite material and analyzed the AE signal. They believed that the AE signal can be used for real-time health monitoring of delamination. Efe Selman [10] conducted fatigue tests on composite cement beams and found that the AE signal is in good agreement with the Sentry Function. Through the buckling experiment, John P. McCrory [11] classify the types of damage in the

composite according to the AE signal. YANG Yu [12] made a compression test on the damaged composite panel after impact and analyzed the AE signal. It is believed that the main form of damage is fiber fracture rather than delamination.

The abnormal signals can be identified by wavelet decomposition [13] and empirical mode decomposition(EMD). Sun Liying found that the intrinsic mode function (IMF) decomposed by EMD technology can be used to find the position of leaked on the pipeline precisely according to the occurrence time of the abnormal signal [14]. By combining EMD technology and wavelet decomposition technology, Zhao Lifeng [15] determined the local damage on the bearing effectively.

From the above research, it can be found that current researches on AE signal of composite materials mainly focus on the static experiments of composite materials, while the impact experiments are relatively less. The AE studies of small-mass high-speed impact are even few. In this paper, composite plates were undergone drop-weight impacts and the small-mass impacts. The EMD technique was used to analyze the AE signal to find the time when composite damage occurs. Finally, the AE signal was compared with the contact force under different impact energies to achieve real-time monitoring of composite damage.

1.2 EMD Technology

EMD is proposed by Huang, N.E [16], in which it is believed that signals can be decomposed into several IMFs and a residual. Different orders of IMF represent the dynamic characteristics of the signal, while the residual reflects the offset of the signal. EMD technology is adaptive, and IMF can be automatically selected by analyzing the signal itself. Therefore, EMD technology is widely used.

The specific steps of EMD technology are as follows:

(1) Assuming that the original signal is $x(t)$, connect all the maxima and minimum points of $x(t)$ by cubic spline to form the upper and lower envelop. The mean of the upper and lower envelopes is defined as $m_1(t)$, and $h_1^1(t)$ is defined as:

$$h_l^1(t) = x(t) - m_1(t) \tag{1}$$

$h_1^1(t)$ is an IMF if it satisfies the following two conditions:

(1) The number of extreme points is equal to the times that the $h_1^1(t)$ across zero axis or the difference of them is equal to 1.
(2) The upper and lower envelopes at any point equal 0.

If $h_1^1(t)$ is the first order IMF $\text{imf}_1(t)$, the calculation goes to step (2). Otherwise $h_1^1(t)$ is treated as $x(t)$, then the above process will be repeated.

(3) Repeat the above steps using the difference between $h_1^1(t)$ and $\text{imf}_1(t)$ as the new signal until the Nth order IMF or the residual is less than pre-set value, or is monotonic. Then can be represented as follows:

$$x(t) = \sum_{i=1}^{n} \mathrm{imf}_i(t) + r_n(t) \tag{2}$$

where $\mathrm{imf}_n(t)$ is the Nth order IMF, $r_n(t)$ is the residual.

2 Impact Experiment

2.1 Drop-Weight Impact Test

The CFRP specimen for drop-weight impact test has a size of 150 × 100 × 3 mm. The impact device is the INATRON CEAST-9350 drop hammer impact tester. The diameter of the hammer is equal to 16 mm, and the weight is 5.3 kg. The impact energy can be changed by adjusting the dropping height of hammer.

The specimen is installed on the support bracket and fixed with clamps. The AE sensor is mounted 5 mm from the impact point, as shown in Fig. 1. Special coupling agent is scribbled between the sensor and plate, and the sensor is fixed by tape to make them contacted tightly. The signal collected by the AE sensor is amplified and recorded at the frequency of 1 MHz. The contact force and AE signals were collected when the impact energy equals 1.1, 1.6, 4, 6, 8, 12, and 15 J respectively.

2.2 Small-Mass Impact Test

The specimen for small-mass impact has a dimension of 240 × 240 × 1.5 mm, and the impact point is located at the center of the plate. The impact equipment is

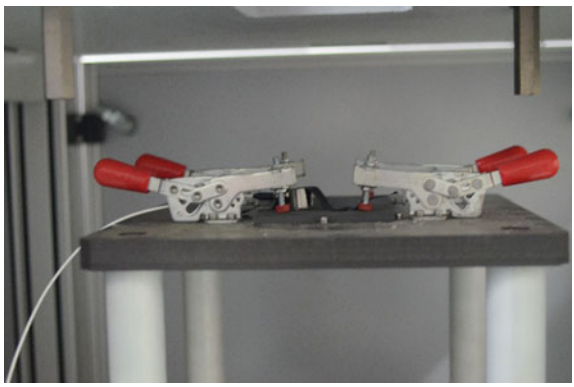

Fig. 1 The composite plate and AE sensor

a multi-angle "mouse-clip" hammer machine and the hammer weights 20 g. It can simulate the case when a small-mass hammer impact a plate freely in a high speed. During the experiment, the rocker arm is wrenched to drive the spring to twist. When the rocker arm is released, the rocker arm accelerates under the driving of the spring. When the rocker arm swings to the horizontal position, it is blocked by the bump, and the rocker arm stops moving. The hammer and the rocker arm are connected by a thin steel wire. The hammer continues to move downward due to inertia, and then impacts the laminate. Different energy can be stored in the spring when the angles of spring change. When the hammer is released, different impact speeds can be achieved, and then the corresponding impact energy can be calculated (Fig. 2).

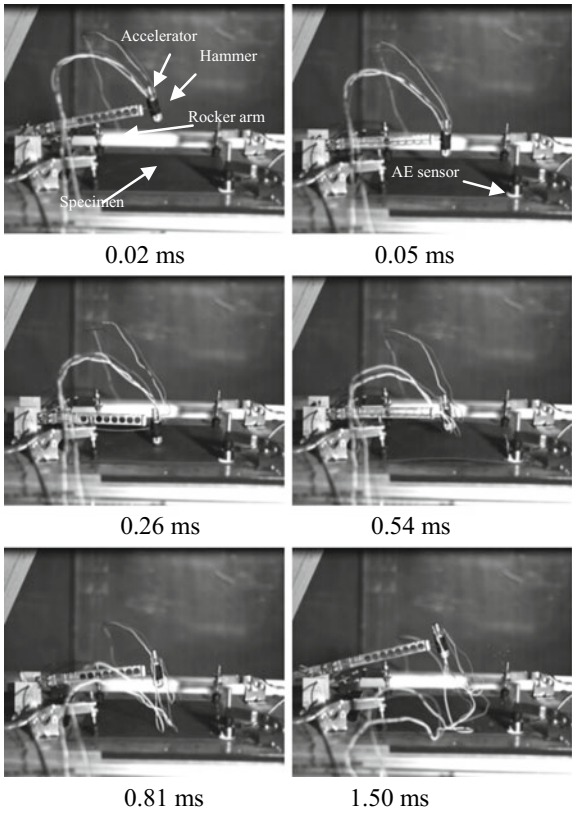

Fig. 2 Small-mass impact at various stages

3 Results

3.1 Drop-Weight Impact Test

The contact force and the AE signal obtained by the drop-weight impact test are shown in Figs. 3, 4, 5, 6, 7, 8 and 9.

After the impact, the specimen was non-destructive inspected with ultrasonic scanning. It was found that when the impact energy equals 1.1 J, the specimen didn't delaminate. When the impact energy equals 1.6 J, the delamination occurred, but the damage area was small, while other specimens delaminates obviously. It can be seen from Fig. 3 that when the impact energy equals 1.1 J, the contact force is smoother except for slight fluctuations at the beginning. However, we can find that, in Fig. 4, when the impact energy equals 1.6 J, a sudden drop occurs when the contact force reaches the maximum at 3 ms. The corresponding force is about 2600 N, which is the delamination threshold load. The sudden drop in contact force is caused by rapid decrease of the stiffness of the laminate after delamination.

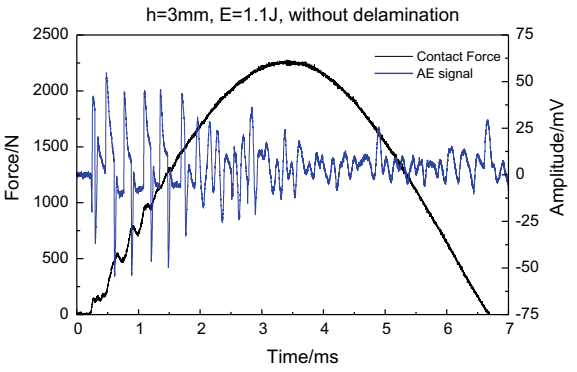

Fig. 3 Force and AE signal (E = 1.1 J)

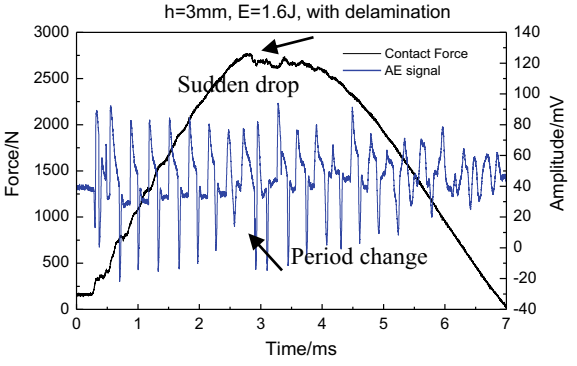

Fig. 4 Force and AE signal (E =1.6 J)

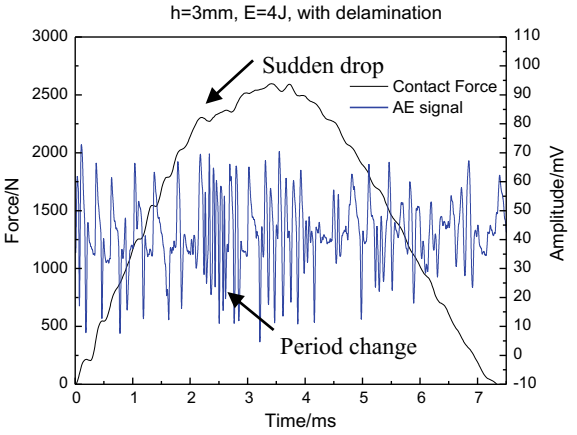

Fig. 5 Force and AE signal (E = 4 J)

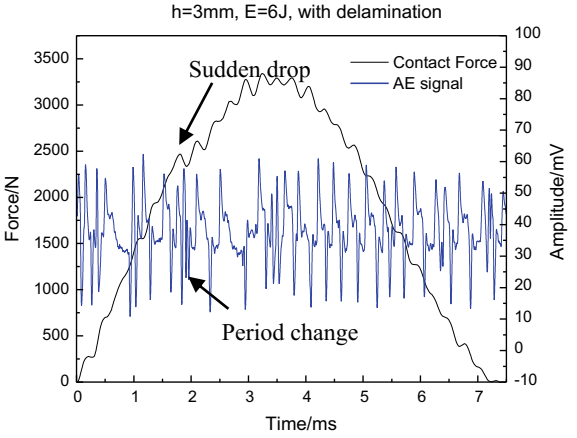

Fig. 6 Force and AE signal (E = 6 J)

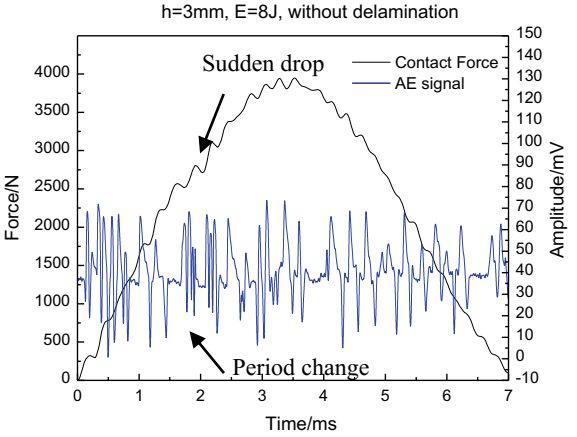

Fig. 7 Force and AE signal (E = 8 J)

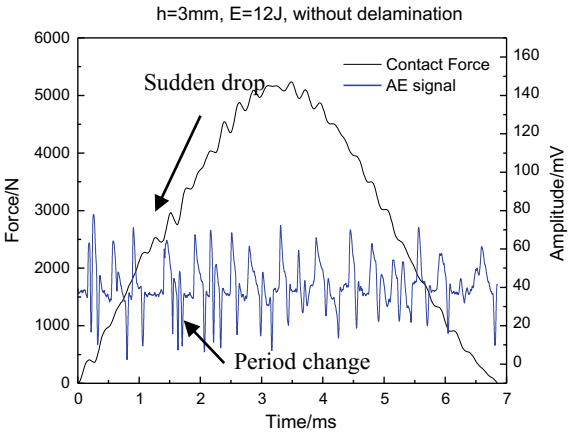

Fig. 8 Force and AE signal (E = 12 J)

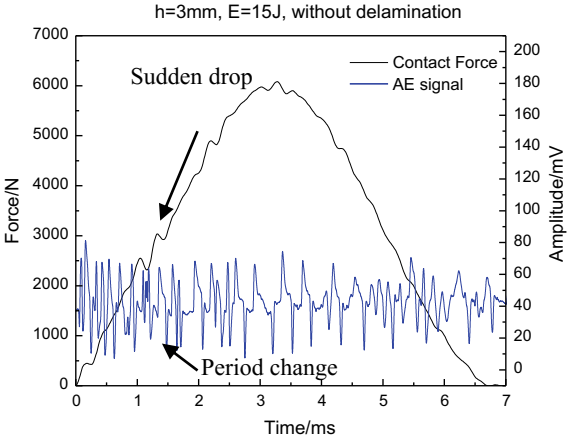

Fig. 9 Force and AE signal (E = 15 J)

Similarly, when the impact energy equals 4, 6, 8, 12 and 15 J, respectively, the contact force in Figs. 5, 6, 7, 8 and 9 has a sudden drop near 2600 N, and then continues to increase to the maximum. Therefore, it can be concluded that when the contact force reaches 2600 N, the laminate would delaminate in the case of big mass impact.

Comparing the AE signals under different impact energies, we can find that when the plate delaminated, a high-frequency signal appears in the AE signal. What's more, the sudden drop in contact force matches well with the high-frequency signal in AE, as shown in Figs. 4, 5, 6, 7, 8 and 9. The IMFs obtained by decomposing the AE signal when the impact energy equals 1.1 and 1.6 J are shown in Figs. 10 and 11.

On the other hand, the failure modes of composite materials can be mainly divided into two categories, namely high-frequency brittle failure mode and medium-low frequency plastic failure mode. The low-frequency brittle mode mainly refers to the cracking of the matrix after impact, while the medium-high-frequency plastic

mode mainly refers to the friction between the fiber bundles, delamination, etc. [17]. Therefore, regardless of the magnitude of the impact energy, the IMF1 decomposed by the AE signal will have an abnormal signal at the beginning, which is due to the matrix cracking.

When the impact energy equals 1.1 J, the plate is not damaged. Therefore, the signal decomposed in Fig. 10a is the noise signal, and the frequency is high, while the amplitude is small. In Fig. 10a, the decomposed IMF1 has an abnormal signal at the beginning, which is a signal from the cracking of the matrix. When the impact energy equals 1.6 J, the composite material has minimal damage. In Fig. 11a, there is an abnormal signal around 3 ms, and the amplitude is large, which is the signal of the delamination, as indicated by the arrow. Figures 11b, c show the noise signals with higher frequency and smaller amplitude. At the same time, the summation of other order IMFs of 1.1 and 1.6 J are shown in Figs. 10d and. 11d. It can be seen that except for the first three order IMFs, which have a large amplitude, the summation of other IMFs' amplitude is small, which can be regarded as a normal state.

When the impact energy rose to 4 J, the amplitude of the singular point due to the damage of the composite is much larger than the noise, so the IMF1 decomposed has

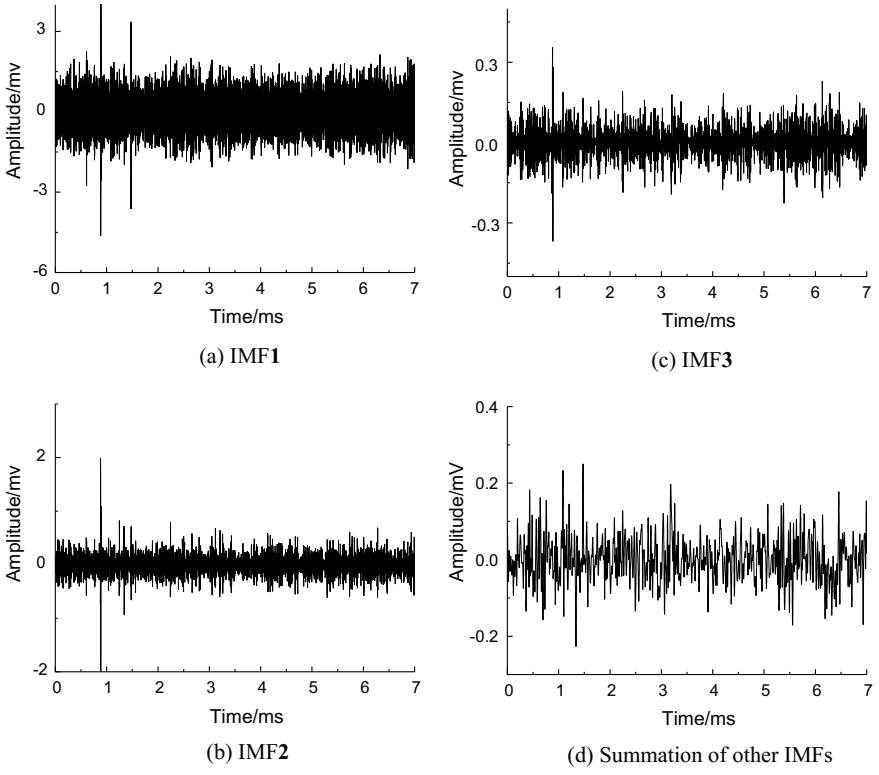

Fig. 10 IMFs (E = 1.1 J)

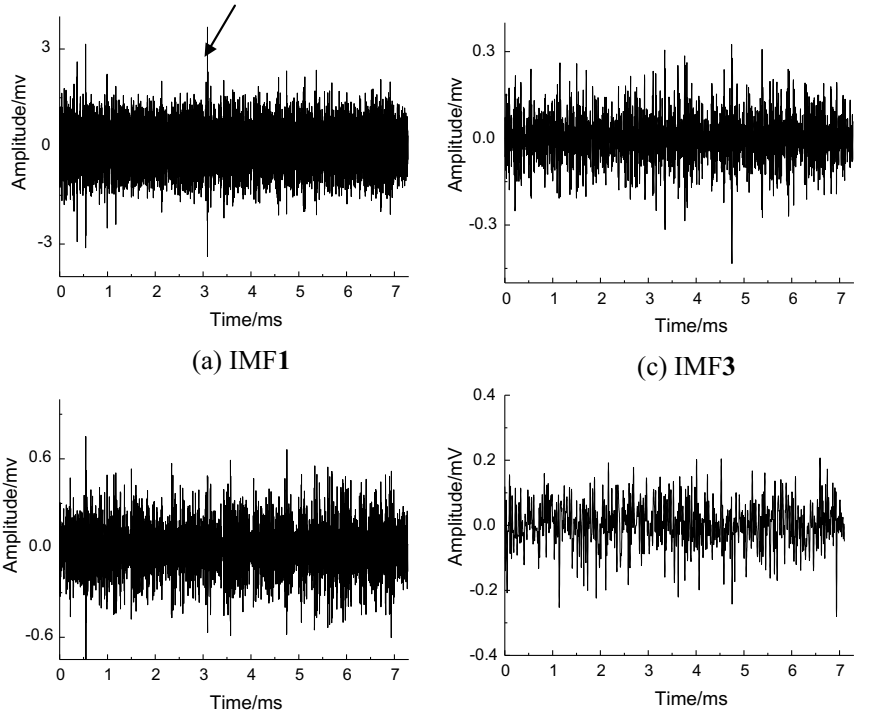

Fig. 11 IMFs (E = 1.6 J)

a higher amplitude and a smaller frequency, as shown in Fig. 12a. Simultaneously, it can be found that due to the obvious delamination damage of the specimen when the impact energy equals 4 J, a fairly obvious abnormal signal can be seen in the first 3 orders of the IMF, as shown in Fig. 12, which is different from that of 1.6 J.

Therefore, when the damage is larger, the abnormal signal is more obvious in the decomposed IMFs, and this feature can characterize the health monitoring signal. The IMF1 s of decomposed AE signal of 6 J ~ 15 J are shown in Figs. 13, 14, 15 and 16.

When the impact energy is gradually increased to 6, 8, 12 and 15 J, as shown in Figs. 13, 14, 15 and 16, the abnormal signal at the beginning of IMF1 is more obvious, that is, the cracking damage of the matrix at the beginning is more obvious. On the other hand, a continuous, high amplitude signal, as indicated by the arrow in Figs. 13, 14, 15, and 16, is caused by delamination, and the time between the abnormal AE signal and the point of the contact force is synchronous.

When the impact energy equals 4 and 8 J, respectively, it can be found that the signal of IMF1 is relatively stable after the first abnormal signal appears, however, as the impact energy increases, it can be found that after the first abnormal signal

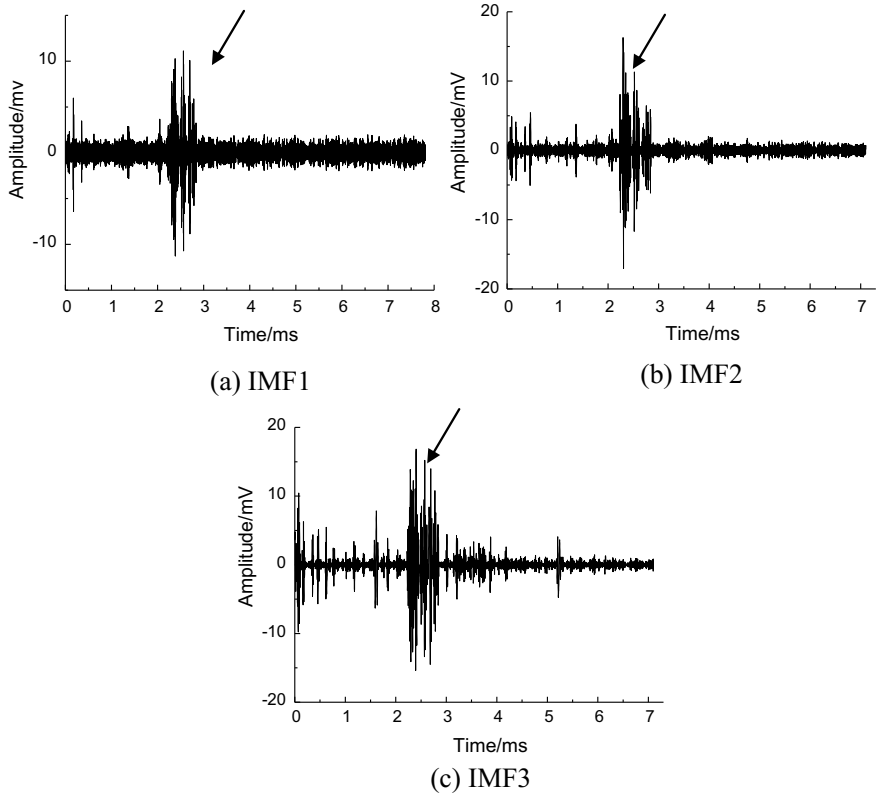

Fig. 12 IMFs (E = 4 J)

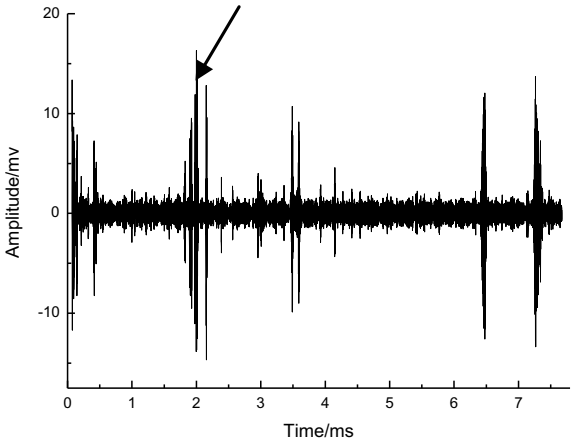

Fig. 13 First IMF (E = 6 J)

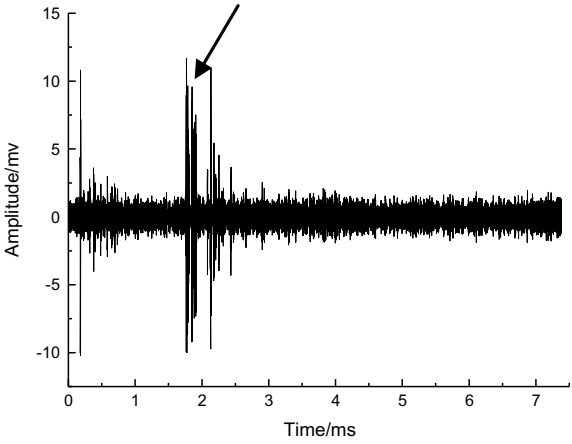

Fig. 14 First IMF (E = 8 J)

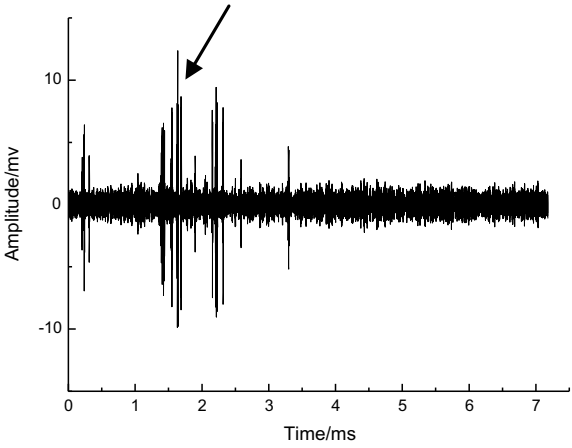

Fig. 15 First IMF (E = 12 J)

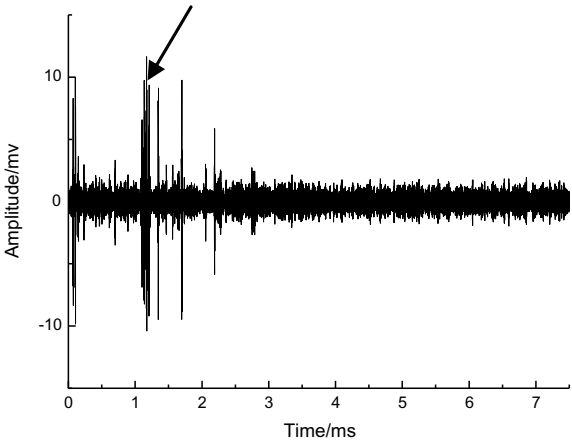

Fig. 16 First IMF (E = 15 J)

appears in IMF1, there are more abnormal signal points when the impact energy equals 6, 12 and 15 J, because matrix damage, new delamination and other complex damage appears after the first delamination.

In addition, the period of various energies are almost equal in drop-weight impact test. When the impact velocity is large, the contact force reaches the delamination threshold force earlier, and the time when the acoustic emission signal shows abnormal is also earlier, which can also help to determine the impact energy. Combined with other measured physical quantities, the AE signal can be used to identify the impact event and determine the damage situation.

3.2 Small-Mass Impact Test

In the small-mass impact test, when velocities are 5.4 and 24 m/s, the corresponding impact energies equal 0.33 and 6.3 J, respectively. The contact force and AE signals are shown in Figs. 17 and 18.

It can be seen from Figs. 17 and 18 that when the impact energy equals 0.33 J, the force curve is smooth before reaching the maximum value, and after reaching the maximum value, the contact force is slowly decreased. However, when the impact energy equals 6.34 J, the force curve has a sudden drop before reaching the maximum value, and then the force rises with oscillation before reaching the maximum due to new delamination and delamination expansion. Ultrasonic non-destructive checking after impact showed that the laminate did not delaminate at the impact energy of 0.33 J, while the laminate was delaminated when the impact energy equals 6.34 J.

By observing the relationship between the AE signal and the force in Figs. 17 and 18, it can be found that when the impact energy equals 0.33 J, the plate didn't delaminate, and at the same time, it can be seen that the frequency of AE signal does not change suddenly and the IMFs decomposed by EMD has no abnormal point, as

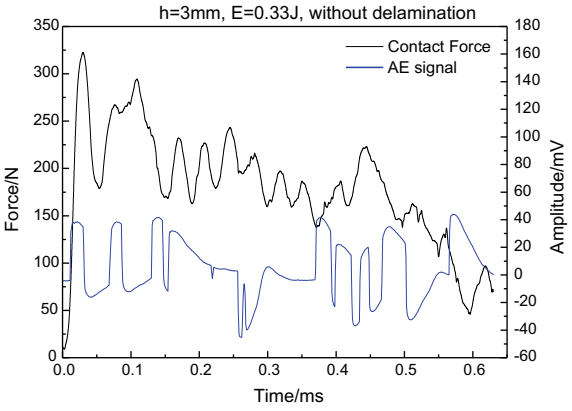

Fig. 17 Force and AE signal (E = 0.33 J)

shown in Fig. 19. As the impact energy increase to 6.34 J, when the contact force reaches 1000 N, a sudden drop occurs and the delamination begins. It is obvious that more high-frequency components appear in the AE signal, as shown in Fig. 18. The frequency of the IMF1 is higher when the impact energy is large. However, as can be seen from Fig. 20, when the force suddenly drops, the characteristics of the high-frequency signal of the AE signal are not obvious. A series of high-frequency AE signal appears when the plates delaminate, and the starting moment represents the moment when damage occurs, but this moment is not obvious. Furthermore, the period of small-mass impact is short, so it's not precise to judge the specific moment and the critical load of delamination. Moreover, when the impact velocity is higher, the impact period is even shorter.

The Fourier transform of the IMF1 is shown in Fig. 21. When the impact energy equals 0.33 J, as shown in Fig. 21a, the maximum amplitude is obtained at a frequency of 500 kHz, which is the high-frequent brittle failure signal generated by the broken of the matrix and signal noise. And other frequency segments have smaller amplitudes.

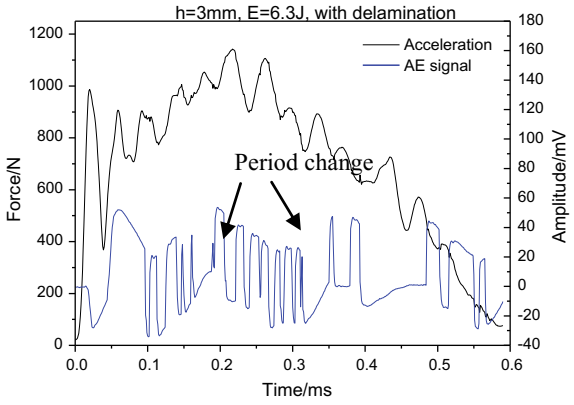

Fig. 18 Force and AE signal (E = 6.3 J)

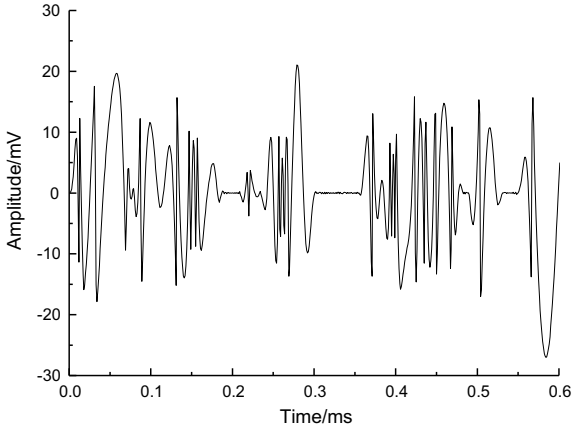

Fig. 19 First IMF (E = 0.33 J)

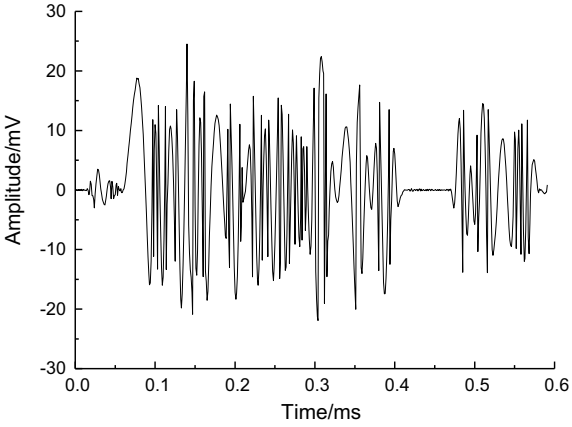

Fig. 20 First IMF (E = 6.3 J)

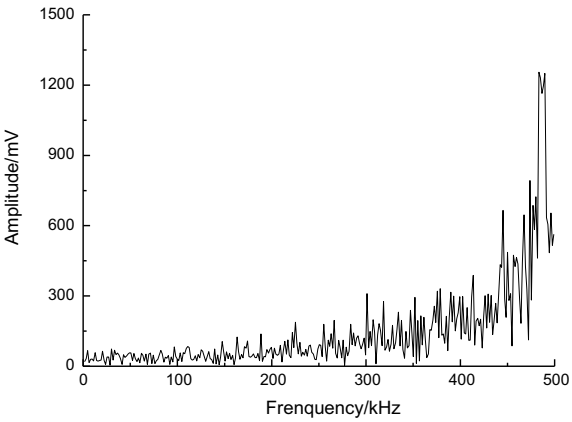

(a) E=0.33 J

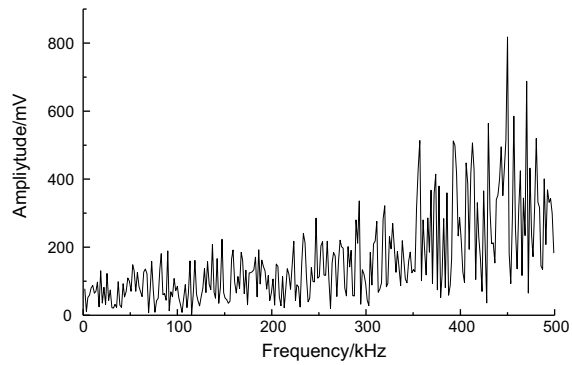

(b) E=6.3 J

Fig. 21 Frequency domain of IMF1

While as shown in Fig. 21b, it can be found that the signal with the largest amplitude appears in the frequency range of 450 kHz when the impact energy equals 6.3 J, mainly due to the delamination and friction between the fibers.

4 Conclusion

The drop-weight impact and the small-mass impact were carried on the laminate. The impact force was directly measured with the drop-weight machine and the "mouse-trap" hammer, and the AE signal emitted during the impact was measured by the AE sensor. By comparing force signals and acoustic signals we can find that:

(1) By measuring the contact force, we can find that the contact force will suddenly drop when the contact force reaches the delamination threshold force, in both large mass impact and small-mass impact.
(2) By comparing the contact force and the AE signal, it can be found that when the plate delaminates, the frequency of the AE signal suddenly increases, and IMFs decomposed by the EMD has an obvious abnormal point. So the AE signal can be chosen as a real-time reference for health monitoring.
(3) In the drop-weight impact test, if there is no abnormal point other than one which is generated when the hammer touches the specimen, the plate didn't delaminate. If the impact energy is high enough, simultaneously, there is another abnormal signal in other order IMFs beside IMF1, which can be regarded as a character of composite material damage.
(4) In the small-mass impact test, since the impact time is short, the real-time health monitoring in the time domain is not precise. But the decomposed IMF1 can be analyzed in frequency domain. If the amplitude of the low-mid frequency signal is high, it can be judged that the composite material is delaminated.

References

1. Olsson, R. (2000). Mass criterion for wave controlled impact response of composite plates [J]. *Composites: Part A, 31*(8), 879–887.
2. Zheng, D., & Binienda, W. K. (2007). Effect of permanent indentation on the delamination threshold for small mass impact on plates [J]. *International Journal of Solids and Structures, 44,* 8143–8158.
3. Wenxun, Y., Zhefeng, Y., Baojun, N., et al. (2017). Contact force measurement and response to damage of composite laminates subjected to small-mass impact [J]. *Science Technology and Engineering, 17*(24), 13–19.
4. Mahdian, A., Yousefi, J., Nazmdar, M., et al. (2016) Damage evaluation of laminated composites under low-velocity impact tests using acoustic emission method [J]. *Journal of Composite Materials*, *51*(4).
5. Hao, C., Xiaoyan, T., Leijang, Y., et. al. (2010). Acoustic emission characteristics of composite laminates under low velocity impact[J]. *Mechanical Science and Technology for Aerospace Engineering*, *29*(11), 1557–1560.

6. Mal, A. K., Shih, F., Banerjee, S. (2003). Acoustic emission waveforms in composite laminates under low velocity impact [J]. *Proc Spie,* 5047.
7. Johnson, M., Gudmundson, P., Johnson, M., et al. (2001). Experimental and theoretical characterization of acoustic emission transients in composite laminates [J]. *Composites Science & Technology, 61*(10), 1367–1378.
8. Fu, T., Liu, Y., Li, Q., et al. (2009). Fiber optic acoustic emission sensor and its applications in the structural health monitoring of CFRP materials[J]. *Optics and Lasers in Engineering, 47*(10), 1056–1062.
9. Martínez-Jequier, J. (2015). Real-time damage mechanisms assessment in CFRP samples via acoustic emission Lamb wave modal analysis [J]. *Composites Part B*, *68*(4), 317–326.
10. Selman, E., Ghiami, A., & Alver, N. (2015). Study of fracture evolution in FRP-strengthened reinforced concrete beam under cyclic load by acoustic emission technique: An integrated mechanical-acoustic energy approach [J]. *Construction and Building Materials, 95,* 832–841.
11. Mccrory, J. P., Al-Jumaili, S. K., Crivelli, D., et al. (2015). Damage classification in carbon fibre composites using acoustic emission: A comparison of three techniques[J]. *Composites Part B Engineering, 68*(5), 424–430.
12. Yang, Y., Sun, X., Yang, S., et al. (2012). Experimental study on compressive failure mechanism of low-velocity-impact-damaged composite aminates[J]. *Acta Materiae Compositae Sinica*, *29*(3):197–202.
13. Zhang, D.L., Xu, D.G., wang, Y. (2000). Demarcation in space domain for local flaw signals of wire ropes and feature extraction in frequency domain based on wavelet transform [J].*ACTA ELECTRONICA SINICA*, (07), 59–62.
14. Sun, L. Y., Li,Y. B., Qu, Z. G., et al. (2007). Study on acoustic emission detection for pipeline leakage based on EMD signal analysis method [J]. *Journal of Vibration and Shock*, *26*(10), 161–164.
15. Lifeng, Z., Xiaoliang, Z., & Jie, S. (2003). Application of EMD and wavelet transform to the detection of signal singularity [J]. *Journal of Ocean University of Qingdao, 33*(5), 759–763.
16. Huang, N. E., et al. (1998). The empirical mode decomposition and the Hilbert spectrum for nonlinear and non-stationary time series analysis. In *Proceedings of the Royal Society Lond*. A, *44*, p 903–995.
17. Shi, Y., Jin-yang, Z., Xia-mei, L. U., et al. (2014) Low-velocity impact response of 3D braided composites by acoustic emission[J]. *Journal of Materials Engineering*, (7), 92–97.

Mathematical Modeling of Heat Transfer Processes in a Wall with a Regular Pseudo-pore Structure

P. Starikov, A. Ionov, S. Seliverstov, I. Borovik and A. Matushkin

Abstract Porous and pseudo-porous structures are widely used in many areas of life, such as medicine, construction and, of course, the aerospace industry. The main advantages of this concept are its weight and economic efficiency, since the use of this method allows using much less material than using hollow structures to obtain similar force structures. However, it is difficult to implement such structures using traditional manufacturing techniques, such as stamping, casting or machining. This is only possible with the use of additive technologies. Filler technology is widely used in the aviation industry, especially in the manufacture of certain engine parts, with the exception of the combustion chamber. Thus, the implementation of porous or pseudo-porous structures using additive technologies can provide the production of structures with fundamentally new properties that can be used in GTE, for example, for more efficient cooling of combustion chambers. In this study, analysis of various spatial structures is performed using a segment with dimensions of 100 mm × 50 mm × 1 mm as an example. In terms of design both classical design methods and specialized software for additive technologies (Materialize Magics and Autodesk Netfabb). For design options in the Ansys CFX CFD package, the characteristics of the heat transfer process in the wall and in the surrounding space are defined. All designs are built with the possibility of their implementation on the existing equipment laser sintering of metal powders (layer deposition). The next stage of the work will be the verification of the calculated results carried out in a model experiment using SLA prototypes and a thermographic study of the thermal state of the wall.

Abbreviations and Acronyms

AM Additive Manufacturing
CFD Computational Fluid Dynamics

P. Starikov (✉) · A. Ionov · S. Seliverstov · I. Borovik · A. Matushkin
School of Propulsion Engineering, Moscow Aviation Institute (National Research University), Moscow, Russia
e-mail: starikov.p@outlook.com

Z. Jing (ed.), *Proceedings of International Conference on Aerospace System Science and Engineering 2018*, Lecture Notes in Electrical Engineering 549,
https://doi.org/10.1007/978-981-13-6061-9_10

FEM Finite Element Method
GTE Gas Turbine Engine
R&D Research and Development
SLA Stereolithography
SLM Selective Laser Melting

1 Introduction

When designing an engine, the combustion chamber is usually not given the proper attention it deserves. Many believe that the main problems in designing a jet engine are a compressor, a turbine and bearings—this is wrong. The real problem is the combustion chamber. Optimization of the combustion chamber is not only to minimize fuel consumption either burn the turbine. No, a good combustion chamber is the main key factor for the operation of a jet engine in general (Fig. 1).
Here are the main reasons:

If the combustion is uneven in certain parts of the flow of the combustion chamber is not heated to the required air temperature. Enthalpy is only slightly increased, and as a result, works little with the flow of the turbine. To compensate for this deficiency, the rest of the air must become much hotter as it flows through the turbine. This uneven temperature distribution leads to an uneven velocity distribution in the guide blades of the turbine and, consequently, to poor overall efficiency. In the worst case, this means that the jet engine will not work at all [1].

Even if the combustion is consistent, problems may arise. The purpose of the combustion chamber is to heat the compressed air. Hot air can then be processed more when its flow and pressure drop occur than is required to compress it. However, if the air is heated during a pressure drop, there will be no effect. This means that combustion should be as closed as possible in the area of the combustion chamber. If the flame front is too long and reaches the turbine zone, the flow continues to heat up. This is undesirable because it leads to the fact that the overall temperature of the stream increases to such an extent that the turbine overheats and burns.

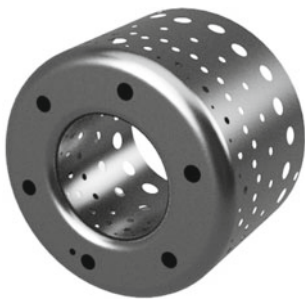

Fig. 1 Example of GTE combustion chamber

Many parameters have an important effect on combustion. Among which fuel is used, fuel delivery method and air flow.

Unfortunately, it is very difficult to determine the cause of the problems in the combustion chamber. The only solution to this dilemma is to conduct systematic experiments and test various designs. However, after many experiments and with the help of a large number of expert advice, an extremely comfortable combustion chamber was developed [2].

1.1 Cooling the Walls of the Combustion Chamber GTE

The GTE combustion chamber operates in very difficult conditions, since the combustion process occurs at high temperatures in an oxidizing environment. The presence of large temperature gradients, sharp thermal shocks. When starting, stopping and changing the operating mode of the engine, large thermal stresses occur in the details of the combustion chamber and the presence of free oxygen at high temperatures leads to gas corrosion and wall fading. Resource combustion chamber determines the resource of the entire engine. In order to provide the necessary resource of the flame tube, the next series of design and technological measures is visible. Currently, there are new, more efficient cooling systems, such as cooling film with irrigation, perforated cooling with irrigation, convection-film cooling. The principle is shown in Fig. 2.

External cooling of the film remains one of the effective methods of thermal protection of the combustion chamber wall. The traditional system of cooling film surfaces in the form of a set of discrete inclined round holes made in the cooled

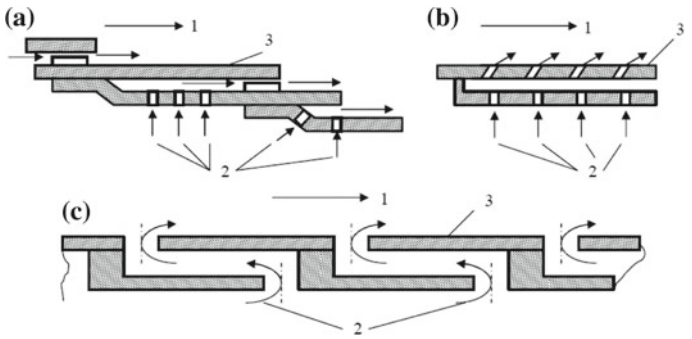

Fig. 2 Systems of combustion chamber cooling

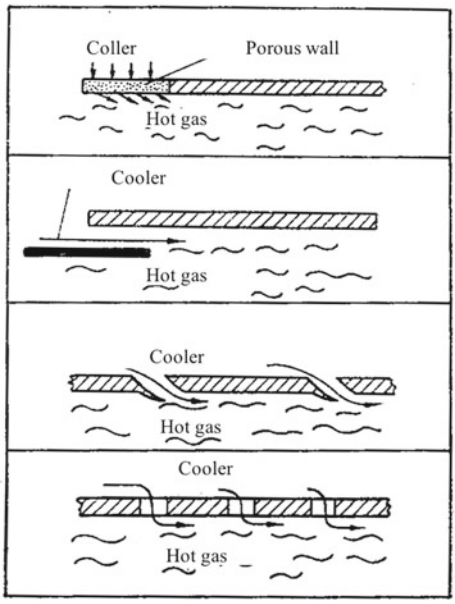

Fig. 3 Ways to organize barrier cooling

wall, is characterized by a number of disadvantages. The main one is low efficiency, caused by the appearance of secondary vortex structures that destroy the coolant film and contribute to the intense suction of the hot stream to the protected surface. In order to reduce these phenomena and improve the spatial uniformity of cooling in the United States and other countries, for several years new configurations of film cooling with openings of a complex (profile) profile have been actively studied: fan-shaped, cantilevered and some others. However, the implementation of such holes with a size of less than one millimeter requires expensive technological equipment and is associated with certain difficulties. Therefore, technical solutions that are not inferior to molded holes for cooling efficiency, but have a simpler production technology (Fig. 3).

With porous cooling, the wall has a large number of small holes evenly distributed over the surface. Such a wall is called permeable or porous. Through the holes, the cooler (cold gas) is blown into the boundary layer of the hot gas flowing around the wall. The flow of the coolant characterizes the flow stress g_{col}, i.e. consumption G_{col} per m^2 of surface F:

$$g_{\text{col}} = \frac{G_{\text{col}}}{F} \tag{1}$$

The cooler flowing out of the holes reduces the velocity and temperature of the outer gas flow near the wall and increases the thickness of the boundary layer. Therefore, the heat transfer from the hot gas to the wall decreases. Figure 4 shows the

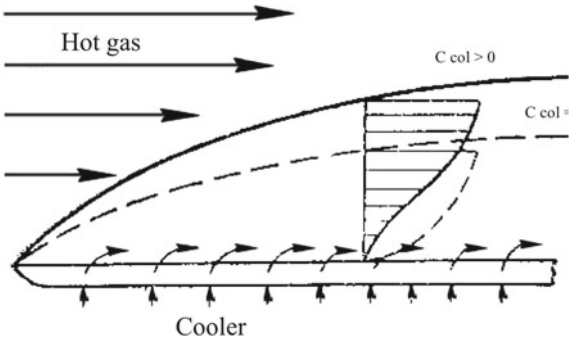

Fig. 4 Ways to organize barrier cooling

boundaries of the boundary layer and velocity profiles in it when the cooler is injected into the boundary layer ($c_{\text{col}} > 0$) and without it ($c_{\text{col}} = 0$) [3].

With a convective-blocking cooling scheme, the output of the cooling medium is achieved by perforating the wall of the combustion chamber. However, the presence of jets coming out of the holes causes a gasdynamic disturbance, and with a large temperature difference between the cooling medium and the wall, thermal stresses and possible destruction occur in it.

2 Pseudo-pores Structure

The use of porous permeable materials for cooling heat-stressed structures allows the realization of cooling methods whose capabilities (in terms of perceived heat load) exceed the limits of other methods. There are two approaches to using porous materials for this purpose. Transpiration cooling the idea of this method is that a relatively small amount of refrigerant is introduced into the boundary layer on the cooled surface through the pores in it. In this case, the fundamental property of the porous material is used—the possibility of a uniform distribution of very low coolant flow rates over a large area of the cooled surface at steady state flow. Inter-channel transpiration. This approach consists in enhancing heat transfer along the cooling flow path by completely or partially filling it with a porous permeable metal compacted with impermeable walls of the flow path. Intensification of heat transfer is provided by a developed inner surface of the porous channels in the volume of the porous material. According to the available experimental data, the intensity of heat transfer on such paths can be two orders of magnitude higher than in ordinary.

The cooling method using pseudo-porous structures is the use of a grid of small holes located in a dense grid. Pseudopores should have a complex geometry. Which will provide greater heat transfer at a lower cooler flow rate. The implementation of this technology is only possible using additive technology. Using AM, we can fully develop the combustion chamber sector, with pseudo-porous wall cooling, which is impossible using traditional technologies.

2.1 Pseudo-pores Structure Efficiency Estimation

The method of Kutateladze-Leont'ev was widely used, in spite of its considerable approximations, since the computational model of barrier cooling of a flat plate is considered in the gradientless flow of the main gas stream with the release of cooling (secondary) air through a continuous slit of small width s with a vanishing thin edge and parallel to the protected surface [4]. At the same time, as a preliminary and qualitative assessment such a simplified approach is quite acceptable.

Consider the sequence of calculations for evaluating the efficiency of cooling with the use of criterial equations. This calculation determines the adiabatic temperature of the gas near the surface of the wall, formed as a result of mixing the air blown through the slits or openings with the unperturbed flow of hot gas. The technique also takes into account the effect on the mixture temperature of the blowing parameter, the non-isothermicity of the flow, the blowing angles relative to the wall surface, the relative distance from the blowing site, and the degree of dispersion of the holes [5].

When preparing the data and the boundary conditions for calculating the plate cooling:

The ratio between the temperatures of cooling air and hot gas:

$$\tau_i = \frac{T_{b.\text{out}\,i} + 273}{T_{gi} + 273} \tag{2}$$

where $T_{b.\text{out}\,i}$ and T_{gi} are gas temperatures

The gasdynamic function $y\left(\lambda_g\right)_i$:

$$y(\lambda_g)_i = \left(\frac{k+1}{2}\right)^{\frac{1}{k-1}} * \frac{\lambda_g}{1 - \frac{k-1}{k+!} * \lambda_g^2} \tag{3}$$

The gasdynamic function $\pi(\lambda_g)_i$:

$$\pi(\lambda_g)_i = \left(1 - \frac{k-1}{k+1} * y(\lambda_{gi}^2)\right)^{\frac{k}{k-1}} \tag{4}$$

Prandtl number:

$$\text{Pr}_i = \text{Pr}_i^* * \pi\left(\lambda_g\right)_i \tag{5}$$

Mass air flow:

$$m_i = \frac{G_{ai} * \sqrt{T_{gi} + 273}}{0.0396 * F_{ai} * \text{Pr}_i * y\left(\lambda_g\right)_i} \tag{6}$$

where: G_{ai}, F_{ai}—the flow rate and gas channel area.

Slot area:

$$S_{si} = \frac{\overline{k_i} * S_i^2}{S_i + \mathrm{Pr}_i} \tag{7}$$

where: $\overline{k_i} = \frac{k}{S}$ and S_s, S is area.

Equivalent slot area:

$$S_{s.\mathrm{eqi}} = S_{s.i} * \eta_{s.i} \tag{8}$$

Complex parameter:

$$A_i = \frac{S_{s.i}}{S_{s.\mathrm{eq}.i}} * m_i^{-1.3} * \tau_i^{-1.25} * \mathrm{Re}_{g.i}^{*-0.25} \tag{9}$$

Cooling efficiency:

$$\begin{aligned} \Theta_{fi} &= 1 && \text{if} \quad A_i \le 3 \\ \Theta_{fi} &= 1.37 * A_i^{-0.285} && \text{if} \quad 3 < A_i \le 3 \\ \Theta_{fi} &= 6.75 * A_i^{-0.95} && \text{if} \quad 11 < A_i \end{aligned}$$

The coefficient that takes into account the blowing angle ψ (given by the table):

$$\varepsilon_{\psi i} = f\left(m_i, \frac{L_i}{S_{s.\mathrm{eqi}}}, \psi_i\right) \tag{10}$$

The coefficient that takes into account the discreteness of the blowing (given by the table):

$$\varepsilon_{\mathrm{discr}.i} = \frac{P_i}{P_i + S_i} * \overline{\varepsilon_g} \tag{11}$$

$$\overline{\varepsilon_g} = f\left(A_i, m_i\right)$$

P—the distance between the cooling air discharge rows.

Efficiency of barrier cooling:

$$\Theta'_{fi} = \Theta_{fi}\left(1 - \varepsilon_{\psi i}\right)\left(1 - \varepsilon_{\mathrm{discr}.i}\right) \tag{12}$$

Wall temperature with barrier cooling:

$$T_{fi} = T_{gi} - \Theta'_{fi}\left(T_{gi} - T_{b.\mathrm{out},i}\right) \tag{13}$$

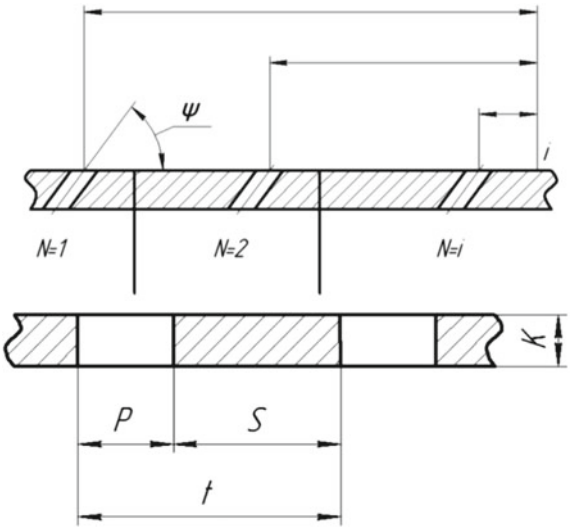

Fig. 5 Arrangement of the channels of the perforation rows

The resulted efficiency of barrier cooling:

$$\Theta'_{fi} = \frac{T_{gi} - T_{fi}}{T_{gi} - T_{b.\text{out},i}} \tag{14}$$

Total cooling efficiency in the presence of several belts barrier cooling is determined by the dependence:

$$\bar{\Theta}_{f\Sigma} = \sum_{j=1}^{J} (1 - \bar{\Theta}_{fi})^{j+1} \; j = 1, 2 \ldots J \tag{15}$$

The above method for calculating the barrier cooling when cooling air is released through slits or discrete holes to the surface of the combustion chamber washed by hot gas can also be used to design walls with a pseudoporous structure. This technique allows you to evaluate the effectiveness of a particular channel geometry and the arrangement of rows (Fig 5).

2.2 Mathematical Modeling of Wall with Pseudo-pores

For numerical calculations, models of the wall sector of the combustion chamber in the Siemens NX CAD system were built. The model was prepared in advance, considering the volume of flowing hot and cold gas. For the experimental models, the walls were made with the same order and number of holes. To simplify calculations,

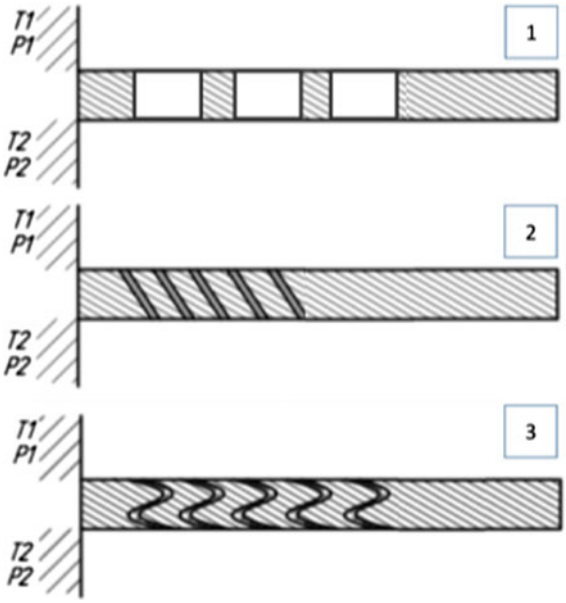

Fig. 6 Cross-sections of plates with perforation and pseudo-pores

a plate with 100 mm × 50 mm × 1 mm cracks with different hole profiles. All holes have the same volume.

To obtain data on the behavior of the flow that flows on a flat plate from cooling pseudopores, calculations were made on a flat plate with various forms of such channels. These calculations were carried out to select the optimal channel shape for use on the wall of the combustion chamber, as well as to analyze structural solutions.

As examples, we selected sections shown in the figure. These schemes allow you to more effectively produce the process of cooling the wall of the combustion chamber of the CCD because of the greater heat transfer from the wall and more correct release of cooling air to the wall surface. In connection with the advent and widespread use of commercial CFD codes, it has become possible to test the effectiveness of various design solutions without creating samples. Since new design schemes at this stage are not widely used in the design of existing walls of combustion chambers, but are a promising direction for development, it is necessary to carefully analyze the prospects for their development and application possibilities.

To evaluate the effectiveness of this cooling scheme, several models of sectors of the cooling wall were built. A wall with a classic perforation (Fig. 6, 1) is for comparison. An also a wall with pseudopores, having a cylindrical profile at an angle (Fig. 6, 2) and a wall with pseudopores having a spiral profile (Fig. 6, 3). The basis was the same sector of the wall of the combustion chamber.

For the initial assessment, the hole and pseudo-points were calculated separately. The calculations were carried out with the following boundary conditions: the flow above the wall ($T1 = 600$ K, $p1 = 35$ bar), the flow below the wall ($T1 = 2000$ K,

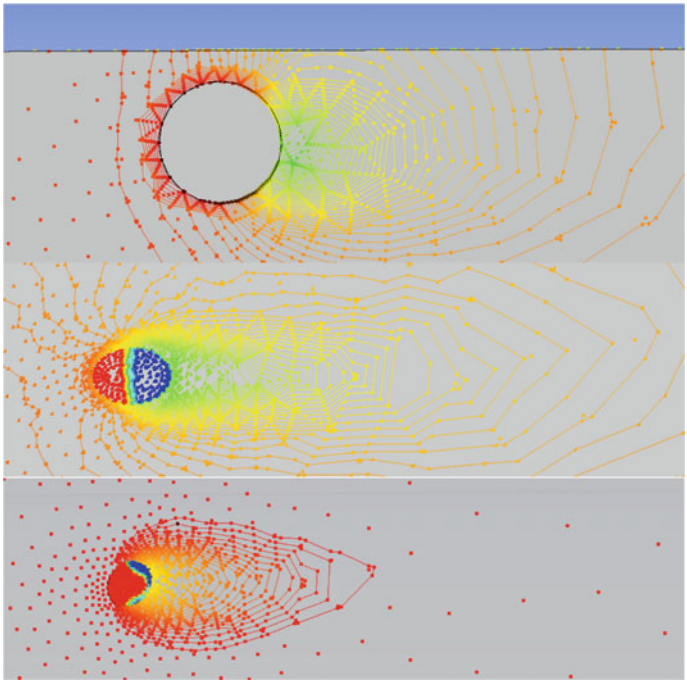

Fig. 7 Results of calculations (1—plate with straight round hole, 2—plate with round pseudo-pore at slope, 3—plate with spiral pseudo-pore)

$p1 = 30$ bar). Values as close as possible to parameters of the real engine. You can see the results in Fig. 7.

These results show us the effectiveness of different channels separately. Obviously, the best temperature gradient will be in a traditional perforated hole. But taking into account the flow rate and the formation of the pseudopod of the boundary layer, there are better indicators at an angle than the 1st option. This already suggests that this method is effective. Spiral pseudopora has low productivity, but for a full assessment of the effectiveness, it is necessary to consider a pseudopore mesh. The following calculation was also performed on three wall samples with different cooling schemes. The section of the wall where the holes are located, as well as consumption through them is the same for all cases.

Calculations at Fig. 8 show the following. Under the same conditions, the first sample with perforation shows the worst cooling performance, with a large coolant flow and poor air curtain formation. As can be seen on the wall, the cooling effect disappears very quickly in this case. Schemes with pseudo-pores display good cooling characteristics due to the fact that complicated channels are used that allow you to take more heat from the wall of the combustion chamber. Also, the cooling effect lasts much longer for this case. Taking into account all this we can conclude that with a lower consumption through the channel, pseudo-pores provide more efficient cooling.

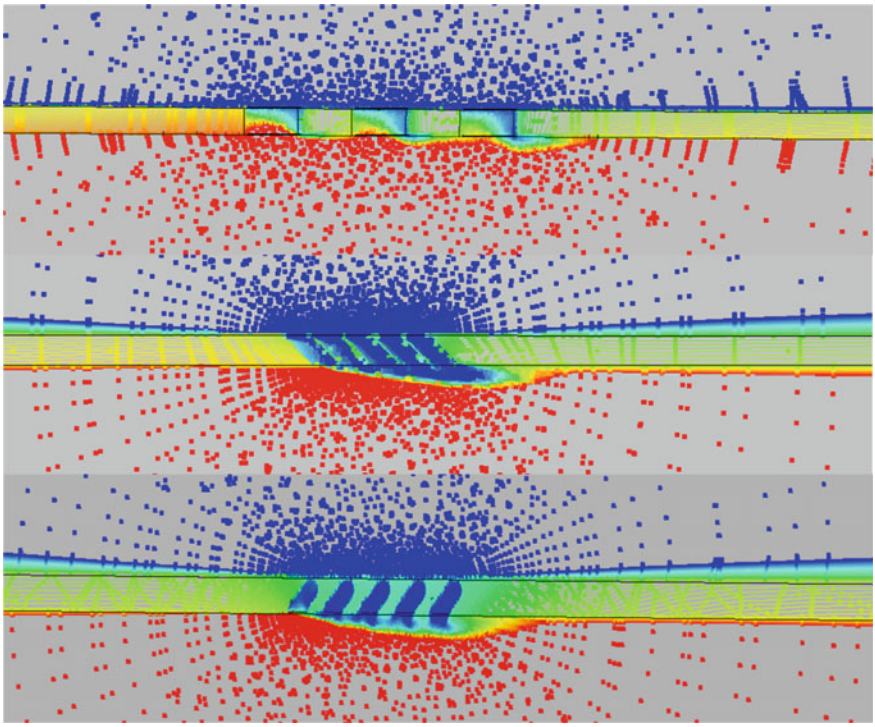

Fig. 8 Results of calculations (1—plate with straight round holeы, 2—plate with round pseudo-pores at slope, 3—plate with spiral pseudo-pores)

2.3 Manufacturing of GTE Combustion Chamber Wall with Pseudo-pores Structure

Combustion chambers consist of elements made of sheet material, interconnected by welding. When the chamber is divided into elements, the possibility and convenience of punching are used. Stamping separate elements are carried out in several transitions, the number of which depends on the shape of the part. After each transition, the workpiece is annealed to relieve internal stresses. During the last transition, called the calibration, the part gets its final dimensions and shape. The accuracy of the dimensions after calibration should be ± 0.1 mm.

The choice of material for the manufacture of individual parts of the combustion chambers is determined by the conditions in which this part works. The most intense unit of the combustion chambers is a flame tube subjected to mechanical vibrations under conditions of high temperatures (up to 1200 K and more) and a chemically aggressive medium. For the production of flame tubes, it is necessary to use materials characterized by the following properties:

- heat resistance, i.e. good strength characteristics at high temperatures (the material must have high limits of strength, long-term strength, fatigue strength, creep and flow);
- fire resistance, i.e. resistant to oxidation, sulfate and vanadium corrosion;
- possibly a minimal degree of blackness and a small coefficient of linear expansion (adherence to these conditions will allow lowering the temperature of the flame tube and the temperature gradients in it, and also reduce the possibility of buckling);
- manufacturability, i.e. the ability to easily handle mechanically, weld well, yield to stamping, and so on.

The listed requirements are most fully met by nickel alloys. Usually, austenitic steels with an increased chromium content are used to produce flame tubes of combustion chamber, since such steels are well resistant to the action of sulfur and other harmful impurities of combustion products [6].

To carry out future experiments, three-dimensional geometric models will perform wall samples at a scale of 1:1 by rapid prototyping, namely laser stereolithography (SLA) on a stereolithographic machine. Laser Stereolithography (SLA) is a 3D printing technology based on layer-by-layer curing of liquid material under the action of a laser beam [7].

Advantages and features of technology

- Making models of any complexity (thin-walled parts, small parts);
- Easy processing of the prototype;
- High accuracy of construction and high quality of the surface;
- The properties of the polymers used make it possible to use the grown prototype as a finished product.

This method makes it possible to obtain a sample for experiment with different manufacturing accuracy quickly and relatively inexpensively: a layer of 25 cm for laser curing of the polymer.

SLM or Selective laser melting is an innovative technology for the production of complex products by laser melting of metal powder using mathematical CAD models (3D metal printing). With the help of SLM create both precise metal parts for work in the structure of units and aggregates, as well as non-assembled structures that change the geometry during operation [8]. Principle of operation shown at Fig. 9.

Benefits:

- Solving complex technological problems
- Production of products with complex geometry, with internal cavities and conformal cooling channels
- Reducing the R & D cycle
- The ability to build complex products without the manufacture of expensive tools
- Weight reduction
- Construction of products with internal cavities
- Saving material in production
- The construction takes place by layerwise addition of the necessary amount of material to the “body” of the product. 97–99% of the powder that is not used in

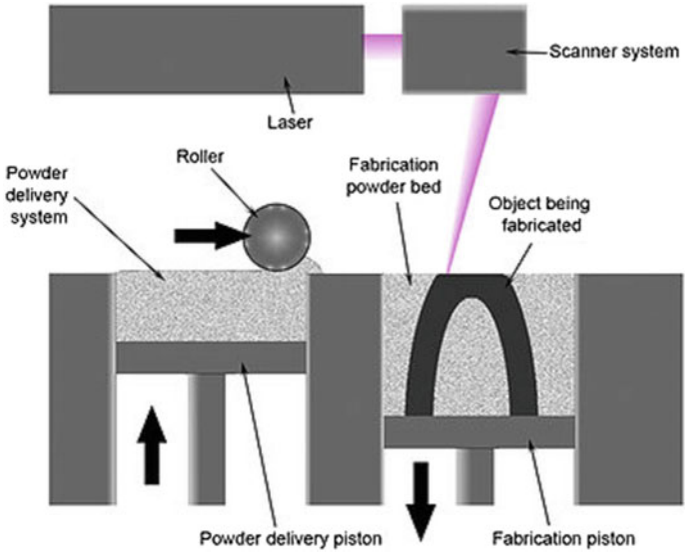

Fig. 9 Principle of operation of SLM

the construction after sieving is recyclable. 3–9% of the material involved in the construction of supports, is recycled together with a substandard unmelted powder that has not passed the sieving operation.

- Reducing the cost of manufacturing complex products, because there is no need to produce expensive equipment.

All these advantages make it possible to realize the production of such a complex structure as the combustion chamber wall of a gas turbine with a pseudo-porous structure. Complex geometry and the required high accuracy can be achieved with this technology.

3 Conclusion

The paper discusses methods for cooling the walls of the combustion chamber of a gas turbine engine, as well as various ways to reduce the temperature of the wall of the combustion chamber. The wall structure of the porous cooling system is analyzed: a new tank cooling system is applied to the wall, in which cooling air is blown into the boundary layer of the wall and most effectively reduces its temperature.

(1) As a result of using a wall structure with a pseudo-porous structure, the unevenness of the temperature state of the outer and inner sides of the wall can be significantly reduced due to more efficient wall cooling, and this will help to avoid overflow of the flow and promote a smoother formation of barrier cooling.

(2) As a result of a comparative analysis of various wall cooling channels, it was found that cooling efficiency can be improved through the use of pseudopores, which are channels of different profiles and directivity. However, this system is technologically more difficult to implement than the traditional system.
(3) Numerical experiments qualitatively confirm the conclusions made above, but a quantitative estimate of the decrease in wall temperature should be obtained on the basis of experimental studies of field samples of wall sectors.

References

1. Starikov, P. A. (2017). *The gas turbine engine fuel system for a winged target*. Bachelor Thesis, Moscow Aviation Institute.
2. Agapov, A. V., Bogdanov, V. N., Borovikov, D. A., Ionov, A. V., Seliverstov, S. D., & Starikov, P. A. (2016). Mathematical identification and design problems of small-size GTE. *Scientific and Technical Herald of the Volga Region № 6*, *120*, 28–32.
3. Shishkin, D. A., & Zelenov, S. N. (2012). In R. E. Alekseeva (Ed.), *Combustion chambers of gas turbine engines*. Nizhny Novgorod: Nizhny Novgorod State Technical University.
4. Matushkin, A. A. (2012). *Constructive improvement of the cooling system for working blades of high-temperature GTE turbines*. Ph.D. Dissertation, Moscow Aviation Institute.
5. Matushkin, A. A., & Nesterenko, V. G. (2010). Constructive methods for improving the film cooling system for working blades of turbines of the VRD. *Electronic Journal-Trudy MAI*, *39*.
6. Tretyakov, A. F. (2012). *Features of the technology of manufacturing turbine blades with porous cooling* (Vol. 13, pp. 1–13). UDC 621.77.04: 627.851.
7. Ugolotti, M., Sharma, M., Williams, Z., Owen, M., Balachandar, S., Ouwerkerk, J., & Turner, M. (2017). Cooling system for 0.1 kN thrust micro-engines: concept design using additive manufacturing. In *58th AIAA/ASCE/AHS/ASC structures, structural dynamics, and materials conference*, 9–13 Jan 2017, Grapevine, Texas.
8. Frick, L. (2013). Additive manufacturing comes to metal foam. *Machine Design*. Open Access Publisher, 26 Apr 2013.

Automatic Power Line Detection for Low-Altitude Aircraft Safety Based on Deep Learning

Xingchen Zhang, Gang Xiao, Ke Gong, Junhao Zhao and Durga Prasad Bavirisetti

Abstract Power line detection (PLD) is of vital importance for the flight security of low-altitude aircraft, such as helicopters and unmanned aerial vehicles (UAVs). This paper firstly summarises past studies on PLD based on image processing technique extensively. Secondly, different from the traditional PLD methods, we propose an approach to detect power lines based on deep learning which has been demonstrated having unparalleled performance in the field of image processing and computer vision. Specifically, the convolutional neural network (CNN) is employed in this study to extract features and thus detecting power lines from images. By utilising CNN, the feature extraction and object detection process are completed jointly unlike traditional PLD methods. A public dataset is used to demonstrate the performance of the proposed approach. This paper also gives recommendations for the future development of PLD.

Keywords Power line detection · Deep learning · Image processing · Low-Altitude flight safety

1 Introduction

Power line detection (PLD) have attracted increasing attentions in recent years. This is mainly because PLD is of great importance and has many important applications in both military and civil fields. For example, PLD is vital for flight safety of helicopter

X. Zhang (✉) · G. Xiao · J. Zhao · D. P. Bavirisetti
School of Aeronautics and Astronautics, Shanghai Jiao Tong University, 800 Dongchuan Road, Shanghai 200240, China
e-mail: xingchen@sjtu.edu.cn

G. Xiao
e-mail: xiaogang@sjtu.edu.cn

K. Gong
School of Computer Science and Software Engineering, East China Normal University, 3663 North Zhongshan Road, Shanghai, China

Z. Jing (ed.), *Proceedings of International Conference on Aerospace System Science and Engineering 2018*, Lecture Notes in Electrical Engineering 549,
https://doi.org/10.1007/978-981-13-6061-9_11

and UAV etc. The United States army reports that they have lost more helicopters to power lines than against enemies in combat [1]. Besides, PLD can be applied in automatic surveillance of electrical power infrastructure [11, 13] and power line inspection [19]. This is very helpful to locate the points of faults on power lines and to diagnose the components equipped on power lines. Also, this helps to save a huge amount of money which is spent on manual power line surveillance.

In past decades, with the continuous increasing of camera resolution, detecting power lines from aerial images directly have become possible, which is not possible previously. Since then, many methods based on traditional image processing techniques have been proposed to detect or recognise power lines, for example using the edge detection and Hough transform. Some of these works are based on visible images, while some others utilise infrared images.

However, there are some shortcomings of traditional image processing-based methods. Firstly, featured used to detect lines are designed manually, which may not be very good, and this process is time-consuming and labour-intensive. Secondly, the frequently-used Hough transform is mainly designed for straight line detection. However, power lines may not always be straight lines. Thirdly, these algorithms may be computationally expensive since pre-processing and time-consuming feature extraction are needed. Also, many prior knowledge about power lines is needed in designing traditional algorithms, however this is labour-intensive to implement.

Consequently, a more robust, accurate, cheap and intelligent PLD method is necessary. Considering the great success of deep learning in various fields, in this work we propose to deal with PLD problem using deep learning.

The following parts of this paper are organised as follows. Section 2 gives some background information about PLD, then Sect. 3 presents a review of PLD approaches based on image processing. Section 4 will present the proposed deep learning framework for PLD and experimental work will be presented in Sect. 5. Then, Sect. 6 will give the results. Finally, Sect. 7 concludes the paper.

2 Background

2.1 Power Line Detection

PLD is an important yet challenging problem. One factor making PLD challenging is the complex or cluttered background with cloud, trees, grasses etc. Figure 1 presents some images containing power lines. As it can be seen, the background varies from human eyes. Another factor is the features of power lines themselves.

Fig. 1 Some power line instances with various backgrounds. Taken from public dataset (https://data.mendeley.com/datasets/n6wrv4ry6v/7)

2.1.1 Features of Power Lines

Power lines in aerial images normally have some features compared to other objects [13, 27]. Firstly, power lines are very small and thin. Secondly, power lines can be approximated reasonably well by straight lines from overhead view. Thirdly, a power line is made of specific metal and has larger light reflection, thus from downward view it is usually brighter than its surroundings. Besides, a power line usually has uniform brightness. Finally, power lines are approximately parallel to each other. This is because the intersection of two power lines usually occurs far out of the image due to the limited size of images, and the intersecting angle of two lines is usually very small, as shown in Fig. 1.

On one hand, these features make the PLD problem even more challenging. On the other hand, these knowledge can be used to guide designing PLD algorithms, like presented by Li et al. [13].

2.1.2 Warning Sphere for Power Lines

Considering the features of power lines, some measures have been taken to help pilots to recognise power lines. One of the most frequently-used methods is the warning sphere. Normally, warning spheres are installed in places near airport as shown in Fig. 2 which illustrates some warning spheres near Shanghai Pudong International

Fig. 2 Warning spheres on power lines near Shanghai Pudong International Airport

Airport in China. Although warning spheres can help to recognise power lines to some extent, it is not quite enough. It is difficult and time- consuming to install warning spheres. What's more, it is not possible to install warning spheres everywhere, image to image, and sometimes it is very difficult to distinguish power lines from background even with thus only a very small part of power lines can have convert these spheres. In addition, sometimes it is possible that these warning spheres fall down, which is dangerous for people or houses beneath these power lines.

2.2 Machine Learning and Deep Learning

In recent years, machine learning and deep learning have attracted great interests in both academic field and industries. The fast development of them is mainly driven by the greatly increased amount of data and computing power.

Machine learning and deep learning have been applied in many fields and have provided significantly better performance than traditional methods. For example, in computer vision [25], robotics [12], medical imaging [15] and even Go [21, 22]. Compared to traditional machine learning algorithms, in past years deep leaning have exhibited better performance in various areas due to its advantages. For instance, it can automatically learning effective features, which has been well demonstrated in many computer vision problems. In addition, although it takes time to train the algorithm, it works quite effectively in detection once trained.

From the literature it can be found that some researchers have started to consider using machine learning to solve PLD problem. However, to the best of our knowledge, there is still no work introducing deep learning to this field. In the present work, we will utilise deep learning to solve PLD problem.

3 Related Work

Generally speaking, there are three main kinds of PLD methods. The first kind is laser-based method. For example, Avizonis and Barron [1] present the very early research on PLD using laser-based method. The second kind is radar-based method as introduced in some studies [18, 20]. The last kind is image- based methods, which are the focus of this work.

3.1 Power Line Detection Based on Traditional Image Processing Method

3.1.1 Detecting Power Lines as Straight Lines

As presented in Sect. 2, power lines can be approximated using straight lines in aerial images. Therefore, one can utilise straight line detection methods to detect those power lines, for instance the Hough transform [9] and Radon transform [26].

Hough Transform

The Hough transform is a classical straight line detection method, which is insensitive to noise and has been frequently applied to detect power lines. The main principle of Hough transform is to convert a line in the Cartesian coordinate into a point in the parametric space (Hough space), as illustrated in Fig. 3.

Li et al. [13, 14] proposed a power line inspection system which consists of three parts. The first part was the Pulse-Coupled Neural Network (PCNN) filter which was used for removing background noise. The second part of the Hough transform was used to detect straight lines. The third part was knowledge based line clustering employed to refine detection results. Specifically, K-means clustering algorithm was utilised. Similarly, the method proposed by Wu et al. [27] consists of three steps. Compared to work of Li et al., the edges of power lines were extracted using the SWIFTS algorithm before the Hough transform was employed to detect power lines. Besides, the Nearest Neighbourhood (NN) algorithm was implemented to distinguish different lines. However, although experiments have shown that the

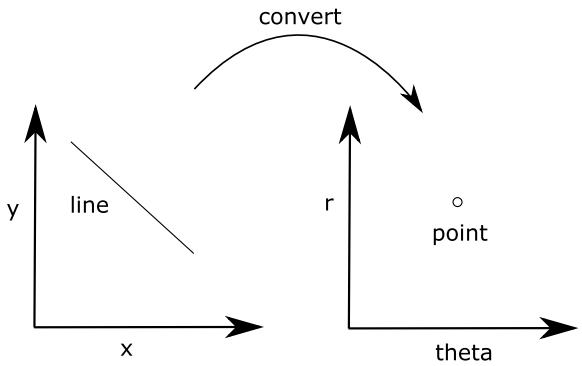

Fig. 3 Mapping of one line in Cartesian space to a point in the Hough space

algorithm presented by Wu et al. [27] is able to detect power lines, it is very time-consuming thus it may not be used in real applications.

Zhang et al. [34] performed study on power line detection and tracking for a UAV-based inspection. In that work, the Hough transform was used to detect lines, followed by a K-means algorithm to cluster and filter straight lines. Then, a Kalman filter was employed to track power lines. Liu et al. [16] also explored to detect power lines through Hough transform, but before applying the Hough transform, they did some pre-processing to obtain clearer images and used morphological operator for edge detection.

Apart from traditional Hough transform, researchers have also proposed some improved Hough transform and applied to PLD problem. For instance, Ji et al. [10] proposed an improved Hough transform and applied it to line detection. In that work, a local operator in the parameter space was defined to help to find peak and avoid parameter tuning needed in traditional Hough transform. Fernandes et al. [8] presented an improved Hough transform, aiming at achieve real-time performance. Specifically, they presented an improved voting scheme in the Hough transform that allows real-time performance for relatively large images. Candamo et al. [3] presented the method to detect thin lines in urban settings using a windowed Hough transform, which can avoid incidental edge alignment produced by noisy edges.

Radon Transform

There are also some works that conduct PLD based on Radon transform, which is another well-known line detection method. For example, Yan et al. [28] conducted PLD based on Radon transform. They firstly extract line segments using Radon transform, and then use grouping method and the Kalman filter to obtain an entire line. They claimed that their method can extract power lines successfully regardless of background complexity.

Researchers have also tried to improve Radon transform to obtain better performance. Chen et al. [7] presented a Cluster Radon Transform (CRT) PLD method

based on improved Radon transform to extract linear feature from satellite image and can reduce/avoid alarm. Cao et al. [5] proposed a Boundary Search Radon Transform (BSRT) by assuming that the initial point of an integral line is on one of the image boundaries.

Other Methods

Some other methods have also been applied in detecting power cables as lines in images. For example, Ceron et al. [6] proposed a PLD method using a Circle Based Search (CBS) method. Yetgin et al. [29] proposed a method based on the EDlines method. Yetgin et al. [33] gave a comparison between three image-based PLD methods, i.e. EDLines, LSD and Hough Transform. They claimed that EDLines method can provide higher accuracy among these three approaches. Song et al. [24] presented an image-based local to global PLD method. Firstly, morphological filter is used to detect a line segment pool, and then these line segments are grouped into whole power line.

3.1.2 Detecting Power Line as an Object

In works presented above, power lines are considered as lines in images, rather than objects. Therefore, line detection method are utilised in those studies. However, it is also possible to detect power lines by recognising them as objects, in order to obtain better detection performance. Candamo et al. [4] presented very early research on this direction and proposed a method by considering the line and its surroundings, using the Gaussian model. Although linear patterns are searched in that work to find wires, the surroundings around lines are also considered to discriminate wires from other visually similar linear patterns. In this case, this method actually consider power lines as objects. Results in that work showed the method can improve detection performance in the condition of highly cluttered urban backgrounds, moderate rain and mist. Luo et al. [17] developed an object-aware PLD method which utilises the object properties of power lines. In that study, apart from RGB images, near-infrared (NIR) images are also employed to assist the detection of power lines.

3.2 Power Line Detection Based on Machine Learning

In the past, most works treated the power line as a straight line, and use method like Hough transform to detect it. However, the power line may not always be straight line, and may not always start from the edge of images. Consequently, the traditional image- based methods may not work well. To overcome these problems, one can turn to machine learning technique. Actually, with the increasing development of machine learning technique, some researchers have tried to conduct PLD problem

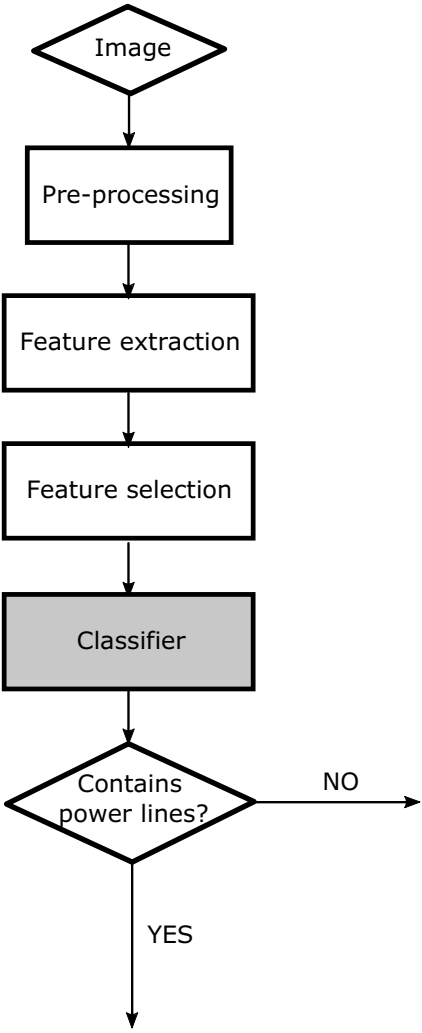

Fig. 4 The flow chart of PLD based on machine learning

with machine learning. When considering using machine learning to solve PLD problem, one can conduct in two ways. The first one is formulating the PLD problem as a binary classification problem, i.e. to judge whether the scene contains power lines or not. At the moment, most works are following this way [30, 31]. The second one is to formulate PLD as a detection problem.

PLD method based on machine learning normally consists of several stages. Firstly, one needs to do pre-processing for images, for instance to resize images and remove noise. Then, features should be extracted and selected in proper way. Finally, the features are fed into classifiers to do classification. The flow chart illustrating the whole process is given in Fig. 4.

Yetgin et al. [30] conducted a study using binary classification to perform power line scene detection. In that work, new feature extraction/selection strategies based on Discrete Cosine Transform (DCT) have been applied to scenes obtained from aircraft-based cameras. The accuracy of their work on a public dataset was around 89.5% when using visible images.

Note that apart from formulating power line detection as a binary classification problem, in some of the above-mentioned works, some machine learning algorithms have been applied as a part of the power line detection method. For instance, in the work presented by Li et al. [13, 14], K-means was utilised. In the work of Wu et al. [27], the Nearest Neighbourhood (NN) algorithm was chosen. In addition to these studies, Bhola et al. [2] proposed a method to detect power lines in UAV remote sensed images using spectral-spatial methods, where the K-means algorithm have also been employed.

4 Method

Unlike traditional PLD methods based on image processing and machine learning, we propose to apply deep leaning to power line detection. Specifically, the convolutional neural network which is famous for handling images is utilised in this study. Besides, we treat the power line detection problem as a binary classification problem, namely we recognise whether the image contains power line or not. In real applications, this method can find the scene containing power lines and then give an alarm to remind pilots. This is in contrast to some studies mentioned above, which detect and locate lines directly in images.

The deep learning framework utilised in this work is presented in Fig. 5. The network structure is very similar to the famous VGG-16 network [23], containing 13 convolutional layers, pooling layers and 3 fully-connected layers. The convolutional kernel size is 3×3. To adapt to PLD problem, the last fully-connected layer is changed to only have two units. In this work, all weights and bias in the network are trained and optimised using labelled training images. Note that the input image should be resized to 224×224 in order to be processed by the deep learning model.

5 Experimental Work

5.1 Dataset

Thanks to the work of Yetgin et al. [32], there is a public power line dataset available online. In the present study, this dataset is utilised to show the effectiveness of the proposed method in finding power lines from images. This dataset contains 4000 visible and 4000 infrared images captured all over Turkey with various backgrounds,

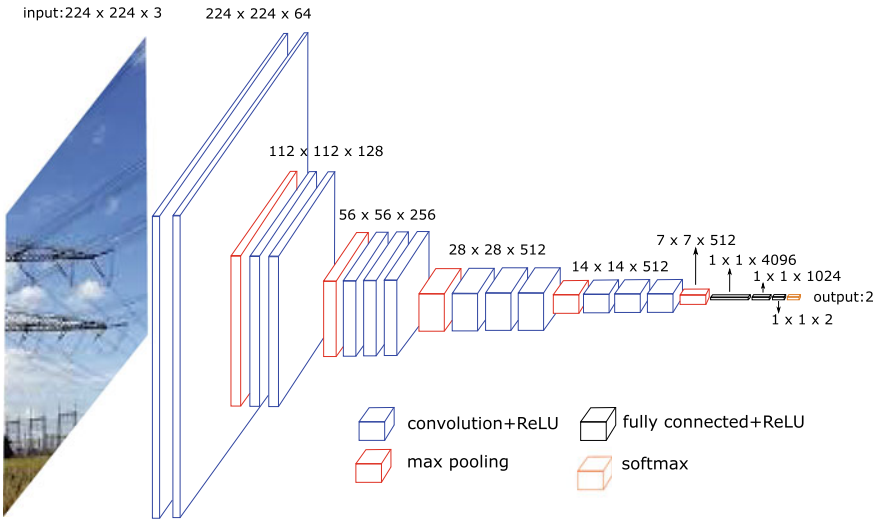

Fig. 5 Power line detection based on convolutional neural networks

Table 1 Main parameters in the training process

Parameter	Value
Epoch	6000
Batch size	20
Loss function	Cross entropy
Learning rate	0.001
Optimisation method	Adam optimizer
Number of training images	3000

temperatures and weather conditions. Among each kind, there are 2000 images with power line and 2000 images without power line. In the present study, only visible images are utilised.

5.2 Training of the CNN Model

Before training the network, all images are resized to the size of 224 × 224 to fit into the requirement of the CNN model. Main parameters of the train process are listed in Table 1. Note that among 4000 visible images in the dataset, 3000 images are used in training set, 1000 are in the test set.

The computer used to train the model is a desktop with an AMD Ryzen 5 1400 Quad-Core Processor (3.20 GHz) and 8 GB RAM. Besides, a NVIDIA Geforce GTX 1070 GPU is equipped. The training time for 6000 epochs is around 7 h. The loss and

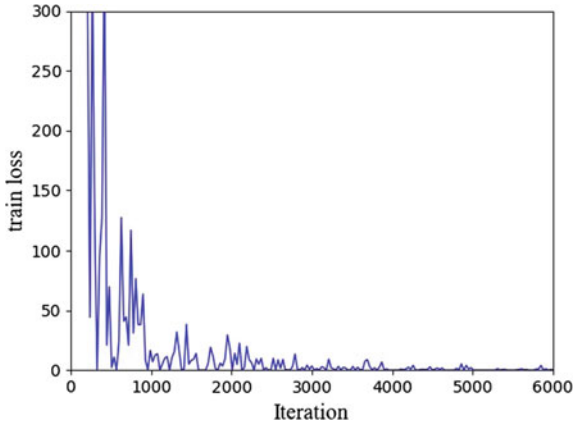

Fig. 6 Loss function value during training process

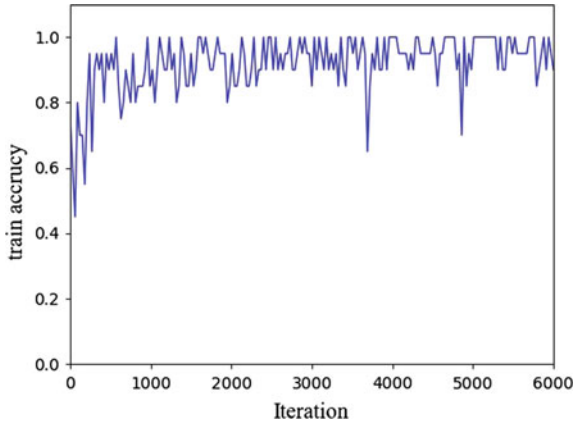

Fig. 7 Accuracy value during training process

accuracy during the training process are given in Figs. 6 and 7, respectively. As it can be seen, the loss has been significantly reduced while the accuracy has been greatly enhanced after training, which indicates the effectiveness of the training process.

6 Results and Discussions

6.1 Results

Two tests have been performed using the trained model to evaluate its performance. In Test 1, 100 images containing power lines from the public dataset are fed into the trained model. In Test 2, 100 images do not contain power lines from the public dataset as well are utilised. Note that these images have not been used in the training

Table 2 Test performance using the trained model

Test	Test dataset		No. of images	Corrected No.	Recall	Precision
Test 1 Test 2	Public, visible images	With power lines	100	95	95.0%	72.0%
		Without power lines	100	63		

process. The test results are listed in Table 2. As it can be seen, 95% of images which include power lines can be correctly recognised, although a part of images which do not have power lines are classified having.

Note that although it takes several hours to train the model, it is very fast to perform testing. This can actually satisfy the requirement of real applications, i.e. the model can work in real time.

6.2 Discussions

As illustrated in Table 2, the proposed deep learning-based method can recognise power lines from various images with the accuracy of 95%. This is significantly higher than the accuracy of traditional image processing methods for the same dataset, which is only 89.5% [30]. To the best of our knowledge, this is the first study that apply deep learning into PLD problem. The significantly enhanced accuracy clearly demonstrate the strength and potential of deep learning in PLD.

However, the precision of above tests is around 72.0%, which means that the trained model will incorrectly find power lines from images which do not include them. In practical applications, this will give some false alarm to pilots.

There are several factors that may affect the performance of the network, which are listed as follows:

- **Network architecture**. It is well-known that the network structure, for instance the number of units, layers and size of kernels, have huge affection on performance of the model.
- **Number of images in the dataset**. Another very important factor in deep learning is the amount of labelled data. Generally speaking, the more data used, the better performance obtained. In this study, we utilised the public power line dataset to train the model. However, 4000 images are not really enough for a network to be trained from scratch, therefore, it can be expected that if more labelled data are available, better performance can be achieved. Alternatively, if advanced techniques which can efficiently utilise limited data were employed, better performance would also be achieved.

- **Hyperparameters in the CNN model**. The hyperparameters in the CNN model, for instance the learning rate, also have affection on the network performance. In this work, we chose these parameters based on experience and trials.

To sum up, compared to traditional image processing-based and machine learning-based methods, deep learning can automatically extract and select effective features through learning from training set. Consequently, deep learning shows good performance in PLD problem although there is still much space to be improved.

7 Conclusion

In this paper, deep learning technique is applied to the power line detection (PLD) problem. Specifically, the convolutional neural network (CNN) is employed. To the best of our knowledge, this is the first public work attempting applying deep learning in PLD problem. Labelled images from public power line dataset are used to train the CNN model and test the feasibility of the proposed method. Experimental results clearly demonstrate that the proposed deep learning method can correctly recognise 95% of images containing power lines, which is much better than traditional image process or machine learning-based approaches.

Acknowledgements This paper is sponsored by National Program on Key Basic Research Project (2014CB744903), National Natural Science Foundation of China (61673270), Shanghai Pujiang Program (16PJD028), Shanghai Industrial Strengthening Project (GYQJ-2017-5-08), Shanghai Science and Technology Committee Research Project (17DZ1204304) and Shanghai Engineering Research Center of Civil Aircraft Flight Testing.

References

1. Avizonis, P., & Barron, B. (1999). Low cost wire detection system. In *Proceedings of 18th Digital Avionics Systems Conference* (Vol. 1, pp. 3–C). IEEE.
2. Bhola, R., Krishna, N. H., Ramesh, K. N., Senthilnath, J., & Anand, G. (2018). Detection of the power lines in UAV remote sensed images using spectral-spatial methods. *Journal of Environmental Management, 206,* 1233–1242.
3. Candamo, J., Kasturi, R., Goldgof, D., & Sarkar, S. (2009). Detection of thin lines using low-quality video from low-altitude aircraft in urban settings. *IEEE Transactions on Aerospace and Electronic Systems, 45*(3), 937–949.
4. Candamo, J., Goldgof, D., Kasturi, R., & Godavarthy, S. (2010). Detecting wires in cluttered urban scenes using a gaussian model. In *20th International Conference on Pattern Recognition* (Vol. 1, pp. 432–435).
5. Cao, W., Zhu, L., Han, J., Wang, T., & Du, Y. (2013). High voltage transmission line detection for UAV based routing inspection. In *IEEE/ASME International Conference on Advanced Intelligent Mechatronics* (pp. 554–558).
6. Ceron, A., I. F. Mondragon, B., & Prieto, F. (2014). Power line detection using a circle based search with UAV images. In *Proceedings of 2014 International Conference on Unmanned Aircraft Systems (ICUAS)* (pp. 632–639).

7. Chen, Y., Li, Y., Zhang, H., Tong, L., Cao, Y., & Xue, Z. (2016). Automatic power line extraction from high resolution remote sensing imagery based on an improved radon transform. *Pattern Recognition, 49,* 174–186.
8. Fernandes, L. A., & Oliveira, M. M. (2008). Real-time line detection through an improved Hough transform voting scheme. *Pattern Recognition, 41*(1), 299–314.
9. Haralick, R. M., Shanmugam, K., & Dinstein, I. (1973). Textural features for image classification. *IEEE Transactions on Systems Man & Cybernetics*, smc-*3*(6), 610–621.
10. Ji, J., Chen, G., & Sun, L. (2011). A novel Hough transform method for line detection by enhancing accumulator array. *Pattern Recognition Letters, 32*(11), 1503–1510.
11. Karakose, E. (2017). Performance evaluation of electrical transmission line detection and tracking algorithms based on image processing using uav. In *International artificial intelligence and data processing symposium* (pp. 1–5).
12. Lenz, I., Lee, H., & Saxena, A. (2015). Deep learning for detecting robotic grasps. *The International Journal of Robotics Research, 34*(4–5), 705–724.
13. Li, Z., Liu, Y., Hayward, R., Zhang, J., & Cai, J. (2008). Knowledge-based power line detection for UAV surveillance and inspection systems. In *Proceedings of 23rd International Conference on Image and Vision Computing, New Zealand* (pp. 1–6). IEEE.
14. Li, Z., Liu, Y., Walker, R., Hayward, R., & Zhang, J. (2010). Towards automatic power line detection for a UAV surveillance system using pulse coupled neural filter and an improved hough transform. *Machine Vision and Applications, 21*(5), 677–686.
15. Litjens, G., Kooi, T., Bejnordi, B. E., Setio, A. A. A., Ciompi, F., Ghafoorian, M., et al. (2017). A survey on deep learning in medical image analysis. *Medical Image Analysis*, *42*, 60–88,
16. Liu, L., Wang, W., Yong, J., & Ren, J. (2016). Automatic extraction of power lines from aerial images based on Hough transform. In *Proceedings of International Conference on Energy, Materials and Manufacturing Engineering*, number Emme, page 78620Q.
17. Luo, X., Zhang, J., Cao, X., & Yan, P. (2014). Object-aware power line detection using color and near- infrared images. *IEEE Transactions on Aerospace and Electronic Systems, 50*(2), 1374–1389.
18. Ma, Q., Goshi, D. S., Shih, Y. C., & Sun, M. T. (2011). An algorithm for power line detection and warning based on a millimeter-wave radar video. *IEEE Transactions on Image Processing, 20*(12), 3534–3543.
19. Santos, T., Moreira, M., Almeida, J., et al. (2017). Plined: Vision-based power lines detection for unmanned aerial vehicles. In *Proceedings of 2017 IEEE International Conference on Autonomous Robot Systems and Competitions (ICARSC)* (pp. 253–259). IEEE.
20. Sarabandi, K., & Park, M. (2000). Extraction of power line maps from millimeter-wave polarimetric SAR images. *IEEE Transactions on Antennas and Propagation, 48*(12), 1802–1809.
21. Silver, D., Huang, A., Maddison, C. J., et al. (2016, January). Mastering the game of Go with deep neural networks and tree search. *Nature*, *529*(7587), 484–489.
22. Silver, D., Schrittwieser, J., Simonyan, K., et al. (2017, October). Mastering the game of go without human knowledge. *Nature*, *550*, 354.
23. Simonyan, K., & Zisserman, A. (2014). Very deep convolutional networks for large-scale image recognition. *arXiv preprint* arXiv:1409.1556.
24. Song, B., & Li, X. (2014). Power line detection from optical images. *Neurocomputing, 129,* 350–361.
25. Szegedy, C., Vanhoucke, V., Ioffe, S., Shlens, J., & Wojna, Z. (2016). Rethinking the inception architecture for computer vision. In *Proceedings of the IEEE Conference on Computer Vision and Pattern Recognition (CVPR)* (pp. 2818–2826).
26. Toft, P. (1996). *The radon transform: Theory and implementation*.
27. Wu, Q., An, J., & Yang, R. (2010). Extraction of power lines from aerial images based on Hough transform. In *Earth observing missions and sensors: Development, implementation, and characterization* (Vol. 7862, p. 78620Q). International Society for Optics and Photonics.
28. Yan, G. J., Li, C. Y., Zhou, G. Q., Zhang, W. M., & Li, X. W. (2007). Automatic extraction of power lines from aerial images. *IEEE Geoscience and Remote Sensing Letters, 4*(3), 387–391.

29. Yetgin, O. E., & Gerek, O. N. (2013). Cable and wire detection system for aircrafts. In *Proceedings of Signal Processing and Communications Applications Conference* (pp. 1–4).
30. Yetgin, Ö. E., & Gerek, Ö. N. (2017a). Automatic recognition of scenes with power line wires in real life aerial images using DCT-based features. *Digital Signal Processing: A Review Journal*, *1*, 1–18.
31. Yetgin, Ö. E., & Gerek, Ö. N. (2017b). Feature extraction, selection and classification code for power line scene recognition. *SoftwareX*.
32. Yetgin, Ö. E., & Gerek, Ö. N. (2017c). Powerline Image Dataset (Infrared-IR and Visible Light-VL). *Mendeley Data*, v7.
33. Yetgin, O. E., Senturk, Z., & Gerek, O. N. (2015). A comparison of line detection methods for power line avoidance in aircrafts. In *Proceedings of 9th International Conference on Electrical and Electronics Engineering (ELECO)* (pp. 241–245).
34. Zhang, J., Liu, L., Wang, B., et al. (2012). High speed automatic power line detection and tracking for a UAV-based inspection. In *Proceedings of International Conference on Industrial Control and Electronics Engineering* (pp. 266–269). IEEE.

A Method for Enhancing Low-Pressure Ignition of n-Decane Based on Increasing Hydroxyl Free Radicals

Yaming Shi, Xiaobin Huang and Hong Liu

Abstract The flight envelope of aircrafts is hard to expand because the ignition of aviation fuel is unstable at low temperature or low pressure. Investigations on the low-pressure ignition phenomenon, like flame shape, soot formation and so on, have been done a lot. However how to enhance fuel ignition at low pressure is still a puzzle until now. This paper uses the fuel additive to enhance low pressure ignition of hydrocarbon fuel through generating more hydroxyl free radicals ($\dot{O}H$) in the fuel combustion. By means of fuel additive design, methoxydiethylborane (MDEB) is selected as a fuel additive in order to promote the low pressure ignition of n-decane. Experimental results show that with the additional 20% MDEB in n-decane, the minimum hot-surface ignition temperature at 1 bar is decreased from 863 to 393 K. The MDEB/n-decane hybrid fuel is able to be ignited at 0.65 bar when temperature is at 443 K. The experimental results are interpreted by the mechanism analysis of additive MDEB in n-decane, which indicates that the oxidization of MDEB produces methoxy free radicals ($CH_3\dot{O}$) and ethoxy free radicals ($C_2H_5\dot{O}$) to attack n-decane, finally generating more hydroxyl free radicals to enhance fuel ignition. This brand-new method based on increasing hydroxyl free radicals in fuel combustion, is meaningful and practical to enhance low-pressure ignition of hydrocarbon fuel and expand the flight envelope of aircrafts.

Keywords Low-pressure ignition · Fuel additive · Free radicals · Chemical mechanism

Y. Shi (✉) · X. Huang · H. Liu
School of Aeronautics and Astronautics, Shanghai Jiao Tong University,
800 Dongchuan Road, Shanghai 200240, People's Republic of China
e-mail: shiyaming@sjtu.edu.cn

X. Huang
e-mail: xbhuang@sjtu.edu.cn

Z. Jing (ed.), *Proceedings of International Conference on Aerospace System Science and Engineering 2018*, Lecture Notes in Electrical Engineering 549,
https://doi.org/10.1007/978-981-13-6061-9_12

1 Introduction

Flight vehicles usually fly in a limited range of velocity and altitude, which is called the flight envelope [1]. It is of great significance for both civil airplane and military airplane to have a larger flight envelope. When the flight altitude of an airplane is higher, the lower ambient pressure environment leads to a more unstable fuel ignition [2]. To be worse, aviation fuel may not be ignited at such a low-pressure condition [3], resulting in the decrease of lift force, engine thrust and so on [4]. Consequently, flight vehicles usually can't fly higher beyond the flight envelope. It is the low-pressure ignition limit of fuel restricts the range of flight envelope. As a result, it is meaningful to investigate on the low-pressure ignition limit of fuel in order to enlarge the flight envelope.

Previous researchers have conducted some experiments on fuel ignition at low pressure. In Fig. 1, a series of experimental data concerning the hot-surface ignition limits of hydrocarbon/air mixtures [5] and aviation jet fuel JP-4/air mixtures [6] at low pressure is illustrated. When the experimental pressure is going down, the minimum temperature for hydrocarbon fuel ignition is increased. The ignitable ranges of hydrocarbon fuels become narrower when pressure is decreased.

A quantity of theoretical research was also conducted to investigate on the chemical reaction at low pressure. Eiwakil et al. [7] built a theoretical model which interprets the collision frequency between the air molecules and fuel vapor and drew the conclusion that the collision frequency was concerned with the ambient pressure. Troe [8] established the master equation for a thermal unimolecular reaction in gases under the low-pressure environment and made the weak collision efficiency factors calculated. Schranz et al. [9] set up a theoretical model which is mainly on the decomposition of ethane in mixtures of strong and weak colliders. Results showed that

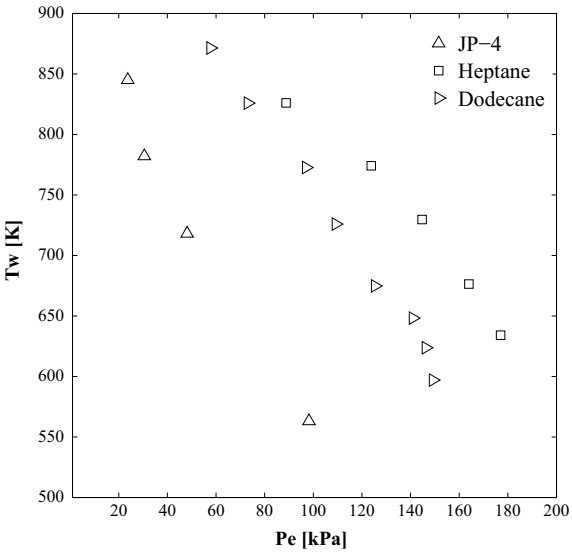

Fig. 1 Minimum hot-surface temperature/pressure ignition limits of JP-4 [6], heptane [5] and dodecane [5]

pressure significantly affects the collision efficiencies of weak colliders, contributing to a final lower reaction rate. From the above theoretical research, it is indicated that the collision frequency between air molecules and fuel vapor decreases as pressure is lowered, leading to a lower reaction rate of fuel combustion.

Recently, some researchers found that some pressure-dependent collision reactions would affect the production of free radicals in the low-pressure ignition. Le et al. [10–12] investigated the ignition characteristics of ethylene at sub-atmosphere. Results indicated that the probability of the collision reaction which has two-body species, is affected by pressure, leading to the less generation of ȮH radicals and a narrower ignitable range when pressure is falling down. Menon et al. [13] researched the effect of chamber pressure on the minimum hot-surface temperature for the ignition of n-hexane/air mixtures. Investigations showed that the hot-surface ignition temperature is greatly sensitive to the chamber pressure. When the ambient pressure is decreased from 100 to 25 kPa, the hot-surface ignition temperature is increased from 950 to 1140 K, owning to the reduced concentration of three-body species which weakens the decomposition of hydrogen peroxide. Consequently, less ȮH radicals are produced and the ignitable range of n-hexane is narrowed.

From the investigations above, the probability of some collision reactions is sensitive to pressure, especially when the fuel ignition is at low pressure. Furthermore, the final production of the free radicals which determine the overall reaction would also be affected by pressure consequently. It is the variation of free radicals concentration contributes to the change of the ignition limits of hydrocarbon fuels. In the fuel ignition reaction, hydroxyl free radicals are the important radicals which are able to enhance the overall reaction rate of hydrocarbon fuel ignition [14]. As a result, it is possible to extend the low-pressure ignition limit of fuel based on accelerating the generation of hydroxyl free radicals in the chemical reaction. However, none of research has been done on extending the low-pressure ignition limit of fuel from the perspective of free radicals.

This paper attempts to use a fuel additive to extend the low-pressure ignition limit of n-decane and analyzes the chemical mechanism of the fuel additive in n-decane, finally propose a method for enhancing the low-pressure ignition of hydrocarbon fuel. Based on the previous work of our group [15], an organoborane compound is selected as the fuel additive in this paper. A low-pressure experiment on the hot-surface ignition is conducted to investigate the effect of the fuel additive on the low-pressure ignition limit of n-decane. The new reaction pathway of the fuel additive in n-decane is analyzed experimentally and the hydroxyl free radicals in the oxidization of hybrid fuel are predicted finally.

2 Materials and Apparatus

2.1 Chemicals

The n-decane (>98% purity (GC), CAS: 544-76-3), MDEB (>97% purity, CAS: 7397-46-8), the compound 1,1-diphenyl-2-picrylhydrazyl (DPPH·) (>97% purity,

Table 1 Two kinds of fuels used for low-pressure experiment

	n-decane (volume,%)	MDEB (volume,%)
Case 1	100	0
Case 2	80	20

CAS: 1898-66-4), benzene (>99% purity, CAS: 71-43-2) and the compound 5,5-Dimethyl-1-pyrroline N-oxide (DMPO) (>98% purity, CAS: 3317-61-1) in the experiments were purchased from the Aladdin Industrial Corporation. Because the fuel additive (MDEB) is soluble with the based fuel (n-decane), it is able to obtain a homogeneous hybrid fuel in any proportions through manual mixing. In Table 1, the pure n-decane and a hybrid fuel with 20% MDEB are tested in the later low-pressure experiment of this paper. The compound DPPH· is sensitive to alkyl radicals, alkoxy radicals and peroxide radicals [16]. In the electron paramagnetic resonance (EPR) experiment, the DPPH· was used as the source of free radicals to demonstrate the existence of the radicals generated by the oxidization of MDEB. It is solid at the room temperature and soluble with the benzene. The compound DMPO is sensitive to alkyl radicals and alkoxy radicals [17]. In the electron paramagnetic resonance experiment, the DMPO was used as the spin trap to capture the radicals generated by the oxidization reaction of MDEB and n-decane.

2.2 Characterization

Figure 2 illustrates the apparatus where the low-pressure ignition of droplet impinging on hot surface was conducted. The pressure inside the chamber, which can be measured by a pressure gauge (accurate to 0.02 bar), is able to be reduced from 1 to 0.1 bar via vacuum pump (2XZ-4, 4Lpmin, Shanghai Neng Sheng Instrument Co., Ltd). The inner dimensions of the stainless steel chamber are 360 mm × 360 mm × 400 mm (length × width × height). Inside the stainless steel chamber, there is a hot surface (100 mm × 100 mm × 20 mm) which is made of titanium alloy because it has the high thermal conductivity. In the center of the surface, there is a concave curvature built for inhibiting the falling droplets from sliding off. The electric heater is embed under the metal surface. The surface temperature, ranging from ambient temperature (around 300 K) to 900 K, is measured by a K-type thermocouple sited underneath the hot surface. A Proportional-Integral-Derivative temperature controller is performed to keep the surface temperature at an average level with an accuracy of ±2 K. The single droplet is generated through a medical syringe. The average diameter of a droplet is approximately 2.5 mm. The height between the needle tip and the hot surface is around 25 mm. Further information could be noticed from the schematic diagram and photograph diagram of the setup in Fig. 2.

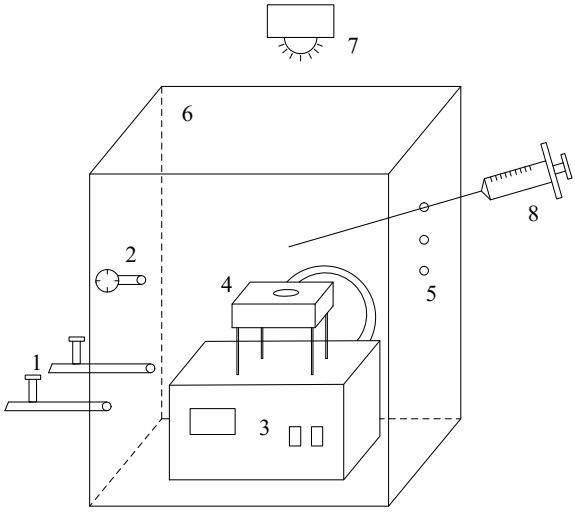

(a) Schematic diagram of the setup

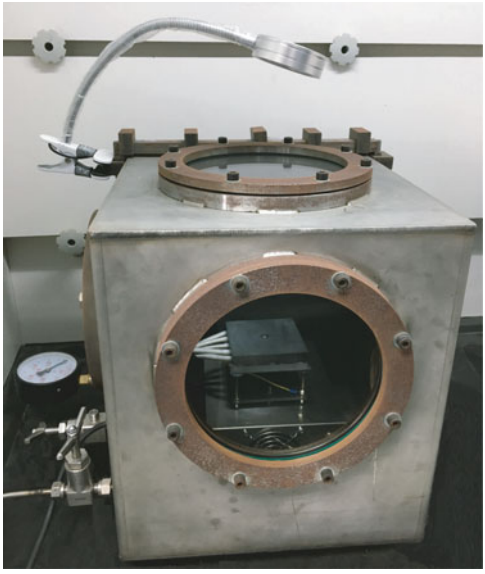

(b) Photograph diagram of the setup

Fig. 2 Details of the experimental equipment. (1) gas inlet/outlet pipes, (2) pressure gauge, (3) temperature controller, (4) heated surface, (5) injection hole, (6) sealed chamber, (7) LED light, (8) droplet generator

Electron paramagnetic resonance (EPR) spectra were acquired with a Bruker EMX EPR spectrometer (Bruker Biospin, Rheinstetten, Germany) at X-band frequency at room temperature. The typical instrument parameters were: Sampling Time, 0.015 s; Field Modulation Amplitude, 0.0001 T; Field Modulation Frequency, 100000 Hz; Microwave Frequency, 9.813701e+09 Hz; Microwave Power, 0.005024 W; Receiver Gain, 30; Receiver Time Constant, 0.01024 s.

Gas chromatography and mass spectrometry (GC-MS) measurements were conducted on a QP2010 GC-MS. Conditions were as follows: column: DB-5 0.25 mm × 0.25 μm × 30 m, column pressure: 10.1 psi, flow-rate: 1 mL/min, injector temperature: 290 °C. Temperature of the column: kept 5 min at 150 °C and then increased to 300 °C at 20 °C/min, holding for 12.5 min scan: 33–500 amu.

3 Results and Discussions

3.1 Low-Pressure Ignition Limits of n-decane-based Hybrid Fuels

In the previous work, our group [15] utilized a fuel additive, MDEB, which diminishes the activation energy of hybrid fuel to a great extent, making the minimum ignition temperature of n-decane decreased a lot. In this research, the organoborane compound (MDEB) is selected as the fuel additive to attempt to extend the low-pressure ignition limit of n-decane.

In this paper, the fuel ignition limit is defined in terms of the minimum hot-surface ignition temperature and the surrounding air pressure [5]. As a result, in the low-pressure hot-surface experiment, the minimum ignition temperature/pressure data of n-decane and n-decane/MDEB hybrid fuel is recorded. Figure 3 illustrates the experimental results of fuel ignition limits of n-decane and n-decane/MDEB hybrid fuel. When the air pressure in chamber is at 1 bar, the minimum temperature for ignition of pure n-decane droplet and the hybrid fuel droplet containing 20% MDEB is 863, 393 K respectively. 20% fuel additive MDEB makes the minimum hot-surface ignition temperature of n-decane at 1 bar decreased by 470 K. While the MDEB/n-decane hybrid fuel is able to be ignited at 0.65 bar when temperature is at 443 K. Consequently, it is proved that the fuel additive MDEB can greatly extend the low-pressure ignition limit of n-decane based on the analysis of experimental data.

3.2 Measurements of the Reaction Pathway of MDEB/n-decane Oxidization

Based on the low-pressure experimental results above, it is demonstrated that the fuel additive MDEB is able to greatly extend the low-pressure ignition limit of

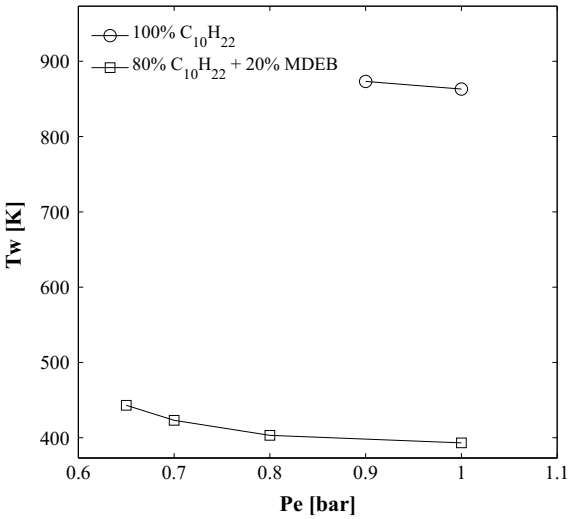

Fig. 3 The low-pressure ignition limits of n-decane and n-decane/MDEB hybrid fuel

n-decane. Furthermore, in this subsection, how the fuel additive MDEB enhances the low-pressure ignition of n-decane is researched in detail from the perspective of chemical mechanism.

During the oxidization of MDEB/n-decane hybrid fuel, MDEB is much easier to be oxidized than n-decane because the p orbits on boron atoms are extremely electron-deficient. Firstly, the oxidization process of MDEB is investigated experimentally. 2 μL MDEB is oxidized under the 473 K pyrolysis temperature. Immediately the oxidized pyrolysis products are analyzed using the gas chromatography and mass spectrometry (GC-MS). From the GC-MS spectrum in Fig. 4, it is indicated that the oxidization of MDEB at 473 K generates the compound 2,4,6-triethylboroxin ($C_6H_{15}B_3O_3$).

Because the GC-MS measurement is unable to identify the radicals generated by the oxidization of MDEB [18], the EPR measurements are employed furthermore [19]. The DPPH· is dissolved in benzene to get the 0.2 mol/L solution. 50 μL DPPH·/benzene solution is monitored by the EPR measurement. In addition, 2 mL DPPH·/benzene solution and 50 μL MDEB solution are mixed with oxygen in the plastic centrifuge tube for 1 min for the further EPR identification. Figure 5 illustrates the EPR spectrum of DPPH· in benzene and the EPR spectrum of DPPH·/MDEB in benzene. The intensity of DPPH· dissolved in benzene has some oscillations at different fields. However, the intensity of EPR signal of DPPH· after adding MDEB is scavenged to none. It is indicated that the oxidization of MDEB generates some radicals. Because DPPH· is sensitive to alkyl radicals, alkoxy radicals and peroxide radicals, the radicals generated by the oxidization of MDEB may be some of them. Moreover, in order to confirm which type of the radicals, DMPO is used as the spin trap to capture the radicals in the oxidization of MDEB. 30 μL MDEB and 60 μL DMPO are mixed with oxygen in the plastic centrifuge tube for 1 min. The

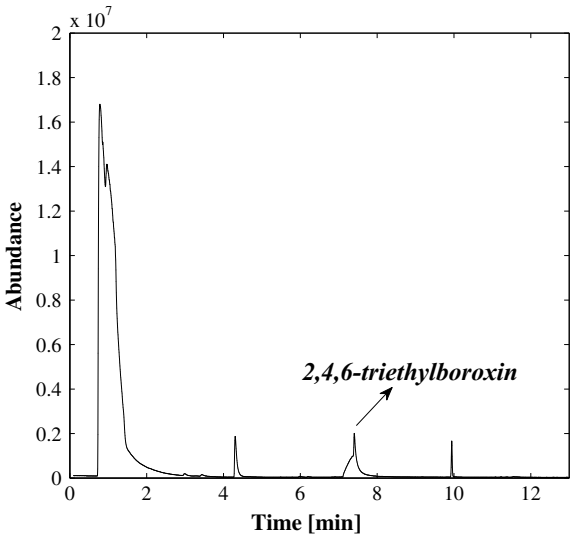

Fig. 4 GC-MS spectrum of the products of MDEB and oxygen

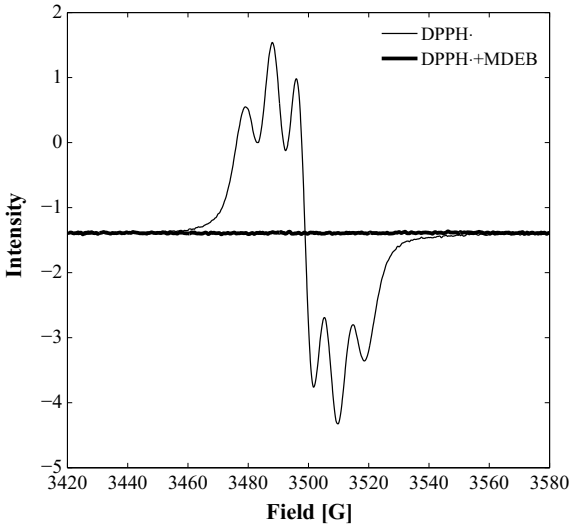

Fig. 5 EPR spectrums of DPPH· and DPPH·/MDEB oxidization adducts

oxidized hybrid fuel is analyzed using the EPR detection. The EPR spectrum of DMPO/MDEB oxidization adduct in Fig. 6 illustrates that the oxidization of MDEB generates alkoxy radicals based on the previous research [20].

Based on the above GC-MS data and EPR spectrum, it is experimentally confirmed that the oxidization of MDEB generates the compound 2,4,6-triethylboroxin and the alkoxy radicals. As a result, the oxidization routine of MDEB can be predicted as illustrated in Fig. 7 (inside the dotted box). The organoborane compound (MDEB) is easy to be oxidized. Firstly, MDEB is oxidized into ethyl peroxy

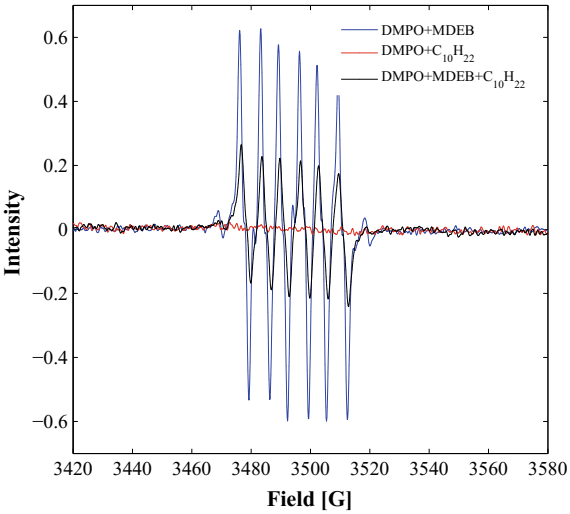

Fig. 6 EPR spectrums of DMPO/MDEB oxidization adducts, DMPO/n-decane adducts, and DMPO/MDEB/n-decane oxidization adducts

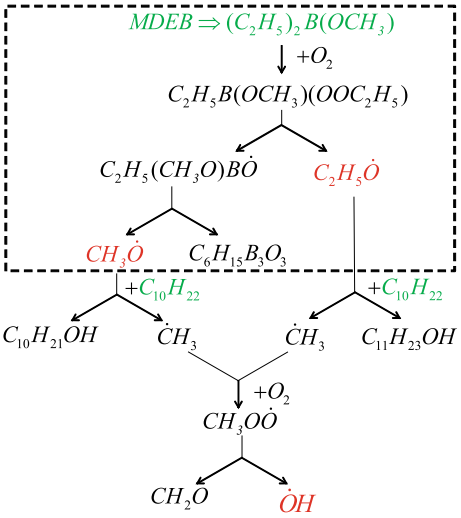

Fig. 7 Modified reaction pathway by adding MDEB in n-decane

methyl borate ($C_2H_5B(OCH_3)(OOC_2H_5)$). A homolytic cleavage of the O–O bund in $C_2H_5B(OCH_3)(OOC_2H_5)$ contributes to the formation of ethyl methoxy boron oxygen free radicals ($C_2H_5(CH_3O)B\dot{O}$) and ethoxy free radicals ($C_2H_5\dot{O}$) respectively. Furthermore, the cyclization reaction of three $C_2H_5(CH_3O)B\dot{O}$ leads to the formation of methoxy free radicals ($CH_3\dot{O}$) and the compound 2,4,6-triethylboroxin ($C_6H_{15}B_3O_3$).

In order to investigate on the influence of the MDEB oxidization on the n-decane ignition, the EPR experiments of DMPO/n-decane and DMPO/MDEB/n-decane are conducted. In detail, 30 μL DMPO and 30 μL n-decane are mixed in the plastic

centrifuge tube for 1 minutes. Similarly, 20 μL DMPO, 20 μL n-decane and 10 μL MDEB are mixed with oxygen in the plastic centrifuge tube for 1 minutes. In Fig. 6, the EPR spectrum of DMPO/n-decane shows that there is no reaction between the DMPO and n-decane. However, the intensity of EPR signal of DMPO/MDEB/n-decane, which is weaker than that of DMPO/MDEB, demonstrates that n-decane reacts with MDEB and oxygen, finally generating alkyl radicals based on the previous EPR research [17]. As a result, after adding n-decane in the MDEB oxidization, the whole chemical reaction pathway may display as illustrated in Fig. 7. After the oxidization of MDEB, n-decane attacks both $CH_3\dot{O}$ and $C_2H_5\dot{O}$, leading to the formation of methyl free radicals ($\dot{C}H_3$). Then the oxidization of $\dot{C}H_3$ contributes to the formation of methyl peroxide free radicals ($CH_3O\dot{O}$). Finally, the decomposition of $CH_3O\dot{O}$ generates $\dot{O}H$, which promotes the chain-branching steps [13, 21], enhancing the overall reaction rate and extending the ignition limit of n-decane.

From the chemical mechanism of MDEB in n-decane, the oxidization of additive MDEB generates $CH_3\dot{O}$ and $C_2H_5\dot{O}$ to attack n-decane, modifying the reaction pathway of n-decane ignition, accelerating the generation of $\dot{O}H$ and extending the fuel ignition limit. The fuel additive MDEB is proved to be able to extend the ignition limit of n-decane through accelerating the generation of $\dot{O}H$ in the fuel combustion. As a result, an innovative method for enhancing low-pressure ignition of n-decane fuel based on increasing hydroxyl free radicals is established.

4 Conclusions

In this paper, the compound MDEB is utilize as the fuel additive to extend the low-pressure ignition limit of n-decane through generating more $\dot{O}H$ in the fuel combustion. The low-pressure ignition experiment demonstrates that the fuel additive MDEB can significantly extend the low-pressure ignition limit of n-decane. Experimental results show that with the additional 20% MDEB in n-decane, the minimum hot-surface ignition temperature at 1 bar is decreased from 863 to 393 K. The MDEB/n-decane hybrid fuel is able to be ignited at 0.65 bar when temperature is at 443 K.

The experimental results are interpreted by the chemical mechanism analysis of MDEB in n-decane, which indicates that the oxidization of MDEB generates $CH_3\dot{O}$ and $C_2H_5\dot{O}$ to attack n-decane, modifying the reaction pathway of n-decane ignition. This newly-built reaction pathway about n-decane ignition accelerates the formation of $\dot{O}H$, finally extending the low-pressure ignition limit of n-decane.

Based on the research above, a new method for extending the low-pressure ignition limit of fuel through accelerating the formation of hydroxyl free radicals ($\dot{O}H$) in the fuel combustion, is proposed in this paper. The investigation is meaningful and applicable in extending the low-pressure ignition limit of hydrocarbon fuel and enlarging the flight envelope of aircrafts to a bigger scale.

Acknowledgements The authors appreciate the funding supports from the Natural Science Foundation of China, under Grant No. 91441205.

References

1. Anderson, J.D. (1999). Aircraft Performance and Design, p. 350. Boston: McGraw-Hill.
2. Fang, J., Tu, R., Guan, J. F., Wang, J. J., & Zhang, Y. M. (2011). Influence of low air pressure on combustion characteristics and flame pulsation frequency of pool fires. *Fuel, 90*(8):2760–2766.
3. Dipiazza, J. T. (1951). Limits of flammability of pure hydrocarbon-air mixtures at reduced pressures and room temperature. Technical report, Technical Report Archive and Image Library.
4. Tao, X., Li, N., & Li, Shaoyuan. (2016). Multiple model predictive control for large envelope flight of hypersonic vehicle systems. *Information Sciences*, *328*, 115–126.
5. Cho, P., & Law, C. K. (1985). Pressure/temperature ignition limits of fuel droplet vaporizing over a hot plate. *International Journal of Heat and Mass Transfer*, *28*(11), 2174–2176.
6. Zabetakis, M. G., Furno, A. L., & Jones, G. W. (1954). Minimum spontaneous ignition temperatures of combustibles in air. *Industrial & Engineering Chemistry Research*, *46*(10), 2173–2178.
7. EI-Wakil, M. M. & Abdou M. I. (1962). *The self ignition of fuel drops in heated air streams*. SAE Technical Paper: Technical report.
8. Troe, J. (1977). Theory of thermal unimolecular reactions at low pressures. i. solutions of the master equation. *Journal of Chemical Physics, 66*(11), 4745–4757.
9. Schranz, H.W., Nordholm, S., & Andersson, L.L. (1989). Pressure dependence of unimolecular reactions: Collision efficiencies in mixtures of weak and strong colliders. *Chemical Physics Letters, 161*(4C5), 432–438.
10. Le, T. M. H. (2015). Flammability Characteristics of Hydrogen and Its Mixtures with Light Hydrocarbons at Atmospheric and Sub-atmospheric Pressures. Ph.D. thesis, Texas A&M University.
11. Le, H.. Nayak, S., & Mannan, M.S. (2012). Upper flammability limits of hydrogen and light hydrocarbons in air at subatmospheric pressures. *Industrial & Engineering Chemistry Research, 51*(27), 9396–9402.
12. Le, H., Liu, Y., & Mannan, M.S. (2013). Lower flammability limits of hydrogen and light hydrocarbons at subatmospheric pressures. *Industrial & Engineering Chemistry Research, 52*(3), 1372–1378.
13. Menon, S. K., Boettcher, P. A., Ventura, B., & Blanquart, G. (2016). Hot surface ignition of n-hexane in air. *Combustion and Flame*, *163*, 42–53.
14. Battin-Leclerc, F., Herbinet, O., Glaude, P. A., Fournet, R., Zhou, Z., Deng, L., et al. (2010). Experimental confirmation of the low-temperature oxidation scheme of alkanes. *Angewandte Chemie International Edition*, *122*(18), 3237–3240.
15. Li, X., Huang, X., & Liu, H. (2018). A composite-fuel additive design method for n-decane low-temperature ignition enhancement. *Combustion and Flame*, *188*, 262–272.
16. Bartoszek, M., & Polak, J. (2012). An electron paramagnetic resonance study of antioxidant properties of alcoholic beverages. *Food chemistry*, *132*(4), 2089–2093.
17. Guo, Q., Qian, S. Y., & Mason, R. P. (2003). Separation and identification of dmpo adducts of oxygen-centered radicals formed from organic hydroperoxides by hplc-esr, esi-ms and ms/ms. *Journal of the American Society for Mass Spectrometry*, *14*(8), 862–871.
18. Ralph, J., & Hatfield, R. D. (1991). Pyrolysis-gc-ms characterization of forage materials. *Journal of Agricultural and Food Chemistry*, *39*(8), 1426–1437.
19. Kajiwara, A., Matyjaszewski, K., & Kamachi, M. (1998). Simultaneous epr and kinetic study of styrene atom transfer radical polymerization (atrp). *Macromolecules, 31*(17), 5695–5701.

20. Towell, J., & Kalyanaraman, B. (1991). Detection of radical adducts of 5,5-dimethyl-1-pyrroline n-oxide by the combined use of high-performance liquid chromatography with electrochemical detection and electron spin resonance. *Analytical Biochemistry*, *196*(1), 111–119.
21. Behrendt, F., & Warnatz, J. (1985). The dependence of flame propagation in h2/o2/n2 mixtures on temperature, pressure, and initial composition. *International Journal of Hydrogen Energy*, *10*(11), 749–755.

A Similarity Comparison Method of Flight Test Points

Yibo Liu, Gang Xiao and Yong Chen

Abstract Civil aircraft flight test has the characteristics of high risk, tight time, and huge cost. How to optimize the flight test task and make it more efficient has become a major concern for major civil aircraft design and manufacturing companies in the world. However, it is difficult to get specific information about related technologies from public references. A similarity comparison method for flight test points was proposed in this paper. The probability of coincidence between different flight test points can be calculated by this method, and the results were used to evaluate the similarity of flight test points, thereby providing a criterion for flight test task optimization. The proposed method was applied to solve a preliminary optimization problem of a flight test task for flight simulator data collection, satisfactory results were obtained. A useful exploration of the digitization and intelligent construction of civil flight test task management system was made also.

Keywords Flight test · Optimization · Flight test point · Probability algorithm · Weighted calculation

1 Introduction

1.1 Research Background

Generally, flight test engineering can be summarised as the engineering associated with the testing, in flight, of an aircraft or item(s) of aircraft equipment. The aims

Y. Liu (✉) · G. Xiao · Y. Chen
School of Aeronautics and Astronautics, Shanghai Jiao Tong University, Shanghai, China
e-mail: liuyibo1995@sjtu.edu.cn

G. Xiao
e-mail: xiaogang@sjtu.edu.cn

Y. Chen
e-mail: mechenyong@sjtu.edu.cn

Z. Jing (ed.), *Proceedings of International Conference on Aerospace System Science and Engineering 2018*, Lecture Notes in Electrical Engineering 549,
https://doi.org/10.1007/978-981-13-6061-9_13

of that testing can be very diverse: they may be to investigate new concepts, to provide empirical data to substantiate design assumptions, or to demonstrate that an aircraft and/or its equipment achieve specified levels of performance, etc. [1]. In the process of designing and developing civil aircraft, flight test is mainly to show the conformity of the civil aircraft model and obtain the airworthiness certificate. The civil aircraft design and manufacturing companies must show that they meet the bureau's current airworthiness requirements for civil aircraft through a series of flight tests [2]. With the development of flight test technology and the increasing number of flight test tasks, saving fuel consumption and duration of flight test has become one of the important goals of the flight test, because it can reduce the cost of flight test and decrease the flight test cycle. Meanwhile, the safety and reliability must be ensured [3]. According to public information, a typical flight test project includes 20,000–40,000 flight test points (FAA 25 PART/ EASA 25 PART/CAAC 25 PART), the completion of these test points requires 2,000–4,000 flight hours, and the cost per flight hour is between $20,000 and $40,000 [4]. The optimization of the flight test task can make it more efficient and reasonable, it has become a major concern for major civil aircraft design and manufacturing companies in the world.

The research work on optimization techniques for flight test tasks started in the 1980s. It was first applied to military aircrafts, then gradually applied to civil aircraft flight tests. In the 1980s, the American Dryden Flight Research Centre developed the ATMMS (Automatically Test Management System) to assist flight test engineers in the preparation of flight test plans, flight test monitoring, and flight simulation. in the 1990s, the United States Boeing Company developed the TPS (Test-Plan System) for the F-22 fighter jet's flight test. By setting up and maintaining the test information database in the TPS, the flight test engineers can quickly formulate the flight test plan in real time according to the execution status of the flight test status point. US Boeing uses TPS to conduct overall planning for Boeing 787 aircraft flight test, combing flight test tasks from different subjects, to efficiently use the flight time of each flight [5]. Chong Yuan, Zhongxin Xiu et al. developed a set of civil aircraft flight test planning and management system (FTPM) which has been validated and applied in practical flight test, which plays a role of reducing flight test sortie and improving the efficiency [6]. Mingshi Huang, Yongzhi Liu et al. designed a flight test management system that is already in use [7]. It has been proved that the reasonable overall arrangement of the entire flight test cycle can indeed reduce the cost of flight tests and shorten the flight test cycle [2].

However, due to commercial competition, technical confidentiality and other reasons, it is difficult to get specific information about related technologies from public references. Due to the lack of necessary technical means and professional tools, flight test engineers can only use their own experience to manually optimize the test task only within their professional field, which increased flight test efficiency poorly. An advanced flight test industry needs to have its own flight test data management system, flight test requirement analysis system, and flight test task optimization system. the amount of relevant key technical information is very limited as mentioned above. Therefore, with the construction of related systems, an independent research of related technologies is very necessary.

1.2 Content of This Article

In this paper, a similarity comparison method for flight test points is studied. Flight test requirements include the flight status that the aircraft needs to reach, the corresponding flight actions and a series of other regulations. These flight status requirements which contain many parameters are called flight test points.

The method defined and calculated the similarity of different flight test points. By comparing the similarities of flight test points, it can be determined whether these flight test points can be arranged in the same flight or not. The result provides the basis for the optimization of flight test tasks, help engineers to arrange flight test points in a more reasonable way to efficiently use the flight time of each flight, thereby achieving the goal of reducing flight test costs and shortening the flight test cycle.

There are five parts in this article. The first part is an introduction of the article which explains the research background, the reason and significance of the research in this field. The second part is data modelling. In this part, a brief introduction of the current flight test workflow shows the necessity of data modelling for flight test data, with the analysis of characteristics of flight test points, the two major parameters are selected. The analysis of characteristics of flight test points also provides the basis for the research of the comparison method. The third part is the details of the similarity comparison method for flight test points, which is the core of this article. In the fourth part, take two sets of flight test points as example. The two sets of flight test points are from flight simulator flight test and prototype flight test respectively, the method studied in this paper will be used to process them and the results will be evaluated to solve a preliminary optimization problem of a flight test task for flight simulator data collection. Use this example to verify the effectiveness of this method. The last part is a conclusion of this article.

2 Data Modelling of Flight Test Original Data

2.1 Current Status of Flight Test Workflow

Take the process of generating a flight test card for a certain type of passenger aircraft as an example. Flight test card is a set of specific flight test requirement that need to be completed in one flight test sortie.

At first, flight test engineers of various subjects compile flight test outlines according to their own professional requirements and submit them to the next department for detailed and concrete processing, so that they can complete the corresponding flight test requirements. Explanation of two terms: Flight test outline is a rough flight conditions and corresponding flight action requirements according to relevant regulations and other professional requirements. Flight test requirement is compiled by the relevant department conducts specific and detailed arrangements based on the flight test outline. Then the flight test requirements are transferred to the front flight

test engineers, and the flight test card for the actual flight task is compiled in light of the conditions such as aircraft configuration requirements and weather conditions.

Due to the lack of necessary technical means and professional tools, the optimization of flight test tasks becomes very difficult to operate and requires a large amount of preparatory work, especially when the task requires processing large amounts of data.

2.2 Flight Test Data Characteristic Analysis

In this article, the method needs to process a large number of flight test point data. Therefore, the flight test data needs to be pre-processed and structured. Before processing those data, the characteristics of flight test data need to be discussed first.

There is a flight test point table from a flight test requirement, as shown in Table 1. Most of the flight test points include parameters of weight, centre of gravity, height, velocity, slat configuration, and other parameters such as landing gear type and Engine. Depending on the requirements of different flight test subject, there are a total of dozens of parameters. Each parameter has different forms according to the relevant regulations. For example, the flight height may be given in specific values, the centre of gravity requirement is given in numerical ranges, and the landing gear status is given in the form of state descriptions.

2.3 Selection of the Major Parameters and Auxiliary Parameters

Most of the flight test points include the four parameters: weight, centre of gravity, height, velocity. The similarity of these four parameters largely determines whether the two flight test points can be considered together or not. Parameters such as height and velocity can be easily changed in a relatively large range during flight, but the

Table 1 Flight test points in table format

Cruise performance test state point						
Weight	Center of gravity	Height (ft)	Velocity	Flap/slat	Landing gear	Engine
High weight	Medium center of gravity	10,000	1.23 VSR–VMO	0 state	Receive	Double engine
High weight	Medium center of gravity	20,000	1.23 VSR–VMO	0 state	Receive	Double engine

weight and centre of gravity cannot, when the value is confirmed, it is difficult to change drastically during the flight, so the flight test points with large differences between weight and centre of gravity can be considered that they are not likely to be arranged in the same flight test sortie, the "distance" of the two points is "too far". Therefore, the weight and centre of gravity are extracted as the major parameters, height and velocity are used as auxiliary parameters, select these four parameters as input and use them to give similarity comparison results and recommendations of flight test points combination.

In view of the fact that there is no mature flight test point data processing system that can be used, the data processing work have to be down manually.

3 Similarity Comparison Method of Flight Test Points

3.1 The Principle of the Method

As described before, the weight and centre of gravity are selected as the major parameters, the height and velocity are selected as auxiliary parameters to calculate the similarity of the flight test points. The two major parameters are given in the form of numerical range in the flight test data. These two parameters are generally not allowed to be adjusted during flight; the forms of the two auxiliary parameters are not uniform, some flight test points adopt specific value form, others are given in numerical range form, both auxiliary parameters can be adjusted during the flight. Due to the difference in importance and the data form, the main parameter similarity and the auxiliary parameter similarity are calculated separately, and then the obtained result is weighted for the final similarity calculation result. The specific calculation method for the similarity of the two kinds of parameters will be described below. In the operation, firstly, the flight test points whose main parameter similarity satisfies the pre-designed requirement are selected, and then the similarity of the auxiliary parameters is considered in the selected flight test points for the second screening and sorting. The flight test point similarity finally obtained is used as the evaluation criterion of the degree of similarity between the flight test points.

3.2 Major Parameter Similarity Calculation Method

As discussed before, the most important parameters should be concerned about are the centre of gravity and the weight. In the flight test requirements, these two parameters are given in the form of numerical ranges, which means the value in actual engineering operation may be any value within the range. Considering this situation, the comparison of similarity can be defined as the calculation of the degree of coincidence of the numerical ranges of the two parameters.

Suppose the values of the parameter X of the two flight test points A and B are [p, q], [m, n] respectively, and the parameter X cannot be adjusted during the flight. The degree of similarity needs to be calculated. Based on point A, the probability density function at point A is $f(x)$. If [p, q] and [m, n] have coincident parts, when the value of parameter X of point A is in this coincidence part, the requirements of the two flight test points on the parameter X are satisfied simultaneously, then the two points have the probability that they can be arranged together. Therefore, the probability that the point A falls on the coincident portion is a criterion for the degree of similarity between the two flight test points. If the coincident section is [a, b], then the probability of coincidence, or the similarity of parameter X is:

$$P = \int_a^b f(x)\mathrm{d}x \tag{1}$$

The principle is shown in Fig. 1. When two or more parameters are given in the form of numerical ranges, the coincident part of the figure becomes the coincident area or volume, as shown in Fig. 2.

The coincidence probability formula becomes a multiple integral:

$$P = \int_{a_1}^{b_1}\int_{a_2}^{b_2}\cdots\int_{a_n}^{b_n} f_1(x_1)\ldots f_n(x_n)\mathrm{d}x_1\ldots\mathrm{d}x_n \tag{2}$$

In summary, the probability that point A may be combined with point B is the probability that point A is within the coincidence range.

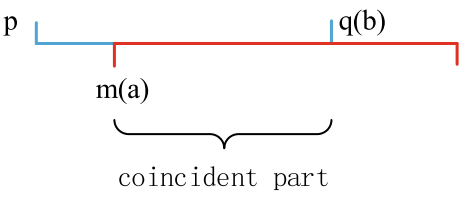

Fig. 1 Coincident part of two points' parameter X

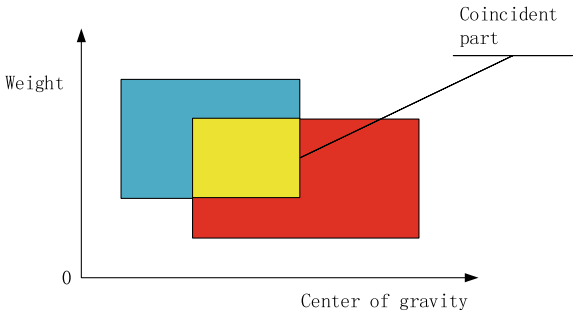

Fig. 2 Multiple parameters for comparison

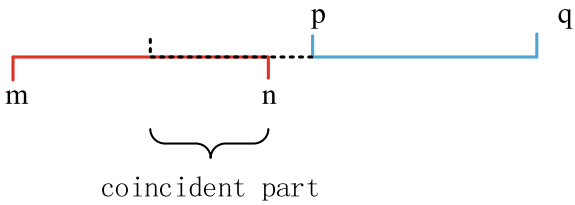

Fig. 3 Considering the change of parameters during the flight

In actual engineering operation, it is necessary to consider fuel consumption and changes in weight and centre of gravity at all stages of the flight [6]. The centre of gravity on some aircraft prototypes can be changed by a device. The weight of the aircraft decreases with fuel consumption, so it is necessary to consider these two variables. After considering the change of parameters in flight, although there is no coincident part in the original parameter requirements of the two flight test points, the value of one flight test point may satisfy the other flight test point requirement as shown in Fig. 3.

As shown in the above figure, the dashed line is outside the range of parameter X of the point A whose range is [p, q], but the dashed range may be reached in the actual flight. If there is a coincident part between this zone and the numerical range of parameter X of the flight test point B whose range is [m n], then these two test points may still be considered in combination with this parameter. The specific method of operation is to expand the value range [m, n] of the non-reference point B to the range [M, N], where the parameter change is considered, and then to overlap with the parameter X of point A.

For example, the parameter weight value range of flight test point A is [70,000, 78,900], the value of point B is [54,360, 66,440], and the change amount of weight change in one flight is −10,000. Based on point A, the coincident part is [70,000, 76,440]. Note that the range of weight changes cannot be made too large, because it means that the two flight test points can only be arranged at the beginning and end of a flight, which will bring difficulties to the actual engineering operation.

The final value of the weight and centre of gravity's similarity is a probability problem. Since it is not known which value the flight test engineers prefer to take in actual operation, it is necessary to assume a form of probability density function, which is the $f(x)$ mentioned before.

This is the statistical law of a large number of random processes. It is assumed that the probability of a flight test point is subject to a Gaussian distribution in this paper.

According to Lindberg-Levy's central limit theorem, set the random variable column $\{X_n\}$, $n = 1, 2, \ldots$ i.i.d. with finite expectation and variance, $\mathrm{E}X_n = \mu$, $\mathrm{D}X_n = \sigma^2 \neq 0, n = 1, 2 \ldots$ then random variable

$$Y_n = \frac{\sum_{i=1}^{n} X_i - n\mu}{\sqrt{n}\sigma} \tag{3}$$

The distribution function $F_n(x)$, for any real number x, satisfy

$$\lim F_n(x) = \lim_{n\to\infty} p\left\{\frac{\sum_{i=1}^{n} X_i - n\mu}{\sqrt{n}\sigma} \le x\right\} = \frac{1}{\sqrt{2\pi}} \int_{-\infty}^{x} \mathrm{e}^{-\frac{t^2}{2}} \mathrm{d}t \tag{4}$$

This theorem describes that under certain conditions, the distribution of normalized random variable columns has a standard normal distribution as the limit distribution [8].

Since the normal distribution can well represent the distribution law of a large number of random variables [8], it is assumed that the probability distribution of the value of the flight test point in the numerical range of the parameter obeys the normal distribution.

If the random variable $X \sim N(\mu, \sigma^2)$, then $P(|X - \mu| < 3\sigma) = 99.7\%$, if the specified numerical range of the test flight test point parameter is [a, b], assume that

$$\mu = \frac{a+b}{2}, \sigma = \frac{b-a}{6} \tag{5}$$

Probability density is set to

$$f(x) = \frac{1}{\sqrt{2\pi}\sigma} \mathrm{e}^{-\frac{(x-\mu)^2}{2\sigma^2}} \tag{6}$$

3.3 Auxiliary Parameter Similarity Calculation Method

Because the auxiliary parameters are not uniform in the flight test data, there are three different forms of data comparison: specific value and specific value comparison, specific value and numerical range comparison, numerical range and numerical range comparison. A unified indicator is needed to compare the degree of similarity of the auxiliary parameters between different data forms. Since the auxiliary parameters can be adjusted during the flight, the maximum adjustment amount is selected as the comparison criterion for the similarity degree of the auxiliary parameters. The maximum adjustment amount means, in the worst case, the flight test point as a reference needs to adjust how much so that this parameter can meet the parameter requirements of another flight test point. This comparison method can consider all three kinds of comparisons.

The following is a description of the similarity calculation method of the auxiliary parameters by taking the height comparison calculation as an example.

1. Specific value and numerical range comparison:

Set flight test point A as the reference, height parameter H_a; flight test point B, height parameter $[H_{b1}, H_{b2}]$.

When $H_{b1} < H_a < H_{b2}$, the height of the flight test point A does not need to be adjusted to meet the requirements of B, the adjustment amount is 0;

When $H_a < H_{b1} < H_{b2}$, the maximum height adjustment of the flight test point A is $(H_{b1} - H_a)$;

When $H_{b1} < H_{b2} < H_a$, the maximum height adjustment of the flight test point A is $(H_a - H_{b2})$.

If test point B is the reference point, then

When $H_{b1} < H_a < H_{b2}$, the maximum height adjustment of the flight test point B is the bigger one of $(H_{b2} - H_a)$ and $(H_a - H_{b1})$;

When $H_a < H_{b1} < H_{b2}$, the maximum height adjustment of the flight test point A is $(H_{b2} - H_a)$;

When $H_{b1} < H_{b2} < H_a$, the maximum height adjustment of the flight test point A is $(H_a - H_{b1})$.

2. Numerical range and numerical range comparison:

Set flight test point A as the reference, height parameter $[H_{a1}, H_{a2}]$; flight test point B, height parameter $[H_{b1}, H_{b2}]$, coincidence interval $[H_1, H_2]$.

If there is a coincident portion, the maximum adjustment amount is the length of the non-coincidence portion of the height parameter of the reference flight test point, as shown in Fig. 4a. If the coincident portion equals to $[H_{b1}, H_{b2}]$, the maximum adjustment amount is the larger non-coincident portion, as shown in Fig. 4b. If the coincident part is the entire interval of the reference flight test point, the maximum adjustment amount is 0. If there is no coincident part, the maximum adjustment amount is as shown in Fig. 4d.

Specific value and specific value comparison:

When both comparison flight test points represent the parameter height in a specific value form, the maximum adjustment amount is the absolute value of the difference between the two values.

Set flight test point A as the reference, height parameter H_a; flight test point B, height parameter H_b. The maximum adjustment amount is $|H_b - H_a|$.

As described above, the similarity of the auxiliary parameters can be evaluated by using the maximum adjustment amount as the evaluation criterion. Since the weighting calculation is finally performed together with the calculation result of the major parameters, it is necessary to convert the maximum adjustment amount into a number within one, this number is defined as the similarity of the auxiliary parameter.

A screening should be performed before the conversion, although the auxiliary parameters can be changed during the flight, but the excessive range of variation will make the combination of the two flight test points inoperable. For the auxiliary parameters, it is assumed that if the adjustment exceeds a certain number M, the two flight test points are impossible to be considered for combination.

After the screening is completed, the auxiliary adjustment amount range is $[0, M]$. When the adjustment amount is 0, the similarity is considered to be the best, and is set to 1. When the adjustment amount is M, the similarity is 0. Let the similarity be y and the maximum adjustment be x, then the function relationship between y and x is:

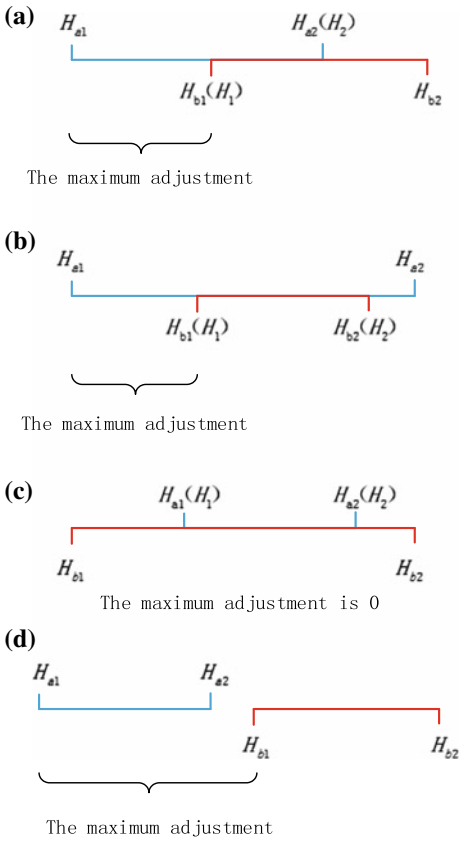

Fig. 4 The maximum adjustment in different situation

$$y = -\frac{1}{M}x + 1 \tag{7}$$

3.4 Specific Operation Flow of Similarity Comparison Method

The specific steps of the similarity comparison of the test flight test point are: setting a probability value P, only the flight test point whose main parameter similarity is greater than this value can perform the next operation; the second screening selects the flight test point whose maximum adjustment amount is less than M. Finally, sort according to the similarity of the flight test points. Proceed as follows:

First screening: major parameter similarity $>P$
Secondary screening: maximum adjustment amount of auxiliary parameter $<M$
Final sorting calculation:

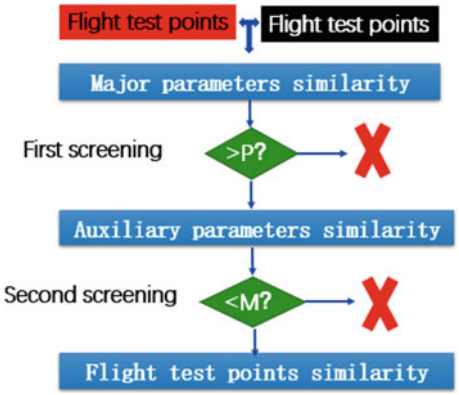

Fig. 5 The process of calculation

flight test point similarity = major parameter similarity × weight 1 + auxiliary parameter 1 similarity × weight 2 + auxiliary parameter 2 similarity × weight 3

Sort according to the flight test point similarity, and output flight test points combination suggestion. The process of calculation is as shown in Fig. 5.

4 Application of Similarity Comparison Method

4.1 Application Background

In current civil aircraft flight test workflow, after the completion of the prototype flight test task, additional flight test sorties are arranged to perform flight test task for flight simulator data collection. Although the flight test task of flight simulator and the flight test task of prototype follow different regulations and different standards, there exists many similar parts, a large number of flight test points can be considered together. In the past, there was not enough emphasis on the flight test points combination work, a lot of repetitive work was performed, which has caused great waste of resources, time, and money. Therefore, the optimization and integration of the flight test task for flight simulator should be considered in the preparation phase of the overall flight test task compilation.

Although the necessity of optimization and integration of flight test task has been recognized, there still lacks tools and methods. The similarity comparison method can offer some help to this task.

In this paper, some flight test point data of flight simulator and flight test point data of prototype are used as the input of the method. The flight test point similarity comparison method can provide a reliable criterion for preliminary optimization of

Table 2 Structured flight test data

Centre of gravity	Weight	Height	Flight test point's name
[22, 34]	[70,000, 78,900]	10,000	Cruise performance test state point 1'
[22, 34]	[70,000, 78,900]	20,000	Cruise performance test state point 2'
[22, 34]	[70,000, 78,900]	30,000	Cruise performance test state point 3'

flight test task of flight simulator data collection. For every flight simulator flight test point, it can be determined that which prototype flight test point it can be combined with.

4.2 The Method Application Process

As mentioned above, the first step is data modelling of the flight test data. As shown in Table 2. Due to the lack of data for parameter velocity, the auxiliary parameter considered in this paper is only height.

The purpose of applying this method for task optimization is to consider as many as possible flight simulator test points in the prototype flight test task. Therefore, use the prototype flight test points as reference to calculate the similarity. According to the method developed in this paper, using weight and centre of gravity as major parameters, height as auxiliary parameter, take prototype flight test points as reference, the similarities between the flight test points of flight simulators and prototype flight test points are calculated. Assume that in one flight, the centre of gravity cannot be adjusted, the fuel consumption is 10 tons. The range of weight change cannot be made too large, so take the variation range as 3 tons.

As mentioned above, the first step is to calculate the similarity of the main parameters, select the flight test points that meet the requirements. The second step is to calculate the maximum adjustment amount of the auxiliary parameter height, screen out the flight test points with the maximum adjustment that meets the requirement. Finally, the similarity of the flight test points is calculated according to the calculation results of the two kinds of parameters, and the flight test points are sorted according to the similarity. After several experiments, 0.75 was selected as P and 5000 was selected as M. Use MATLAB to implement this method.

Because the number of flight simulator flight test points is relatively small, the output table is designed in the following form: For each flight simulator flight test point, a set of prototype flight test points that meet the requirements is given.

As shown in Table 3, the first column is the index of the flight test points of the flight simulator, and the second column is the collection of flight test points of the prototype that meet the screening conditions and stored in cell format in MATLAB. Open one of the cells, where the flight test points are sorted according to the flight test point similarity.

As shown in the Table 4, it is a demonstration of a set of flight test points of the prototype, these flight test points are sufficiently similar to the flight simulator flight test point "Cruise performance flight test points1". The first column is the name of the flight test point, the second column is the main parameter similarity, and the third column is the maximum adjustment of height. The fourth column is the similarity of the flight test point. It can be seen that the point whose main parameter similarity is 0.8056, the height maximum adjustment is 0, its similarity is 0.8639, which is better than the flight test point with the main parameter similarity of 1 but the maximum height adjustment is 5000 ft. This result shows that the selected weights are reasonable.

Based on the results above, a table was formulated for the engineers, for every flight simulator flight test point, the original data of the selected prototype flight test points are given, left to the engineers for final manual judgment.

Relying on the method proposed in this paper, a lot of manual work was eliminated. The flight test engineers can directly perform further optimization work based on the calculation result.

Based on the idea of the method, a prototype software was developed for the similarity calculation of flight test points. The main UI interface is shown in Fig. 6.

Table 3 Calculation result display form

Name of flight simulator flight test point	Prototype flight test point set
Deceleration time and distance flight test points 1	'No similar flight test points'
Single engine failure trim flight test points 1	14 × 4 cell
Single engine failure trim flight test points 2	14 × 4 cell
Cruise performance flight test points 1	19 × 4 cell
Cockpit roll control step-by-step input rollover response flight test points 1	14 × 4 cell

Table 4 Flight test point similarity calculation result

Name of the prototype flight test point	Main parameter similarity	Maximum adjustment of height	Similarity of the flight test point
The Highest cruise velocity flight test point 4	1	0	1
The Highest cruise velocity flight test point 5	1	0	1
Lateral manipulation -double engine work flight test point 2	0.8056	0	0.8639
Cruise performance test state point 2	1	5000	0.7

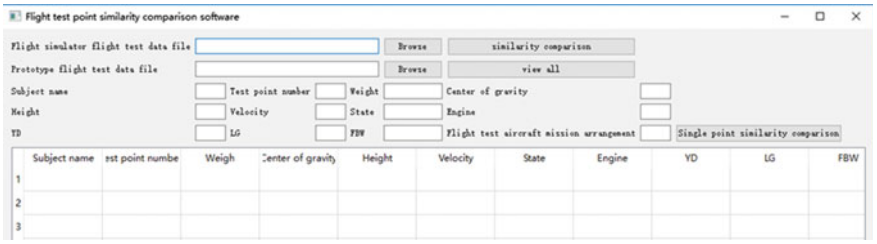

Fig. 6 The main UI interface of the prototype software

5 Conclusion

A method to compare the similarity of flight test points was proposed in this paper. Based on the analysis of the flight test point data characteristic, centre of gravity and weight were selected as two major parameters, height and velocity as auxiliary parameters. Assuming that the major parameter probability is subject to a Gaussian distribution, with consideration of the maximum adjustment of auxiliary parameters, the similarity of different flight test points was calculated. With some flight test data as input, the method was used to solve a preliminary optimization problem of a flight test task for flight simulator data collection, satisfactory results were obtained. Based on the idea of the method, a prototype software was developed. It was approved that the application of this method can successfully eliminate a lot of manual work.

Acknowledgements This paper is sponsored by National Program on Key Basic Research Project (2014CB744903), National Natural Science Foundation of China (61673270), Shanghai Pujiang Program (16PJD028), Shanghai Industrial Strengthening Project (CYQJ-2017-5-08), Shanghai Science and Technology Committee Research Project (17DZ1204304) and Shanghai Engineering Research Center of Civil Aircraft Flight Testing.

References

1. Stoliker, F. N. (2005). *Introduction to flight test engineering (Introduction aux techniques des essais en vol)*. NATO RESEARCH AND TECHNOLOGY ORGANIZATION NEUILLY-SUR-SEINE (FRANCE).
2. Feng, S. D. (2014). *Research and Implementation of Digitalized Management System for Civil Aircraft Flight Test Task*. Shanghai: Jiao Tong University.
3. Shen, H. L., Yu, Y. J., & Liu, C. (2000). Study on Optimal Ordering Problem of Flight Test Maneuvers. *Journal of Nanjing University of Aeronautics & Astronautics*, *32*(3), 312–317.
4. Lampe, T., Bergwall, L., Marle, et al. (1992). Test-plan to kung: an automated flight test planning environment applied to the JAS-39 gripen flight test program. *Saab-Scania AB, Sweden*, *4*, 11–21.
5. Yan, Z. K., Guo, B. Z., & Ding, Z. T. (2014). Investigation and Realization of Flight Test Task Optimization for Civil Aircraft. *Civil Aircraft Design and Research*, *2014*(3), 12–16.
6. Yuan, C., Xiu, Z. X., Tian, H. L., et al. (2014). Research on Flight Test Planning and Management for Civil Aircraft. *Civil Aircraft Design and Research*, *2014*(3), 1–4.

7. Huang, M. S., & Zheng, Q. (2000). The design and implementation of flight test management system. *Flight Dynamics*, *18*(4), 14–16.
8. Department of Mathematics, Huazhong University of Science and Technology. (2008). *Probability Theory and Mathematical Statistics*. Peking, China: Higher Education Press.

Author Index

B
Bao, Huan, 39
Bavirisetti, Durga Prasad, 53, 169
Borovik, I., 155

C
Chen, Chen, 1
Chen, Yong, 197

D
Duan, Dengping, 105

F
Fang, Jicheng, 137

G
Gong, Ke, 169

H
Hongya, Tuo, 1
Huang, Xiaobin, 185
Hu, Shiqiang, 121

I
Ionov, A., 155

L
Li, Yuanxiang, 1
Liu, Hong, 185
Liu, Yibo, 197

M
Ma, Lin, 93
Matushkin, A., 155
Ma, Wei, 39

S
Seliverstov, S., 155
Shi, Yaming, 185
Starikov, P., 155
Svetlana, Koval, 69

T
Tuo, Hongya, 1

W
Wang, Minghua, 121
Wang, Quanbao, 105

X
Xiao, Gang, 53, 169, 197

Y
Yang, Mingsui, 39
You, Qingwen, 137
Yu, Yin, 93
Yu, Zhefeng, 137

Z
Zhang, Dapeng, 17
Zhang, Xingchen, 53, 169
Zhao, Junhao, 53, 169
Zhao, Liuyue, 105
Zhou, Pingfang, 105
Zhou, Yongjun, 1
Zhou, Yu, 1
Zhou, Xiang, 17

Z. Jing (ed.), *Proceedings of International Conference on Aerospace System Science and Engineering 2018*, Lecture Notes in Electrical Engineering 549,
https://doi.org/10.1007/978-981-13-6061-9